Not everything that can be counted counts.
Not everything that counts can be counted.
– Albert Enstein.

A bold speculative thought may often prove more seminal
than a body of carefully assembled facts.
– Pierre Gloor.

In the appropriate minds
pretty pictures lead to pretty problems
and to entirely new fields.
– Benoit Mandelbrot.

University of Alberta

Diffusion tensor tractography of temporal lobe epilepsy

by

Luis CONCHA LOYOLA 

A thesis submitted to the Faculty of Graduate Studies and Research in partial fulfillment of the requirements for the degree of **Doctor of Philosophy**.

in

Medical Sciences – Biomedical Engineering

Edmonton, Alberta
Spring 2008

Your file Votre référence
ISBN: 978-0-494-45410-7
Our file Notre référence
ISBN: 978-0-494-45410-7

Abstract

Temporal lobe epilepsy (TLE) is the most common form of localization-related epilepsy and is generally refractory to medical treatment. The lesion most frequently associated with it is unilateral mesial temporal sclerosis (MTS), characterized by neuronal loss and gliosis of the mesial temporal structures. Despite being a relatively common disorder, its pathogenesis and pathophysiology remain largely unknown. In recent years, it has become increasingly recognized that TLE is a network disorder that involves the interaction between several temporal and extra-temporal structures.

Diffusion tensor imaging (DTI) is a novel and invaluable tool for the study of the brain's connectivity. The directional information on the diffusion of water molecules gained by DTI can be exploited to reconstruct the three-dimensional structure of white matter tracts (a method known as tractography). Most notably, DTI is able to detect (non-invasively and in a short time) the microscopic characteristics and integrity of tissue.

In this dissertation, DTI and tractography were utilized to assess the tissue integrity of several white matter bundles in patients with TLE. Through this method, *bilateral* abnormalities of white matter integrity were found in temporal and extra-temporal structures (fornix, cingulum, external capsules and corpus callosum) in patients with TLE and *unilateral* MTS. Given the lack of normalization upon seizure freedom after surgical resection of the sclerotic structures, these abnormalities are likely not due to functional fluid shifts caused by seizures themselves, but due to structural changes. While the extra-temporal abnormalities are also seen in TLE patients without MTS, the limbic changes (i.e. in the fornix and cingulum) appear to be exclusive to the presence of MTS. Electron microscopy examination

of the fornix resected during TLE surgery reveals that patients with MTS have less axons and that they are less tightly packed than those patients without MTS. These histological abnormalities likely are the underlying mechanism for the observed diffusion abnormalities.

In conclusion, abnormalities of the brain's connectivity that are specific to TLE and MTS have been demonstrated, which may play a crucial role in the mechanism of TLE. Future work is needed to estimate the timing of apparition of these abnormalities and the genesis of TLE.

To my family, my wife,
and the children in our dreams.

To my grandfather,
for showing me how beautiful curiosity can be.

ACKNOWLEDGEMENTS

First and foremost, I would like to thank my supervisors, Christian and Don, who helped me greatly throughout my degree. I appreciate that they took their chances when they accepted to supervise a clinician with absolutely no engineering/physics background, their patience during my slow initial learning period, and their friendship. Their multiple and thorough corrections to all my papers and abstracts were invaluable; their use of red ink was remarkable, turning every comment into improvements in my work. They are both excellent supervisors, and together they make a fantastic team. They taught me not only science but, most importantly, to think like a scientist. I look forward to a life of collaborations with them. No matter how much time passes, they will always be my supervisors.

Thanks are due to all my Professors at the University of Alberta. I truly enjoyed learning from Drs. Peter Allen, Alan Wilman and Richard Thompson who, along with Christian, taught me all I know about NMR. Dr. Richard Snyder gave the most amusing lectures on the basics of BME. Dr. Kelvin Jones re-kindled my interest in basic neurophysiology and sparked my enthusiasm in simulations and all the fun world of computational neuroscience. Drs. Richard Camicioli, Nick Coupland and Sanjay Kalra always had interesting comments about my work, and working with them has been a pleasure. I also appreciate the constructive input given by Dr. Paolo Federico.

Hanging out with and learning from other students has been great. Superbright Atiyah Yahya and my former office-mate Keith Wachowicz helped me during my first courses. Chilo Bonilla, fellow Mexican, taught me how to use Matlab, now indispensable to me, and became one of my closest friends, despite the fact that he's moved far away. Thanks to Catherine, fellow tractographer and statistics expert, and her husband Marc Lebel (who still manages to beat me a squash) for their interesting discussions on DTI and MRI in general, Catherine's encouragement for my running, and their overall friendship. Yusuf Bhagat taught me how to use the scanner and analyze my data. Rob Stobbe (another person who I have yet to beat at squash) never ceases to amaze me with his best-in-the-world Sodium images and his modesty when presenting them. It was fun writing this thesis at the same time as Jacob Ellegood wrote his, sharing notes, racing to finish every Chapter, and freaking out weeks before our final Defense dates. I also have to thank Gaolang Gong for teaching me lots more about tractography and

image manipulation, and for introducing me to the delicious Hot-Pot (so spicy that even Mexicans are scared!). Nikolai Malykhin was always my toughest critic when it came to tractography, and I truly appreciate that, as it made me improve my methods and obtain more reliable data. Thanks to Alexander Leemans, for teaching me tractography-related stuff and how to typeset using LaTeX.

Thanks to Beau Sapach, not just for keeping my computer in top shape, but for coding the tools I used for the microscopy analysis. Of course, thanks to Maisie Goh for saving my life all those times when I had paperwork that was past due time. Thanks also to Gritchie for her administrative support and her nice way of doing her job.

Dr. Matt Wheatley was very kind to allow me to go into the operating room during epilepsy surgeries and for supplying the specimen of the fimbria/fornix for analysis. Dr. Daniel Livy has been instrumental in the microscopic study of the fornix. Without them, that particular study would not have been possible. I also need to thank Drs. Barry Sinclair and Nazam Ahmed who taught me a lot about epilepsy. Daphne Quigley helped me with the scanning of epilepsy patients; her big smile and amazing football stories made the scan time seem quite short. Lori Robertson helped me collect patient data (and reimbursements!).

Although time has passed, I still need to thank my Professors from Medical School in Mexico. It was them who planted the seed of curiosity in me and encouraged me to follow the path I am currently in. Thanks to the Universidad Autónoma de San Luis Potosí and the Promep for supporting me financially during my degree.

Big thanks and cheers to all the Mexican gang in Edmonton. Special thanks are due to Daniel Torres for teaching me about 3D visualization and working with me create a fantastic animation, to Sandra Olarte, for her statistical advice, and to Paco Jimenez and Karla Barron for being such good friends.

Thanks to the numerous patients and control subjects who volunteered their time and allowed me to scan them. Being very still for nearly an hour on a shaking, narrow, loud and tube-like structure is certainly more difficult than it would seem.

I have to thank my family, who made me who I am. I would be lost without their teachings and their never-ending love. My dad taught me the value of hard work, and my mom taught me how to always do things right. I also thank my sister and my brother for always cheering me on.

And finally, but very importantly, I have to thank my wife, Arodi. She has always encouraged me in all that I have done, even when it meant being apart for three years when I came to Edmonton, while she stayed in Mexico finishing her Residency. She is not only a wonderful physician, but an amazing woman. I find it incredible that she has the patience to listen to me when I get a crazy idea at 2am. Being with her, and being loved by her, are the best things I can dream of.

Table of Contents

List of Tables

List of Figures

List of Abbreviations

λ_{1-3} Eigenvalues, organized in descending order of magnitude, page 17

ν_{1-3} Eigenvectors corresponding to the eigenvalues, page 17

$\lambda_{\parallel}$ Parallel diffusivity ($\lambda_{\parallel} = \lambda_1$), page 20

$\lambda_{\perp}$ Perpendicular diffusivity ($\lambda_{\perp} = [\lambda_2 + \lambda_3]/2$), page 20

ADC Apparent Diffusion Coefficient, page 13

CSF Cerebro-spinal fluid, page 14

DTI Diffusion tensor imaging, page 19

DWI Diffusion-weighted imaging, page 12

EEG Electro-encephalogram, page 41

EPI Echo-planar imaging, page 18

FA Fractional Anisotropy. Equation 2.13, page 22

FACT Fiber-assignment by continuous tracking, page 27

FOV Field of view, page 36

GM Gray matter, page 13

MD Mean diffusivity, page 18

MRI Magnetic resonance imaging, page 46

MTS Mesial temporal sclerosis, page 61

NMR Nuclear Magnetic Resonance, page 9

ROI Region of interest, page 31

SPM Statistical parametric mapping, page 32

TLE Temporal lobe epilepsy, page 48

WM White matter, page 14

Part I

Introduction

CHAPTER 1

JUSTIFICATION

Epilepsy is a diverse and common group of disorders of which temporal lobe epilepsy is the most common of the localization-related forms. Furthermore, temporal lobe epilepsy is generally very refractory to medical treatment. Since the decade of the fifties, however, surgical resection of the temporal structures has proven to be a successful treatment for these patients, in particular when they have an associated lesion identified on neuroimaging. The presence of a visually evident lesion has a tremendous positive impact on the success rate of surgery. For this reason, great attempts are made in all neuroimaging fields in order to increase the rate of detection of very subtle lesions that are not otherwise visible with conventional imaging.

In the field of magnetic resonance imaging, in particular, several contrast mechanisms and post-processing schemes have been proposed. These new techniques have certainly increased the diagnostic yield of this form of imaging, although an important sub-group of patients with temporal lobe epilepsy remain elusive to the demonstration of brain lesions. Nevertheless, based on clinical observation, it is presumed that these so-called *non-lesional* patients indeed have some sort of abnormality that remains to be identified.

Although epilepsy is unquestionably a disorder of the gray matter, as seizures are generated in it, it is the white matter that is responsible for the propagation of the abnormal electrical activity. For obvious reasons, most imaging groups have focused their efforts on the gray matter and have made considerable ad-

vancements in the field. The white matter, however, has apparently been largely neglected by many research groups in the study of epilepsy, assumed to play a merely passive role in the propagation of seizures.

In 2003, we wondered if one could detect the down-stream effects of gray matter changes (neuronal death, in particular), in the underlying white matter in patients with temporal lobe epilepsy. It has been known for over a century that the neuronal axons degenerate following an insult to the soma. It had been previously demonstrated that such distant fiber degeneration can be detected by measuring the diffusion characteristics of water molecules. Hence, we hypothesized that the white matter, extending from a region of gray matter where an important number of its neurons were dead, would show the particular pattern of water diffusion abnormalities linked to secondary degeneration. At that time, less than a dozen peer-reviewed articles had used diffusion tensor imaging in the study of epilepsy, and less than a third of those focused on the white matter. Tractography was still in its infancy. The idea was to use this technique to show evidence of a lesion in the elusive non-lesional temporal lobe epilepsy patients. However, in order to test the validity of our assumption, it was first necessary to study a group of patients with known and focal neuronal death linked to their epileptic disorder. This is the essence of a lesion known as mesial temporal sclerosis, commonly seen in temporal lobe epilepsy and typically visible on conventional imaging (Section 3.2.3). With these patients, it was not hard to figure out where to look for white matter abnormalities, for their disorder is focalized to the temporal lobe and its interconnected components, all part of what is called the limbic system. We decided to focus on two important temporal lobe white matter structures: the fornix and the cingulum. To look for the abnormalities, a novel technique known as *tractography* would be used to virtually dissect these white matter structures and to analyze the diffusion properties of the tissue. The patients with mesial temporal sclerosis had the added benefit of having such a lesion only on one hemisphere of the brain, allowing a direct comparison to the presumed healthy side to be made. Chapter 4 details the methodology utilized and Chapter 5 the results obtained from this experiment.

The information on the white matter was not amenable to pin-point the side with mesial temporal sclerosis. This was, however, not due to a lack of abnormalities on that side. Surprisingly, these patients showed *bilateral* white matter abnormalities, despite having *unilateral* suspected neuronal death. Although these results precluded the use of this particular method for clinical purposes, it was an intriguing and novel finding that posed new and exciting questions that needed to be resolved. What are these white matter abnormalities? Why are they bilateral? Are they related to ongoing seizures? Do they disappear upon cessation of seizures? Are they present in patients with non-lesional temporal lobe epilepsy? Are they present in other forms of epilepsy? Are they a cause or a consequence of epilepsy?

This dissertation addresses some of these questions and attempts to provide some insight into the pathophysiology of temporal lobe epilepsy through the study of the interconnecting white matter, which we now believe is more than just a bystander. This thesis is organized into three parts: Part I will introduce the bio-physical principles of the methodology utilized throughout (Chapter 2) and present the important aspects of temporal lobe epilepsy (Chapter 3). Part II compiles the experiments performed to address specific questions on the characteristics of the identified white matter abnormalities. Finally, Part III brings the information gained together and provides concluding remarks on what was learned.

Chapter 2

Diffusion Tensor Imaging and Tractography

2.1 Diffusion of water molecules

All molecules with a temperature above absolute zero (i.e., >-273.15 °C) are in constant motion. This phenomenon was first described in 1828 by Robert Brown[1], based upon the observation of random motion of grains of pollen suspended in water. Although grains of pollen are considerably larger than individual molecules, the behaviour described by Brown is similar to that seen in molecules [a]; thus, the molecular phenomenon is commonly referred to as Brownian motion. Diffusion is thermally driven and in the simplest case is completely stochastic, with each molecule describing a "random walk" over time. For example, if a single water molecule suspended in an infinite sea of calm water could be followed over time, the path would appear to be completely random, with equal probabilities of going anywhere at each time step. The longer we observed, the farther the water molecule could be from where it started. However, having equal probabilities of moving in any direction, the *average* displacement over time would be zero.

Albert Einstein mathematically solved Brown's observations[2]. Let us consider several water molecules diffusing freely, each one with an initial position r at time

[a] In fact, the motion of the grains of pollen was secondary to the diffusion of water molecules in which they were suspended in.

$t = 0$. If we allow them to diffuse for a period of time τ, each water molecule will then be in position r'. The diffusion coefficient D can be found by:

$$D = \frac{1}{6\tau} \left\langle \mathbf{R}^T \mathbf{R} \right\rangle \tag{2.1}$$

where $\mathbf{R} = r' - r$. The spin displacement in time is considered over the spin ensemble (angled brackets). The root mean square displacement over time t is given by:

$$rms_n = \sqrt{2nDt} \tag{2.2}$$

where n is the number of dimensions. The displacement of water molecules in one dimension is exemplified in Figure 2.1.

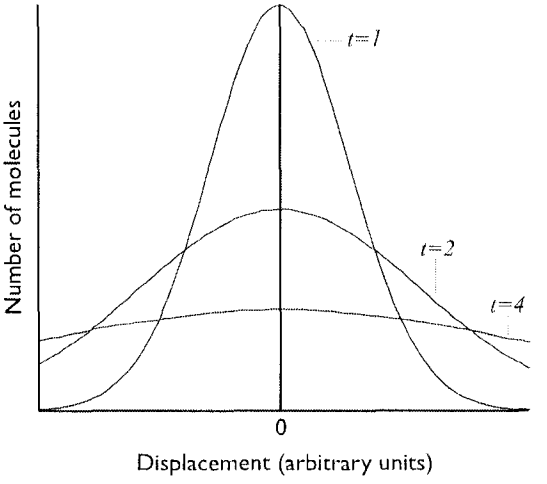

FIGURE 2.1: **One-dimensional displacement of water molecules over time.** An arbitrary number of water molecules with *position* = 0 at $t = 0$ diffuse over time. The gaussian displacement profile broadens as time passes.

Recall that diffusion is random (i.e., isotropic) and, therefore, D is directionally independent. The magnitude of D is dependent on the viscosity and temperature of the medium, and the size of the molecule. D of water at 37 °C is around 3.04 $\times 10^{-3}$ mm^2/s [3].

For the case of water molecules, the solute and the solvent are the same molecule, and the phenomenon is properly termed self-diffusion, for which the

simple random walk model can appropriately predict its behavior. Examples of self-diffusion of water molecules can be seen in Figure 2.2. For the remainder of this thesis, the term *diffusion* is used to refer to the self-diffusion of water molecules.

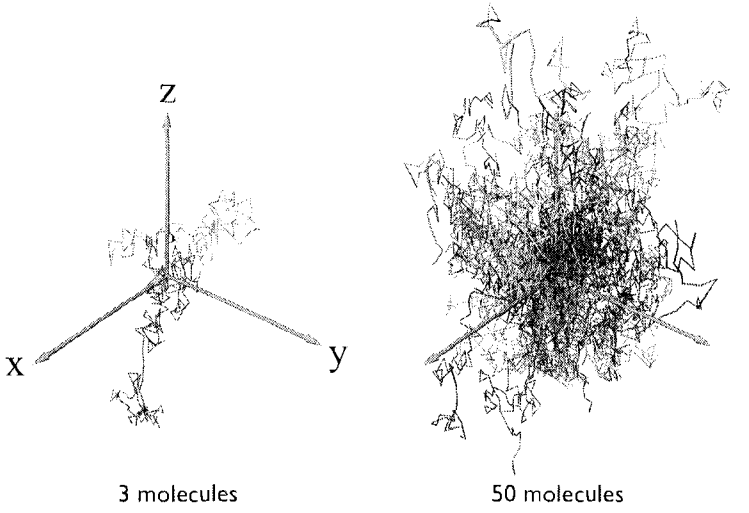

FIGURE 2.2: **Simulation of random walk over 100 time steps of 3 and 50 water molecules.** The direction of each molecule is randomly defined at each time step. Over time, the water molecules have a non-zero probability of visiting any position in space but have, on average, moved little (if any) from the origin.

2.1.1 Measuring diffusion with nuclear magnetic resonance

The effects of diffusion on the NMR signal have been known since the 1950s, when the spin-echo was described by Hahn[4]. A few years later, Carr and Purcell published their paper on quantitative T2 measurements, in which they recognize the importance of diffusion and even measure D of a water sample[5]. In 1956, Torrey modified Bloch's equations to include a diffusion term[6]. These first attempts to measure D were based on the use of a constant perturbation of the main magnetic field which, among other problems, made the distinction of D-related effects from transverse relaxation difficult.

However, it was the work of Stejskal and Tanner[7] in the sixties that facilitated the quantitative measurement of molecular diffusion coefficients by the use of a

pulsed gradient spin echo sequence (PGSE). The basic idea is to encode the spatial position of water molecules (spins) at $t = 0$, invert the spin phase with a π-pulse, and decode the spin position after time τ. The spin position is encoded and re-coded with the use of magnetic field gradients (Figure 2.3). In more detail: After the application of a $\pi/2$ radio-frequency pulse that places the net magnetization in the x, y plane with zero-phase, a magnetic field gradient with amplitude G and duration δ is turned on, which imparts a phase to the spins according to their spatial position. A π radio-frequency pulse then reverses the spins' phase. A second magnetic field gradient with the same characteristics as the first one (with a separation of $time = \Delta$) causes non-moving spins to re-gain their original phase. The NMR signal (echo) is acquired at this point. If the spins move during the time between the two magnetic field gradients (due to diffusion or any other cause), the spins will not re-phase completely, which causes less NMR signal to be acquired. Note that the field gradients are applied linearly in one dimension, providing diffusion sensitization only to spins moving in that particular direction. That is, if a spin moves perpendicularly to the field gradient direction, it will not contribute to the loss of NMR signal. The signal can be acquired through a spin-echo, as described above, or through a stimulated echo[8]. The latter approach, being heavily T1-weighted, minimizes the loss of signal through transverse relaxation, although its very nature translates into a 50% reduction of the original available signal.

By modifying the characteristics of the PGSE sequence, one can increase or decrease the sensitivity to diffusion. If the amplitude of the gradients is increased (G), spins will require less motion to experience a different magnetic field, thus increasing phase change. Alternatively, one can allow the spins to diffuse for a longer period of time, increasing the probability of the spins to dephase. The diffusion time is expressed as $\Delta - \delta/3)$, where the $\delta/3$ correction accounts for the diffusion which occurs during the time in which the gradients are turned on[7]. The sensitivity to diffusion is expressed as:

$$b = \gamma^2 G^2 \delta^2 \left(\Delta - \frac{\delta}{3} \right) \tag{2.3}$$

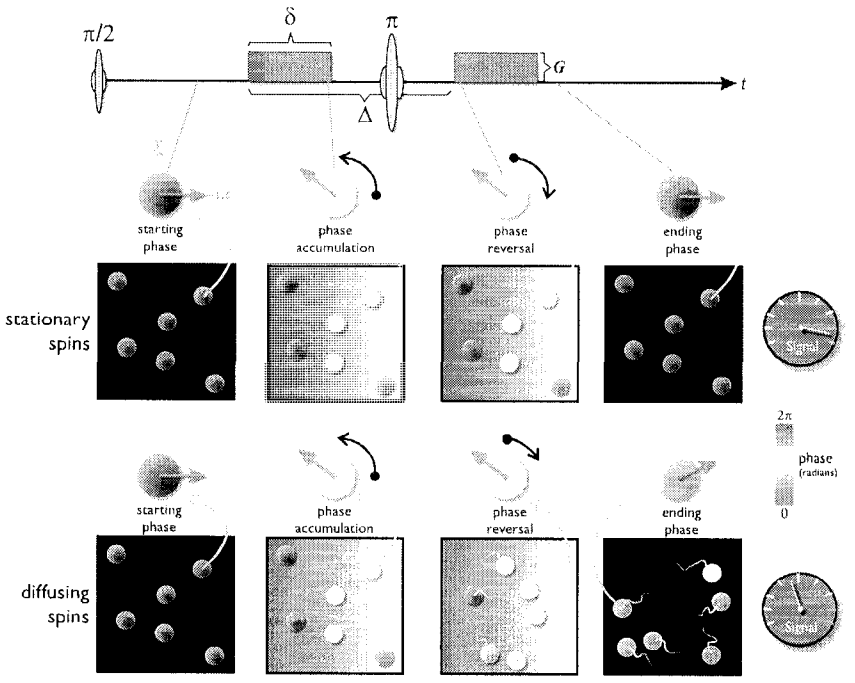

FIGURE 2.3: **Pulsed gradient spin echo sequence.** The spatial position of water molecules is encoded as phase by the use of a magnetic field gradient with duration δ and magnitude G. A π pulse inverts the spin phase. A second magnetic field gradient, identical to the first one, refocuses the phase of all stationary spins. Moving spins do not experience the same magnetic field before and after the refocusing pulse and the ensemble is not homogeneously refocused, resulting in loss of signal. The modification of this sequence, utilized in this dissertation, is presented in Figure 2.20.

where γ is the gyromagnetic ratio of hydrogen protons (42.58 MHz/T). Equation 2.3 assumes that the local field gradients (independent of the diffusion-sensitizing gradients) are minimal in the sample. In areas of large magnetic susceptibility differences, local magnetic field gradients are induced. Local gradients would impart further phase shifts to the spin that would not be fully recovered by the second gradient pulse, confounding the measurement of D. Any other magnetic field gradients or inhomogeneities present during the PGSE sequence must be present and equal during both diffusion sensitizing gradient pulses in order to correctly infer D. The tissue boundary between air and tissue is an example of this problem. Luckily, these effects are localized (more on this on Section 2.5.2).

The diffusion-sensitizing gradients need not be rectangular, as is expressed in the above equation, in which case the area of the pulse should be equal to that of the ideal rectangular pulse. The use of non-rectangular gradient pulses does not affect the measurement of D[9].

The amount of NMR signal available in a diffusion-sensitive experiment decays exponentially according to D (Figure 2.4), and is expressed as:

$$\frac{S}{S_0} = e^{-bD} \tag{2.4}$$

where S is the signal intensity obtained with the diffusion gradient on, and S_0 is the corresponding signal intensity obtained without the use of diffusion sensitizing gradients. This equation can also be written as:

$$\ln\left(\frac{S}{S_0}\right) = -bD \tag{2.5}$$

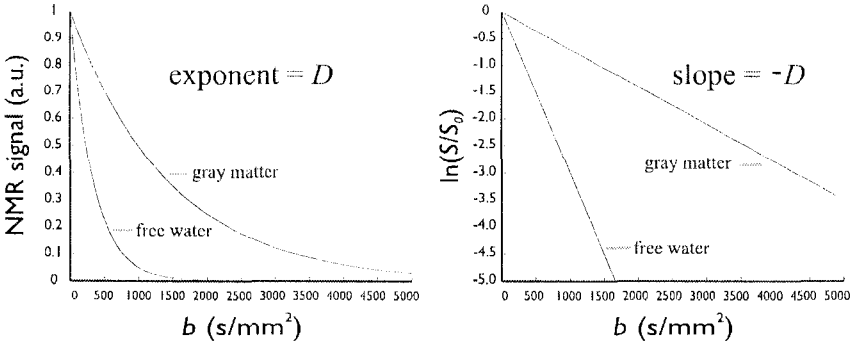

FIGURE 2.4: **NMR signal vs. diffusion sensitization.** The NMR signal is plotted as a function of b (equations 2.4 and 2.5) for gray matter ($D = 0.7 \times 10^{-3} mm^2/s$) and freely-diffusing water at 37°C ($D = 3 \times 10^{-3} mm^2/s$).

While originally developed for measuring D in samples, the PGSE and its variants can be used in MRI. In this case, the volume of interest is divided into n pixels (picture elements, in the two-dimensional case) or voxels (volume elements, in the three-dimensional case), and the diffusion coefficient can be calculated in each individual pixel or voxel. This approach is known as diffusion-weighted imaging (DWI)[10] and is now routinely used in the detection of ischemic brain injury[11].

The diffusion-sensitizing gradients, as well as the radio-frequency pulses, must be turned on during a certain time, providing an effective diffusion time $\Delta - \delta/3)$ that is around 50-100 ms. In biological tissues, the diffusion of water molecules depends not only on viscosity and temperature, but also on semi-permeable barriers such as cellular membranes. In order to measure viscosity, the diffusion time must be very short, limiting the interactions between the water molecules and semi-permeable barriers. Such short diffusion times are difficult to attain, as they require very strong gradients to be applied for a short period of time (δ). Tanner and Stejskal recognized the effect of diffusion barriers and were the first to propose the idea of measuring restricted diffusion of water molecules by varying the delay between the gradient pulses[12]. For this reason, the term *Apparent* Diffusion Coefficient (ADC) is used when referring to D in biological tissues, as measured with NMR. This is, however, far from being a drawback, as the *apparent* part of ADC is what allows us to make inferences on tissue micro-structure.

2.1.2 Water diffusion in the brain

In order to understand the behaviour of water diffusion in the brain, we must briefly discuss the basic properties of the four major tissue types that reside in the intra-cranial cavity:

Gray matter (GM) This tissue contains the neuronal bodies and glial cells. It has a gray-brown color, hence its name, and is distributed at the surface of the cerebral hemispheres and cerebellum, as well as the sub-cortical nuclei (thalamus, caudate, etc). It is composed of more than 100 000 million neurons, and an even greater number of glial cells. Around 90% of all the neurons in the brain reside on the cerebral cortex[13], which has a width of around 1-5 mm and is organized in layers. It makes 45% of the total brain volume in young adulthood[14].

White matter (WM) Composed of axons and oligodendrocytes, it provides connections between near and distant portions of the brain. Its color is due to the myelin content. In young adults, it has an approximate volume of

450 cm^3 (35% of the brain volume) and the myelinated axons alone account for more than 118 000 km[15].

Cerebro-spinal fluid (CSF) With a total volume of less than 150 ml, this transparent liquid bathes the brain and spinal cord, being completely exchanged 3-4 times per day. It is 99% water, and has less than 10 cells per mm^3[16]. It represents 10% of the total brain volume[14].

Blood The blood flow through the whole brain in a young adult is 15-20% of the cardiac output, between 750-1000 ml/min[16]. It accounts for around 10% of the total brain volume[14].

Water diffusion is not completely free in biological systems, due to the presence of cellular membranes and organelles, as well as characteristic tissue architecture. These features pose barriers to diffusion and cause *anisotropy* (i.e., diffusion is not equal in all directions). The white matter in the brain, which consists of several bundles of axons interconnecting distant discrete portions of the brain, shows a high degree of architectural coherence. It therefore also shows the highest degree of anisotropy in the brain.

Axons with similar trajectories are bundled together to form fasciculi (also referred to as tracts or fiber bundles, Figure 2.5). Each axon can be surrounded several times by lipid-rich myelin sheaths, manufactured by oligodendrocytes. The myelin sheaths are periodically interrupted along the axon in the nodes of Ranvier, forcing the propagation of action potentials to be saltatory and therefore faster. Axons have various diameters that range from <1 μm to approximately 15 μm. Given the diffusion coefficient of water molecules at body temperature, a single water molecule can show a displacement of around 10 μm in 50-100 ms[17], certainly enough for it to encounter several axonal membranes and other barriers. Myelin, being a lipid bilayer was wrongly assumed to be the *only* source of diffusion anisotropy. Anisotropy is indeed present in non-myelinated nerves[18–20], but its presence modulates the degree of anisotropy[20–24]. The presence of anisotropy in non-myelinated nerves points at intact cellular membranes as one of the major sources of anisotropy of water molecules[18,20]. The longitudinally-oriented micro-

tubules within axons, as well as fast axonal transport, appear to be minimally involved in the generation of diffusion anisotropy[25]. When axons are organized coherently and tightly packed, as in fasciculi or bundles, the impermeable effects of the myelin sheaths and the axonal membranes combine, causing the overall diffusion measurements of white matter to be anisotropic[26,27]. The biophysical mechanisms of diffusion anisotropy have been previously reviewed[27].

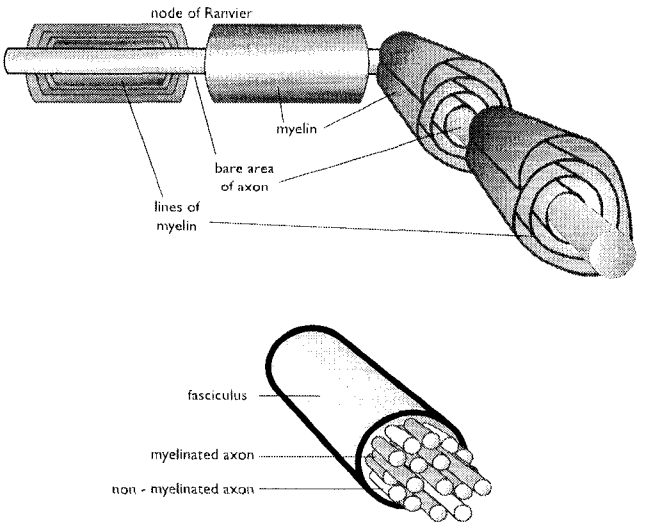

FIGURE 2.5: **Basic structure of white matter.** Some axons are engulfed in a spiral-like fashion by extrusions of the cytoplasm of oligodendrocytes, forming the myelin sheaths. The myelin insulation is interrupted at the nodes of Ranvier. Myelinated and non-myelinated axons are bundled together to form fasciculi.

The gray matter, albeit being organized in layers and functional columns, does not show the same degree of architectural coherence as the WM. The neuropil (the dendrites and axons that interconnect the neuronal bodies *within* the cortex), particularly, is tangled and does not show a coherent architecture. For this reason, the diffusion of water in the cortex does not show a high degree of anisotropy. The CSF, being essentially water, shows fast diffusion that is virtually isotropic. Lastly, diffusion of water in blood is difficult, if not impossible, to measure given the fast flow occurring simultaneously.

2.2 The diffusion tensor

Given the anisotropy of diffusion in organized tissues, a scalar measure such as D is not enough to represent the three-dimensional profile of the movement of water molecules. In the simplest case, in which the orientation of the tissue is known *a priori*, such as peripheral nerve, it is possible to quantify diffusion anisotropy by measuring the ADC using diffusion-sensitizing gradients oriented both parallel and perpendicular to the tissue, and obtaining the ratio between the two (anisotropy = $\frac{ADC_{\parallel}}{ADC_{\perp}}$). The orientation of the tissue, however, is typically not known in advance, as is the case of the white matter. Basser and colleagues introduced the formalism of the diffusion tensor in 1994[28,29], which overcomes said problem and permits the quantification of ADC in any direction. Most importantly, the diffusion tensor provides important information on the micro-structure and orientation of organized tissue.

The three-dimensional representation of equation 2.5 is:

$$\ln\left(\frac{S}{S_0}\right) = -\sum_{i=1}^{3}\sum_{j=1}^{3} b_{ij}D_{ij} \tag{2.6}$$

$$= -\left(b_{xx}D_{xx} + 2b_{xy}D_{xy} + 2b_{xz}D_{xz} + b_{yy}D_{yy} + 2b_{yz}D_{yz} + b_{zz}D_{zz}\right) \tag{2.7}$$

in matrix form:

$$\ln\left(\frac{S(\mathbf{b})}{S_0}\right) = -\text{trace}(\mathbf{bD}) \tag{2.8}$$

where each element in $\mathbf{b}$ and $\mathbf{D}$ corresponds to a particular one-dimensional direction of diffusion sensitization. From these equations, the tensor can be constructed as matrix of the form:

$$\mathbf{D} = \begin{bmatrix} D_{xx} & D_{xy} & D_{xz} \\ D_{xy} & D_{yy} & D_{yz} \\ D_{xz} & D_{yz} & D_{zz} \end{bmatrix} \tag{2.9}$$

Notice that $\mathbf{D}$ is a symmetrical matrix, where D_{xy}, D_{xz} and D_{yz} are repeated in the upper-right and lower-left corners, since $D_{xy} = D_{yx}$, $D_{xz} = D_{zx}$ and $D_{yz} = D_{zy}$. If the medium is isotropic, then $D_{xx} = D_{yy} = D_{zz}$, and the off-diagonal elements, D_{xy}, D_{xz} and D_{yz} are zero.

Although any number (>6) of diffusion gradient directions can be used, most studies utilize the gradient scheme described by Pierpaoli *et al.*[26] (shown in Figure 2.6), where x, y and z represent the scanner's gradient coils. These diffusion gradients are independent of any other gradients necessary for the creation of the image (e.g., phase and frequency encoding gradients). Such a gradient scheme (i.e. having multiple gradients on simultaneously) provides resultant gradient amplitudes that exceed that obtained along the physical axes and is therefore considered "efficient", as it provides high b values in a shorter period of time (i.e. the gradient pulse length can be shorter), reducing the echo time and T2 relaxation over the read-out period (yielding higher signal-to-noise ratio per unit time)[30]. There has been considerable debate regarding the optimal number of diffusion gradient directions, with different conclusions derived on the surrogate marker chosen to compare direction schemes. In terms of having a high probability of accurately describing the orientation of the tensor, it seems to be advantageous to use more than six directions, overestimating the tensor calculation[30]; contrarily, six directions appear to be sufficient to accurately estimate diffusion anisotropy[31], as long as the diffusion gradient directions point to the vertices of a icosahedron, as in Figure 2.6.

A property of second rank tensors is that they can be diagonalized, leaving three non-zero elements along the main diagonal of the matrix, which are called *eigenvalues*. The eigenvalues are ordered according to their magnitude, with λ_1 being the largest and λ_3 the smallest in magnitude. The mathematic relationship between the principal coordinates of the diffusion tensor and the laboratory frame is described by the *eigenvectors* (v_{1-3}). The eigenvalues reflect the diffusivity in a given direction, according to their associated eigenvector and have direct biological interpretations. For example, in the case of white matter, the longest eigenvalue (i.e. λ_1) reflects the axonal state, whereas the eigenvalues associated to $v_{2,3}$ confer information regarding the integrity of myelin sheaths[21,32] (Chapter 8).

It is easier to understand the diffusion tensor when considering its geometrical representation, which is an ellipsoid whose axes are determined by the three eigenvalues, and its orientation by the eigenvectors (Figure 2.7). The ellipsoid can

x	y	z
1	0	1
-1	0	1
0	1	1
0	1	-1
1	1	0
-1	1	0

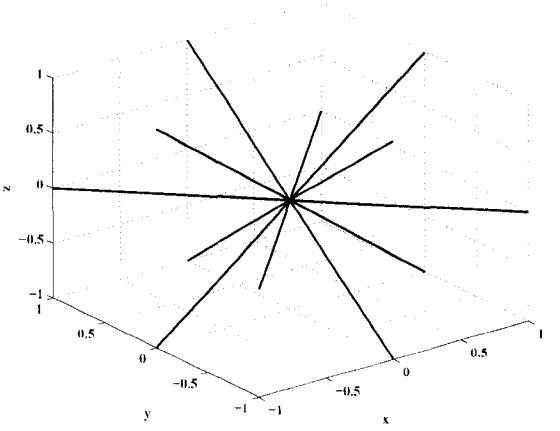

FIGURE 2.6: **Diffusion gradient directions.** The diffusion gradient directions are plotted in three dimensions. Diffusion-weighted images are aquired in six non-planar and non-colinear diffusion gradient directions in order to obtain enough information to build the diffusion tensor.

be conceptualized as the surface on which a spin at the origin will diffuse to with equal probability if the diffusion is Gaussian. The ellipsoid's surface represents the root mean square diffusive displacement of water. The trace of the tensor ($\text{trace}(\mathbf{D}) = \lambda_1 + \lambda_2 + \lambda_3$) is equivalent to the size of the ellipsoid, while the mean bulk diffusivity in all directions (the three-dimensional ADC) is given by:

$$ADC = \frac{\text{trace}(\mathbf{D})}{3} = \frac{\lambda_1 + \lambda_2 + \lambda_3}{3} \tag{2.10}$$

The terms Mean Diffusivity (MD), $trace/3$ and ADC are used interchangeably in the literature. *Trace* ADC is also sometimes used to refer to MD, although it formally refers to MD×3.

In DWI, a pair of diffusion-sensitizing gradients is used before the imaging acquisition scheme. Echo-planar imaging (EPI)[33–35] is typically the imaging sequence utilized, as it is one of the fastest imaging schemes available in MRI (alternative imaging schemes are discussed in page 38). In EPI, a single excitation pulse is utilized, and the entire image is formed in less than a quarter of a second. The single-shot nature of EPI translates into a single set of gradients being required for diffusion sensitization (Figure 2.20). The diffusion gradients are applied in one di-

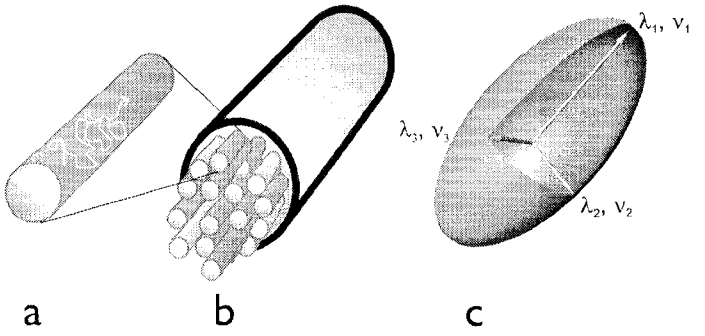

FIGURE 2.7: **The diffusion tensor.** Anisotropic diffusion of water molecules (a) in highly organized tissue, such as white matter (b) results in an elongated diffusion tensor, visualized as an ellipsoid (c). The largest axis of the ellipsoid corresponds to the largest eigenvalue (λ_1). Thus, the principal diffusivity of water molecules is parallel to the eigenvector corresponding to λ_1.

mension (Figure 2.6), therefore sensitizing the image to diffusion in one direction (in addition to their inherent T2-weighting given by the long echo times typically required). Areas of the images containing most of their water molecules diffusing in a direction that is parallel with the diffusion gradient direction will show a decrease in signal, when compared to the non-diffusion weighted image. Thus, the ADC of those regions will be high. Contrarily, regions where diffusion is perpendicular to the diffusion gradients will not show such a marked drop in signal intensity. Having calculated the ADC on a per-pixel basis, one can produce quantitative maps of diffusivity where the gray scale is related to ADC, as in Figure 2.8. It is important to note that areas of hyper-intensity seen on DWI typically appear as dark regions on the quantitative ADC maps. The first EPI-DWI images were presented in 1988 by Avram and Crooks[36]. Without a doubt, diffusion-weighted imaging has had a tremendous impact in the diagnosis of ischemic brain lesions, where it has become a virtually indispensable tool[11,37,38].

DWI is inherently a one-dimensional technique. By obtaining at least six DWI, each with a different (non-colinear and non-coplanar) diffusion gradient direction (and one image without diffusion sensitization, $b = 0$ s/mm^2), and obtaining their respective ADC maps on a pixel-by-pixel basis, we acquire all the necessary

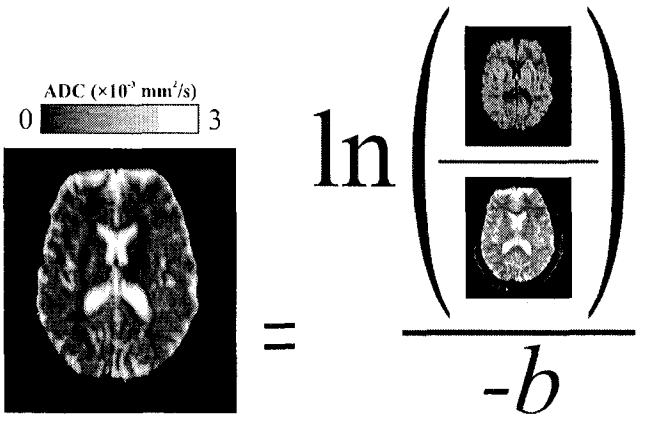

FIGURE 2.8: **Quantitative apparent diffusion coefficient map.** The ADC is calculated on a pixel-by-pixel basis from the DWI and the non-diffusion weighted images according to equation 2.5. The diffusion gradient is applied in only one direction; $b = 1000$ s/mm^2. Notice the fast diffusion of CSF in the ventricles, represented as bright pixels in the quantitative ADC map.

information to build the diffusion tensor. The tensor is computed in a pixel-by-pixel fashion (Figure 2.9), giving rise to diffusion tensor imaging (DTI).

Higher moments of the diffusion tensor provide information on the degree of diffusion anisotropy, because they characterize different ways in which the diffusion tensor deviates from the isotropic case. These scalar measures facilitate the interpretation of the tensor and, being derived from the eigenvalues, have the advantage of being *rotationally invariant*. The simplest case is the ratio of the principal diffusivities (λ_1/λ_3), or more intuitively, the ratio of the diffusivity parallel to the orientation of the tissue ($\lambda_{\parallel} = \lambda_1$) vs. the perpendicular diffusivity ($\lambda_{\perp} = \frac{\lambda_2+\lambda_3}{2}$). The major drawback of this approach is that it requires sorting of the eigenvalues and, as such, is very sensitive to noise contributions[39].

Other scalar measures of anisotropy can be constructed independently of the order of magnitude of the eigenvalues. The *Volume ratio*[40] is defined as:

$$VolumeRatio = \frac{\lambda_1\lambda_2\lambda_3}{\left(\frac{\lambda_1+\lambda_2+\lambda_3}{3}\right)^3} \tag{2.11}$$

and represents the volume of an ellipsoid divided by the volume of a sphere whose radius is the mean diffusivity. Thus, the values of Volume Ratio range from

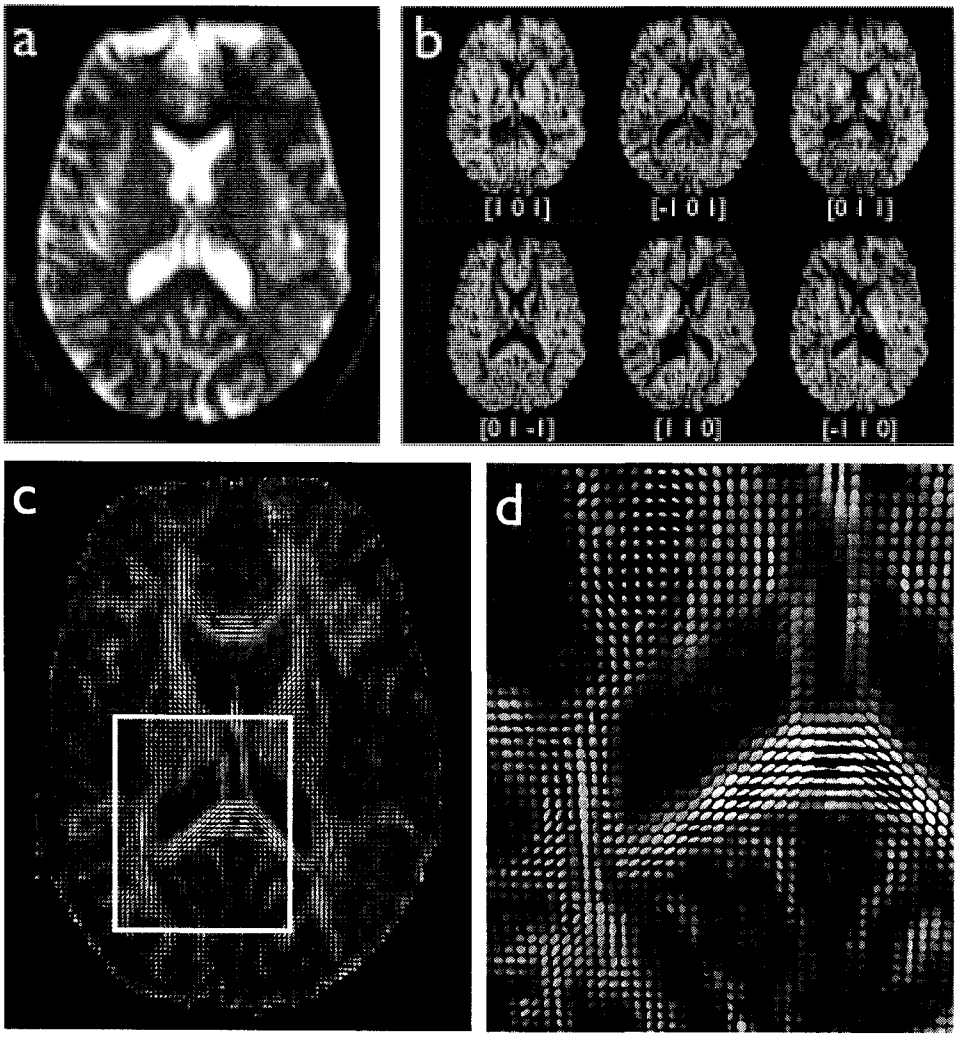

FIGURE 2.9: **Calculation of the diffusion tensor.** The diffusion tensor is calculated pixel-by-pixel, based on the non-diffusion weighted image (i.e., $b = 0\,\mathrm{s/mm^2}$, panel a) and six DWI, each one with a different diffusion gradient direction ($b = 1000\,\mathrm{s/mm^2}$, panel b). Diffusion gradient directions are expressed as $[x\ y\ z]$. Notice how particular brain regions change contrast depending on the direction of the diffusion gradient applied. Individual ADC maps (not shown) are computed according to equation 2.5 (see Figure 2.8). Upon diagonalization, the resulting diffusion tensors are visualized an ellipsoid per pixel (see Figure 2.7), with their color intensity related to the degree of anisotropy (c, with zoomed region in d). Notice the orientation of the ellipsoids resembles the expected white matter orientation, for instance the splenium of the corpus callosum in d, interconnecting the two cerebral hemispheres. The diffusion tensors in the internal capsules appear smaller because they are oriented through the imaging plane, according to the rostro-caudal orientation of this white matter bundle (which demonstrates the three-dimensional nature of the diffusion tensor).

0 to 1, with 0 being the highest anisotropy and 1 being the complete isotropic case. Because of this, some authors prefer to use the term 1−Volume Ratio[39].

The Relative Anisotropy ratio (RA) is another measure of anisotropy, which represents the coefficient of variation of the eigenvalues. This measure was used before in crystallography[41], ranges from 0 (isotropic) to $\sqrt{2}$ (infinite anisotropy) and is expressed as:

$$RA = \sqrt{\frac{1}{3}} \frac{\sqrt{(\lambda_1 - \text{trace}(\mathbf{D}))^2 + (\lambda_2 - \text{trace}(\mathbf{D}))^2 + (\lambda_3 - \text{trace}(\mathbf{D}))^2}}{\text{trace}(\mathbf{D})} \tag{2.12}$$

However, perhaps the most widely utilized measure of anisotropy is the Fractional Anisotropy index (FA)[42], which measures the fraction of the magnitude of the tensor that can be ascribed to anisotropic diffusion. It ranges from 0 (isotropic) to 1 (infinite anisotropy), thus making FA more intuitive than RA. It is defined as:

$$FA = \frac{\sqrt{3}}{\sqrt{2}} \frac{\sqrt{(\lambda_1 - ADC)^2 + (\lambda_2 - ADC)^2 + (\lambda_3 - ADC)^2}}{\sqrt{\lambda_1^2 + \lambda_2^2 + \lambda_3^2}} \tag{2.13}$$

Visually, FA is represented as ellipsoids with varying degrees of sphericity (given by the eigenvalues) as can be seen in Figure 2.10.

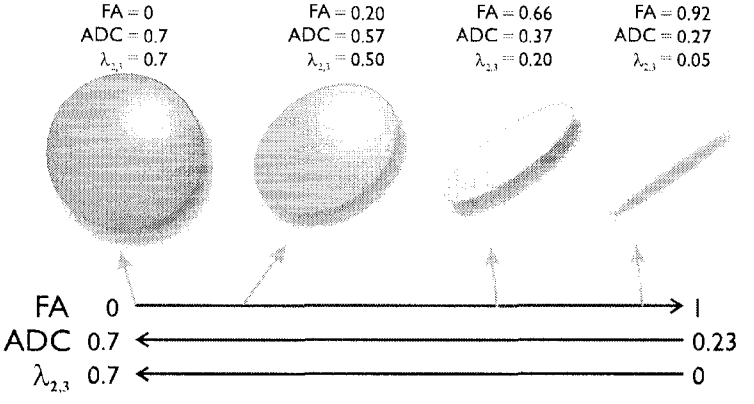

FIGURE 2.10: **Diffusion tensor ellipsoids of varying degrees of anisotropy.** Four diffusion tensor ellipsoids ranging from pure isotropy to very high anisotropy are shown. In all cases λ_1 has been kept constant at 0.7 $\times 10^{-3}$ mm^2/s. $\lambda_\perp$ (i.e., λ_2 and λ_3) is progressively reduced, increasing the anisotropy and reducing the ADC. FA is dimensionless, ADC and eigenvalues have units $\times 10^{-3}$ mm^2/s.

The quantitative anisotropy indices, as well as the eigenvalues and individual tensor components can also be displayed as maps relating the gray scale intensity to the desired measure on each pixel (Figures 2.11 and 2.12). Indeed, any color-mapping can be used and is not limited to a gray scale (for examples, see Chapters 5 and 8).

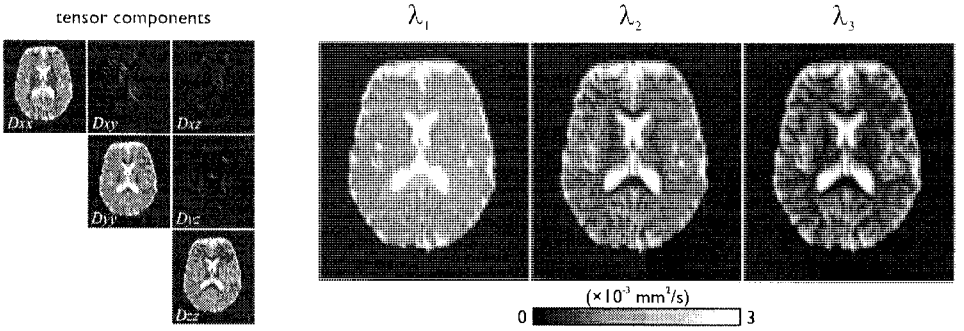

FIGURE 2.11: **Quantitative diffusion maps.** The tensor components, as well as the eigenvalues are displayed as maps, where the pixel intensity is related to quantitative diffusion parameters.

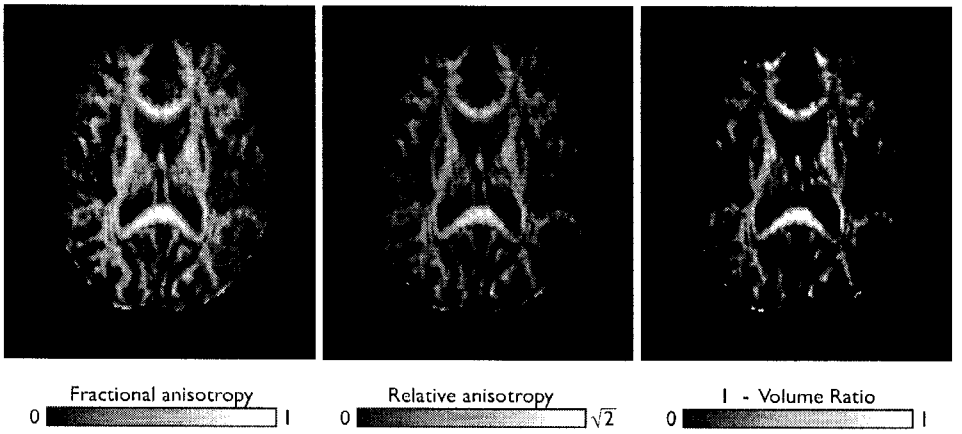

FIGURE 2.12: **Quantitative diffusion anisotropy maps.** Three measures of diffusion anisotropy are shown. Notice how the white matter shows large values in all three quantitative maps, due to its high architectural coherence.

Lastly, the three-dimensional orientation of the diffusion tensor can also be displayed on two-dimensional images (slices) using different approaches. In the first approach, exemplified in Figure 2.9, each diffusion ellipsoid is visualized (the visualization can be simplified by displaying boxes or lines to represent the ten-

sor). This approach, albeit being elegant and appealing to the eye, is extremely complicated and difficult to interpret. A further reduction of this theme is to display v_1 per pixel as a quiver-plot. The main disadvantage of these methods is that it becomes difficult to visualize the correct orientation of the arrows/ellipsoids when they are oriented orthogonally to the plane being viewed (e.g. the diffusion ellipsoids of the internal capsule incorrectly appear to be isotropic and small in Figure 2.9, panel d). Other approaches have produced gray scale maps of the polar and azimuthal angles of v_1, which requires two maps to be viewed simultaneously[43,44]. A clever and intuitive approach is to utilize color to represent the orientation of the white matter tracts[45–49]. The most widely utilized method today is that proposed by Pajevic and Pierpaoli[50]. In the latter method the x, y and z components of v_1 are mapped to the red, green and blue components of a full-color image, respectively (Figure 2.13). However, doing only this will highlight all the tensors in the image, regardless of their anisotropy. Since low anisotropy regions can have slightly different eigenvalues just because of noise contributions, the largest eigenvalue will be randomly oriented[51]. Thus, the cortex and CSF-filled spaces will incorrectly appear to have a preferred direction. In order to overcome this problem, the vector components are multiplied by some anisotropy index (e.g., FA). This will match the pixel intensity to the degree of anisotropy, and the color will reflect the tensor orientation; furthermore, low anisotropy regions do not overwhelm the image. Another advantage of this method is that the color encoding is independent of the slice orientation.

The analysis of the diffusion tensor is not restricted to the measures of anisotropy outlined above. An intuitive method proposed by Westin[52] represents the tensor as a combination of its linear (CL), planar (CP) and spherical components (CS):

$$CL = \frac{\lambda_1 - \lambda_2}{\sqrt{\lambda_1^2 + \lambda_2^2 + \lambda_3^2}} \tag{2.14}$$

$$CP = \frac{2(\lambda_2 - \lambda_3)}{\sqrt{\lambda_1^2 + \lambda_2^2 + \lambda_3^2}} \tag{2.15}$$

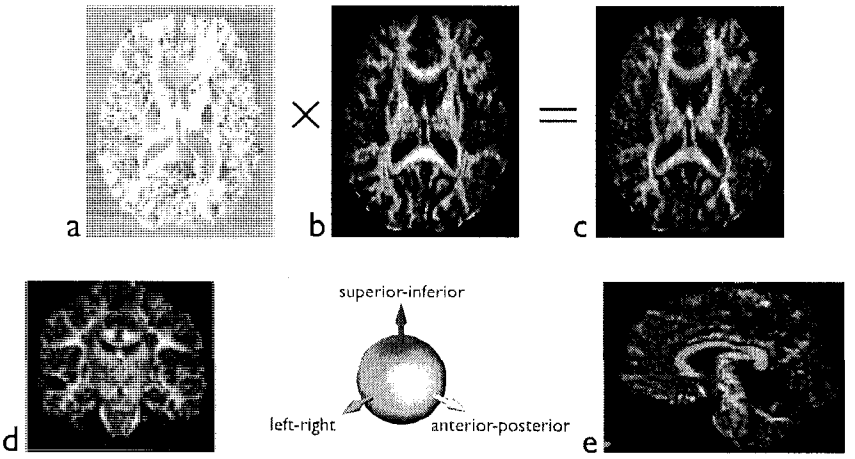

FIGURE 2.13: **Color maps of principal diffusivity.** The x, y and z components of the principal eigenvector v_1 are mapped to the red, green and blue components of a full color image (a). In order to highlight areas of high anisotropy, the color map is multiplied by some anisotropy map, in this case FA (b). The resulting color map (c) shows the three-dimensional orientation of the tissue, regardless of the orientation of the slice (c-e).

$$CS = \frac{\lambda_3}{\sqrt{\lambda_1^2 + \lambda_2^2 + \lambda_3^2}} \tag{2.16}$$

The normalization by the norm of the tensor causes each measure to range between 0 and 1, and the sum of the three shape measures is unity. Each of these components can be easily visualized simultaneously using a barycentric plot[53], and the overall anisotropy index (CA) is defined as the sum of the linear and planar shape measures:

$$CA = CL + CP = 1 - CS \tag{2.17}$$

This method can also be visualized as quantitative maps (Figure 2.14). The main disadvantage of the shape component approach is its sensitivity to the ordering of the eigenvalues, which is not an issue in anisotropy measures such as FA or RA.

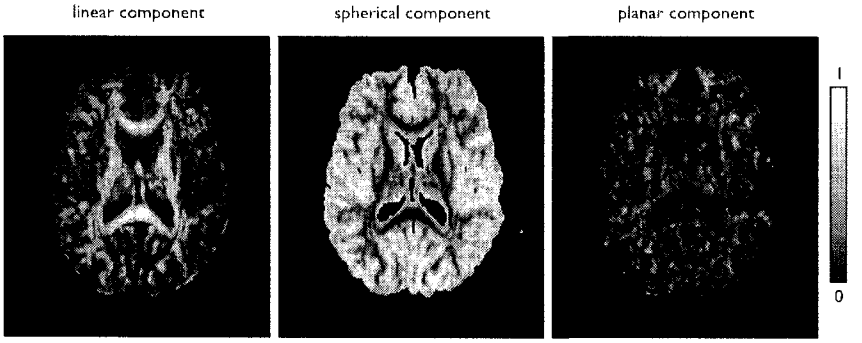

FIGURE 2.14: **Geometrical components of the diffusion tensor.** The diffusion tensor visualized as its spherical, linear and planar components, the sum of which is unity.

2.3 Tractography

As discussed in section 2.2, the diffusion tensor calculated in each pixel of the images has an orientation that is parallel to the architecture of highly organized and coherent tissues (such as white matter and skeletal muscle). A typical DTI data set includes several contiguous slices that form a volume, where the tensor is calculated in each voxel. The three-dimensional nature of the tensor and the volume of images acquired lend themselves to the visualization of the underlying tissue using computer algorithms.

In the case of the brain, the white matter is distinctly organized into macroscopic fasciculi that are readily discernable on the color maps (e.g., the corpus callosum is bright red near the midline of panel c in Figure 2.13). The first approach to virtually dissect individual fiber bundles used the color maps to segment voxels of similar characteristics[54]. Shortly thereafter, a technique previously utilized in the visualization of vector fields, called *streamlines* was adapted for the visualization of white matter bundles. Several streamline-tractography algorithms have been developed in the past decade[55–58], with the first reports published in 1998 by Basser[59] and Jones[60]. Essentially, all algorithms "seed", or begin, a streamline in those voxels with anisotropy above a certain threshold. The lines are then propagated by a user-defined length according to v_1 until they meet a termination criterion, which often is reaching a voxel with low anisotropy (in order to avoid

continuing into CSF-spaces, cortex or even air), or if the line deviates by an angle that is considered biologically implausible.

Throughout this thesis, the fiber-assignment by continuous tracking (FACT)[55] algorithm was employed (Figure 2.15). In this particular algorithm, all the voxels in the data set that show an FA value above a certain threshold (typically in the range of 0.25 to 0.30) are "seeded" and each line is propagated according to v_1. Every time the line meets the boundary between two voxels, it queries the direction of v_1 and FA of the voxel being pointed at. If the FA value is below a stopping threshold (similar to the starting threshold), or if the angle at which it would turn is large and biologically implausible (e.g., $>70^\circ$) the streamline is truncated. The algorithm is run a second time, since v_1 is bidirectional. Deciding the direction of the tract at voxel intersections as opposed to every fixed-length step (which requires interpolation of the tensor) increases the computational efficiency. The selection of the anisotropy and curvature thresholds is user dependent and are often tailored to the goal at hand (i.e. the tracts of interest). If the FA threshold is set too high the chance of erroneous propagation is minimized at the expense of obtaining less tracts and making the dissection more difficult. Contrarily, a very low FA threshold (e.g. < 0.10) will force the algorithm to initiate the propagation in areas where the direction of principal diffusivity could be biologically meaningless or determined by noise contributions (e.g. in CSF). The same idea applies to the termination FA threshold[61,62]. The curvature threshold is often made very strict when analyzing tracts with minimal curvature, such as the cortico-spinal tract. For the analysis of cortico-cortical U-fibers, the threshold must be relaxed, as these connections bend sharply within the subcortical white matter.

The FACT algorithm was chosen given its good performance on curved tracts and computational speed as compared to other algorithms[63] (calculation of the tensor field and generation of the fiber tracts in an entire data set of full brain coverage is performed in less than two minutes). DTI-studio[64], the software utilized to perform tractography, was obtained directly from Drs. Susumu Mori and Hangyi Jiang (Johns Hopkins University). This software has the advantage of having powerful tools for the virtual dissection of the tracts (see below).

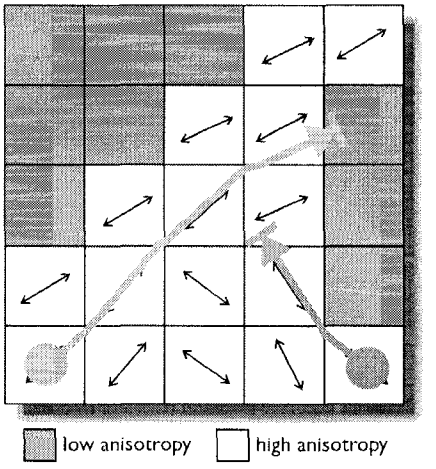

FIGURE 2.15: **Fiber-assignment by continuous tracking.** All the voxels in the data set with high diffusion anisotropy are "seeded". In this simplified two-dimensional example, two of the resulting tracts are shown. The lines propagate in the same direction as the principal diffusivity of the voxel (black bidirectional arrows), changing their course every time they encounter a boundary. The orange tract stopped when it reached a voxel with low anisotropy, while the blue tract stopped when it attempted to make a sharp turn.

All the line propagation algorithms can be started from either only specific seed regions (determined by the user) or by seeding the entire brain. The problem with the first approach is that one can only obtain the same number of tracts as the number of seeds, limiting the number of tracts that intersect the area of interest. With the second approach, thousands of tracts are obtained, then the user selects only those passing through a specific region, generally providing better results, particularly in areas of "branching" of the bundles[56]. With whole-volume seeding, it is therefore absolutely necessary to perform virtual dissection of the bundles of interest, based on *a priori* knowledge of their course. The dissection is carried out using Boolean operators, excluding all the resulting tracts that do not meet the desired criteria. Since the majority of the white matter bundles have a unique path not shared by the surrounding fasciculi, the investigator can easily provide landmarks through which the tracts must intersect (Figures 2.16 and 2.17). The majority of tracts require at least two tract-selection regions to be successfully dissected. Guidelines have been published for the virtual dissection of some tracts[65–67], although it is sometimes necessary to perform some additional

adjustments for their accurate depiction, due to differences in image quality, acquisition, etc.

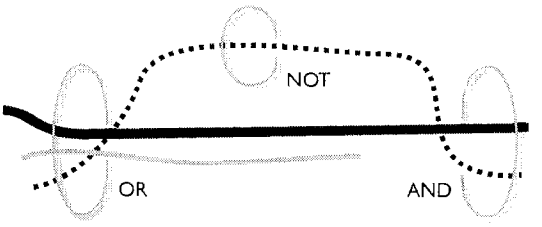

FIGURE 2.16: **Virtual dissection in tractography.** After seeding all the voxels in the volume with high anisotropy, only the tracts of interest are retained for visualization and further analysis. This is accomplished by strategically placing areas through which the tract of interest must pass. The OR operator selects all the tracts going through the region. However, the thin gray tract does not pass through the AND operator and is discarded. Finally, the dotted tract, showing a bizarre path, is discarded using a NOT operator.

An important consideration of line-propagation algorithms is that errors accumulate as the lines are propagated. That is, for each voxel there is a certain noise contribution to the tensor estimation and, as the lines propagate and visit consecutively more voxels, the probability of the tract showing a random deviation increases. The amount of uncertainty in the orientation of the tensor can be calculated and visualized using the bootstrap procedure[68]. However, in order to do so, it is necessary to obtain the individual images for each gradient direction prior to averaging. The DTI protocols used in the present thesis utilized on-line image averaging, thereby increasing the signal-to-noise ratio and reducing the total number of images on each data set to one per slice per diffusion direction; thus, the estimation of orientation uncertainty using the bootstrap method is precluded. Nonetheless, one can use the error accumulation favorably, as tracts with incorrect paths (determined by the noise contribution) are clearly visible and can be easily deleted using the NOT boolean operator.

There is another approach to tractography that does not result in synthetic tracts representing the maximum likelihood pathway, but in the probability of a certain connection residing in each voxel, appropriately termed *probabilistic* tractography[69]. The method's main advantages are that it inherently characterizes the

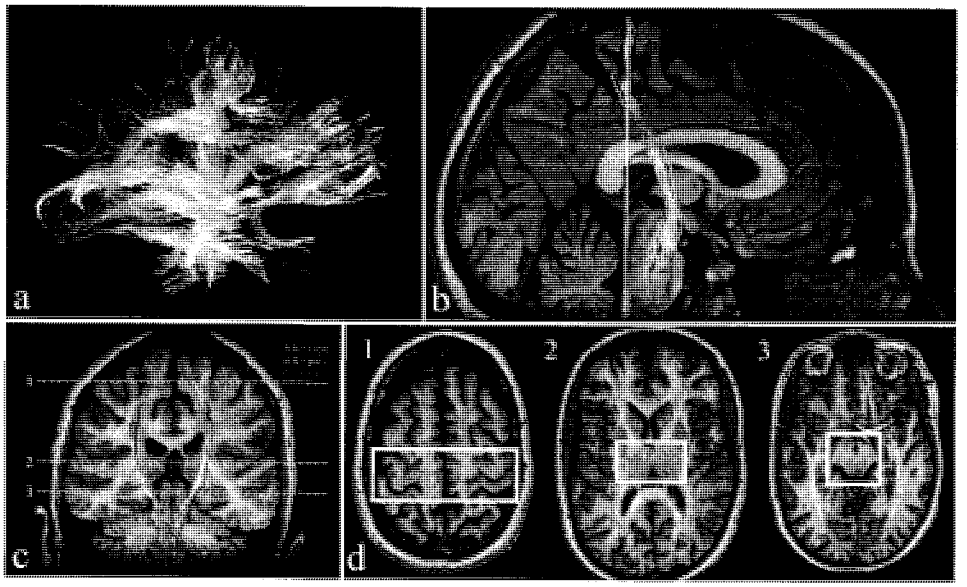

FIGURE 2.17: **Virtual dissection of the cortico-spinal tract.** All the high-anisotropy voxels in the data sets are seeded, resulting in over 200,000 tracts, 30% of which are visualized in panel a. In order to virtually dissect this particular tract of interest, the tracts must pass through three regions (based on *a priori* anatomical knowledge of the trajectory of the bundle) identified in panel d. The resulting tract (b and c), is colored according to anisotropy. In panels b-d, the principal diffusivity is denoted by red, green and blue components, overlaid on high-resolution T1-weighted images for better appreciation of anatomical detail.

uncertainty of the tensor model, it can be used in areas of low anisotropy (such as the cortex and subcortical gray matter) and it is robust to noise. Probabilistic tractography has been used to successfully segment the nuclei of the thalamus, based on their projections to the cortex[70]. The disadvantage of this tractography method is that it finds all the possible areas of the brain with a non-zero probability to connect to a "seed" region, which often include more than one white matter bundle. Therefore, if the goal is to identify individual fasciculi, the deterministic line-propagation methods are preferred.

2.4 Methods for the quantitative analysis of the diffusion tensor

As discussed above, the diffusion tensor and its derived measures can be visualized as maps, which allows the visual examination of quantitative diffusion parameters. Additionally, there are methods to extract these parameters from previously calculated maps in one or several subjects.

Regions of interest The analysis of regions of interest (ROI) is perhaps the easiest to understand and perform. In this approach, a two- (or three-) dimensional outline is manually drawn around the structure of interest. Alternatively, a fixed-size geometrical shape (e.g. a box or a circle) can be placed within the structure of interest. The voxels included in the region are queried for the desired parameters and their values are averaged in order to provide a single measurement per ROI. Since all the quantitative diffusion maps from the same subject are spatially aligned, the same ROI can operate on each of the maps independently. That is, for a particular structure in a single subject, the operator needs to outline the structure of interest only once, and obtain the values of ADC, eigenvalues, FA, etc. The direct measurement of the quantitative diffusion maps provides a straightforward approach for the testing of hypotheses made *a priori*. The drawback is that ROIs are placed manually, making this a time-consuming and user-dependant procedure. This method is used in Chapters 6 and 7.

Tract-based analysis The tract of interest is depicted using tractography on each subject, and all the voxels contributing to the tract are treated as a three-dimensional ROI. This approach has the advantage of utilizing the semi-automated nature of tractography, where the tract-selection regions can be loosely defined (Figure 2.17), minimizing the user dependence of the method. That is, the user does not have to precisely outline a structure of interest, but merely provide one (or more) wide area(s) through which a tract must pass and take advantage of Boolean operators (Figure 2.16) and anatomical knowledge of the tract's trajectory. Most importantly, certain structures with a thin cross-section and/or curved

paths are more easily depicted using tractography than with several ROIs. As with ROIs, the investigator must choose the structures to be analyzed in advance. This method is used in Chapters 4 through 8.

Statistical parametric mapping The analysis of each structure on each subject can be a cumbersome and lengthy process if the sample size is large. Essentially, in statistical parametric mapping (SPM) the brain volumes of the subjects included in the study are "morphed" and made to match a template (or atlas) as closely as possible, after which statistics are performed on a pixel-by-pixel basis. Significant differences are then highlighted on the template, showing the regions of the brain that differ between the groups studied. This method was borrowed from voxel-based morphometry of brain volumes[71,72] and, although it is very appealing, it suffers from several problems, the biggest of which is the fact that image morphing (normalization) of individual volumes to the template is never perfect. In particular, while the general shape, size and position of two different brains can be adequately matched, the individual subtle differences of intra-parenchymal structures cannot[73]. In order to overcome this problem (and to satisfy the statistical requirements of the method), the normalized images are generally blurred using a gaussian kernel. Although it technically is a user-independent analytical method, in reality the user must select several different parameters, such as the width of the gaussian blurring kernel, that can greatly influence the results and the conclusions derived from them[74,75]. Its biggest advantage (a disadvantage in inexperienced hands) is the fact that the investigator need not have a hypothesis *a priori*, which is useful in conditions where there is no knowledge of the location of suspected abnormalities.

Tract-based spatial statistics This is a new approach recently put forth by Smith *et al.*[76], which minimizes the problems of SPM and allows full-brain comparisons to be made with no *a priori* hypothesis. In this method, the FA maps are aligned to a template, and from the average of all the FA maps a "skeleton" of the white matter tracts is obtained. Then, a skeleton map is created for each subject by

projecting his/her FA maps onto the standard space and populating the skeleton with the FA values from the nearest relevant tract centre. This attempts to position all the subjects in the same space, with every voxel representing exactly the same white matter structure. After this is accomplished, voxelwise statistics across subjects can be performed. Similarly to SPM, significant differences are highlighted, from which probabilistic tractography can optionally be initiated. The disadvantage of this method is that it only analyzes a relatively small proportion of all the available white matter, namely only those voxels with high anisotropy. Valuable information from a great number of voxels in several white matter structures is lost. Furthermore, many white matter tracts (e.g. the cortico-spinal tract) are organized somato-topically (i.e. they have an anatomically-defined order within them), making the analysis of its central portion a potential bias.

2.5 Shortcomings of DTI

2.5.1 The model

The diffusion tensor model can accurately identify the tissue architecture in cases where there is homogeneity of the structure within the voxel sampled. However, not all areas of the white matter show homogeneity, particularly in regions where two or more fiber populations cross each other. In these cases, the diffusion tensor model cannot identify the complex orientation of the tissue. The reason behind this failure is that in DTI, a single Gaussian diffusion compartment is assumed to exist within each voxel. The addition of two prolate (i.e., $\lambda_1 > \lambda_{2,3}$) tensors results in an oblate tensor (i.e., $\lambda_1 > \lambda_2 = \lambda_3$) (Figure 2.18). Thus, the problem lies in the model itself, and the over-estimation of the diffusion tensor by the acquisition of images with multiple diffusion gradient directions is not helpful.

It is common to find areas of low anisotropy deep within the white matter of the brain which one could incorrectly consider lesions. For example, the region where the superior longitudinal fasciculus (anterior-posterior orientation) intersects the corona radiata (superior-inferior) and the corpus callosum (left-right) appears as a black "hole" on FA maps. Furthermore, since most line-propagating

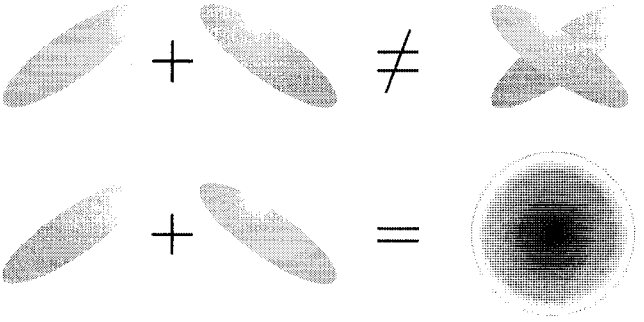

FIGURE 2.18: **Addition of diffusion tensors.** When two fiber populations with different orientations occupy the same space, the tensor model is unable to differentiate the two orientations, as the addition of two perpendicularly oriented prolate diffusion tensors results in an oblate ellipsoid.

tractography algorithms stop when they reach an area of low anisotropy, these tracts are typically truncated at this point. Probabilistic tractography, not being limited by regions of low anisotropy where the orientation is uncertain, will progress in many directions. The uncertainty in these areas will be represented by voxels farther along the path having lower probabilities associated with them[69].

The true diffusion function in areas of fiber crossings is complex. For this reason, model-free descriptions of the diffusion profile have been advanced[77–80], commonly referred to as Q-space imaging or high-angular resolution diffusion imaging. Briefly, the diffusion function is related to the MR signal by the Fourier transform with respect to the experimental diffusion wavevector q (the diffusion gradient and its direction)[7,81]. Q-space methods utilize high angular resolution at high b values and a great number of diffusion gradient directions (generally more than 100). The diffusion sensitivity (b) is increased in order to augment the contrast between the fast diffusion component of the two (or more) fiber populations[81]. The goal is to accurately sample the diffusion profile in each voxel. In the case of a single fiber population, the diffusion profile resembles a peanut (diffusion is greatest only in the main axis of the peanut), while in the case of two or more populations the peanut turns into a symmetric multi-lobed structure similar to a flower. Notably, the peaks of the diffusion profile do not correspond to the fiber directions. In order to obtain these, the Funk-Radon transform is utilized[80].

Once the fiber orientation(s) have been found, modified tractography algorithms can depict white matter bundles, even at areas where they intersect. Although these model-free diffusion measurements are very useful, they have not received as wide attention as DTI has, perhaps due to the very long acquisition times required, the great amount of data needed to recreate the diffusion profile and, most importantly, the fact that DTI scalar measures are more easily interpreted from a biological point of view. High-angular, model-free diffusion analyses were not performed in this dissertation, as the biological correlates of DTI are better known than those of these newer methods.

Both DTI and Q-ball imaging share a drawback, which is their inability to discern afferent from efferent fibers. That is, while the connectivity between two areas can be inferred and visualized, its directionality remains unknown.

2.5.2 Imaging artifacts

Typically, human in-vivo DTI experiments use voxel volumes that range from 6 to 20 mm^3. Given this restriction, only those white matter bundles with dimensions considerably larger than the voxel size can be correctly identified and characterized. Large structures, such as the corpus callosum, the internal capsules or the fornix can therefore be adequately depicted, but several small—yet important—connections cannot be reliably identified with DTI.

It is important to remember that the tensor information available on each voxel corresponds to the weighted average of all the tissue classes residing within it. Thus, if a particular voxel is occupied by CSF and highly coherent WM, the resulting tensor will not be highly anisotropic, but somewhat isotropic (it is even likely that it will tend more towards the isotropic case, given the very fast diffusion of CSF and the high signal obtained from it with conventional DTI—the long TE utilized favors long T2 species). Indeed, *partial volume averaging*, as this artifact is known as, can be reduced by increasing the resolution of the images (effectually reducing the voxel size, minimizing the possibility of having more than one tissue type per voxel). An increase in resolution comes at a high price, as it is inversely related to the signal-to-noise ratio with fixed acquisition times. The largest source

of worrisome partial volume averaging in DTI is signal contamination with CSF, particularly in those WM bundles in close proximity of CSF. Fortunately, virtually all the signal arising from CSF can be specifically nulled, limiting its contribution to the resulting tensor in voxels with partial volume. This technique (presented in more detail in Chapter 4 and utilized in Chapters 5 to 7) is based on the differences in longitudinal relaxation of CSF and brain tissue. Briefly, an inversion pulse is applied prior to excitation of the sample, by a time calculated from the T1 constant of CSF. The sample is then excited precisely when the longitudinal magnetization of the CSF passes through zero, but that of other tissues is finite.

The resolution of current DTI techniques is restricted by the imaging sequence used to acquire the data, which is in turn restricted by the hardware (particularly the gradient strength). EPI is generally utilized, since it allows very fast imaging, which is absolutely necessary given the large number of images needed to construct a DTI volume (for example, with six diffusion gradient directions, one non-diffusion weighted image per slice, eight averages and 60 slices: $7\times8\times60=3360$ images) and to minimize motion artifacts. The short acquisition time attained with EPI is accomplished by using a single spin excitation radio-frequency pulse (i.e., a single 90° pulse), after which the entirety of *k*-space is filled in by alternating between positive and negative frequency-encoding gradients preceded by blips of the phase-encoding gradient (Figure 2.19). Patient motion is thus minimized, as every image is essentially a "snapshot" of the current position.

Alas, in MRI speed comes at a price. Two very apparent artifacts seen in DTI are caused by the EPI sequence, both of which are even greater at higher field strengths. The first potential EPI artifact is called N/2 or Nyquist ghost. Inconsistencies of the even and odd echoes cause phase offsets that result in a ghost shifted by half of the field-of-view (FOV) pixels in the phase-encode direction, relative to the real image. If the FOV is large enough, these ghosts appear outside of the real image and are not obtrusive. This, however, is not always the case, for which several correction methods have been proposed that either acquire additional reference data[82–84] or utilize post-processing schemes[85,86]. The second EPI artifact is due to magnetic field inhomogeneities that alter the phase of the spins,

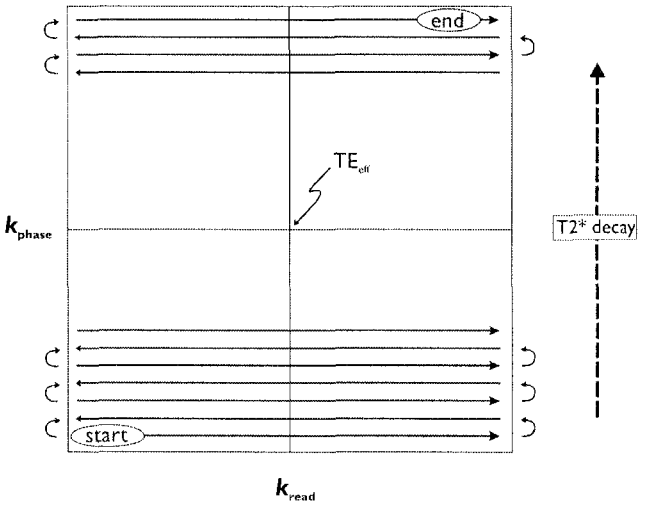

FIGURE 2.19: **Acquisition trajectory of EPI in k-space (frequency domain).** After a single excitation, alternating lines of k-space are acquired, preceded by "blips" of the phase-encoding gradients. The effective TE (TE_{eff}) is determined by the acquisition line that traverses the center of k-space. The signal available decays according to the tissue's $T2^*$ constant along the acquisition of k-space.

with a subsequent misinterpretation of their location in space. The magnetic susceptibility difference are made more evident by the $T2^*$ signal decay that occurs during the EPI read-out in the phase-encoding direction (Figure 2.19). *Geometric distortions*, as this second artifact is known as, are most apparent near tissue interfaces, particularly if they possess very different magnetic susceptibilities, such as air and tissue. Hence, this artifact is evident near the para-nasal sinuses or at the base of the skull, where it would seem like the brain has been "squashed" (for anterior-posterior phase-encoding) or sheared (in left-right phase-encoding). As with N/2 artifacts, several methods have been published that attempt to minimize off-resonance artifacts[87–90]. The long acquisition times can be reduced by concatenating the acquisition of k-space using two or more EPI read-outs (at the expense of at least doubling the total image acquisition time)[91,92]; or by reducing the number of k-space lines acquired via partial phase Fourier, or parallel imaging[93–98].

Although it is true that motion is minimized in *each* of the EPI-DWI acquisition, two special notes must me made. First, motion can occur *between* successive acquisitions, producing a mismatch within different diffusion gradient directions,

making the calculation of ADC meaningless (recall that ADC is computed in a pixel-by-pixel fashion). Second, subtle, involuntary motion artifacts can arise due to physiological phenomena, such as the low amplitude pulsations of the brain and CSF[99]. This subtle motion potentially leads to artifactually high estimations of ADC[100]. The acquisition of the images based on the cardiac cycle (i.e. cardiac or pulse gating/triggering) has been reported to minimize pulsation artifacts[100,101]. In this approach, every image is acquired at precisely the same time regarding the pulsation wave (e.g. 500 ms following the R wave). This comes at the expense of increasing the scan time[100]. The use of CSF-suppression (Chapter 4) complicates the use of cardiac/pulse gating, but also diminishes the effects of pulsation artifacts, reasons for which we did not perform any form of gating in the studies discussed herein.

The second source of artifacts in DWI and DTI are the diffusion gradients themselves. The fast alternating gradients produce additional eddy currents that adversely affect the main magnetic field. Residual magnetic fields caused by the eddy currents produce image translations and geometric distortions. The DTI sequence utilized throughout this thesis is based on a twice-refocused, single-shot EPI sequence[102] (Figure 2.20). This sequence is a modification of Stejskal and Tanner's spin-echo sequence (Figure 2.3) that separates the diffusion-encoding gradient pair into two pairs (each pair with its respective refocusing pulse). The decomposition of the diffusion gradients minimizes eddy currents prior to the EPI readout, producing less geometric distortions and image translations. This is of particular importance since the DWI images must spatially match the non diffusion-weighted image in order to properly calculate the ADC in each pixel. However, as the read-out is based on EPI, the images still suffer from slight geometric distortions in the anterior-posterior direction (the phase-encode direction); fortunately, these distortions are far away from the white matter bundles of interest (see for example the frontal lobes in Figure 2.9, panel a).

Another effect of the long EPI readout is the susceptibility to chemical shift effects. In particular, fat and water have different resonant frequencies (separated by 3.3 parts per million, 210 Hz at 1.5T), which result in a fat-derived image ghost

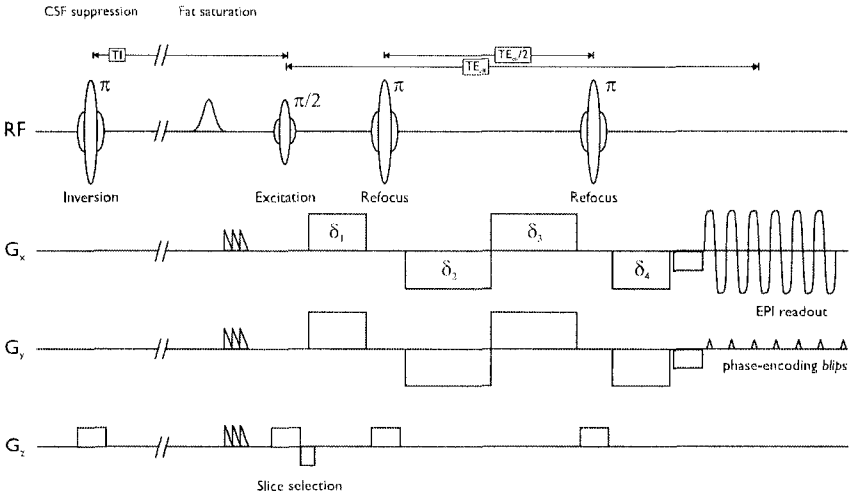

FIGURE 2.20: **Twice-refocused, CSF-suppressed, EPI-based DTI sequence diagram.** A slice-selective inversion pulse is applied before the excitation pulse, separated by an inversion time (TI) of around 2200 ms (see Chapter 4). This selectively suppresses signal from CSF, based on its long T1. Spectral fat suppression is utilized prior to excitation. A set of four diffusion-sensitizing alternating gradients is utilized, which compensate for their induced eddy-currents, minimizing image distortions. An EPI readout train encodes the spatial information. In this particular example, the diffusion gradients have been applied in the x (read) and y (phase) directions.

that is spatially shifted (in the phase-encode direction) of the water-derived image. This problem is easily overcome by the utilization of spectral fat suppression prior to excitation. In this approach, fatty tissues are selectively excited using a radio-frequency pulse on resonance with the precessional speed of fat protons, after which the residual transverse magnetization is dephased ("spoiled") with a gradient pulse (Figure 2.20). The excitation of water molecules follows immediately, and the resulting signal is devoid of fat contributions.

The DTI sequence utilized in this dissertation had slight geometric distortions in the most anterior aspect of the frontal lobes and near the base of the skull that were not compensated for by the twice-refocused approach. However, these artifacts lie distant to the areas of interest and do not affect the measurements performed. Even the hippocampus is far enough from the petrous bone to escape this artifact. We used a left-right frequency-encoding scheme and, therefore, geometric distortions occur in the anterior-posterior direction (causing, for example,

the frontal poles to appear compressed). N/2 artifacts were minimal and not intrusive in the images acquired, occupying mostly the empty space in the image due to the ample FOV employed.

Given the limitations of the EPI technique, alternatives for the acquisition of diffusion-weighted images have been developed[103–108]. However, these newer methods are far from being as widely available as single-shot EPI based DTI. Furthermore, they require the use of several excitation pulses (i.e. they are not "single-shot"). These extra excitation pulses increase the time needed to acquire the image, increasing the susceptibility to subject motion and the total scan time. Also, given the great number of images acquired during a typical DTI session, the extra radio-frequency power deposited on the subject could reach unacceptable levels and cause heating. Despite the presence of the above-mentioned imaging artifacts inherent to it, EPI still provides an appropriate balance between acquisition speed, image quality and radio-frequency deposition.

It is worth noting again that even if very-high resolution images could be acquired with adequate quality and devoid of all imaging artifacts, the ability of DTI to differentiate between two or more fiber populations is limited to the tensor model itself. Finally, while the biophysical mechanisms of diffusion anisotropy have been studied in animal models[27], it is not yet known if the same mechanisms underly the diffusion anisotropy seen in human white matter. As such, the inference of tissue integrity through the analysis of the diffusion tensor requires important assumptions that have not been thoroughly validated in humans. The basis of anisotropy in human tissue is studied in Chapter 9.

CHAPTER 3

EPILEPSY

3.1 Definition and general characteristics

The definition of *seizures* was put forth in the second part of the XIX Century by Hughlings Jackson, and is still valid today: "seizures are the result of an occasional, sudden and excessive discharge of grey matter"[109]. In *epilepsy*, there are recurrent and unprovoked seizures. In practice, any seizure disorder that cannot be explained by easily reversed, transient metabolic or toxic conditions is considered epilepsy[110]. Thus, epilepsy is not one, but many different syndromes with very different etiologies and pathophysiologies, all sharing the presence of abnormal, synchronized electrical activity. Due to this heterogeneity and the large number of syndromes under the broad term of epilepsy, such disorders are classified according to their seizure types and electro-encephalogram (EEG)[111,112].

According to the most commonly used classification scheme, proposed by the International League Against Epilepsy, seizure types are classified as:

1 **Partial Seizures** These type of seizures arise in a restricted part of the brain in one hemisphere. Their manifestations can be motor, somatosensory, autonomous or psychic symptoms. They are further sub-classified as:

   A **Simple partial Seizures** There is a focal clinical manifestation, but consciousness is not impaired.

B **Complex partial seizures** In addition to the focal clinical manifestation, there is an impairment of consciousness. Frequently, the patient will perform motor automatisms.

C **Partial seizures evolving to secondarily generalized seizures** After a variable period of focal clinical manifestations, the seizure activity globalizes, with the apparition of generalized clinical semiology. Typically, the secondary generalization is so dramatic that it overshadows the initial focal signs, causing the false impression that the patient experienced a primary generalized convulsion. A simple partial seizure can generalize without first evolving into a complex partial seizure.

2 **Generalized seizures** The principal characteristic of this group is that the seizure activity involves both hemispheres from the beginning. Consciousness is characteristically lost or impaired.

A **Absence seizure** Consciousness is lost and regained rapidly, with the patient commonly ceasing whatever activity he/she was performing. Historically known as "petit mal" seizures.

B **Myoclonic seizures** These seizures involve sudden brief involuntary movement of a shock-like nature.

C **Clonic seizures** Seizures with motor manifestations characterized by repetitive, rhythmic jerking.

D **Tonic seizures** Defined as rigid violent muscular contractions of the trunk and limbs, which are generally short and accompanied by pupil dilation and eye deviation.

E **Tonic-clonic seizures** Historically known as "grand mal" seizures, these are perhaps the most easily recognizable and dramatic convulsions. In the first phase, consciousness is lost at the same time as the body adopts an unnatural rigid pose, causing the patient to fall. The contraction of respiratory musculature provokes a loud moan or cry. Incontinence is not uncommon. The rigidity gradually evolves into shaking (the

clonic phase). Profuse salivation, coupled with lack of swallowing and atypical respiration leads to frothing at the mouth. These seizures are generally shorter than sixty seconds, although the time perceived by witnesses tends to be much longer.

F **Atonic seizures** There is generalized loss of muscle tone, affecting posture and causing the individual to fall to the ground, unable to protect himself from the fall (also known as drop-attacks).

3 **Unclassified epileptic seizures** Includes all seizures that cannot be classified because of inadequate or incomplete data or because they defy classification.

While the different seizure types are the principal characteristic of the epilepsies, there are numerous syndromes with overlapping seizure types, leading to the saying "seizures are to epilepsy as cough is to pneumonia". Therefore, it is practical to classify the epileptic disorders as *syndromes* (i.e. groups of signs and symptoms that occur together in a particular condition). The classification takes into consideration two factors: (i) Seizure origin (i.e. focal or generalized) and (ii) etiology. When there is a clearly apparent cause of the disorder, it is considered to be "secondary" or "symptomatic" epilepsy. However, in some syndromes a cause is presumed but not identified (commonly with some degree of mental retardation), and is therefore called "cryptogenic" (from *crypt* meaning "hidden"). "Idiopathic" epilepsies have no apparent cause, but are believed to be genetic in nature.

The classification of epilepsy syndromes is extremely useful; it was put forth by the International League Against Epilepsy in 1989 and remains largely unchanged[112]. The abridged version follows.

1 **Localization-related** This includes most forms of epilepsy with a focal onset. They are further sub-classified according to their etiology (symptomatic, idiopathic or cryptogenic). Certain seizure foci (e.g. temporal, frontal, parietal or occipital lobes) have very specific and reproducible seizure manifestations that aid in the localization of the seizure generator.

2 **Generalized** More than 16 different syndromes are covered under this umbrella term, ranging from benign neonatal convulsions to the terribly disabling Lennox-Gastaut syndrome.

3 **Undetermined whether focal or generalized** As the name implies, these epilepsies show generalized tonic-clonic seizures in which clinical and EEG findings do not permit classification as clearly generalized or localization-related.

4 **Special syndromes** These are situation-related syndromes, such as febrile convulsions, isolated status epilepticus or seizures due to an acute metabolic or toxic event.

Considering all forms of epilepsy, the prevalence ranges from 5-17/1,000 people, with 40-150 new cases per 100,000 persons diagnosed annually[113]. These numbers are so large that it is uncommon for any person not to know of at least one other person with some form of epilepsy. Epilepsy affects both genders nearly equally, regardless of socioeconomic state. The largest annual incidence is seen at the extremes of life, with developmental, congenital and infectious disorders as common origins in children, and symptomatic (e.g. secondary to stroke or trauma) epilepsies in the elderly population. Disability due to epilepsy accounts for approximately 1% of the global burden of disease, which ranks epilepsy just after major affective disorders, dementias and alcohol dependence among primary disorders of the nervous system[114]. Most patients with epilepsy have no other disabilities, but conditions that cause epilepsy often cause other disabilities. The most common of these are cognitive and motor problems, followed by somatic and psychiatric diseases[115,116].

It is now important to note a very special distinction between epilepsy patients, regardless of the epileptic syndrome, and that is the issue of *medical intractability*. In general, it is not necessary to perform extensive diagnostic evaluations in patients who respond well to medication and in whom gross lesions have been ruled out (e.g. tumors, hemorrhage, etc). However, approximately $1/3$ of all patients with

epilepsy cannot be adequately controlled with appropriate medical therapy[117–120]. Patients who respond to medication typically do so using a single anti-epileptic drug. In fact, the chance of being seizure free is inversely related to the number of anti-epileptic drugs used, and this chance is less than 5% when three or more drugs are employed[121]. It is the medically intractable epilepsy group to which we now turn our attention.

3.1.1 Diagnosis

The diagnosis of the epilepsies involves several complementary tests. The goal is to acquire enough information regarding the patient's seizures as to correctly classify the epilepsy syndrome at hand. If the syndrome is localization-related and does not respond to medication appropriately, the origin of the seizures must be sought in order to evaluate the plausibility of its surgical resection and potential cure. A valuable piece of information the clinician has is the manifestation of the seizures. It is imperative to evaluate the semiology of the seizures (ictal period), but also the inter-ictal behaviour of the patient (the period of time when the patient is not experiencing seizures and not immediately after or preceding an episode) and the post-ictal period. The clinical manifestations of seizures can be easily misjudged by untrained eyes, particularly if they involve secondary generalization. More often than what is commonly thought, seizures have a focal origin that then evolves to a generalized tonic clonic convulsion. The focal manifestation can be as subtle as limb jerking, numbness or tingling, an epigastric non-specific "sensation", perception of an odd smell, *déjà-vu*, visual anomalies, etc. It is these subtleties that generally aid most to the localization of the seizure onset, as particular areas of the brain have typical seizure types. However, care must be taken when relying on clinical clues to infer the seizure generator, as the first clinical manifestation could be the result of spread of seizure activity that started in non-eloquent cortex.

The synchronization of the electrical activity of the pyramidal cells in the cortex of the brain can be detected using surface electrodes in a standard EEG. Most of the time, the EEG is performed in the inter-ictal period, when its sensitiv-

ity varies from 30 to 80%[122]. Long-term (3-15 days) EEG and video monitoring greatly increases the power of this diagnostic tool, as they allow electro-clinical correlations to be made and provide important information regarding the lateralization of seizure onset[123]. While the scalp EEG has great temporal resolution, it has very low spatial resolution, cannot detect small areas of epileptic activity and commonly cannot detect abnormal activity arising from deep gray matter structures. Furthermore, a large portion of cortex must be involved in epileptiform activity for it to be detectable with surface EEG[124]. For these reasons, it is sometimes necessary to perform invasive intra-cranial EEG, via surgical placement of depth electrodes or sub-dural grids.

Imaging has become a very important factor in the diagnostic work-up of the epilepsies, with MRI being the most sensitive and flexible imaging modality. Its high spatial resolution and excellent soft tissue contrast allow the detection of small lesions. Its advantages became clear in the 1980s, when coronal T2-weighted images began to be used for the detection of mesial temporal sclerosis (Section 3.3). Different tissue contrasts and slice orientations are utilized within a given imaging session, and are pieced together by the clinician in order to refine a diagnosis. Not only structural information is gained, but tissue characteristics and functional changes can also be demonstrated. X-ray computed tomography plays an important role in the first approach to a patient with newly-diagnosed seizures, and is very useful to rule out large lesions such as skull fractures, tumors, hemorrage, etc. However, computed tomography does not provide much information in the diagnostic work-up of patients with medically intractable epilepsy in whom the above mentioned special conditions have been ruled out. Due to the lack of penetration of ultrasound waves through the skull, ultrasonography is virtually useless for brain imaging in the adult population. Nuclear medicine is occasionally used for the lateralization of location-related epilepsies. Single-photon emission computed tomography (SPECT), in particular when co-registered to high-resolution MRI, has shown to correctly localize seizure foci in around 70% of the cases[125,126]. The sensitivity of SPECT, however, depends largely on the type of epilepsy at hand, and the injection time of the isotope after a well-identified

seizure[126]. Positron-emission tomography (PET) has a high sensitivity (80% or more, depending on the type of epilepsy)[127], but is not routinely utilized in all centers, largely due to its limited availability. Furthermore, both PET and SPECT have sub-standard spatial resolution, as compared with MRI.

3.1.2 Epileptogenesis

As we have seen, there are many different epilepsy syndromes, each with particular clinical and para-clinical characteristics. It is not surprising, then, that their underlying causes are different from one another. A thorough discussion of the various epileptogenic mechanisms is outside the scope of this dissertation, and only a few important factors will be considered. It is important to note that the mechanisms driving epileptogenicity are still not completely understood, particularly those present in chronic epilepsies, as they are difficult to differentiate from the long-term effects secondary to epilepsy *per se*. Epileptogenesis can be studied at several levels, ranging from molecular interactions to large cortical networks.

The cells that generate seizures are, for the most part, normal. Their basic tissue characteristics have only been slightly modified, exaggerated or uncontrolled[128]. The brain's plastic abilities imply these slight modifications. Thus, brain regions with great plastic potential are more likely to be the focus of epileptiform activity[129]. It is perhaps for this reason that the hippocampus, involved in memory and cognition, is a common source of seizures.

Most idiopathic generalized epilepsies have a molecular cause[130]. Single mutations in genes involved in trans-membrane voltage potentials can cause abnormal electric discharges, such as alterations in the function of ion channels, neurotransmitter receptors or any molecule that directly or indirectly modifies these two. For example, defects of the T-type Calcium channel in the thalamus are thought to be linked to childhood absence seizures[131].

A very common idea on epileptogenesis is incomplete inhibition, due to alterations in γ-Aminobutyric acid (GABA) or its receptors. GABA is the most common inhibitory neurotransmitter in the brain. However, the GABA system is complex and not exclusively inhibitory. Nonetheless, it is clear that it plays

a very important role in some forms of epilepsy, as evidenced by the fact that epileptiform activity can be produced artificially by blocking its receptors[132] and that benzodiazepines (which modulate the GABA receptor) are one of the many medical treatments of epilepsy available. Many GABA-ergic neurons in the brain are interneurons that provide inhibitory feed-back and feed-forward to pyramidal cells. That is, interneurons modulate the activity of the effector circuits. The role of interneurons is discussed in more detail in the context of temporal lobe epilepsy.

The principal excitatory neurotransmitter, glutamate, has also been implicated in the genesis of epileptic discharges. The effects of increased excitability due to glutamate are not only acute (in the form of epileptic discharges), but also chronic, in the form of cell death. Repetitive, short-spaced trains of action potentials via glutamate allow an excessive influx of Calcium ions into the cell[133], which results in neuronal damage and death. Literally, these neurons fire themselves to death. Cell damage, in turn, can lead to modifications of the neural circuitry, some of which are epileptogenic as well. The osmotic changes that occur during the uncontrolled and prolonged firing stage are presumed to result in cytotoxic edema, which can be sometimes be detected with DWI[134–140]. Cell death, as will be seen in section 3.2.3 can be detected with conventional imaging (i.e. T2) and DWI.

The epileptogenesis of temporal lobe epilepsy is considered in more detail in Section 3.2.3.

3.2 Temporal lobe epilepsy (TLE)

Of all the localization-related forms of epilepsy, temporal lobe epilepsy (TLE) is the most common[141], and one of the most refractory to medical treatment[142]. TLE can be sub-classified according to its origin as mesial or neocortical, although the clinical manifestations of both are quite similar[143,144]. Patients with TLE suffer from simple or complex partial seizures, occasionally with secondary generalization. More than half of the patients with TLE experience simple partial seizures, or auras, that are intricate in nature and often difficult to describe[145]. The most

commonly reported aura is an epigastric sensation ("butterflies in the stomach"). Unexplained fear is also common in these auras[146], as are phenomena of *déjà-vu*, depersonalization or olfactory hallucinations. Complex partial seizures are stereotypical and by definition include the inability to respond to the environment. As such, the patient does not seem to be unconscious, but performs oro-alimentary and motor automatisms (lip smacking, chewing, humming, smiling, fumbling, pulling). A useful and reliable lateralizing sign is dystonic posturing of the upper limb contralateral to the seizure generator[147], while the ipsilateral limb performs motor automatisms. Sometimes at the end of the seizure, patients will wipe their nose with the hand ipsilateral to the epileptogenic temporal lobe[148]. These events generally last only a few minutes, but the post-ictal period is noticeably long (as opposed to other forms of localization-related epilepsy—such as frontal lobe epilepsy—where the patient returns to his normal self rapidly after the seizure). In the post-ictal state, the patient is confused, amnesic and tired.

Although interictal EEG abnormalities are usually demonstrated, the deep location of the mesial temporal structures makes their detection sometimes difficult using surface electrodes.

3.2.1 Anatomy of the temporal lobe and the limbic system

When discussing the anatomy of the temporal lobe in relation to TLE, it is prudent to consider its relation to the limbic system and its connections to other areas of the brain. The limbic system (Latin *limbus*: "border" or "edge") encompasses several gray and white matter structures that are involved in emotion, motivation and memory. The limbic system includes the hippocampus, amygdala, cingulate gyrus, hypothalamus and its mammillary bodies, the orbitofrontal cortex, parahippocampal gyrus, the thalamus and the olfactory bulb. Although the interplay between these structures is now involved in what we could consider "high mental processes", the limbic system is a primitive structure which developed to manage fear secondary to an external stressor (such as a predator) and appropriately channel the responses of fight or flight. Certainly also of primal importance is memory, spatial memory in particular, if an animal was to successfully return

to a place with abundance of food. In 1878, Paul Broca called these parts of the brain *le grand lobe limbique*[149]

The hippocampus and fornix

The hippocampus is an outstanding example of inventiveness of name-giving[150]. The reason for its name stems from its macroscopic appearance which (in the axial view and with a certain degree of imagination) resembles a sea-horse. The name was coined by Giulio Cesare Aranzi in 1564[151]. The hippocampus has been given several different names and has been sub-divided in different, overlapping fashions. Samuel Soemmerring (b. 1755), the same person who created the nomenclature used today for the cranial nerves, called the hippocampus the *gerollte Wulst* (rolled in gyrus), perhaps the most appropriate and informative name for this structure[151]. The name *cornu Ammonis* (Amon's horn) was given to the hippocampus by Noguez in 1726 and Garengeot in 1728[151]. The reason behind this name is that longitudinal sections of the hippocampus reveal a ram's horn-like architecture, resembling those adorning the head of the Egyptian god. The term "cornu Ammonis" is reserved for the gray matter that is continuous with the parahippocampal gyrus. The most commonly used subdivision of the hippocampus was put forth by Lorente de Nó (who worked with Ramón y Cajal), which describes four sections, termed CA1 to CA4[152]. Also included in the modern-day definition of the hippocampus is the dentate gyrus, a layer of gray matter that interlocks with the cornu Ammonis. Anatomical descriptions of the hippocampus often confuse the reader, which tends to ignore the three-dimensional extent of this structure and to think of it as a single slice of tissue, often coronal, as most books describe it this way (compare Figures 3.1, 3.2 and 3.3 to 3.4). In reality, the hippocampus is a long structure that extends anterior to posterior and bends medially. It has three main portions, namely the head, the body and the tail.

The cornu Ammonis is in effect the continuation of the entorhinal cortex into the hippocampus. However, the superficial layer of the entorhinal cortex ends in the region of the presubiculum, while the deeper one turns into the subiculum, whose cell layer then flattens to form the dense band of pyramidal cells in the

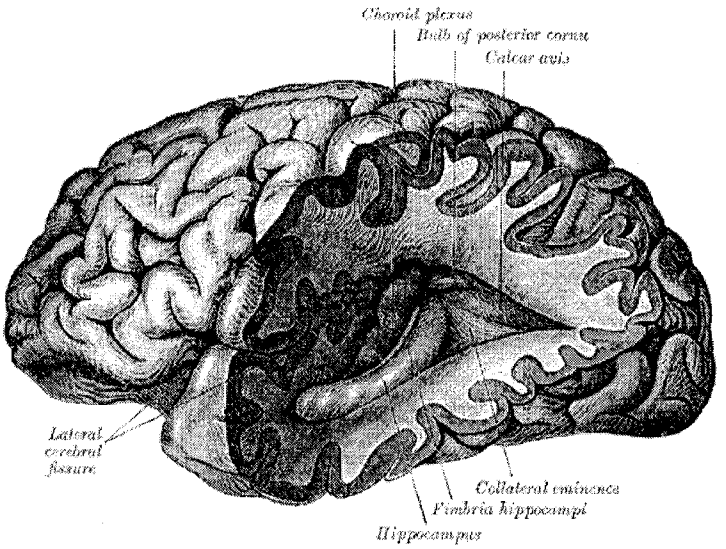

FIGURE 3.1: **Gross anatomy of the hippocampus (lateral view).** The hippocampus is seen in its full anterio-posterior extent after removal of the temporal lobe. Notice gradual thickening of the fimbria and its detachment from the hippocampus to form the fornix. Figure from Gray's Anatomy of the Human Body (public domain)[153].

cornu Ammonis[154]. As mentioned above, the cornu Ammonis can be subdivided in four sub-regions, CA1-CA4 (CA4 is also commonly referred to as the hilus, and its most abundant neuronal species is the mossy cell), according to histologic differences of its main cellular layer[152] (Figure 3.4). The cornu Ammonis has six layers (not to be confused with six cortical layers). Starting from the ventricular surface, the first layer is the *alveus*, a thin layer of axons that join together and form the fimbria. Second is the *stratum oriens*, which contains mostly interneurons (basket cells) and is crossed by the axons of the pyramidal layers as they reach the alveus. The *stratum pyramidale* is the main element of the cornu Ammonis, as it contains the pyramidal cells and interneurons. The *stratum radiatum* consists of apical dendrites from the pyramidal neurons. The *stratum lacunosum* is composed of axons from the perforant fibers and Schaffer collaterals (see below). Lastly, the *stratum moleculare* blends with the dentate gyrus and mostly contains the arborizations of apical dendrites of pyramidal neurons. Notably, the pyrami-

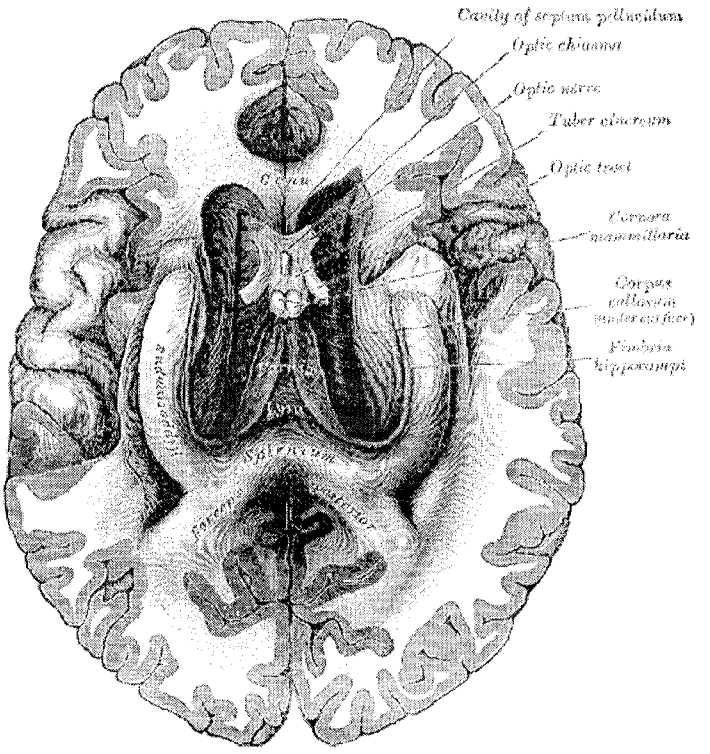

FIGURE 3.2: **Gross anatomy of the hippocampus (axial view).** The C-shape of the hippocampus, fimbria and fornix is seen from below. Notice the fusion of the crura of the fornices at the midline, forming the body of the fornix. Figure from Gray's Anatomy of the Human Body (public domain)[153].

dal neurons have dendritic arborizations so large, that they reach all layers of the hippocampus, where they synapse with different neuronal populations.

The dentate gyrus envelopes the CA4 segment. On the temporal surface, it can be seen as a toothed bulging, the *margo denticulatus* (Figure 3.3). It only has three layers: the *stratum granulosum* contains soma of granular neurons, whose axons reach CA3-4. The *stratum moleculare* and the *polymorphic layer* have very few interneurons.

The coronal anatomy of the hippocampus is quite similar throughout its length, although the fimbria is gradually thicker and eventually detaches from the hippocampus and forms the fornix (Figure 3.3).

The main function of the hippocampus appears to be the consolidation of new memories. Through connections with the entorhinal cortex, the hippocampus is

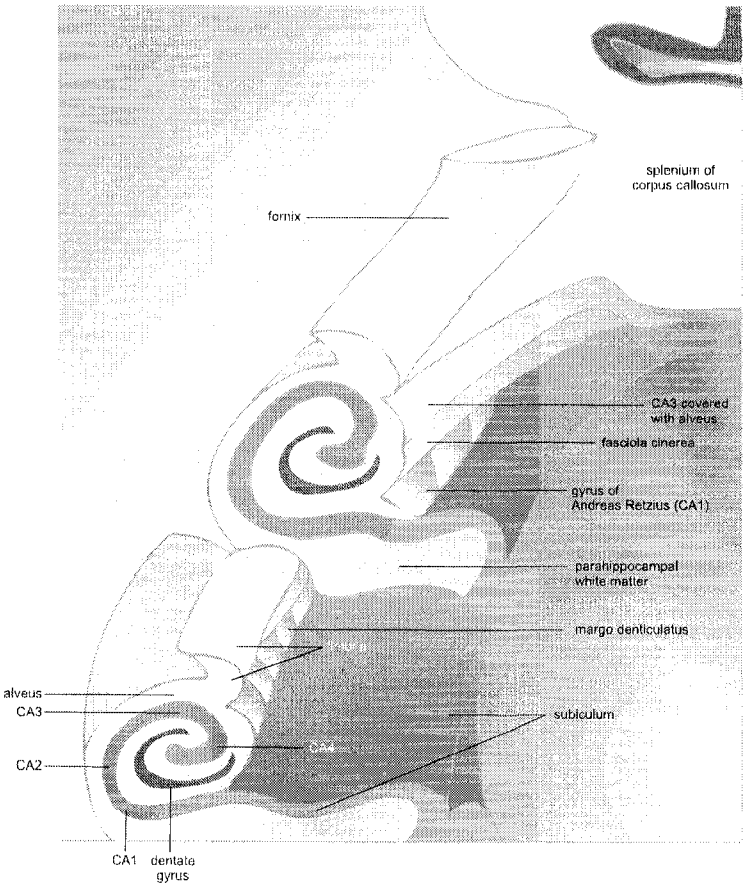

FIGURE 3.3: **Three-dimensional structure of the hippocampus.** Two coronal cuts are made to expose the hippocampus at two levels, namely the head and the body. This allows a clearer visualization of the anatomy, resembling a rolled-in tube. The fornix is transected at the level of the crus. From this vantage point of view, it is evident that the hippocampus is an invagination of the temporal cortex.

connected virtually to the entire brain and acts as a funnel for the classification of information. All types of memory are modulated by the hippocampus (semantic, episodic and spatial). In order to perform its functions, hippocampal neurons are remarkably plastic. This enhanced plasticity is believed to be the substrate for its epileptogenesis. Damage to both hippocampi produces a permanent state of anterograde amnesia; that is, the patient is unable to build new memories, but does not forget past events[155]. Interestingly, these patients can learn new skills, but they do not remember how or when they learned them.

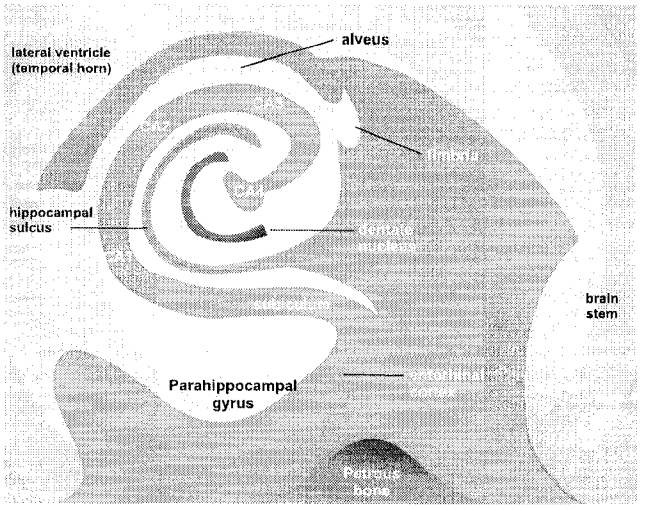

FIGURE 3.4: **Coronal anatomy of the hippocampus.** A single coronal slice at the level of the head of the hippocampus reveals the interlocked position of the dentate nucleus and the cornu Ammonis. The entorhinal cortex is continuous to the subiculum and the cornu Ammonis, which is subdivided into four subsections (CA1-CA4). A thin strip of white matter, the alveus, lies on the ventricular surface of the hippocampus, and converges to form the fimbria and the fornix.

The amygdala

The amygdala is a group of gray matter nuclei located deep within the medial temporal lobes, anterior-superior to the head of the hippocampus. It is shaped like an almond, hence its name. The cortical and medial nuclei are involved in olfaction, while the basal, lateral and central nuclei are limbic. It appears to be involved in emotional learning, Pavlovian conditioning and memory modulation. Ablation of both amygdalae produces Klüver-Bucy syndrome, characterized by hypoemotionality, loss of fear, hypersexuality and hyperorality[156,157].

The parahippocampal gyrus

This is a broad term to refer to the tissue surrounding the hippocampus, up to the medial aspect of the fusiform gyrus. It includes the perirhinal and entorhinal cortices (Brodmann's areas 35 and 36; and 28 and 34, respectively). The entorhinal cortex is the principal input to the hippocampus, to which it funnels information from all sensory and motor systems. The parahippocampal cortex continues pos-

teriorly and superiorly with the cingulate cortex. The term "gyrus fornicatus" refers to both the parahippocampal and the cingulate gyri.

The septal region

Located on the medial surface of the cerebral hemispheres, right below the rostrum of the corpus callosum, this area consists of two gyri and two sulci. The lateral and medial septal nuclei are subcortical gray matter nuclei included within the septal region. The importance of the septal region (aside from its clear implications in pleasure[158]) is evident when considering its connections to and from the hippocampus (see below).

The cingulate cortex

A long, curved gyrus that wraps around the corpus callosum, situated in the medial aspect of each hemisphere. The word *cingulum* means belt, in latin, and *cingulate* is the derived adjective. The white matter within the cingulate gyrus is commonly referred to as the cingulum, particularly in its supra-callosal region, but it can also be used for the infra-callosal (temporal) portion, as an alternative to "parahippocampal white matter". The word cingulum is preferred in this thesis. The cingulate cortex contains Brodmann's areas 23, 24, 26, and 29 to 32.

The mamillary bodies

A pair of easily visible protuberances located on the posterior aspect of the ventral surface of the hypothalamus. It is composed of two gray matter nuclei, namely lateral and medial.

3.2.2 Connectivity of the limbic system

Every portion of the brain is connected, directly or indirectly, to several other areas of the brain. However, one of the more studied set of connections are those that link the different anatomical components of the limbic system. In 1937, James Papez[159] proposed what was to become one of the most important circuits in

cognitive neuroscience, in which he described a closed circuit between the hippocampus, thalamus, hypothalamus and cingulate cortex (Figure 3.5). The circuit of Papez is central to memory, emotion, and epilepsy.

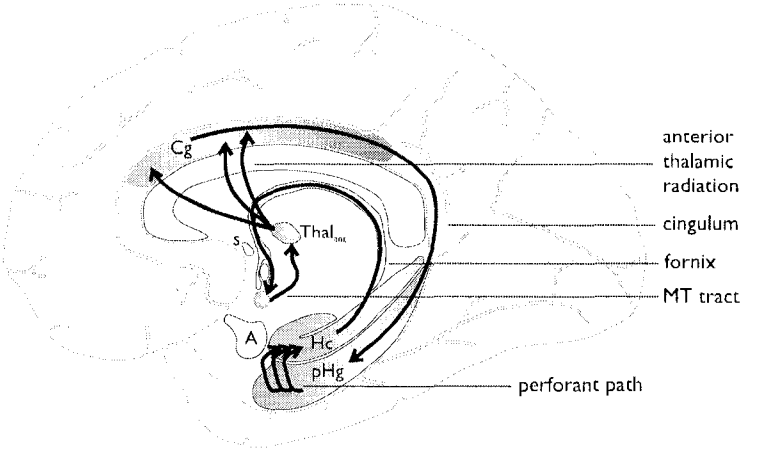

FIGURE 3.5: **The circuit of Papez.** The hippocampus receives information from the entorhinal cortex in the parahippocampal gyrus through the perforant path. The fornix in turn directs information to and from the hippocampus and the mammillary bodies of the hypothalamus, which are communicated with the anterior nuclei of the thalamus via the mamillo-thalamic (MT) tract (bundle of Vicq d'Azyr). The supra-callosal portion of the cingulate cortex receives afferents via the anterior thalamic radiation. The cingulate cortex is continuous with the parahippocampal gyrus, and the subjacent white matter, the cingulum, completes the circuit. All connections are bi-directional. Arrows are shown only for didactic purposes, as to highlight the concept of a closed circuit. Cg: cingulate gyrus; s: septal nuclei; $Thal_{ant}$: anterior thalamic nuclei; A: amygdala; Hc: hippocampus; pHg: parahippocampal gyrus.

Hippocampal projections run through the *fimbria and fornix* and reach the mammillary bodies of the hypothalamus. From there, a small-diameter (<1 mm) bundle of axons reaches the anterior nuclei of the thalamus, called the *mamillothalamic tract* or *Vicq d'Azyr's bundle*. The connection between the anterior thalamic nuclei and the cingulate cortex is made through a collection of axons that penetrate the corpus callosum. The *anterior thalamic radiation*, as it is called, is hence not a bundle or fascicle, but loosely defined anatomically. As commented in section 3.2.1, the parahippocampal gyrus is continuous with the cingulate cortex, and the white matter within them, the *cingulum*, provides the necessary connections

between these two structures. The entorhinal cortex, part of the parahippocampal gyrus, connects back to the hippocampus via the *perforant path*, whose name is secondary to the fact that these fibers must penetrate the subiculum to reach the dentate gyrus and the cornu ammonis. Although it is generally described as a uni-directional loop, in reality all the connections in the circuit of Papez are bi-directional. Furthermore, it is an over-simplification of the complex reciprocal connections of the limbic system. The bi-directionality of the fibers mean that this circuit is not closed, as suggested by Papez and by Shipley[160]. The discussion of all known limbic connections is clearly beyond the scope of this dissertation and the reader is referred to the thorough work of Gloor[161]. For the purpose of this thesis, two limbic bundles are very important: the fornix and the cingulum. Due to their relatively large size and diameter, and their lack of crossing with other fiber bundles, these two tracts are the only white matter components of the circuit of Papez that are amenable to study with diffusion tensor imaging (the technical reasons behind this are discussed in section 2.3).

The fornix As more fibers join the fimbria, it eventually detaches in the posterior region of the hippocampus, forming the *crus* of the fornix. It then turns medially into the lateral ventricles, bends rostrally underneath the isthmus of the corpus callosum and meets its contralateral counterpart, to which it fuses and forms the *body* of the fornix. The body of the fornix continues anteriorly immediately beneath the body of the corpus callosum, then abruptly turns inferiorly, is bisected by the anterior commissure (forming pre- and post-commissural *columns*), and finishes in the the septal region and mammillary bodies of the hypothalamus. Thus, the fornix has a C-shape that is slightly bent inwards (Figures 3.3, 3.5 and 5.2), from which its name is derived (latin for "arch"). This curved white matter bundle, approximately 3-5 mm in diameter, contains hippocampal afferents and efferents that are both myelinated and un-myelinated[161,162]. In humans, it is composed of nearly two million fibers [a], a number that is disproportionately

[a] For comparison, the corpus callosum contains roughly 300 million fibers[163], and the corticospinal tract has slightly more than one million fibers[164].

large when compared to other animals[165,166]. The majority of the hippocampal efferents arise in the subiculum, and not in the cornu ammonis[167]. The few efferents from the cornu ammonis synapse in the septal region, which projects back to the hippocampal formation. The post-commissural subicular efferents terminate mostly in the mamillary body of the hypothalamus, although a few fibers synapse in the midline and anterior thalamic nuclei. The septal region sends fibers to the hippocampus via the fornix that are both cholinergic and GABAergic. In non-primate species, the fornix provides two commissural connections (ventral and dorsal), while in humans the ventral hippocampal commissure appears to have vanished[168]. The dorsal commissure [b] is sparse and communicates the presubiculum and entorhinal cortex of each hemisphere [c][171]. It must be noted that the fornix described above corresponds to what is formally known as *subcallosal* fornix. Thus, there exists a *supracallosal* fornix which travels with the cingulum fibers (some of which eventually pierce the corpus callosum and join the subcallosal fornix). For practical purposes, the term fornix refers exclusively to the subcallosal component. A word of caution must be made in light of the complexity of the fornix, in the sense that the studies presented throughout this dissertation cannot discern individual fiber populations from the plethora of distinct (and discrete) connections traveling through the fornix.

The cingulum This very heterogeneous fiber bundle runs along the entire length of the parahippocampal and cingulate gyri (Figure 3.5). It contains very long association fibers that interconnect the parahippocampal region with the cingulate cortex, but also a large number of short association fibers that connect adjacent regions of the fornicate gyrus. Also included in its supra-callosal portion, are fibers that are part of the anterior thalamic radiation. The cingulum provides connections with virtually the entire brain, as it connects the frontal, parietal, occipital and temporal lobes, and subcortical gray nuclei. Similarly to the fornix, this is

[b] dorsal psalterium or lyra Davidis.

[c] Electrical stimulation of a hippocampus does not evoke a response in the contralateral hippocampus[169,170].

a bi-directional pathway, and the same cautionary words regarding its analysis apply.

Intrahippocampal circuitry It is important to discuss the two recognizable pathways in the intrahippocampal circuitry, namely the polysynaptic and direct pathways, for the understanding of epileptogenesis of TLE and the normal function of the hippocampus.

Polysynaptic intrahippocampal pathway (Figure 3.6(a)) The entorhinal cortex, serving as a funnel for information coming from virtually all somatosensory and association cortices, projects its axons through the subiculum to reach the dentate gyrus via the perforant path. These fibers are mostly excitatory and contact the dendrites of granular cells. The granular cells, in turn, send their axons, the glutaminergic *mossy fibers*, to CA3 and CA4. The pyramidal cells of CA3 and CA4 have axons that enter the alveus and fimbria, but these axons have branches called *Schaffer collaterals* that reach CA1. Although some fibers from CA1 enter the fimbria directly, most axons of CA1 synapse in the subiculum, which sends its fibers through the post-commissural fornix. Phylogenetically speaking, this pathway is primitive and appears to be involved in episodic and spatial memory.

Direct intrahippocampal pathway (Figure 3.6(b)) This is a more evolutionary advanced pathway. The entorhinal cortex projects its axons directly to CA1, via a route that is different from the perforant path, and skipping connections with the dentate gyrus or CA3/CA4. The neurons in CA1 project to the subiculum, which in turn projects back to the entorhinal cortex. From there, fibers reach the temporal and frontal cortices. The main input to the direct pathway is the perirhinal cortex, and is believed to be involved in the recognition and memorization of objects, and in semantic memory.

The intrinsic modulation of hippocampal activity is provided by collaterals of the pyramidal neurons in the cornu Ammonis, which provide feedback to other close and distant pyramidal neurons. A second modulatory mechanism is pro-

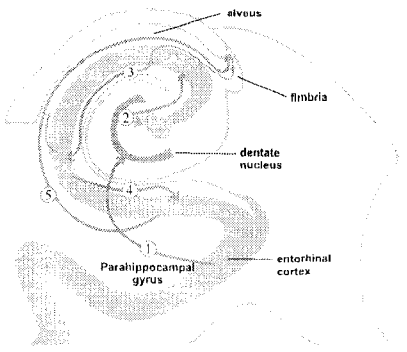

(a) **The polysynaptic intrahippocampal pathway.** 1: Perforant path. 2: Mossy fibers. 3: Schaffer collaterals. 4: Fibers from CA1 to the subiculum. 5: The subiculum provides the majority of output fibers that form the fornix.

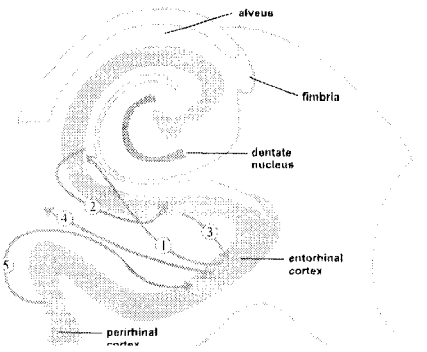

(b) **The direct intrahippocampal pathway.** 1: Direct connection between the entorhinal area and CA1. 2: CA1 to subiculum fibers. 3: The subiculum projects back to the deep layers of the entorhinal cortex. 4: To temporal and frontal association cortices. 5: The entorhinal cortex receives inputs from the perirhinal cortex.

FIGURE 3.6: **Intra-hippocampal circuits**

vided by a species of interneurons called *basket cells*[172]. Basket cells receive inputs from pyramidal neurons, to which they provide inhibitory feedback. These interneurons also modulate the activity of dentate granule cells through a relatively complex mechanism: Mossy cells are stimulated by the perforant path at lower voltages than dentate granule cells. Mossy cells excite the basket cells, which in turn inhibit the dentate granule cells (Figure 3.7). The importance of these modulatory systems will become apparent in section 3.2.3.

Connections of the amygdala Two major systems connect the amygdala with other regions of the brain: the *stria terminalis* and the *ventral amygdalofugal pathway*. The stria terminalis connects the amygdala with the hypothalamus and septal region. The stria terminalis travels along the medial border of the caudate nucleus along its entire path, providing a curve that is very similar to the fornix. The ventral amygdalofugal pathway connects it to the brain stem, the lateral hypothalamus, association cortices (orbital, insular, prefrontal), striatum and thalamus. These fibers travel through several other distinct white matter bundles, such as

the uncinate and the inferior longitudinal fasciculi. Short fibers communicate the amygdala and the subiculum and cornu Ammonis of the hippocampus.

3.2.3 Mesial temporal sclerosis

The term mesial temporal sclerosis (MTS) refers to a specific lesion of the hippocampus and other mesial temporal structures (such as the amygdala, uncus and parahippocampal gyrus), characterized by selective neuronal loss and gliosis. It is the most common lesion in temporal lobes resected for intractable seizures, present in around $^2/_3$ of cases[173–175]. The cell loss in the hippocampus is not global (as is in ischemic lesions), but shows a specific pattern. In particular, neuronal loss is prominent in CA1, CA3 and CA4, with sparing of the neurons in CA2. There is also another histopathological form, termed "end folium sclerosis", in which only the hilus (CA4) is affected. Another common histopathological feature of MTS is granule cell dispersion, in which the granule cells lose their tightly packed distribution, with subsequent thickening and blurring of the dentate nucleus[176]. The temporal white matter of patients with MTS occasionally shows ectopic gray matter neurons, although it is not clear if this is a consistent abnormality specific to MTS[177,178].

The first known reference to this pathology was published in 1825[179], but was not given much attention at first. Scattered reports kept appearing for the next fifty years, which were compiled in 1880 by Sommer[180], who was the first to provide a direct link between the microscopic findings of MTS and clinical characteristics that now seem like TLE. This view was later confirmed by Bratz in 1899[181]. The etiology of MTS is a matter of considerable debate as of this day. The first two hypotheses directly confronted their corresponding authors in the 1920s, with Spielmeyer suggesting a vascular pathophysiology[182], and Vogt and Vogt a (yet unsupported) metabolic cause[183,184]. The lack of hard evidence for a metabolic theory meant that it was Spielmeyer's vascular theory which was favored for the next fifty years, supported by Penfield and Gastaut[173,185]. However, as time passed, the vascular theory was discarded, as ischemic lesions were

shown not to produce the typical, selective pattern of neuronal loss seen in typical MTS[186,187].

The Vogts, with their theory of "pathoclisis", which stated that, due to unknown metabolic factors, certain areas of the hippocampus are more vulnerable to damage than others, were on the right track. It was not until twenty years ago that such metabolic factors were identified. The first is the large amount of (*N*-methyl-*D*-Aspartate, NMDA) [d] glutamate receptors in CA1 as compared to other regions[188–190], and the second factor is the reduced amount of calcium-buffering proteins in CA1 and CA3, namely calbidin and chromogranin A[191–193]. The consequences of these two factors combined is an increased susceptibility to *excitotoxicity*, in which neurons are literally "excited to death"[194,195].

Epileptogenesis of mesial temporal sclerosis

Although it is still unclear if MTS is the cause or the consequence of TLE, it appears certain that it can perpetuate an epileptogenic condition. Animal studies have shown that repetitive electrical stimulation of the perforant path produces pathological damage similar to that seen in MTS, with pyramidal neuron and mossy cell loss of CA3, with sparing of basket cells and pyramidal neurons of CA2[196,197] [e]. This suggests excitotoxic damage via glutaminergic mossy fibers. If, however, inhibitory interneurons survive, how can this lesion be excitatory and epileptogenic? A possible explanation lies in the *dormant basket cell hypothesis*, which states that the death of mossy cells (due to their reduced excitation threshold from the perforant path) reduces the excitatory input necessary for basket cells to perform their inhibitory functions upon the dentate granule cells[198] (Figure 3.7).

Another effect of mossy cell death is the synaptic reorganization of dentate granule cells. In particular, the axonal branches that normally innervate the mossy

[d] NMDA receptors are 10 times more permeable to Ca^{++} than to Na^{+}.

[e] The pattern of hippocampal damage resembles, but is not identical to, MTS. Particularly, CA1 pyramidal cells are not affected after perforant path stimulation. Sustained CA3 stimulation can, however, destroy CA1 cells[198].

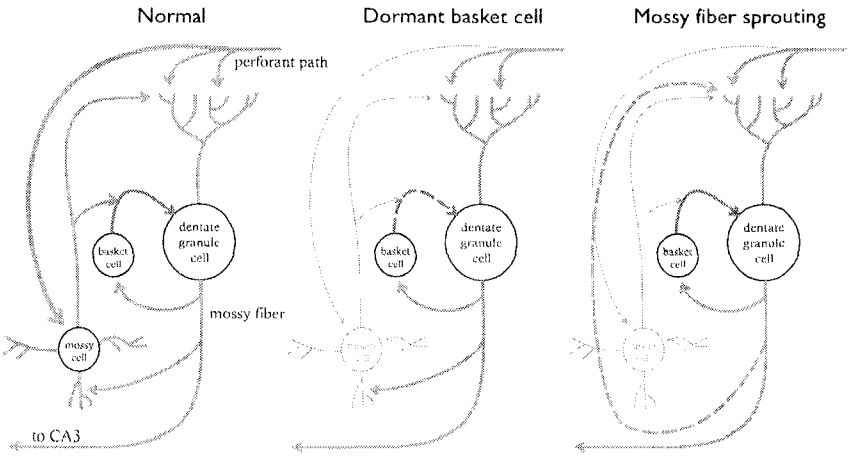

FIGURE 3.7: **Proposed mechanisms of epilepsy in MTS.** Schematic view of the normal intra-hippocampal modulatory circuits in the normal and abnormal conditions. Orange arrows indicate excitatory fibers, blue arrows indicate inhibitory connections. The death of hilar mossy cells (gray neurons in the last two panels) produces a reduction of the inhibitory action of basket cells upon dentate granule cells (dashed blue arrow) or aberrant sprouting of the mossy fibers (dashed orange arrow), which provide excitatory feedback to dentate granule cells. In both hypotheses, the end result is an increased excitation of dentate granule cells.

cells (i.e. the mossy fibers) *sprout* to reach alternative contact points within 2-8 weeks[199,200] (Figure 3.7). Although the exact targets of these sprouting projections have not been identified, it is believed that these aberrant connections provide an excitatory feedback loop to the dentate granule cells[201–203], although it is also possible that they represent a compensatory mechanism[204]. The aberrant connections contain a considerable ammount of Zinc within them, which allows their microscopic visualization using Timm's stain method[205]. Mossy fiber sprouting has been reported in animal models of epilepsy[206,207], as well as in resected human hippocampi of TLE patients[208–211].

An important question is whether MTS causes TLE or if TLE results in MTS (the so-called chicken-egg problem)[212]. Generally, patients with TLE had some sort of *initial precipitating injury* in the first four or five years of their life, but recurrent, unprovoked seizures do not appear until several years later, during which they appear to be healthy[141]. Common initial precipitating injuries include febrile seizures, head trauma, birth injury and infection of the central nervous system[213].

Interestingly, 2-4% of all children suffer from febrile seizures between the ages of one and five, but the majority of them do not develop epilepsy.[214,215]. Looking back from the other end shows a very different picture, as approximately $^2/_3$ of patients with TLE have a history of febrile seizures[216–218]. This situation has led to the belief that febrile seizures can only result in TLE if they occur in patients with an underlying predisposing factor. Hence, febrile seizures could be considered as a "second hit" in the popular *two-hit hypothesis*[213,219]. This hypothesis is very attractive and sound, in the sense that it explains why not all children with febrile seizures end up having epilepsy. The nature of the "first hit", however, has remained elusive.

Epidemiological studies have suggested that the occurrence of seizures is a self-facilitated phenomenon[220], and several histological abnormalities have been reported to be correlated with disease duration, age at seizure onset or number of generalized seizures[221–224]. In patients with TLE, the volume of the hippocampus and extra-hippocampal structures has also been found to progressively decline over time[225–233]. Similarly, a gradual decrease of the putative neuronal marker N-acetyl-aspartate, as measured with magnetic resonance spectroscopy, has been demonstrated in the temporal lobes of patients with TLE[234,235], although this decline appears to be reversible upon seizure freedom[236]. It has been suggested that the largest factor leading to neuronal loss within the hippocampus is the initial precipitating injury[222]. Upon establishment of TLE and ongoing seizures, further neuronal loss develops, albeit at a slow rate. These ideas make MTS both a cause and a consequence of TLE, and suggest that only with very long disease durations could MTS develop in the absence of an initial precipitating injury. Insight into this question is provided in Chapter 7.

3.3 Imaging of temporal lobe epilepsy

The different imaging modalities that are used in the clinical evaluation of patients with TLE are reviewed in this section. Section 3.3.3 reviews relevant imaging

studies that may not impact clinical decision-making on an individual basis, but provide insight into the biological mechanisms of TLE.

3.3.1 Qualitative assessment of conventional MRI

There is no doubt that neuroimaging has changed the way we look at all forms of epilepsy, and that it has facilitated the diagnosis of several epilepsy syndromes. It has become an absolutely necessary part of the evaluation of patients with TLE and, as the Commission on Neuroimaging of the ILAE states:

> MRI is essential for presurgical evaluation [...] Epilepsy surgery should never be contemplated without an MRI examination, apart from exceptional circumstances, such as a specific contraindication (e.g. cardiac pacemaker)[237] [f].

A typical MRI protocol for surgical evaluation of TLE should include both T1- and T2-weighted images, preferably in coronal and axial orientations, as well as a high-resolution three-dimensional volume acquisition. Axial slices, in particular, should be acquired with an angle that makes the slices run parallel to the long axis of the hippocampus. These slices are generally prescribed using a para-sagittal slice, where the parahippocampal white matter is clearly visible (Figure 3.8). Care must be taken to avoid a "tilt" in the slices, as asymmetries of the hippocampal size or signal intensity caused by this could erroneously be attributed to pathology.

The most common visually-evident MRI abnormality of MTS is increased hippocampal T2 signal[238,239] (Figure 3.8). The abnormal signal intensity is thought to be directly related to the increased water content in the tissue secondary to neuronal loss and gliosis[240–242]. An enlarged hippocampal fissure (itself a normal variant), having intense T2 signal, should not be confused with tissue signal abnormality. This is more difficult to evaluate when thick slices are utilized and partial volume averaging artifacts dominate. Therefore, it is recommended to use CSF-signal-suppressed sequences, such as fluid-attenuated inversion recovery

[f] It is noteworthy that, despite this strong recommendation, TLE surgery was successfully performed in the pre-MRI era.

(FLAIR)[243–245]. Evidence of T2 signal abnormalities are usually defined subjectively, by comparing the mesial temporal lobe structures of one hemisphere to the other. Thus, bilateral abnormalities are often difficult to identify. The counterpart of increased hippocampal T2 signal in MTS is a decreased signal intensity in T1-weighted images. In general, T2 signal abnormalities are more conspicuous than T1 signal decrease, although the spatial resolution of T1-weighted images is typically higher [g], which allows for better visualization of the morphology of the mesial temporal structures.

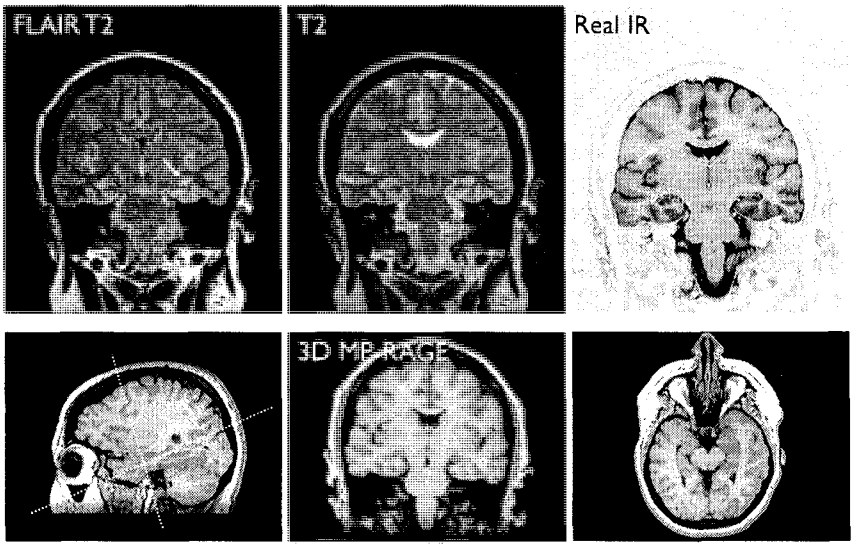

FIGURE 3.8: **Clinical MRI of MTS.** MTS can be reliably detected using coronal T2-weighted images, particularly in CSF-supressed (FLAIR) images. Hippocampal increased T2 signal is evident in the left hippocampus (arrow), as is slight atrophy. The inversion recovery image with real reconstruction (Real IR) shows the hippocampal anatomy in great detail and highlights hippocampal atrophy as compared to the contralateral hemisphere. The bottom row shows three reconstructed slices from a three-dimensional volume using magnetization-prepared rapid acquisition gradient echo (3D MP-RAGE). The dotted lines in the parasagittal slice show the prescription of the coronal and axial slices, relating them to the long axis of the hippocampus. The high resolution of the MP-RAGE images allow for the visual estimation and quantitation of volumes of the mesial temporal structures.

[g]Often due to the three-dimensional acquisition scheme utilized in heavily T1-weighted gradient echo images (e.g. 3D MPRAGE, Figure 3.8).

Another common abnormality seen in MTS is hippocampal atrophy (Figure 3.8). This feature is perhaps one of the most utilized by neuroradiologists, in particular when arbitrarily-defined, oblique two-dimensional reconstructions can be made from a three-dimensional volume. The decreased hippocampal volume is directly related to the degree of neuronal loss[246–248], and the sensitivity of this finding is high[238–240,249]. It is not uncommon to find hippocampal atrophy in the absence of T2 signal abnormalities in MTS and, for this reason, obtaining high resolution images is always recommended[250]. The internal architecture of the hippocampus can only be seen using sub-millimeter resolution with good gray/white matter contrast. High-field imaging and special surface coils aid in the visualization of the mesial temporal structures[251,252]. Improvements in resolution and contrast mechanisms will lead to images that resemble histopathological sections and will further improve the diagnosis of MTS.

Anterior temporal white and gray matter signal abnormalities can be seen in around half of the patients with MTS and are related to diverse mechanisms, such as ectopic white matter neurons, gliosis, inflammatory changes and deposits of corpora amylacea[253]. These abnormalities must not be confused with temporal cortical dysplasia. It appears that the abnormalities seen in the anterior temporal lobe are signs of an abnormal development of this lobe, with persistence of immature cell types and suboptimal myelination[254].

Using the appropriate above-mentioned clinical MRI sequences, and in the hands of a neuroradiologist experienced in the diagnosis of epilepsy, MTS can be detected in around 90% of the cases[255]. Notably, around $1/5$ of patients with TLE have some other lesion in addition to hippocampal sclerosis ("dual pathology")[254].

3.3.2 Quantitative assessment

T2 relaxometry Over the last decade, great attempts have been made in order to reduce the subjectivity of the evaluation of MRI and to increase their sensitivity. T2-weighted images, already quite sensitive, still benefit from quantitative treatment, which increases their diagnostic yield[256,257]. T2 relaxometry provides a means to directly quantify the time constant that produces the high signal inten-

sity on conventional T2-weighted images. On conventional T2-weighted images, only a single (and late) echo is obtained (typically around 90 ms). Tissues with a short T2 will give a very weak signal, if any, at this late time point and appear dark, whereas tissues with a long T2 will still provide a considerable amount of signal and appear bright. In order to quantify the T2 constant of each tissue, at least two different echoes must be acquired, and a (typically mono-exponential) decay curve is fitted to these points. The exponent that best fits this curve is equal to the T2 constant of each pixel. Quantitative T2 maps can then be constructed by relating T2 values to a color scale or gray values (Figure 3.9). The first reported use of T2 relaxometry in epilepsy utilized a modified Carr-Purcell-Meiboom-Gill sequence that provided 16 echoes[256], and is nearly identical to the one utilized throughout this thesis. It is possible, however, to fit a mono-exponential decay with less echoes, although the measurements are less precise[258–261]. The main advantages of the acquisition of only two echoes is that it reduces the signal contribution from stimulated echoes. It is known that white matter shows a multi-exponential decay[262,263] and, therefore, its T2 constants can only be found by a multi-exponential fit that invariably requires several echoes[264]. Gray matter and CSF, on the other hand, appear to have a mono-exponential decay. Several parameters in dual or multi-echo T2 relaxometry sequences can affect the estimation of T2 values, such as number of echoes, their spacing and the time at which the first one is acquired[264]. Unfortunately, T2 values are not truly "absolute", in the sense that one cannot compare them from one study to another, which means that each study must have its own set of control subjects.

Volume measurements Quantitative volume estimation of the mesial temporal structures has been performed with very good results for over 15 years[265] and is a simple and reliable method for the detection of hippocampal sclerosis. In the simplest case, the volumes of the temporal structures are defined by manually outlining each one on individual slices, integrating the area within all the drawn regions and multiplying this value by the slice thickness. As simple as it sounds, outlining the hippocampus and other mesial temporal structures is no easy feat,

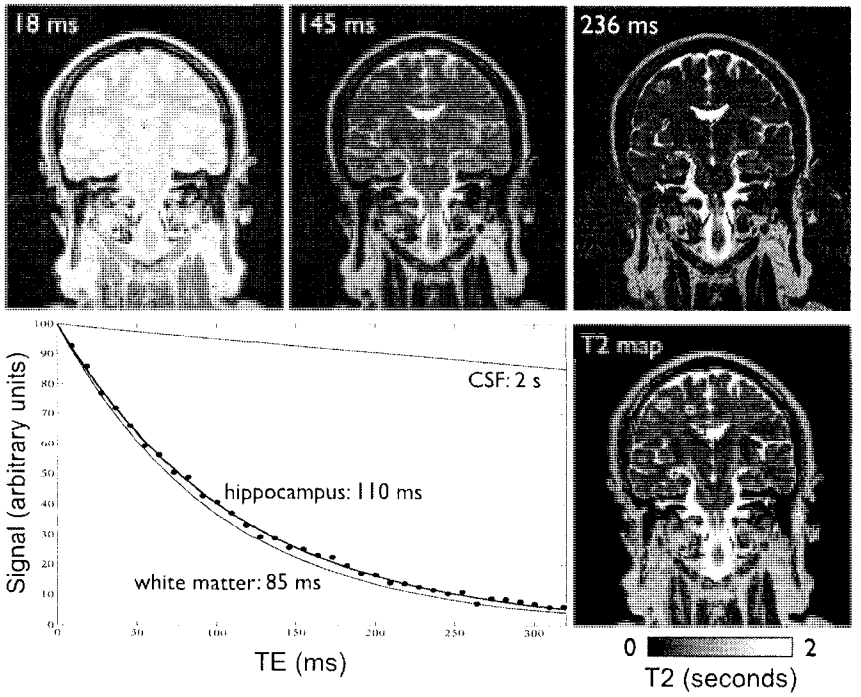

FIGURE 3.9: **T2 relaxometry.** Three coronal images (out of 32) are shown, acquired at increasingly long TE. Notice the loss of signal from gray and white matter, but not from CSF. The graph shows the acquired signal intensity from the hippocampus (black circles) and its corresponding fitted mono-exponential decay, as well as the fitted decay curves from white matter and CSF. The exponent of the best fit is equal to the T2 value of every pixel, which can be displayed as gray levels in the quantitative T2 map. The squares in the T2 map show the locations of the regions shown in the graph.

and it is one prone to errors and subjectivity. Furthermore, not all research centers define the boundaries of the structures in the same matter, which makes comparisons between studies difficult. Atrophy of the fornix, albeit rare, can be used as a lateralization sign[266–269]. Automated tissue segmentation can be accomplished in a number of ways that are independent of the user[270]. The segmentation of gray and white matter can be performed throughout the whole brain, which allows for large-scale group analyses using voxel based morphometry, a close relative of statistic parametric mapping (page 30) which can detect atrophy or hypertrophy of virtually any structure, without the need to make *a priori* hypotheses[72].

Magnetic resonance spectroscopy (MRS) Several studies have demonstrated that MRS can correctly lateralize TLE in patients with[271–275] or without MTS[276]. The most commonly reported metabolic abnormalities are reduced NAA and increased choline (Cho) concentrations. The ratio between NAA and creatine (Cr) can be abnormal in both temporal lobes of patients with TLE, but the asymmetry between the two correctly identifies the epileptogenic hemisphere in the vast majority of patients[277]. It has been suggested that a reduction in the concentration of NAA is indicative of neuronal loss, and that the changes in Cho concentration reflect gliosis[278]. However, the fact that NAA concentration returns to normal values if seizures are eliminated suggests temporary and reversible neuronal dysfunction[236,279–281] or the presence of reactive astrocytes[282] (and not neuronal death).

Other forms of imaging

Single-photon-emission computed tomography (SPECT) This is a valuable tool for the detection of an epileptogenic focus. Contrary to conventional MRI, this imaging method (along with proton-emission tomography) emphasizes functional data, at the expense of lower spatial resolution. In the interictal period, the temporal lobe shows normal or reduced metabolism. In contrast, the mesial temporal structures show a dramatically increased metabolism in the ictal period[283]. The sensitivity of ictal SPECT greatly increases when the administration of the radioisotope (^{99}Tc) occurs early in the course of the seizure[284]. The interpretation of SPECT is generally subjective, based on signal asymmetry, with more than 10% being considered abnormal. SPECT, in particular ictal-interictal scans, can be co-registered to MRI scans [h], which facilitates their interpretation and often point to an initially overlooked anatomical abnormality evident on clinical MRI[126]. Care must be taken when interpreting SPECT images, as 1/2 to 3/4 of TLE patients can have areas of hyperperfusion contralateral to the seizure generator (so-called "mirror images")[285].

[h]Subtraction ictal SPECT with co-registration on MRI (SISCOM).

Positron-emission tomography (PET) A powerful functional imaging method, PET can detect the presence of a radioactively-labeled molecule in the brain. There is some degree of flexibility in the type of molecules that can be labeled, but two in particular are used in TLE: 2-deoxy-2[^{18}F]fluoro-*D*-glucose (FDG) and ^{11}C-flumazenil. FDG is utilized to measure glucose metabolism, while flumazenil can detect $GABA_A$ receptors. Although PET images can be quantitatively analyzed, it is common practice to evaluate the degree of asymmetry of the tracer uptake. FDG PET shows focal interictal hypometabolism in around 90% of patients with TLE[286]. If MTS can be reliably identified with conventional MRI, FDG-PET does not add any useful information[287] but, in TLE cases without clear EEG or MRI lateralization, FDG-PET can detect ipsilateral hypometabolism with a sensitivity of 50%[288,289]. There are several potential disadvantages to PET that have limited its use in the clinical setting, primary amongst them are the cost and short half-life of the tracers used, and its low resolution.

Functional magnetic resonance imaging (fMRI) Invented and widely popularized in the decade of the nineties, fMRI is designed to detect hemodynamic changes that are coupled to increased neuronal activity. The increased focal cerebral perfusion that results from increased focal neuronal firing can be detected using blood oxygen mediated contrast [290,291] and via perfusion-weighted images[292–294]. fMRI is generally analyzed in terms of signal change between periods of neuronal activity and inactivity using voxel-wise analyses such as SPM. The periods of activity/inactivity in the case of simple motor or sensory paradigms can be easily manipulated and commanded but, in the case of the spontaneous and erratic behaviour of interictal spikes, these periods can only be determined with simultaneous EEG recording with live interpretation. Using simultaneous fMRI and EEG, it is possible to detect focal abnormalities in the ictal and peri-ictal states that are concordant with electroclinical data[295–300]. The spatial resolution of fMRI is sufficient for most purposes, which contrasts with its low temporal resolution, which is on the order of seconds. The low temporal resolution is caused by the complex and slow hemodynamic response that is coupled to the neuronal

activity[301,302], and to the fact that fMRI is generally acquired using EPI images. One of the primary clinical applications of fMRI in epilepsy is the identification of eloquent cortical regions that need to be spared from surgical resection but are suspected to lie near the resectable epileptogenic tissue, although it is sometimes still necessary to perform electro-cortical mapping in the operating room.

There is considerable interest in the ability to non-invasively identify the regions of the brain involved in language and memory. The gold standard used nowadays is the intracarotid amobarbital test (Wada test), in which an anesthetic is administered directly to either one of the internal carotid arteries, allowing the function of the other hemisphere to be evaluated in isolation. The Wada test is, therefore, moderately invasive and has a small risk of stroke or other complications. Futhermore, the mesial temporal structures (involved in memory and verbal abilities) is not thoroughly irrigated by the internal carotid system. fMRI is a good candidate to perform this evaluation. There has been good agreement between fMRI and the Wada test for the evaluation of language dominance, with concordance between the two studies as high as 91%[303–305]. Assessment of memory functions has also been recently performed with fMRI with encouraging results[306–310]. Care must be taken when interpreting language or memory-related fMRI tests, as it is not uncommon that cortical regions that are not crucial to these functions are highlighted as such.

3.3.3 Relevant imaging studies in TLE

As described above, many imaging modalities can detect abnormalities in the ipsilateral hippocampus in patients with MTS. This, however, merely points to the diverse changes that the sclerotic tissue undergoes, most of which (or their indirect effects) can be readily identified using conventional MRI. Certainly more interesting are the abnormalities commonly found in the contralateral temporal lobe and even in regions other that the temporal lobes in patients with clear TLE. There is also a great drive in the research community to identify structural, functional or metabolic changes that will help differentiate mesial from lateral TLE, and clues that will help clarify the genesis and prognosis of TLE and MTS.

For example, it has been shown that regions of hypometabolism outside the temporal lobes are associated with worse surgical outcome[311]. Such extratemporal PET abnormalities are not uncommonly reported[287,312–315]. In particular, FDG-PET shows more diffuse abnormalities, while benzodiazepine-receptor studies demonstrate decreased binding localized to the ipsilateral anterior mesial temporal region[312]. More recently, it has been demonstrated that non-lesional TLE patients have metabolic abnormalities in the lateral temporal cortex, whereas patients with TLE and MTS have hypometabolism in the mesial temporal structures, suggesting that these two are truly different disorders[316].

Similarly, fMRI studies have demonstrated diffuse abnormalities in patients with TLE. Using EEG/fMRI, several areas of activation *and* deactivation (not confined to the temporal lobes) were found in a mixed group of TLE patients[317]. Although the block-design is the cornerstone of fMRI, in recent years there has been great interest in the identification of the functional cortical connectivity via the analysis of the time-course of the resting state BOLD-related signal changes[318,319]. The so-called "default mode network" seen in healthy individuals appears to be disrupted in patients with TLE, with several areas of the brain showing inactivation during interictal epileptiform discharges[320]. Using this new approach and block-design fMRI, the cortical networks involved in language have been shown to be atypical in patients with TLE[321,322], in particular when the epileptogenic temporal lobe is in the dominant hemisphere[323,324]. Given the difficulties of simultaneous EEG and fMRI recordings, resting-state fMRI is a promising tool for the detection of regions of epileptogenicity, in particular when the analysis is based on the time-clustering of BOLD signal changes[325,326]. This analytic method, although quite appealing, has still to prove reliable and sensitive enough to be used in the clinical setting.

Around $^1/_2$ of TLE patients show bilateral temporal lobe MRS abnormalities[271,282,327–329] and their presence is indicative of poor surgical outcome[330,331]. Spectroscopic abnormalities have also been found in the thalamus[332,333] and the frontal, parietal and occipital lobes[333] of patients with MTS. Reductions in NAA concentrations, in particular, appear to be more marked in patients with TLE in

the presence of MTS[334]. For this reason, it is the asymmetry ratio between the two hippocampi that can help lateralize the epileptogenic region. As noted before, it is difficult to infer the biological interpretation of NAA concentrations in epilepsy, given its normalization upon seizure freedom. The use of ^{31}P MRS permits the identification of specific metabolites that ^{1}H MRS cannot reliably detect, such as phospocreatine (PCr), adenosine triphosphate (ATP) and inorganic phosphate (P_i). Reductions in PCr are related to its increased hydrolysis to maintain constant ATP concentrations in situations of high energy demand. In contrast with FDG-PET studies, ^{31}P MRS has shown increased metabolic activity in TLE[335,336]. Similar to the reversible changes of NAA concentrations, ^{31}P MRS metabolic indices also return to normal one year after cessation of seizures[337,338].

In patients with TLE and normal conventional MRI, the quantitative analysis of conventional MRI contrasts has an *overall* low yield of detection of abnormalities that match electroclinical information[339]. This by no means indicates that quantitative analytical methods have little to offer in the research of TLE, but only that clinical decisions should not be based solely on these methods at this point. Furthermore, specific analytical methods and contrasts may prove highly valuable in certain forms of epilepsy. T2 relaxometry, for example, has proven its ability to lateralize TLE in patients with normal MRI[257,340]. T2 relaxometry data has also been analyzed using SPM methods, with the identification of focal temporal and extratemporal abnormalities (frontal, parietal, anterior cingulate) in patients with MTS[339,341]. Perhaps the most utilized type of images that have been given the quantitative treatment is the high-resolution T1-weighted data sets, as these are typically acquired in every imaging investigation of TLE. Volumetric measurements have demonstrated bilateral hippocampal atrophy in patients with TLE[250,342–348]. As a matter of fact, it has been suggested that the entire hemisphere ipsilateral to the seizure generator is reduced in volume[345]. Extrahippocampal, bilateral gray and white matter volume reductions in the temporal and extratemporal regions in patients with TLE have also been reported[349–363]. Besides volumetric analyses, the shape of the hippocampus can be analyzed[364,365], which can show subtle atrophy in portions of its anatomy that are specific to TLE[348].

Several studies have utilized VBM in the study of TLE patients. Reduced gray matter concentration has been reported in the ipsilateral and contralateral dorsal prefrontal cortex[366–368], parahippocampal gyrus, cingulate[367–370], thalamus[367,368,370–372], and in the cerebellum[368]. Of interest, patients with TLE but without MTS appear to lack these extended abnormalities of the gray matter[373], and patients with left MTS seem to have more extended and marked extrahippocampal abnormalities[374]. Reductions in white matter concentration have also been found in the corpus callosum[367] and the temporal[367,371] and fronto-parietal lobes[375]. Overall, VBM studies have shown abnormalities of the gray and white matter throughout the brain, both ipsilateral and contralateral to the epileptogenic temporal lobe, occasionally with conflicting results.

The thickness of the cortex was reportedly thinner bilaterally in several areas of the brain in patients with TLE, both within and outside the temporal lobe[232,376,377]. The use of texture analysis on conventional MRI of patients with TLE and unilateral MTS showed bilateral hippocampal abnormalities[378,379] and ipsilateral reduced gray and white matter volume and blurring of the gray/white matter junction in the temporal lobe[380].

Magnetization transfer imaging[381] has shown a very low yield in the detection of lesions in focal epilepsies[339] or the lateralization of TLE[382], but appears to be useful in the detection of malformations of cortical development[383]. Recently, however, correlations between vocabulary and cognitive tests and magnetization transfer ratio of the fusiform, middle and superior temporal gyri have been found in TLE patients with interictal psychosis (but not in those who were non-psychotic)[384,385].

Several DWI and DTI studies have shown various abnormalities in TLE. The fact that there is is a considerable decrease in water diffusivity in the epileptogenic tissue in the acute postictal state has been repeatedly demonstrated in several forms of epilepsy, both in animal models and humans, over the last decade[386–391]. Notably, the diffusivity normalizes within a few days and remains elevated in the interictal state when there is persistent tissue changes. The time course of these changes are thought to represent cytotoxic edema in the postictal state, followed

by sclerosis, gliosis and concomitant increased intercellular water in the chronic stage. Although changes in hippocampal diffusivity have been proposed as a means to lateralize TLE with varied but overall good results[135,392–399], the contralateral hippocampus is not devoid of abnormalities[397,400–402] [i], which in some cases normalize following cessation of seizures[403]. However, due to the high sensitivity of conventional imaging, it appears as though DWI can only confirm the lateralization of TLE in cases where the former has already demonstrated a lesion[404]. Despite this, there is value in the measurement of diffusion parameters of the hippocampus in TLE, as the overall diffusivity of the epileptogenic hippocampus shows a moderately strong correlation with disease duration[396]. The amygdala and the thalamus ipsilateral to MTS have also shown abnormally increased diffusivity [397,405].

The white matter of patients with TLE has also been reported to have abnormal diffusion parameters. Using DTI and SPM analysis, the temporal white matter of patients with TLE showed increased diffusivity and reduced diffusion anisotropy[406]. In a study of two patients with TLE, the splenium of the corpus callosum showed a transient decrease of water diffusivity following acute seizures[407]. In another study of 15 patients with TLE in the interictal state, the corpus callosum and the external capsules showed reductions in diffusion anisotropy and increased diffusivity perpendicular to the tracts[408]. In patients with non-lesional TLE and interictal psychosis, there were reductions in diffusion anisotropy of the frontal and temporal lobe white matter[409]. A very recent study demonstrated reduced diffusion anisotropy in the uncinate fasciculus ipsilateral, but not contralateral, to MTS[410].

* * *

As any reader will undoubtedly think by now, there is a great body of evidence to support that temporal lobe epilepsy is not confined to the temporal lobes. On

[i] There is discrepancy amongst reports of abnormal diffusivity in the contralateral hippocampus. Increased ADC was reported in [402] and [400], while it was found reduced in [401] and [403].

the other hand, the fact that the vast majority of patients with TLE and unilateral MTS experience a worthwhile reduction in seizures (most of times a total abolishment) is the clearest indicator that, more often than not, these patients have a single seizure generator. The presence of these diffuse brain abnormalities, the generalization of seizures and the cognitive defects associated with TLE suggest that it is, however, a disorder of the normal brain network. The foundation for any network is its connectivity and, as of today, the ideal method to investigate brain connectivity in the living person is diffusion tensor imaging and tractography. Despite this, the study of white matter in epilepsy has been overshadowed (understandably) by the study of gray matter.

The work I performed in the last five years at the University of Alberta has focused on the white matter of patients with TLE. When I started working on this project, there only were a dozen or so reports on the use of diffusion tensor imaging in epilepsy, and only a handful of those had focused on the white matter. The fornix and cingulum had not yet been investigated with the aid of tractography in temporal lobe epilepsy. For this I developed an imaging/analysis protocol that is described in Chapter 4. Using such methodology, we found *bilateral* limbic (and extra-limbic) white matter diffusion abnormalities in patients with *unilateral* MTS (Chapter 5). These abnormalities do not resolve upon seizure freedom (Chapter 6). Furthermore, limbic—but not extra-limbic—abnormalities appear to be linked to the presence of MTS (Chapter 7). The pattern of abnormalities seen are similar to those seen in abnormalities of axonal membranes, myelin sheaths, or both, such as those present in Wallerian degeneration of white matter (Chapter 8). Lastly, a direct electron-microscopy study of the fimbria/fornix of patients who underwent resective TLE surgery is presented in Chapter 9, which attempts to widen our understanding of the abnormalities present in the fornix of patients with TLE and to provide the first direct correlation between DTI parameters acquired *in vivo* and the underlying histology.

Part II

Experiments

CHAPTER 4

CEREBRO-SPINAL FLUID SIGNAL SUPPRESSION

Abstract

The limbic system, relevant to memory and emotion, is an interesting subject of study in healthy and diseased individuals. It consists of a network of grey matter structures interconnected by white matter fibers. Although gray matter components of this system have been studied using MRI, the connecting fibers have not been analyzed to the same degree. Cerebro-Spinal Fluid (CSF) signal contamination of the fornix and cingulum, the two major white matter tracts of the limbic system, can alter Diffusion Tensor Imaging (DTI) measurements and affect tractography. We investigated the effect of CSF signal suppression on fiber tracking of the limbic connections and characterized the diffusion properties of these structures in healthy volunteers. Nine healthy individuals were scanned with standard and CSF-suppressed DTI. Tractography of the fornix and cingulum was performed for both acquisition methods. We report mean diffusivity and fractional anisotropy measurements of the crus, body and columns of the fornix, and descending, superior and anterior portions of the cingulum. Diffusion measurements were improved and tractography was facilitated using CSF-suppressed DTI. In particular, tract volume increased, while decreases of the mean diffusivity and increases of diffusion anisotropy more accurately represented the underlying tissue by minimizing deleterious partial volume averaging from CSF. This was particularly true for the fornix, as it is in closest contact to CSF. Diffusion measurements throughout the limbic connections were consistent in healthy volunteers. We recommend the use of CSF suppression when performing diffusion tensor tractography of the limbic system.

A version of this Chapter was published in:
Concha L., Gross D.W. and Beaulieu C. Diffusion tensor tractography of the limbic system. *AJNR American Journal of Neuroradiology* 2005. 26(9):2267–74.

4.1 Introduction

The limbic system has a very important role in high level mental processes, such as memory and emotive behaviour and is composed of a group of inter-connected gray and white matter structures which create a loop in each cerebral hemisphere[411]. In 1937, James Papez[159] described an important set of connections in the limbic system which linked the hippocampus, mamillary bodies, thalamus, cingulate and parahippocampal gyrus. While other structures have subsequently been integrated into the limbic system (such as the amygdala, the septal region and the olfactory bulb), the Circuit of Papez contains most of the principal limbic grey and white matter structures. The two most visible white matter connections in this circuit are the fimbria/fornix, which projects from the hippocampus to the septal region and mamillary bodies, and the cingulum, which connects the enthorinal cortex and the cingulate gyrus.

Both the gray and white matter components of the limbic system have been studied using MRI in several brain disorders, such as epilepsy[357–359,367,412], dementia[413,414] and schizophrenia[415]. Until recently, the study of white matter bundles was restricted to post-mortem dissection or slice-by-slice evaluation by in-vivo medical imaging both in terms of the tissue's signal intensity and/or volume measurements. However, recent advancements in Magnetic Resonance Imaging (MRI) allow virtual in-vivo dissection of major white matter bundles in the brain[65]. White matter fibers are depicted based on the behaviour of water movement, as measured with Diffusion Tensor Imaging (DTI), and are later reconstructed in three dimensions using a technique known as Diffusion Tensor Tractography[55,56,61,416].

DTI can provide indirect measures of the functional integrity of white matter and has been previously used in the study of limbic structures both in healthy[417] and diseased individuals[418–422]. Diffusion measurements are usually performed by manually defining Regions of Interest (ROI) on 2-dimensional image maps or by performing voxel-based analysis of spatially normalized images. Manual ROI drawing has three disadvantages:

i) it is user-dependant,

ii) it is time consuming (ROIs must be drawn slice by slice), and

iii) it is sometimes very difficult to delineate a white matter bundle based solely on anatomical scans and/or diffusion anisotropy maps.

While voxel-based analysis (e.g., Statistical Parametric Mapping, SPM) does not suffer any of these disadvantages, image data sets must be normalized to a standard space by means of non-linear registration, the downside being that the original data is typically modified and smoothed with a Gaussian filter (in order to satisfy statistical assumptions and to compensate for the imperfections of the spatial normalization)[72,423].

The use of tractography to outline a volume from which to extract various diffusion parameters (i.e., mean diffusivity, fractional anisotropy) is a promising technique[424–426] as it diminishes the three disadvantages of manual ROI drawing and does not require spatial normalization of the images. White matter bundles are segmented semi-automatically by means of tractography using tract selection regions that are less susceptible to user bias than ROI drawing. Such an approach has been shown to be reproducible[425] and is typically faster than manual ROI-based analyses. The poor delineation of the cingulum and fornix on apparent diffusion coefficient or fractional anisotropy 2-dimensional maps, coupled with their curved trajectories, make tractography an ideal tool for their study. Diffusion tensor tractography has been used to delineate the fornix and/or cingulum in healthy volunteers[65,417,427], as well as patients with epilepsy[422] but, to our knowledge, no study has reported the diffusion characteristics of all the different portions of the fornix (crus, body and columns) and cingulum (descending, superior and anterior portions) in healthy, young adults.

Since the fornix and cingulum are adjacent to Cerebro-Spinal Fluid (CSF) spaces (i.e., the ventricles and inter-hemispheric fissure), the delineation of the tracts and their absolute diffusion parameters may be adversely affected by partial volume with the rapid, isotropically diffusing CSF. The use of a Fluid-Attenuated Inversion Recovery[243] component prior to a DTI imaging sequence greatly mini-

mizes CSF signal contamination, although at the expense of a significant increase in acquisition time and a reduction in signal-to-noise ratio (SNR)[428–430]. The effects of CSF signal suppression on diffusion tensor tractography have been evaluated recently for the corpus callosum[431] but its consequences on subsequent tract-derived quantitative analyses of diffusion parameters and its implications on the fiber tracking of the limbic system have not been examined.

The objectives of this study were twofold: (1) to examine the effect of FLAIR for CSF suppression on quantitative diffusion tensor tractography and (2) to report diffusion parameter values along the fornix and cingulum in healthy, young adult volunteers. These results will provide a solid basis to guide future studies of the limbic connections with disease.

4.2 Methods

Approval of the research protocol was obtained from the Institutional Health Research Ethics Board of the University of Alberta and informed consent was obtained from all participants.

Image acquisition Nine healthy subjects, with a mean age of 28±5 years (range 23 to 36) were scanned using a 1.5 T Siemens Sonata scanner. Both standard and FLAIR DTI sequences used were identical with the exception of the inversion pulse and the number of slices. Both data sets were acquired using a dual spin-echo, single shot echo-planar imaging sequence with the following parameters: slice thickness=2 mm, no inter-slice gap, TR=10 s, TE=88 ms, FOV=256×256 mm^2, matrix=128×128 (partial phase Fourier: 6/8; interpolated to 256×256), 6 diffusion directions, b=1000 s/mm^2, 8 averages. The voxel dimensions at the time of acquisition were 2×2×2 mm^3, which resulted in voxel dimensions of 1×1×2 mm^3 after interpolation of the data. The FLAIR DTI sequence used an inversion time (TI) of 2200 ms and acquired 26 slices, while the standard (non-FLAIR) DTI acquired 63 slices (acquisition time for both imaging schemes was 9:30 min each). The slice orientation and the center of the slices were identical for both techniques. Since

more slices were acquired using standard DTI, only the 26 slices present in both data sets were used for fiber-tracking and further analysis. The calculated signal-to-noise ratio (SNR) on the non-diffusion weighted ($b = 0$ s/mm^2) images for the standard DTI data sets was, on average, 65 ± 2, while that of FLAIR DTI was 47 ± 1.

Fiber tracking Tensor processing of the images and fiber tracking were performed on a PC running DTIstudio (Johns Hopkins University), which used the FACT algorithm[55]. Tracts were initiated by seeding the entire data set in those voxels with a fractional anisotropy (FA) value >0.3. The tracts were propagated until they reached a voxel with an FA <0.3 or if the propagating line deviated by an angle >70°.

Tract selection Fiber tracking is a two-step, semi-automatic process in which all tracts are first extracted in the entire data set by the tracking algorithm as outlined above. Subsequently, individual tracts are selected manually. In order to virtually dissect a tract, it must be isolated from the original mass of tracts by judicious placement of tract-selection regions drawn (based on *a priori* anatomical knowledge of tract projections) on the 2-dimensional images or maps in any orientation[56,427,432]. The most common approach is to isolate the tracts by selecting them only if they penetrate one or more such regions (see Figure 1 in references[65,427]).

We experimented with several schemes for tract selection using different locations of tract selection regions. Initially, tracts were selected only if they traversed two or more regions drawn at great distance from each other, which caused a great number of tracts to be discarded, as they were shorter in length, albeit having an anatomically correct orientation. This strict selection scheme, although theoretically appealing, was impractical for the fornix and cingulum. On the other hand, if several regions were drawn closely and tracts were selected if they traversed any of them, there was a tendency to include several erroneous tracts and to overestimate the volume of the bundles. We found that we could use some of the strictness of the first approach, combined with the flexibility of the second, in or-

der to be able to select medium-length tracts with correct orientation while still restricting their path.

Thus, we selected three different portions of each tract separately (Figures 4.1, 4.2 and 4.3). Tracts were selected if they penetrated a selection region located halfway along the tract, and any of two selection regions drawn at the extremes of the portion we wished to study. Tract selection regions and the resulting portions of the tracts that were analyzed are shown in Figures 4.2 and 4.3 for the fornix and cingulum, respectively. As can be seen from the figures, the tract selection regions must not precisely outline the tracts, but simply contain them. Tractography and subsequent measurements were performed separately for the right and left fornix and cingulum in each subject.

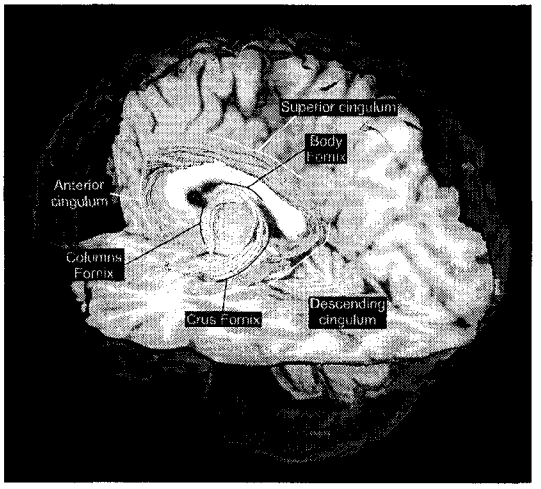

FIGURE 4.1: **Diffusion Tensor Tractography of the fornix and cingulum in a healthy individual.** Three-dimensional fiber tracking of the fornix (green) and cingulum (orange) overlaid on an anatomical, T1-weighted 3D-MPRAGE volume. The anatomy of these two fiber bundles can be thought as two nested semi-circles. The tracts shown were selected by brute force for display purposes only. The labeled portions of the tracts (indicated by yellow lines for the cingulum and black lines for the fornix) were analyzed subsequently using judicious tract selection regions, as shown in figures 4.2 and 4.3

Diffusion measurements and volume analysis FA and mean Apparent Diffusion Coefficient (mean ADC) values were queried at each tract's voxel locations

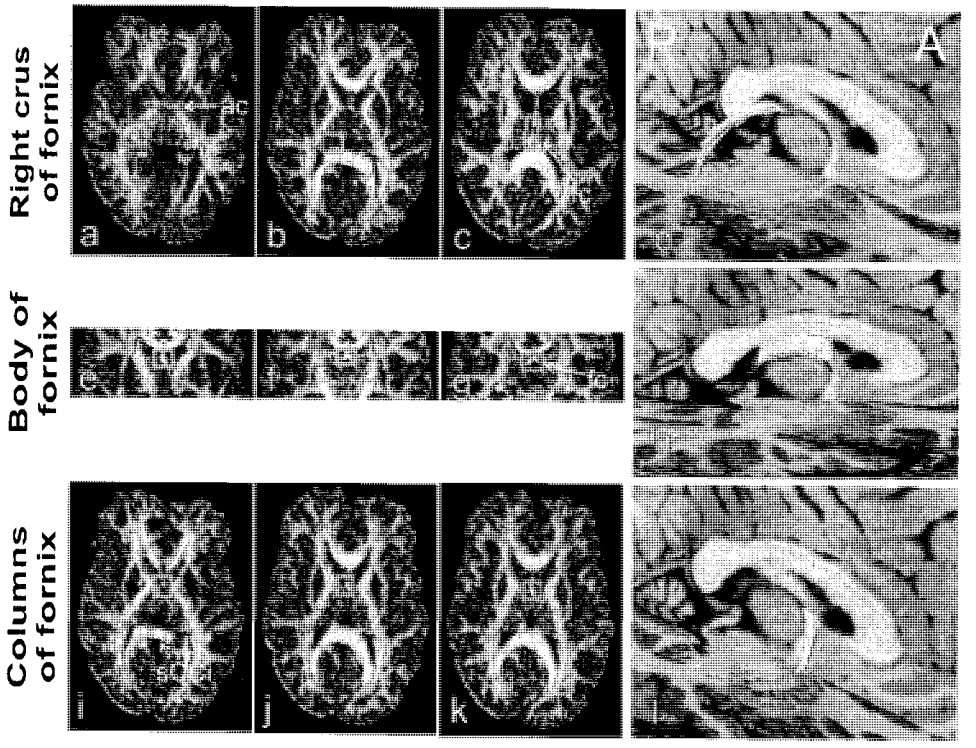

FIGURE 4.2: **Region of Interest placement for selection of individual portions of the fornix.**The fornix was selected in three distinct portions, as this enhances the selection accuracy. For each portion, tract-selection regions were manually drawn on either FA or principal diffusivity color maps. In order to be selected, the tracts had to go through the middle tract-selection region (green boxes in b, f and j) and through either one of the extreme regions (a or c; e or g; i or k, for the crus, body and columns, respectively). The FA maps presented are derived from CSF-suppressed DTI. The same procedure was repeated for the standard DTI data sets using identical tract selection regions. The resulting FLAIR DTI-derived tracts of a healthy subject are presented in 3-dimensional views overlaid on anatomical 3D-MPRAGE axial and sagittal slices (d, h and l). Subsequent analyses of all segments were performed only between the two extreme tract selection regions. [A: anterior, P: posterior, ac: anterior commissure, fc: fusion of the crura, sCCi: inferior border of the splenium of the corpus callosum. Image (e) is 0.5 cm posterior to the vertical AC line. Image (k) is parallel to the inferior border of the body of the fornix]

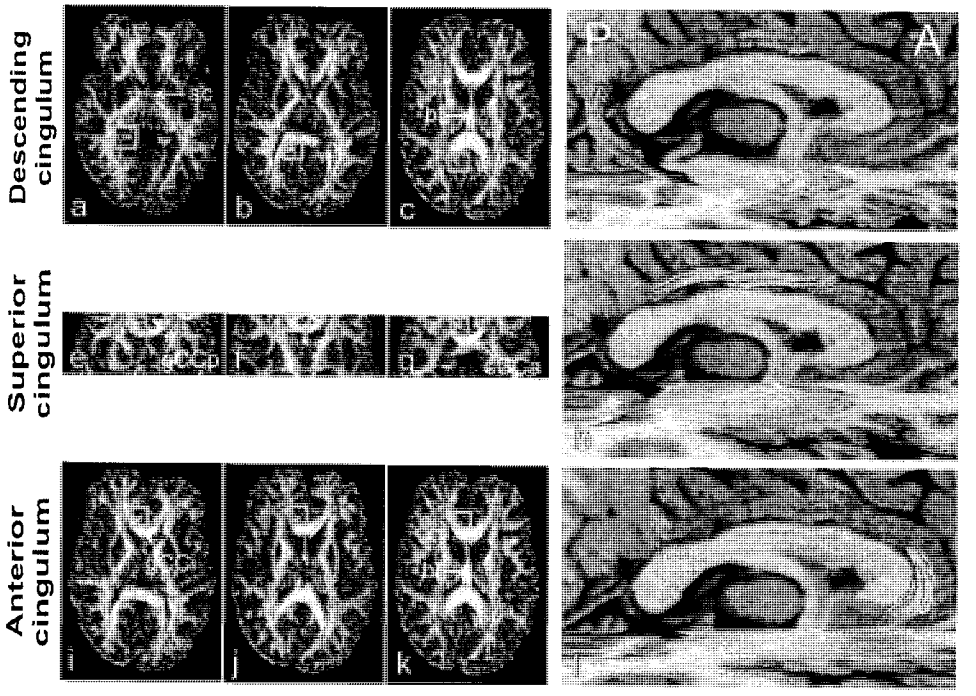

FIGURE 4.3: **Region of Interest placement for selection of individual portions of the cingulum.** Three portions of the cingulum, namely the descending, superior and anterior portions, were selected after fiber-tracking of the entire volume in both standard and FLAIR DTI data sets. For each portion, tract-selection regions were manually drawn on either FA or principal diffusivity color maps. In order to be selected, the tracts had to go through the middle tract-selection region (orange boxes in b, f and j) and through either one of the extreme regions (a or c; e or g; i or k; for the descending, superior and anterior portions, respectively). The FA maps presented are derived from CSF-suppressed DTI. The same procedure was repeated for the standard DTI data sets using identical tract selection regions. The resulting FLAIR DTI-derived tracts of a healthy subject are presented in 3-dimensional views overlaid on anatomical 3D-MPRAGE axial and sagittal slices (d, h and l). Subsequent analyses of all segments were performed only between the two extreme tract selection regions. [A: anterior, P: posterior, ac: anterior commissure, bf: body of fornix, gCCp: posterior border of the genu of the corpus callosum, sCCa: anterior border of the callosal splenium, gCCi: inferior border of the callosal genu]

using an in-house program. A single measurement of either FA or mean ADC for each tract portion per subject was calculated by averaging all the voxels present in the tract. The same procedure was followed for both imaging techniques. For volume measurements, the number of voxels containing at least one fiber was counted, and the result was multiplied by 2 mm^3 (the interpolated voxel volume).

Tract volume, FA and mean ADC measurements were restricted to the sections of the tracts between the two most extreme tract selection regions, thereby assuring that changes in measurements were not due to longer fibers. The landmarks used for parcellation are shown in Figures 4.2 and 4.3 for the fornix and cingulum, respectively.

Given the sample size, the normality of the data cannot be guaranteed. Therefore, statistically significant differences were assessed by two-tailed Wilcoxon's signed ranks tests for each measurement. Results are reported as significant if they had a $p < 0.05$.

4.3 Results

4.3.1 The role of FLAIR in tractography

Overall, tract selection of all the portions of the fornix was easier and more reliable when tracking was performed on FLAIR DTI data sets. In particular, the crus of the fornix could be easily selected in its entirety employing a single tract selection region in 13/18 cases when CSF suppression was performed, as opposed to only one case when standard DTI was used (Figure 4.4). This was due to the fact that the voxels belonging to the crura had FA values (0.15–0.25) below the tracking threshold of 0.3 when no CSF suppression was performed. These particular voxels, alleviated from the deleterious partial volume averaging, increased their FA values to around 0.30-0.40 with the use of FLAIR DTI, which resulted in a continuous fornix from body to crus. The cingulum, on the other hand, did not show this subjective difference in the ease of tract selection in its descending and superior portions. However, the anterior portion was easier to reconstruct as

it typically had a greater number of voxels included when CSF suppression was performed (Table 4.1).

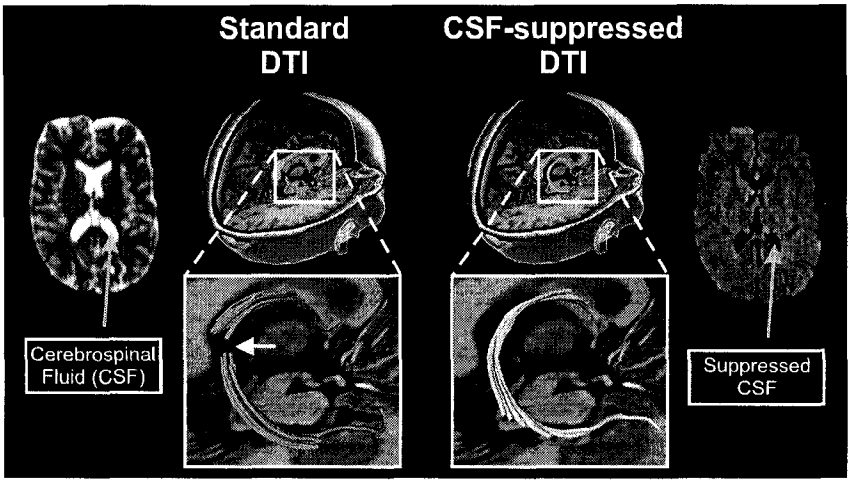

FIGURE 4.4: **Qualitative assessment of the role of CSF suppression in tractography.** Due to CSF signal contamination, the crus of the fornix is difficult to depict with fiber tracking derived from standard DTI data sets. Tissue voxels belonging to the top portion of the crus of the fornix (yellow arrow) suffer partial volume averaging and their diffusion anisotropy drops below the fiber tracking FA threshold (0.3) to values that range from 0.15 to 0.25. When CSF suppression is performed, the same region contains higher anisotropy values (around 0.30-0.40), and its voxels are included by the tracking algorithm, which results in a complete depiction of the structure. The axial non-diffusion weighted images ($b = 0$ s/mm^2) show the bright CSF signal in standard DTI, which is suppressed with FLAIR DTI. The portions of the fornix are overlaid on T1-weighted, anatomical 3D-MPRAGE axial and sagittal slices.

As can be seen in Table 4.1, both tracts showed a significant increase in diffusion anisotropy in two of their three portions when measurements were derived from FLAIR DTI data sets, relative to Standard DTI. The most consistent increases of FA occurred at the levels of the crus and body of the fornix, where it occurs concomitantly with a reduction in mean ADC. Although this reduction in mean diffusivity was large (particularly in the body of the fornix), mean ADC values remained high in the fornix when compared to the cingulum, which could be attributed to incomplete CSF suppression at the level of the ventricles due to pulsation artifacts, since cardiac gating was not used in this study[433,434]. Furthermore,

		Cingulum			Fornix		
		Descending	Superior	Anterior	Crus	Body	Columns
FA	Standard	0.48±0.02	0.66±0.02	0.44±0.02	0.49±0.02	0.54±0.05	0.52±0.02
	FLAIR	0.50±0.02	0.65±0.03	0.48±0.03	0.53±0.02	0.61±0.03	0.54±0.03
	Difference	0.02±0.01	-0.01±0.01	0.05±0.03	0.03±0.02	0.07±0.05	0.01±0.04
	p	**0.011**	**0.04**	**0.027**	**0.011**	**0.015**	0.29
ADC ($\times 10^{-3}$ mm^2/s)	Standard	0.75±0.03	0.71±0.02	0.72±0.03	0.96±0.1	1.45±0.1	0.99±0.07
	FLAIR	0.75±0.02	0.72±0.01	0.73±0.03	0.89±0.04	1.0±0.04	0.95±0.06
	Difference	0±0.02	0.01±0.01	0.01±0.01	-0.06±0.08	-0.44±0.13	-0.04±0.08
	p	1	0.14	0.16	**0.05**	**0.008**	0.16
Volume (mm^3)	Standard	504±136	1196±504	168±30	244±136	572±96	174±44
	FLAIR	600±196	1508±492	260±72	540±130	724±126	292±110
	Difference	110±120	312±391	120±43	196±87	150±138	118+81
	p	0.123	**0.036**	**0.018**	**0.008**	**0.015**	**0.011**

TABLE 4.1: **Diffusion parameters and volume of limbic connections.** Fractional Anisotropy (FA), mean apparent diffusion coefficient (ADC, $\times 10^{-3}$ mm^2/s) and volume (mean ± standard deviation) are presented for three portions of the fornix and cingulum depicted with tractography derived from DTI data sets with and without CSF suppression (FLAIR and Standard, respectively). Except for the superior portion of the cingulum, all structures showed no inter-hemispheric asymmetry and are therefore presented as collapsed data (i.e., [left+right]/2). FLAIR DTI resulted in significant increases of fractional anisotropy in the descending and anterior portions of the cingulum and the crus and body of the fornix, as well as decreases of mean ADC in the crus and body of the fornix. A significant increase in tract volume (mm^3) with CSF suppression is also observed in 5/6 cases.

there is hardly any reduction in mean ADC at the level of the columns of the fornix, which seems to coincide with the lack of increase in diffusion anisotropy.

The volume of the resulting tracts was significantly increased in all the portions of the fornix and in two out of the three portions of the cingulum when DTI was performed with CSF suppression. Such an increase in volume was brought about by the inclusion of more voxels for tractography, due to their increased diffusion anisotropy measurements (above the fiber-tracking FA threshold of 0.3). Furthermore, more voxels with an FA above the tracking threshold translates into more seeding points, which facilitates tract reconstruction.

4.3.2 Diffusion characteristics in the limbic system

We only found asymmetry of diffusion anisotropy in the superior portion of the cingulum (FA right=0.63±0.02, left=0.66±0.03; p=0.017), which is consistent with

previous studies[417,418,420,421]. Due to this, the results presented in Table 4.1 show collapsed data per subject (i.e., [left+right]/2). It is clear from Table 4.1 that diffusion anisotropy lies within a tight range throughout the limbic system, being highest in the superior portion of the cingulum and the body of the fornix. As with any other brain tissue, mean ADC remains relatively uniform, with the exception of the portions that suffer incomplete CSF suppression in which partial volume averaging persists (i.e., body and columns and, to some extent, the crus of the fornix).

4.4 Discussion

Diffusion Tensor Imaging is rapidly becoming a widely available imaging technique with a myriad of applications. The possibility of discerning the orientation of white matter bundles and the ability to reconstruct their three-dimensional structure in-vivo has opened the door to selective studies of fiber tracts both in healthy and diseased human brain.

DTI can be adversely affected by a number of factors, such as inaccurate sorting of eigenvalues due to low SNR, and partial volume averaging[42]. Partial volume averaging results when two or more different tissue types that are contained within one voxel yield an MRI signal intensity that is the weighted sum of each tissue's signal. Thus, this artifact is more conspicuous as the voxel size increases (i.e., imaging resolution worsens) and when the various tissues have vastly different measurable properties. For example, CSF shows fast, isotropic water diffusion as opposed to the slower, highly anisotropic water diffusion seen in white matter tracts. Two approaches can be taken to minimize this artifact. The first is to acquire the images with very small voxels[42], although this can dramatically decrease SNR. The second approach is to null the signal arising from CSF using an inversion recovery pulse with an inversion time tailored to the T1 of CSF (FLAIR) prior to the otherwise typical diffusion tensor imaging sequence[428–430]. The use of FLAIR has the disadvantages of increasing the scan time due to the longer repetition time required and decreasing the SNR by around 30% (assuming constant

repetition time). The increase in scan time per slice translated into a smaller brain coverage in FLAIR DTI (26 slices) as opposed to standard DTI (63 slices). On the other hand, diffusion measurements derived from FLAIR DTI represent the underlying tissue more accurately, especially in regions of high CSF contamination, such as near the ventricles and sulci. If precise measurements of diffusion properties of susceptible tissues are sought, the use of FLAIR is recommended and the increased scan time is justified. Although our current imaging sequence could be improved with an increase in the number of diffusion directions and/or averages[435], the repetition time needed to fit the inversion recovery pulse for CSF signal suppression would make the additional acquisition time impractical for a clinical setting.

Diffusion tensor tractography of the limbic system can, therefore, benefit from FLAIR, since significant portions of the cingulum and fornix are affected by CSF signal contamination. As can be seen in Table 1, the tractography algorithm is able to depict thicker tracts when FLAIR is used, particularly in the fornix. Furthermore, the diffusion measurements derived from the FLAIR data sets are more likely to approximate the real tissue properties. The principal eigenvector of an anisotropic diffusion ellipsoid does not change its orientation when an isotropic diffusion tensor is added. Therefore, it is tempting to argue that a simple reduction of the FA threshold would provide accurate tract depictions even in the presence of CSF contamination. However, using an FA threshold <0.25 for fiber tracking greatly increases the number of erroneous tracts and the variability in tract depictions[425]. Furthermore, even if the tract is outlined anatomically correct, the diffusion parameters, such as mean diffusivity and fractional anisotropy, will be adversely affected by the contaminating CSF signal.

The FACT fiber-tracking algorithm we used[55] reconstructs all the tracts existing in a volume by seeding all the voxels that have an FA above a certain threshold (0.3 in our study). With judicious placement of more than one tract selection region, it is not necessary to precisely outline the bundle of interest, but merely to contain it within a well-defined area. Although this reduces the user dependence

on tract selection, it is still necessary to follow the same general guidelines for all subjects in a study.

We saw important improvements both in the overall appearance of the tracts and the diffusion measurements derived from them when CSF suppression was performed. This was particularly important in the anterior portion of the cingulum and the crus and body of the fornix. The anterior portion of the cingulum travels very close to the CSF present in the inter-hemispheric fissure, which could be responsible for the reduced FA and number of voxels included in the tract derived from standard DTI. The three portions of the fornix studied are bathed by CSF, which accounts for the significant differences of FA and mean ADC seen in the crus and body when FLAIR is used. These changes in diffusion anisotropy were in part responsible for the improved reconstruction of the tracts (Figure 4.4). Interestingly, the columns of the fornix did not show a significant increase in FA or a decrease in mean ADC as would be expected.

Previous studies have reported mean ADC values to lie in the vicinity of 0.7 $\times$ 10^{-3} mm^2/s throughout the white matter[26,428]. Overall, mean ADC values in all portions of the fornix were higher than those expected. This could be due to incomplete CSF suppression by the inversion pulse, which occurs when non-inverted spins in CSF enter the imaging slice as a result of pulsation[433,434]. Incomplete CSF suppression could also be responsible for the absence of changes in the columns of the fornix when FLAIR was used. Cardiac gating has been shown to minimize pulsation artifacts[100,101] but, due to its nature, its combination with an inversion-recovery pulse for CSF suppression is not straightforward. Nevertheless, alternative CSF-suppression techniques that are insensitive to pulsation exist[436,437], but their use has not yet become widespread and were not evaluated in this study.

Previous studies have evaluated fractional anisotropy in the superior and anterior portions of the cingulum in healthy controls, although the nomenclature used for the different portions of these tracts varies amongst reports. Sun et al.[419] performed ROI analysis of the anterior section of the cingulum (in the boundaries between the superior and anterior portions, as defined this study) and reported an

FA of 0.64, which is similar to the values we found in the superior portion of the cingulum. Wang *et al.*[421] found an average FA of 0.51 for the left and 0.44 for the right hemisphere using multi-slice ROIs located in approximately the same region as that described by Sun *et al.* They also analyzed the region between the superior and descending portions of the cingulum and reported an FA of 0.39 and 0.42 for the left and right hemispheres, respectively. These two areas were not analyzed in our present study. Kubicki *et al.*[418] found an average FA value of 0.50 and 0.47 for the left and right superior portions of the cingulum of healthy controls in a multi-slice, segmentation-based analysis, which is lower than our FA findings of 0.66 and 0.63 (left and right, respectively) using FLAIR DTI. Using tract-based analysis, Gong *et al.*[417] radially divided the cingulum in two sections: one that contains the anterior portion and half of the superior portion (as described in our study) and a second section that comprises the posterior half of the superior portion of the cingulum. They found the posterior half to have higher FA values than the anterior half, although these were in general lower (0.35 and 0.45 for the anterior and posterior sections) than those we report. It is important to notice that previous studies have not utilized CSF-suppressed DTI and that they employ a different analysis method than the one described here. We recently reported diffusion measurements for the descending portion of the cingulum and the crus of the fornix in healthy individuals and in patients with mesial temporal lobe sclerosis[422], but the remaining portions of these tracts were not evaluated in our prior study.

At the current resolution which DTI can achieve in a clinical setting, it is not possible to perform tractography of other limbic connections, such as the mammillo-thalamic tract or the anterior thalamic radiations. Our findings however suggest that tractography based DTI analysis of the fornix and cingulum can provide reproducible findings and that this information can be used to indirectly study the axonal integrity of white matter tracts within the limbic system in a variety of brain disorders.

4.5 Conclusions

As expected from previous studies using 2-dimensional DTI analysis, diffusion tensor tractography benefits from CSF suppression, both in the ease for fiber tracking and tract selection, and the diffusion measurements derived from the delineated tracts. This is particularly true if the tract of interest is near CSF spaces, such as the fiber bundles of the limbic system, which justifies the increased scan time and acceptable reduction in SNR. A similar benefit could be anticipated in any other tract near CSF spaces, such as the corpus callosum.

Using a strict tract selection method, the fornix and cingulum can be reliably depicted using diffusion tensor tractography. As there is small inter-subject variability in diffusion measurements in these two important and very interesting limbic connections, this technique is applicable for clinical research in a variety of patient populations. We recommend the use of CSF suppression when performing tractography of limbic connections.

* * *

4.6 Appendix

Tractography of those fiber bundles that are not in close contact with CSF would not likely benefit from the inversion recovery pulse described here. This was exemplified by the superior portion of the cingulum, which showed minimal benefit with the use of FLAIR as compared with standard DTI. Although not part of the limbic system, the cortico-spinal tract was assessed similarly to the fornix and cingulum and, as expected the FLAIR treatment did not improve tractography nor did it alter the quantitative diffusion parameters (Figure 4.5). However, the analysis of the cortico-spinal tract was restricted to its most cranial aspect, namely

The appendix did not appear in the published version of this Chapter.

above the cerebral peduncles. It is the portions of the tract that are below said structure that come in close contact with CSF. The benefit of CSF suppression was however not assessed at this lower level, due to the coverage of the sequence employed. However, it is our belief that CSF suppression could play a role in this portion of the tract, as well as in the study of the optic radiation (in close contact to the lateral ventricles).

The imaging and analysis protocol presented herein was utilized throughout this dissertation.

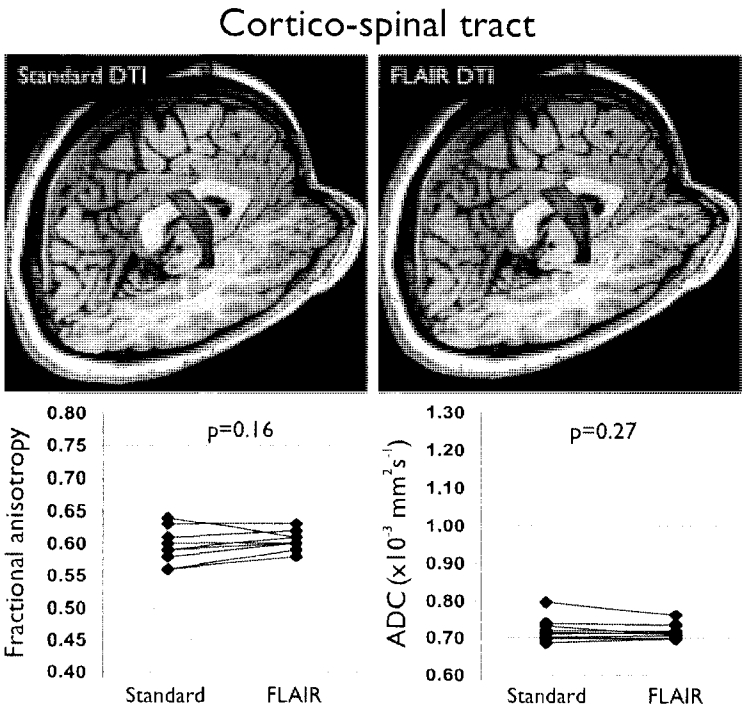

FIGURE 4.5: **Tractography of the corticospinal tract.** Qualitative and quantitative analysis of the use of CSF-suppression shows lack of benefit when the tract of interest is not in close contact to CSF, such as the corticospinal tract in its cranial portion. The limited coverage of FLAIR DTI did not permit to evaluate this tract below the brain stem or above the corona radiata.

Figures 4.6 and 4.7 show individual two-dimensional FA maps calculated from DTI with and without the use of CSF-suppression. While the anatomical coverage of the standard DTI protocol is considerably larger than that of FLAIR DTI (full brain volume when not using CSF-suppression) and slightly noisier, the quan-

titative diffusion parameters obtained from white matter structures adjacent to CSF-filled spaces are more accurate when CSF suppression is utilized. The fusion of the fornix, as well as the most superior aspect of the crura is more prominent on FLAIR DTI (Figure 4.7, center panel) than on the corresponding slice on standard DTI (Figure 4.7, third row, first column). White matter structures lying distant from CSF spaces do not show striking differences between the two imaging protocols.

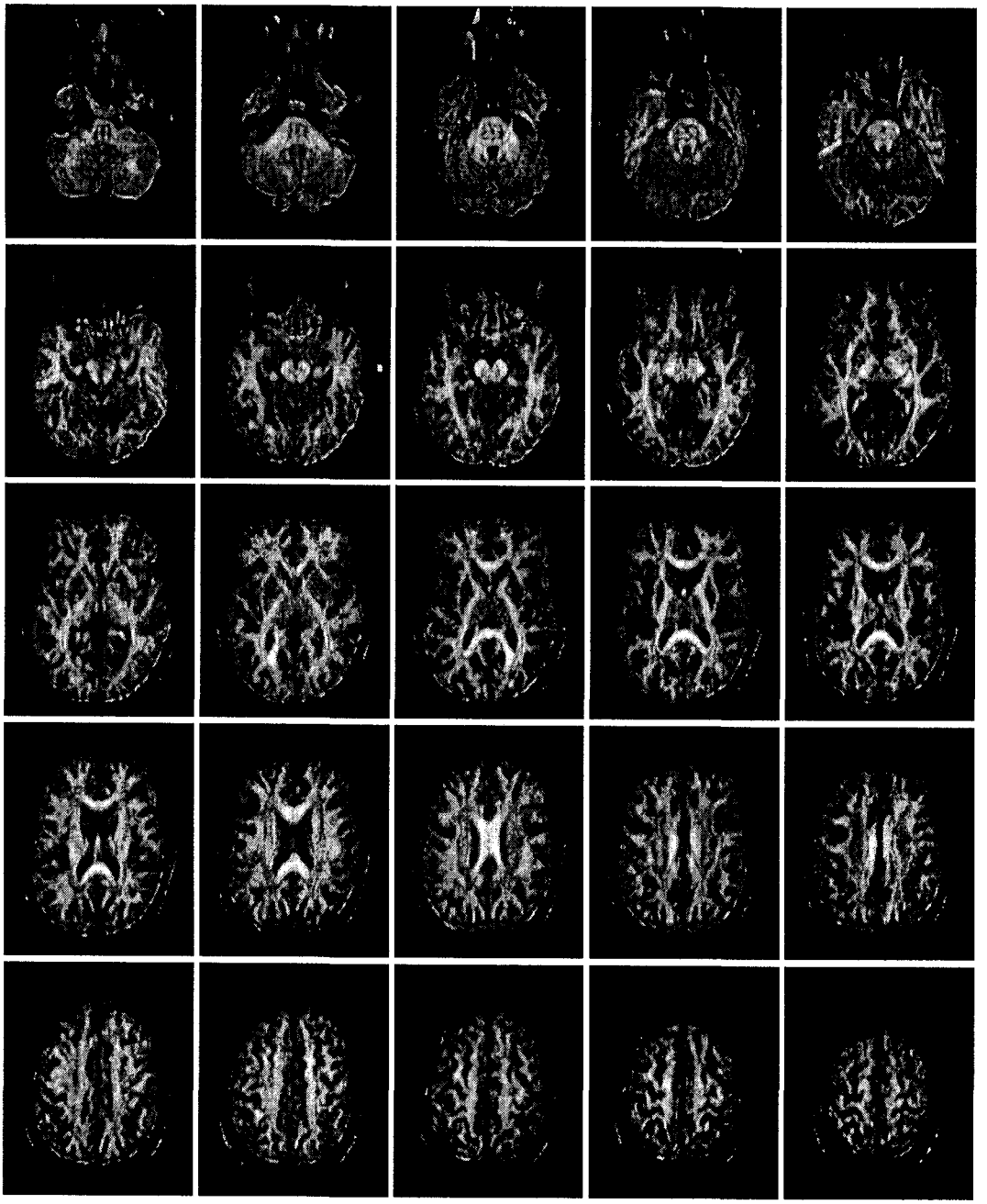

FIGURE 4.6: **FA maps derived from standard DTI.** Twenty-five representative two-dimensional FA maps are shown (2 mm slice thickness), derived from a non-CSF suppressed DTI data set of a healthy 26 year-old woman. The full standard DTI volume consisted of 63 slices. Individual images have been cropped for displaying purposes.

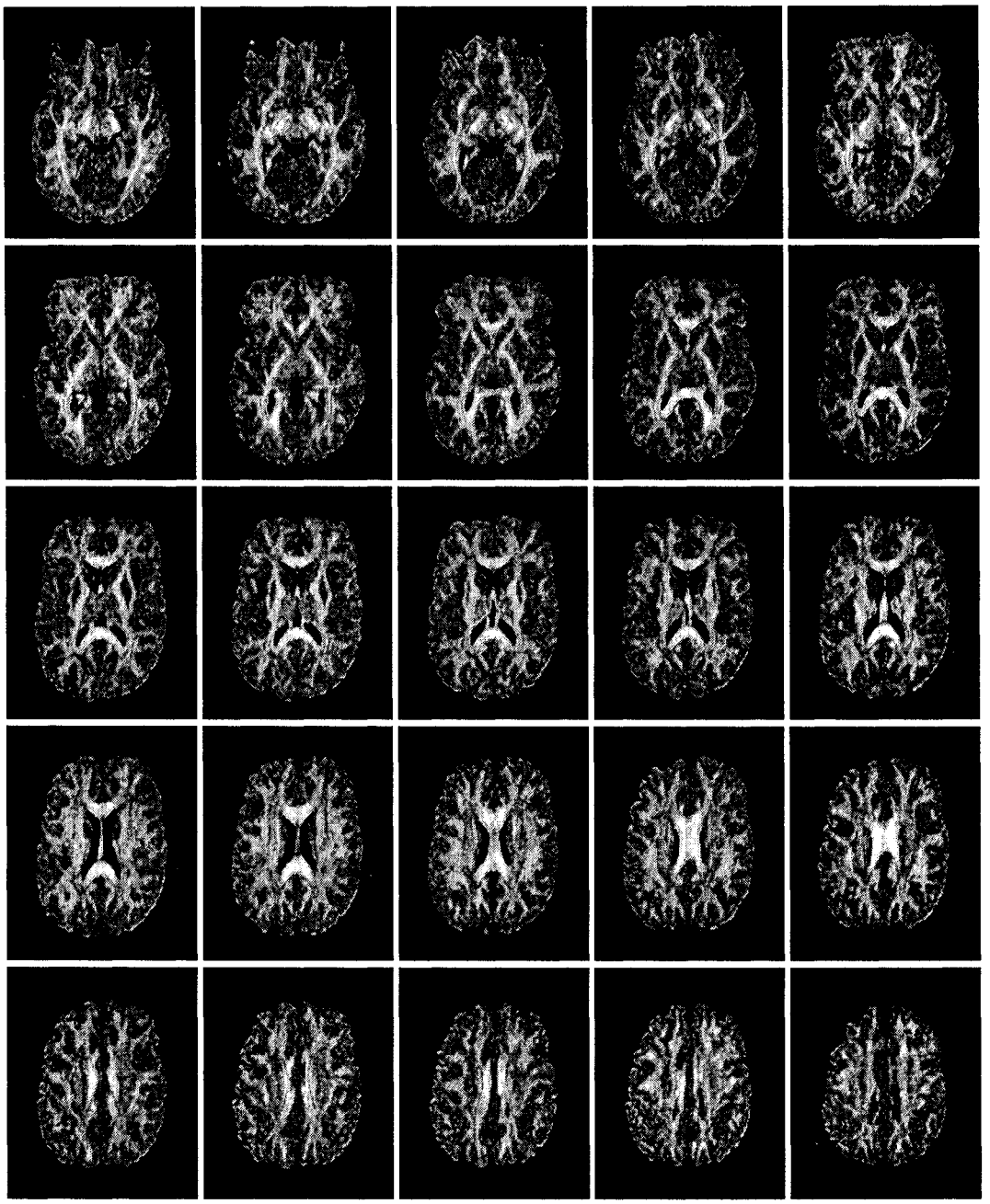

FIGURE 4.7: **FA maps derived from FLAIR DTI.** FA maps derived from a CSF suppressed DTI data set (2 mm slice thickness) of the same subject presented in Figure 4.6. The most superior slice of this data set is not shown.

Chapter 5

Temporal white matter abnormalities in unilateral MTS

Abstract

Diffusion Tensor Magnetic Resonance Imaging (DTI) can acquire quantitative information on the micro-structural integrity of white matter structures and depict brain connectivity in vivo based on the behaviour of water diffusion. DTI-derived tractography has been used for virtual dissection of the fornix and cingulum in healthy subjects, but not in patients with temporal lobe epilepsy (TLE). Eight patients with medically intractable TLE and unilateral mesial temporal sclerosis (MTS) and nine healthy controls were imaged using DTI. Fiber-tracking was performed to delineate the fornix and cingulum, which were quantitatively analyzed. Bilateral symmetrical reduction in fractional anisotropy (FA) was observed in the fornix of patients with TLE along with an increase in water mobility perpendicular to the axis of the fibers. The findings in the cingulum are similar to those of the fornix with the exception of significantly increased bulk diffusivity in the latter. We observed strikingly symmetrical bilateral abnormalities of axonal integrity in the fornix and cingulum in a series of patients with unilateral MTS. Our findings suggest that TLE with unilateral MTS is associated with bilateral limbic system pathology.

A version of this Chapter was published in:
Concha L., Beaulieu C. and Gross D.W. Bilateral limbic diffusion abnormalities in unilateral temporal lobe epilepsy. *Annals of Neurology* 2005. 57(2):188–196.

5.1 Introduction

Temporal lobe epilepsy (TLE) with mesial temporal sclerosis (MTS) is the most common focal epilepsy syndrome[141]. MTS is characterized by cell loss and gliosis[161] and, while it can be detected with conventional Magnetic Resonance Imaging (MRI), quantitative MRI measures are more sensitive in detecting hippocampal pathology[241,257,260,261]. Indeed, one of the primary goals of non-invasive imaging studies is to lateralize the hemisphere with MTS in order to guide surgical intervention, since evidence of unilateral MTS is an important predictor of good surgical outcome[246,438–440]. The fimbria-fornix (from here on referred to as fornix) and cingulum are two of the most visible limbic white matter bundles, both containing afferent and efferent connections to and from the hippocampus[161]. Abnormalities in the fornix and cingulum have been demonstrated in a number of disease states including Alzheimer's disease[414,441], Schizophrenia[415,418,419,442] and TLE[269,357–359].

The integrity of the axonal micro-environment can be indirectly evaluated using Diffusion Tensor Imaging (DTI), which relies on measuring the diffusion of water and its directionality in three dimensions. Given the parallel organization of nerve fibers, water diffusion is normally hindered by membranes in the direction perpendicular to their principal axis (i.e., anisotropic)[18,27,443], whereas in a medium that lacks barriers to water movement, such as cerebro-spinal fluid (CSF), water diffusion is isotropic. Anisotropy can be quantified in each voxel using the index of Fractional Anisotropy (FA) with values ranging from zero (fully isotropic) to one (diffusion is favored in one axis and hindered in the remaining two)[42]. In normal fiber tracts water diffusion is anisotropic (i.e., high FA), whereas in degenerated fibers the FA drops substantially[444–446]. The reduction of FA in degenerated tracts is believed to result from axonal membrane breakdown (i.e., fiber loss)[444] and an increase in extra-cellular matrix due to myelin degradation[445]. The Apparent Diffusion Coefficient (ADC) yields the mean bulk mobility of water (removing directional information, and is hence termed mean diffusivity, MD) and the eigenvalues (λ_1, λ_2, λ_3) correspond to the directional apparent diffu-

sion coefficient either along the fiber tracts (λ_1) or perpendicular to them (λ_2 and λ_3).

DTI evaluation in patients with TLE and unilateral MTS has demonstrated increased MD and decreased FA of the ipsilateral hippocampus[394,447]. DTI abnormalities have also been demonstrated in several white matter tracts in patients with TLE including the external capsule, internal capsule and corpus callosum[408].

Diffusion Tensor Tractography is an exciting new technique capable of performing virtual in-vivo dissection of cerebral white matter bundles[65]. While tractography has been used to visualize the fornix and cingulum in normal subjects[65,427], DTI analysis of these structures in epilepsy patients has not been performed. The objective of this study was to determine whether evidence of axonal degeneration within the fornix and cingulum could be detected in vivo in a group of epilepsy patients with unilateral MTS. This is the first study reporting the use of DTI to evaluate the axonal state in the fornix and cingulum in patients with TLE.

5.2 Subjects and Methods

Approval of the research protocol was obtained from our institutional Health Research Ethics Board and informed consent was obtained from all participants.

Subjects: Eight patients with medically intractable epilepsy and unilateral MTS and nine healthy volunteers were evaluated. All patients had unilateral MTS based on the interpretation of their clinical MRI (including coronal T2-weighted images and T1-weighted 3DMPRAGE). The mean age of patients and controls was 36±15 years (range: 19-59) and 28±4.6 (range: 23-36), respectively, with no significant age difference between groups (Student's t-test, p=0.18). The median time between the last seizure and the study MRI was seven days (range 12 hours to 3 months). History and clinical investigations for patients are summarized in Table 5.2.

Patient	Age (y.)	Onset of Seizures	Febrile seizures	Other history	Seizure pattern	Neuro-psychology	EEG		MRI		Other imaging
							Interictal	Ictal	MTS	Other	
1	23	6m	no	meningitis 6m	CPS	L mes T	LT	LT	L	—	—
2	35	18y	no	minor trauma	CPS	no deficits	RT	RT	R	—	—
3	53	39y	prol.	—	CPS + GTC	L mes T	LT	LT	L	—	PET—LT
4	59	12y	no	—	CPS + GTC	L lat. T	LT>RT	Unclear	L	—	—
5	20	3y	no	coma 3y	CPS	L lat. T	LT	LT	L	**	—
6	44	18m	no	meningitis 3m	CPS	L lat. T*	BiT	*late RT	L	LT atrophy	SPECT: LT NCtx
7	36	17m	prol.	—	CPS	R mes T, lat. F	RT	RT	R	—	—
8	20	6m	yes	—	CPS	—	LT	LT	L	—	—

TABLE 5.1: **Summary of temporal lobe epilepsy patient clinical information.** CPS: complex partial seizures, GTC: generalized tonic clonic seizures, R: right, L: left, mes: mesial, T: temporal, F: frontal, BiT: independent bitemporal, LT>RT: independent bitemporal with left temporal predominance, lat.: lateral, PET: interictal fluoro-deoxyglucose Positron Emission Tomography, SPECT: ictal and interictal Single Photon Emission Computerized Tomography, NCtx: neocortex, prol: prolonged.
* First ictal EEG changes were consistently observed in the right temporal region 30-40 seconds after the first ictal clinical manifestations. ** Left anterior temporal lobe white matter demonstrated diffuse increased signal on T2 weighted image.

Image Acquisition Images were acquired using a Siemens Sonata 1.5T MRI scanner. Coronal T2 relaxometry with coverage of the hippocampus was used to quantify MTS[241,257,260,261]. T2 relaxometry used a high resolution multi-echo sequence with 32 echoes, 10 slices, 3 mm slice thickness, 3 mm inter-slice gap, FOV=230×210 mm^2, matrix=192×176 (interpolated to 384×352), TR=4430 ms, TE_1=9.1 ms, TE spacing=9.1 ms, NEX=1, scan time=8:13 min. Axial fluid attenuation inversion recovery (FLAIR) DTI with coverage of the fornix and cingulum was used to evaluate the integrity of the white matter tracts. The FLAIR component suppresses signal from CSF and minimizes partial volume averaging artifacts[428,430]. The FLAIR DTI sequence used spin-echo Echo Planar Imaging (EPI) with 26 axial slices, 2 mm thickness with no inter-slice gap, TR=10 s, TE=88 ms, TI=2200 ms, FOV=256×256 mm^2, image matrix=128×128 (partial phase Fourier: 6/8; interpolated to 256×256), 6 diffusion directions, b=1000 s/mm^2, 8 averages,

scan time=9:30 min. These parameters resulted in $2\times2\times2$ mm^3 acquisition voxel dimensions, interpolated to $1\times1\times2$ mm^3.

Post-processing Images were transferred to a Sun Workstation running MRVision (MRVision Co., Winchester, MA), where maps for T2, FA, MD, eigenvalues (λ_1, λ_2 and λ_3) and their corresponding eigenvectors were created.

T2 analysis The signal decay was fitted to a mono-exponential curve in a voxel by voxel basis. Regions of Interest (ROIs) outlining each hippocampus were manually drawn in three consecutive slices and the T2 values for all slices were averaged to provide a single T2 value for each hippocampus for all subjects.

Fiber Tracking Diffusion Tensor Tractography was used to depict the fornix and cingulum since they otherwise would have been difficult (if not impossible) to outline manually in the 2D diffusion images. The FLAIR DTI dataset was transferred to a PC running DTIstudio (Johns Hopkins University), which uses the FACT fiber tracking algorithm[55]. All tracts in the dataset were computed by seeding each voxel that had an FA >0.3. The tracts propagated until they reached a voxel with an FA <0.3 or turned at an angle >70°. Based on anatomical knowledge of fiber projections, tracts belonging to each fiber bundle were selected by placing Regions of Interest (ROI)[56,427,432] at two distant portions of the tract in axial views (Figure 5.1). In the majority of the controls only two ROIs per tract were needed to depict the fornix and the cingulum entirely (Figure 5.2), whereas for most of the patients' fornices (whose computed tracts were usually shorter in length and did not reach the initial two ROIs simultaneously) additional ROIs had to be drawn in anatomically guided locations (aided by principal eigenvector color-coded maps) on axial slices between the first two ROIs. Fibers that were clearly not part of these tracts were manually deleted.

DTI analysis Tract coordinates were used to query the FA, MD and eigenvalues maps for those voxels containing at least one tract (repeated coordinates were discarded to avoid measuring the same voxel repeatedly, as multiple tracts can

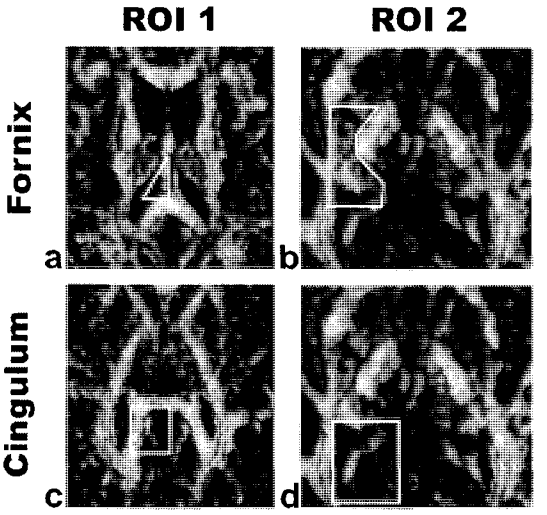

FIGURE 5.1: **Tract selection.** Region of Interest (ROI) placement for tract selection of the fornix (a, b) and cingulum (c, d). Placement of ROIs was based on a priori anatomical knowledge of tract projections. ROIs for tract selection must include the bundle of interest but do not have to precisely outline it. For the fornix, the first ROI was placed around each crus of the fornix at the level where their fusion is visible (a), while the second ROI was placed at the level of the cerebral peduncles encompassing the hippocampal tail (b). The cingulum was selected by placing the first ROI at the level of the inferior border of the corpus callosum (c) and the second ROI at the level of the cerebral peduncles (d). For all subjects the two initial ROIs were placed in the same anatomical locations. For control subjects two ROIs were adequate to select the fornix and the cingulum (Figures 5.2 and 5.4). In some cases, typically patients, additional ROIs were needed on axial slices between the first two in order to depict the entire structure. The resulting patients' tracts show less continuity, as seen in Figure 5.4. Diffusion measurements are obtained from the voxels that form the three-dimensional structures derived from tractography, not the ROIs used for tract selection.

penetrate the same voxel). Those voxels containing at least one tract were averaged in each slice and all the slices were averaged together resulting in a single value for each bundle in each subject. For both structures, we analyzed the axial slices between the levels of the mamillary bodies and the fusion of the crura. These portions of the tracts were analyzed in order to maintain left/right fornix separation and to measure the segment of the cingulum that is the least heterogeneous and most related to the temporal lobe. On average, 14 slices (approximately 475 voxels for the fornix and 250 for the cingulum) were included for each tract

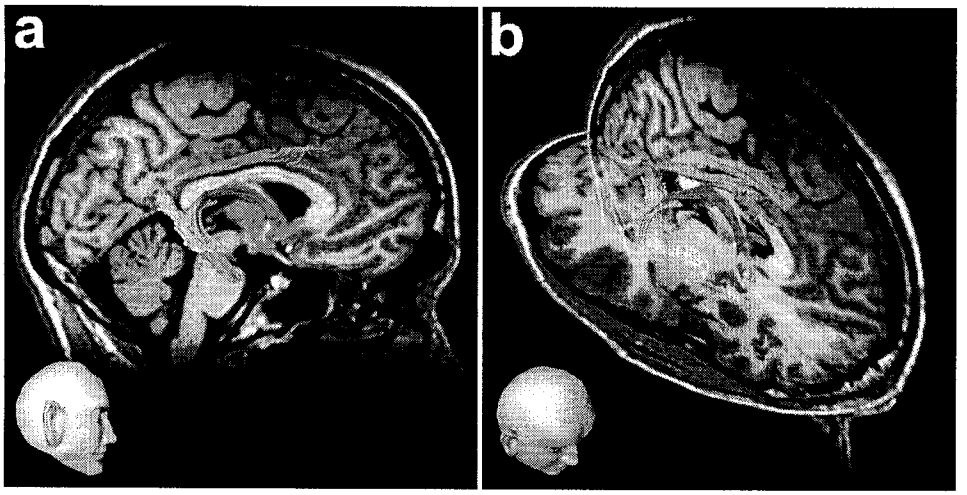

FIGURE 5.2: **Diffusion tensor fiber tracking of fornix and cingulum in a healthy control.** 3D representation of the fornix (blue) and cingulum (orange) are shown overlaid on mid sagittal (a) and on mid sagittal and axial semi-transparent MPRAGE anatomical scans (b). The portions of the tracts which are closely associated with the hippocampal formation were analyzed for the quantitative diffusion measurements (highlighted in light blue and yellow for the fornix and cingulum, respectively).

(Figure 5.2). It is important to note that the diffusion measurements are obtained from the voxels that form the three-dimensional structures derived from tractography, not the ROIs used for tract selection. As there is a relative user-dependence on the depiction of tracts, we assessed the intra-rater variability of our results, demonstrating variability of 1 ± 2 % (r=0.88) for patient and control groups. The use of more than two ROIs for fiber selection (which was often needed in the patient group) did not significantly change the results in the controls. Although we did not evaluate inter-rater variability, prior reports have demonstrated this to be very low when multiple tract selection regions are used and the FA threshold for tracking is above 0.25[425,448].

Statistical analysis Hotelling's T2 test (the multivariate generalization of Student's paired t-test)[449] was used to evaluate the right-left symmetry of the fornix and cingulum for patients and controls. For control subjects a small but statistically significant difference in FA was observed for the fornix (right=0.52 ± 0.03;

left=0.55±0.02; p=0.03) with no asymmetry for the cingulum (right=0.51±0.04; left=0.49±0.03; p=0.30). No asymmetry was observed for either the fornix (p=0.5) or cingulum (p=0.63) of patients. As the asymmetry of the fornix for controls was very small and no asymmetry was observed in the fornix or cingulum for patients, subsequent analysis was performed comparing control data (with left and right measurements collapsed) to patient data, either ipsilateral or contralateral to MTS. Multivariate Analysis of Variances (MANOVA) was used to assess between group differences in DTI measurements (with age included as an independent variable). The eigenvalues were evaluated separately from FA and MD, as the former two are derived from the eigenvalues and should not be included in the same analysis[449]. If a significant difference among the groups existed, post-hoc pair-wise comparisons were performed using Scheffe's method. Separate statistical tests were performed for the fornix and cingulum.

5.3 Results

T2 relaxometry Quantitative T2 analysis demonstrated that on the affected hemisphere all patients had hippocampal T2 greater than two standard deviations of the mean of controls, i.e., 115±3 ms (Figure 5.3). Three patients also showed an increased T2 on the contralateral hippocampus, although the highest T2 value corresponded to the side suspected to be sclerosed by clinical imaging in all three cases. These measurements confirm unilateral MTS in five subjects and imply asymmetrical bilateral MTS in the remaining three.

Fiber tracking A noticeable difference was observed in tracing both fiber bundles (particularly the fornix) in patients as compared to controls, such that more fiber-selection regions were required to perform adequate delineation of the fibers in the patient group, with the final results showing less continuity of the tracts (Figure 5.4). It is important to note that since the fiber tracking algorithm only considers voxels with an FA value >0.3 an unknown number of voxels from potentially degenerated tracts have not been analyzed. This could make our DTI

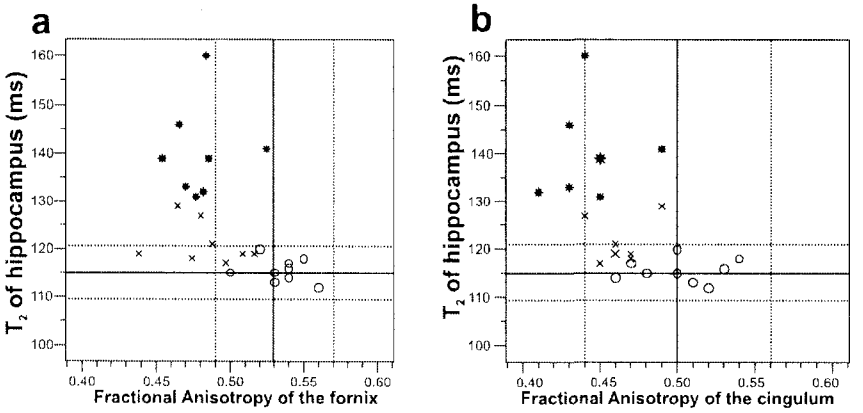

FIGURE 5.3: **T2 values in the hippocampus versus Fractional Anisotropy (FA) of the fornix and cingulum in individual subjects.** ○ Controls (mean of left and right); ★ Patients, ipsilateral to Mesial Temporal Sclerosis (MTS); × Patients, contralateral to MTS. Solid lines represent the mean of the control subjects and dashed lines represent ± 2 SD. (a) All patients show ipsilateral increases in T2 of the hippocampus, while three show bilateral T2 changes. 7/8 patients show significant (-2 SD) reductions in fractional anisotropy of the ipsilateral fornix. Interestingly, 5/8 patients show significant FA decreases in the fornix contralateral to the previously identified sclerosed hippocampus; three of these five patients also show elevation in T2 of the contralateral hippocampus, suggesting bilateral changes that were missed by regular clinical MRI. (b) 4/8 patients show a decrease in diffusion anisotropy on the cingulum ipsilateral to MTS. However, none of the patients demonstrated FA values above the mean of the controls and 7/8 had FA values below 1 SD of the mean of the controls both ipsilateral and contralateral to MTS.

measurements an under-estimation of the severity of degradation of both the cingulum and the fornix in patients. Furthermore, the number of voxels forming the controls' extracted fornices was 572±156, while the patients' tracts included less voxels (ipsilateral=420±150, p=0.06; contralateral=429±98, p=0.04). The number of voxels included in the cingulum was similar between controls (230±71) and patients (250±71 and 278±91 for ipsilateral and contralateral, respectively).

DTI measurements in the fornix FA values for the fornix were observed to be less than two standard deviations of control values in seven of eight subjects on the side ipsilateral to MTS and in five of eight subjects on the contralateral side. Furthermore, none of the patients had FA values higher than the mean of the controls (Figure 5.3). A significant difference in FA for the fornix was observed between

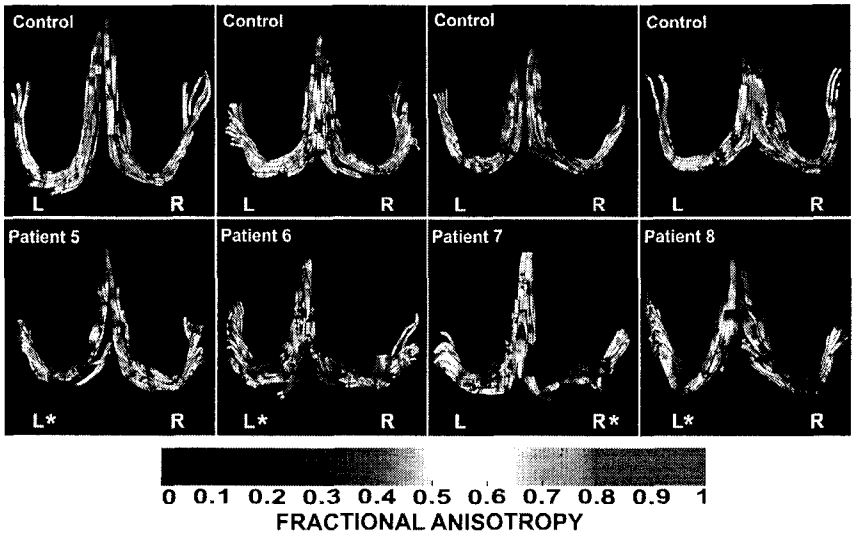

FIGURE 5.4: **DTI-derived tractography of the fornix in four healthy controls and four patients with unilateral Mesial Temporal Sclerosis (MTS).** Bilateral 3D visualization of fornix (viewed from above) where FA values are color-coded for each voxel. The hemisphere with MTS is denoted by an asterisk (L=left, R=Right). Note that the patients show overall lower FA values and less continuous tracts bilaterally as compared with the controls. These results imply marked degradation of the fornix in both hemispheres.

the control group (0.53±0.02) and patients ipsilateral (0.48±0.02, p=0.00004) and contralateral (0.48±0.02, p=0.0002) to MTS, with no difference between ipsilateral and contralateral sides in patients (p=0.58) (Figures 5.4 and 5.5). No difference in MD was observed between groups. The MANOVA test for eigenvalues in the fornix showed: no significant difference in λ_1 between groups, increased λ_2 ipsilateral (p=0.01) and contralateral (p=0.034) to MTS and increased λ_3 contralateral (p=0.04), but not ipsilateral (p=0.11) to MTS (Figure 5.5). Based on the small but significant asymmetry of the fornix in controls, a side to side comparison of patients and controls (i.e., comparing homologous hemispheres) was performed using MANOVA which again demonstrated bilateral symmetrical diffusion abnormalities in patients. No correlation was observed between age and FA of the fornix for either patients or controls.

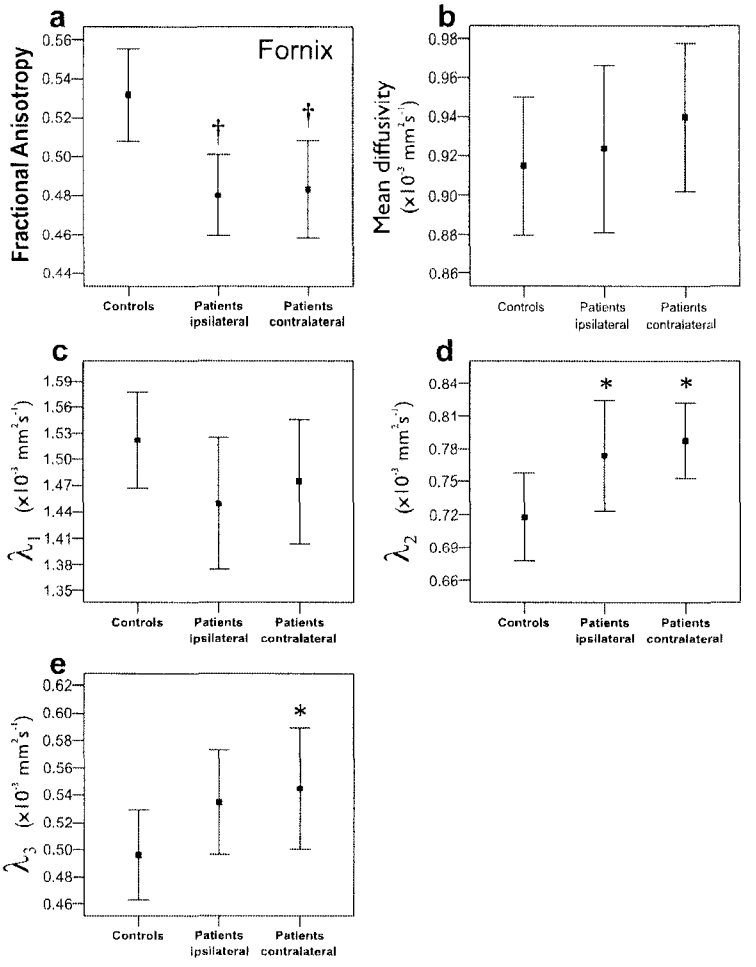

FIGURE 5.5: **DTI measurements in the fornix of controls (n=9) and patients (n=8) ipsilateral and contralateral to the mesial temporal sclerosis (MTS).** Fractional Anisotropy (FA), mean diffusivity and eigenvalues (λ_1, λ_2 and λ_3) are shown for the region of the fornix highlighted in Figure 5.3 (mean $\pm$ SD). The orientational integrity of the fiber tracts (i.e., FA) is reduced bilaterally to a similar extent whereas the mean diffusivity of water is unchanged. The reduction in FA is mainly due to an increase in water diffusion perpendicular to the fiber tracts (λ_2, λ_3). This pattern is consistent with Wallerian degeneration. Significant differences between controls and patient values ipsilateral and contralateral to MTS are indicated (*$p<0.05$ and †$p<0.01$).

DTI measurements in the cingulum FA values for the cingulum were less than two standard deviations of control values in 4/8 patients ipsilateral, and in 1/8 patients contralateral to MTS (Figure 5.3). However, none of the patients had FA values above the mean of the controls, and 7/8 patients had FA values below one standard deviation of the mean of controls, both ipsilateral and contralateral to MTS. The mean FA for the cingulum was 0.50±0.03 in controls, while the patients had a mean FA value of 0.44±0.02 in the cingulum ipsilateral to MTS (a 12% reduction, p=0.0004) and a mean FA value of 0.46±0.02 in the contralateral side (an 8% reduction, p=0.01), with no difference between ipsilateral and contralateral sides in patients (p=0.1). Contrary to the findings in the fornix, MD was significantly increased bilaterally (ipsilateral: 0.82±0.02 $\times 10^{-3}$ mm^2/s, p=4.0 $\times 10^{-5}$; contralateral: 0.79±0.02 $\times 10^{-3}$ mm^2/s, p=0.01), when compared to the control group (0.75±0.02 $\times 10^{-3}$ mm^2/s) (Figure 5.6). λ_1 showed no difference between the groups, while λ_2 was bilaterally increased in the patient group (p=0.0001 and p=0.02 for ipsilateral and contralateral to MTS, respectively); λ_3 also showed a bilateral increase in the patients (p=4.0 $\times 10^{-3}$ and p=0.007) as compared to controls, indicating an increase in water mobility perpendicular to the principal axis of the fibers. No correlation was observed between age and FA of the cingulum for either patients or controls.

5.4 Discussion

Axonal Wallerian degeneration is a process that occurs following neuronal injury. Its demonstration in vivo can help delineate the down-stream effects of any disorder resulting in neuronal loss or death. Wallerian degeneration has been studied before using diffusion magnetic resonance measurements, and it is characterized by reduced anisotropy, either slightly increased[445] or normal mean water diffusion (i.e., MD)[444,446], reduced diffusivity parallel to the principal axis of the fiber (i.e., 1), and increased water mobility perpendicular to it (i.e., λ_2 and λ_3)[444–446]. The fornix and cingulum were the focus of this study as they are the most prominent white matter tracts within the limbic system. As the fornix contains hippocampal

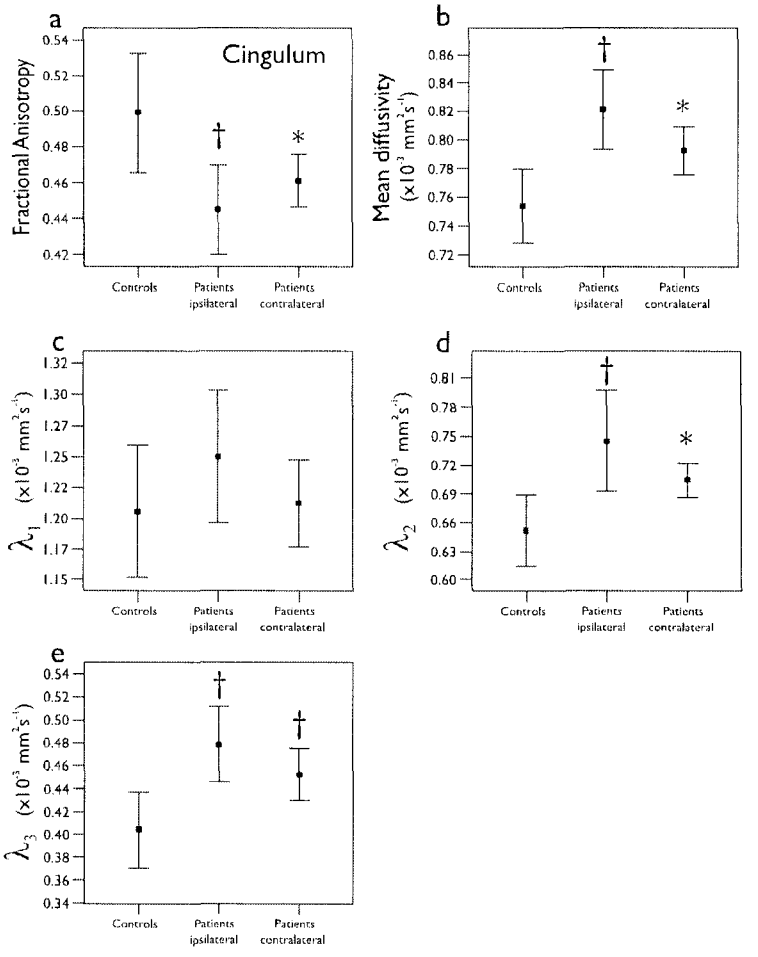

FIGURE 5.6: **DTI measurements in the cingulum of controls (n=9) and patients (n=8) ipsilateral and contralateral to the mesial temporal sclerosis (MTS).** Fractional Anisotropy (FA), mean diffusivity and eigenvalues (λ_1, λ_2 and λ_3) are shown for the descending portion of the cingulum highlighted in Figure 5.3 (mean ± SD). The orientational integrity (i.e., FA) of the tract is markedly reduced bilaterally and, unlike the fornix, the mean diffusivity of water is elevated. The reduction in FA is due to increases in the diffusion coefficient perpendicular to the length of the fiber tract, namely λ_2 and λ_3. Significant differences between controls and patient values ipsilateral and contralateral to MTS are indicated (*$p<0.05$ and †$p<0.01$).

efferent fibers (predominantly to the mamillary bodies and septal region) we expected to see downstream Wallerian degeneration within the fornix ipsilateral to MTS. The portion of the cingulum most closely related to the hippocampus was chosen in an attempt to characterize changes in limbic connections in this patient population (though Wallerian degeneration was not necessarily expected in this fiber bundle since relatively few axons originate from the hippocampus[161]).

Our bilateral symmetrical findings in the fornix (reduced FA, normal MD, and increased eigenvalues perpendicular but not parallel to the tract) are consistent with axonal degeneration within the fiber tract[444–446]. While the observed changes were relatively small (a 10% reduction in FA), this is likely explained by the fact that the fornix is a heterogeneous structure containing bi-directional fibers interconnecting multiple brain regions (including the hypothalamus, septal region, mamillary bodies and mesial temporal structures)[161]. Although it is not possible to confirm which fibers in the fornix have degenerated, several possible hypotheses can be raised. Based on the known selective pattern of cell loss observed in pathological studies of MTS (prominent cell loss in CA1, CA3, CA4 and prosubiculum with relative sparing of CA2 and the subiculum)[141,450] it is unlikely that degeneration of the subiculum-mamillary body pathway is responsible for our findings. With prominent cell loss in CA1, a reasonable explanation may be degeneration of the CA1-septal pathway. However, while previous histological studies have demonstrated bilateral hippocampal cell loss in some patients with TLE, an asymmetry between the two sides was observed[451,452]. Also, previous volumetric studies of the fornix have demonstrated asymmetries which corresponded to the side of unilateral MTS[357,358]. Based on these observations, if CA1 cell loss was solely responsible, we would have expected to see an asymmetry of the fiber tract integrity in our results (i.e., ipsilateral fornix demonstrating more profound FA changes).

Two possible explanations for our observation of bilateral symmetrical changes in the fornix are degeneration of commissural fibers interconnecting the two hippocampi or degeneration of the hippocampal afferent pathways. While the commissural hypothesis remains a possibility, these are believed to be small fiber bun-

dles and it is the second possibility that is perhaps the most intriguing. It has been shown that lesions in the fimbria-fornix system render the hippocampus extremely seizure-prone[200,453,454]. If a patient had underlying degeneration of subcortical hippocampal afferents bilaterally, it is possible that this person would be more susceptible to the development of a hippocampal epileptic focus following an insult (such as febrile seizures).

While similar reductions in FA were observed for both the fornix and cingulum in TLE patients, the cingulum showed an elevated mean diffusivity of water (i.e., the MD). While the changes in the cingulum could represent degeneration of fibers not originating in the hippocampus (as we suspect to be the case in the fornix), the different pattern of change (elevation in MD) suggests the possibility of a different underlying mechanism. Elevated MD has been reported in vasogenic edema (resulting from an increase in the extra-cellular fluid space)[455–457]. As all patients had medically intractable epilepsy, it is possible that the observed MD changes in the cingulum represent chronic fluid shifts from ongoing seizures.

Despite the asymmetry in hippocampal T2 relaxometry results, symmetrical bilateral diffusion anisotropy reductions were observed in both the fornix and cingulum. While our findings ipsilateral to MTS were predicted based on pathological studies demonstrating asymmetrical hippocampal cell loss[141,241,451] and MRI evidence of reduced fornix volume ipsilateral to MTS[357,358], our finding of symmetrical fornix and cingulum abnormalities in a highly selected group of patients with unilateral MTS was unexpected. Although the number of patients evaluated in this study is relatively small, our findings suggest that temporal lobe epilepsy is associated with bilateral limbic system pathology even in patients with unilateral MTS. As many authors have demonstrated a high chance of surgical cure in patients with unilateral MTS[246,438–440], it is our assumption that despite our findings of bilateral limbic system abnormalities, patients with unilateral MTS do have a single epileptogenic zone. Whether the limbic abnormalities are a result of ongoing seizures or whether patients with bilateral limbic system abnormalities have increased susceptibility to the development of MTS and TLE remains uncertain.

⋆ ⋆ ⋆

5.5 Appendix

After the demonstration of limbic white matter diffusion abnormalities in patients with MTS, we wondered if the extra-temporal white matter also suffered analogous changes. In a slightly larger sample of TLE patients with unilateral MTS (n=11), we showed that the external capsules and the genu and splenium have abnormal diffusivity in a pattern similar to the one shown here (i.e. reduced FA and increased $\lambda_{\perp}$). This finding was published in the journal *Epilepsia* in 2006[458]. Thus, it became evident that patients with unilateral MTS have extensive white matter abnormalities lying well beyond the sclerotic hippocampus. However, the white matter is not globally affected. In the above mentioned study, for example, we did not find diffusion abnormalities of the internal capsules (similarly to the report of[408]) and, in a voxel-wise analysis of 35 patients with unilateral MTS, the white matter diffusion abnormalities appeared to be related mostly to the temporal lobe white matter, the cingulum bundle, the corpus callosum and a region near the superior longitudinal fasciculus[401]. We now questioned if the white matter changes were functional and reversible fluid shifts (next Chapter). Also, we wanted to know if these limbic white matter abnormalities are related to MTS. Were they present in patients with TLE but without such a mesial temporal lesion? The study of this question is presented in Chapter 7.

The appendix did not appear in the published version of this Chapter.

Chapter 6

Irreversibility of white matter diffusion abnormalities in MTS patients

Abstract

Bilateral white matter Diffusion Tensor Imaging (DTI) abnormalities have been reported in patients with temporal lobe epilepsy (TLE) and unilateral mesial temporal sclerosis (MTS) but it is unknown whether these are functional or structural changes. We performed a longitudinal study in patients with unilateral MTS who were seizure free one year after surgery in order to determine if the observed pre-surgical white matter diffusion abnormalities were reversible. Eight TLE patients with unilateral MTS who were seizure free following anterior temporal resection and twenty-two healthy subjects were recruited. DTI was performed prior to surgery and at one year follow-up. Tractography and region-of-interest (ROI) analyses were performed in the fornix, cingulum, genu and splenium of the corpus callosum and external capsules. Diffusion tensor parameters were compared between groups and before/after surgery in the patient group. The fornix, cingulum and external capsules showed bilateral abnormal diffusion parameters pre-operatively (i.e. decreased diffusion anisotropy and increased mean and perpendicular diffusivities). The fornix and cingulum ipsilateral to the resected mesial temporal structures showed signs of Wallerian degeneration at one year follow-up. The contralateral tracts of the fornix, cingulum and external capsules, as well as the genu of the corpus callosum, failed to show a normalization of their diffusion parameters. Conclusions: The irreversibility of the white matter DTI abnormalities upon seizure freedom suggests underlying structural abnormalities (e.g. axonal/myelin degradation) as opposed to functional changes (e.g. fluid shifts due to seizures) in the white matter.

A version of this Chapter was published in:
Concha L., Beaulieu C., Wheatley B.M. and Gross D.W. Bilateral white matter diffusion changes persist after epilepsy surgery. *Epilepsia* 2007. 48(5):931–40.

6.1 Introduction

Mesial temporal sclerosis (MTS) is the most commonly observed underlying pathology in temporal lobe epilepsy (TLE) and MRI evidence of unilateral MTS is predictive of good outcome with resective surgery[459]. However, there is now growing evidence that patients with TLE and unilateral MTS have bilateral temporal and extra-temporal abnormalities of gray[174,349,350,363,405,451,460] and white matter[355,422,458,461]. While it has been suggested that evidence of diffuse pathology in patients with TLE and unilateral MTS is predictive of poor surgical outcome[460], several studies indicate that their presence does not preclude a favorable surgical outcome[342,360,458,461]. The relationship between these diffuse abnormalities and the seizure disorder remains largely unknown. While it is possible that these changes are a direct consequence of seizures (either acute functional or chronic structural changes), it has also been suggested that they could represent an underlying predisposing factor in the development of TLE[350].

Diffusion tensor magnetic resonance imaging (DT-MRI), a technique sensitive to micro-structural properties of neural tissue[27,28], has demonstrated significant differences of diffusion parameters in the fornix, cingulum, corpus callosum and external capsules in patients with TLE[408,422,458]. The pattern of diffusion parameters (i.e. reduced diffusion anisotropy and increased mean and perpendicular diffusivities) is compatible with irreversible structural axonal/myelin abnormalities in the white matter tracts[21,32]. Another potential explanation for diffusion changes in patients with epilepsy is fluid shifts related to ongoing seizures. Reductions of the mean apparent diffusion coefficient (ADC) have been shown to reverse back to normal in animal models[388,462,463] and patients with status epilepticus[135,138,140,390,464]. Although most studies have focused on the gray matter, similar reversible diffusion abnormalities have been reported for the splenium of the corpus callosum following status epilepticus in humans[407]. Changes in the osmotic properties of intra- and extra-cellular spaces have also been shown to reversibly alter the diffusion parameters of water molecules in highly-structured white matter (e.g. the optic nerve)[465].

Likewise, longitudinal magnetic resonance spectroscopy studies have demonstrated bilateral normalization of temporal lobe N-Acetylaspartate (NAA) in TLE patients who are seizure free following surgery[236,279–281,466]. The concentration of NAA appears to recover exponentially over time, on average showing a 50% recovery within six months[281] and thus the original reduction of NAA is assumed to reflect transient metabolic dysfunction due to ongoing seizures[236,281].

Following temporal lobe resection, fiber tracts with significant efferents from the mesial temporal structures (i.e. the ipsilateral fornix and cingulum) are expected to undergo Wallerian degeneration. As the contralateral fiber tracts contain few direct efferent connections from the resected grey matter, downstream axonal/myelin degradation following surgery is expected to be minimal. The purpose of the present study was to determine whether pre-surgical white matter diffusion properties, particularly those in the contralateral fiber tracts, normalize (compatible with a functional change directly related to seizures) or remain abnormal (compatible with irreversible structural abnormalities, e.g. axonal or myelin degeneration) in patients with TLE and unilateral MTS who are seizure free one year following anterior temporal resection.

6.2 Subjects and Methods

Approval of the research protocol was obtained from the University of Alberta Health Research Ethics Board, and informed consent was obtained from all participants. Of the eleven patients previously reported[458] , eight were entirely seizure free at one year follow-up with the remaining three patients experiencing a worthwhile reduction in seizures (seven patients included in the present study were part of the pre-operative assessment reported in[422]). Histopathological confirmation of hippocampal sclerosis was available in all cases. As our goal was to investigate the effect of seizure freedom upon white matter integrity, only seizure free patients were included (n=8), along with 22 healthy controls (16 male, 8 female; mean age: 31, range: 19-54 years). There was no statistically significant difference in age between the two groups. All patients were imaged before their surgical intervention

Subject	Age	Gender	Duration of TLE (y.)	Time between preoperative imaging and surgery	Time between surgery and postoperative imaging	Ipsilateral hippocampus T2 (ms)[a]	Contralateral hippocampus T2 (ms)[a]	Type of surgery[b]
1	22	F	19	14 m	13 m	146*	119	Left selective AH
2	39	F	35	5 d	19 m	139*	117	Right selective AH
3	22	M	17	4 m	14 m	132*	119	Left ATR
4	61	F	47	4 m	18 m	160*	118	Left ATR
5	53	F	14	1 m	12 m	139*	129*	Left selective AH
6	38	F	17	10 m	12 m	133*	127*	Right ATR
7	25	M	17	4 m	13 m	141*	119	Left selective AH
8	39	F	12	25 m	12 m	126*	116	Left selective AH

TABLE 6.1: **Individual information on patients with temporal lobe epilepsy and unilateral mesial temporal sclerosis.**
[a] Hippocampal T2 was measured pre-operatively and values outside two standard deviations from the mean of the control group (115 ± 3[458]) are denoted by an asterisk.
[b] Selective AH: selective amygdalo-hippocampectomy; ATR: anterior temporal resection.

(8 ± 8 months) and one year after surgery (14 ± 3 months) using the same protocol. The pre-operative hippocampal T2 values have been reported previously[458] and are reproduced in Table 6.1, along with individual patient information.

All imaging was performed on a 1.5T Siemens Sonata scanner. The imaging protocol consisted of cerebro-spinal fluid suppressed DTI with coverage of the limbic structures using 2x2x2 mm^3 voxel resolution (interpolated to 1x1x2 mm^3) and 6 diffusion gradient directions with $b = 1000$ s/mm^2. The diffusion images were processed using DTIstudio (Johns Hopkins University, Baltimore, MD), for both tractography and region of interest (ROI) analyses. The fornix and cingulum ipsilateral and contralateral to MTS were depicted using tractography using the fiber assignment by continuous tracking (FACT) algorithm[55], while the external capsules (ipsilateral and contralateral to MTS) and the genu and splenium of the corpus callosum were analyzed using manually placed ROIs on a single axial fractional anisotropy (FA) map at the mid-level of the thalamus[458] (Figure 6.1). Manual ROIs are sufficient for the latter three structures as they are readily identified on 2D axial slices. These white matter structures were selected for analysis

as they are either directly related to the mesial temporal structures (fornix and cingulum) or have been previously shown to have abnormal diffusion parameters (external capsules and corpus callosum)[408,458]. Detailed methods for image acquisition and data analysis have been previously published by us[422,422,458].

For both tractography and ROI - based analyses, four measurements were obtained: fractional anisotropy (FA), mean apparent diffusion coefficient (ADC) and diffusivity parallel and perpendicular to the tracts ($\lambda_{\parallel}$ and $\lambda_{\perp}$ respectively). The fornix and cingulum were analyzed between the axial levels of the superior margin of the hippocampus and the fusion of the crura of the fornix. This was done to maintain clear left/right separation and to focus on the temporal regions of these bundles (Figure 6.1). A small asymmetry of diffusion parameters of the fornix in healthy controls had been previously reported[422], which was not replicated in the present study with a larger sample. As there was no statistically significant difference of the DTI parameters between the left and right hemispheres in the control group (n=22), measurements from paired structures (i.e. the external capsules, fornices and cingula) were averaged to obtain a single value per individual (i.e. (left+right)/2) in the control group, and separated into ipsilateral and contralateral to MTS in the patient group.

Multivariate and single-variable tests were carried out comparing the white matter measurements between groups. The comparisons between pre- and post-operative measurements in the patient group were performed using the paired versions of Hotelling's T^2 and Student's t tests (multivariate and single-variable, respectively), while those between the patient groups (i.e. pre- or post-operative) and the control group were performed using the equivalent unpaired versions of the aforementioned tests.

In order to validate the reproducibility of our measurements over time, ten of the control subjects were imaged two times with an inter-scan interval ranging from eight to 12 months. Tractography and ROI analyses were performed and assessed for intra-subject reliability using Pearson's correlation coefficient (r). ROI-based analyses proved to be highly reproducible over time, with r values of 0.99, 0.85, 0.98 and 0.96 for FA, ADC, $\lambda_{\parallel}$ and $\lambda_{\perp}$, respectively. Tractography anal-

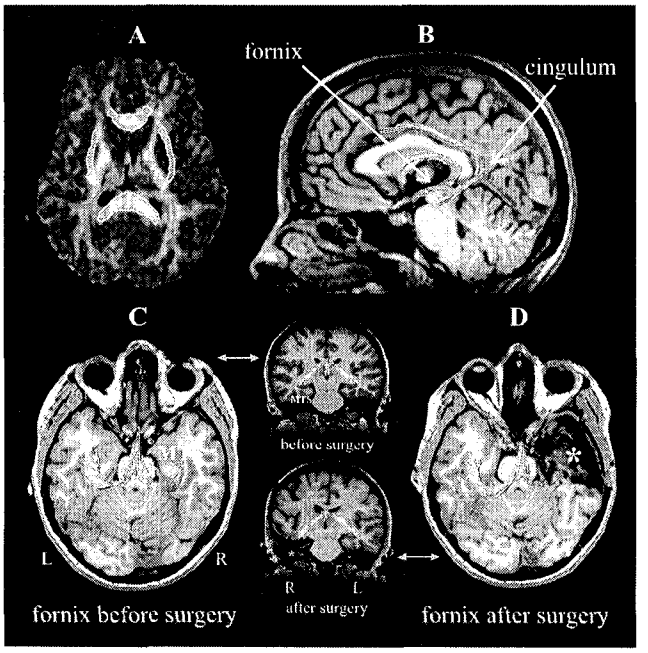

FIGURE 6.1: **Diffusion tensor imaging and tractography of the fornix in a representative case of unilateral mesial temporal sclerosis (MTS).** (A) Diffusion parameters from the genu and splenium of the corpus callosum and the external capsules were analyzed by manually outlining regions of interest. (B) The fornix and cingulum (ipsilateral and contralateral to MTS) were depicted using tractography. The tracts are overlaid on high-resolution T1-weighted images. Only the regions highlighted in green were quantitatively analyzed. (C and D) Axial and semi-transparent coronal views of the fornices. After right anterior temporal lobe resection (asterisk), the ipsilateral fornix was much more difficult to depict with diffusion tractography (consistent with downstream Wallerian degeneration).

yses were also reproducible, albeit not to the same degree as ROI analyses, with r values of 0.80, 0.98, 0.97 and 0.85. On average, all diffusion parameters varied by less than 1.7% over time (-0.1±1.3%). Intra-rater reliability was very high for both ROI and tractography analyses, with r values >0.95 for all measurements. Tractography and ROI analyses were performed by a single investigator (LC). The pre-operative diffusion abnormalities reported previously[422,458] (Chapter 5) were reproduced in the present study.[a]

[a]Recall that 7/11 patients included in this study were also reported in Chapter 5.

6.3 Results

The fornix, cingulum and external capsule *ipsilateral* to MTS showed abnormal diffusion parameters pre-operatively, characterized by increased perpendicular diffusivity (i.e. $\lambda_\perp$) with normal parallel diffusivity (i.e. $\lambda_\parallel$), which causes an increase of the mean diffusivity and a reduction of diffusion anisotropy. At one year follow-up, the fornix and cingulum were difficult (and in one case impossible) to depict with tractography, as their diffusion abnormalities became much more evident after surgery (Figures 6.1 and 6.2). This observation is consistent with downstream Wallerian degeneration of these white matter bundles which would be expected following surgical resection of the mesial temporal structures (Figures 6.3, 6.4 and Table 6.2).

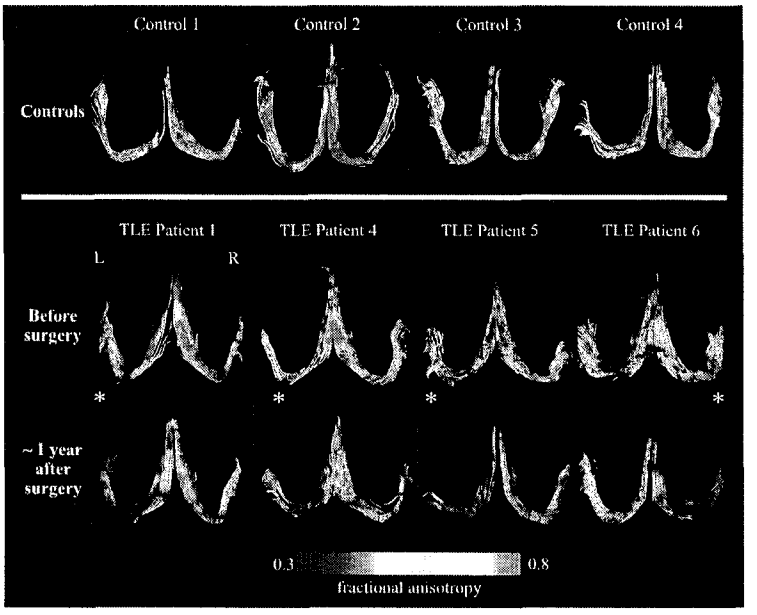

FIGURE 6.2: **Diffusion tensor tractography of the fornix ipsilateral and contralateral to mesial temporal sclerosis (*) in four representative TLE patients and four control subjects.** The patients showed bilaterally reduced fractional anisotropy pre-operatively as compared with the controls. The fornix ipsilateral to the surgical resection of the mesial temporal structures was further degraded after surgery, likely due to the expected Wallerian degeneration. Interestingly, the fornix contralateral to the resection failed to normalize its low diffusion anisotropy upon seizure freedom.

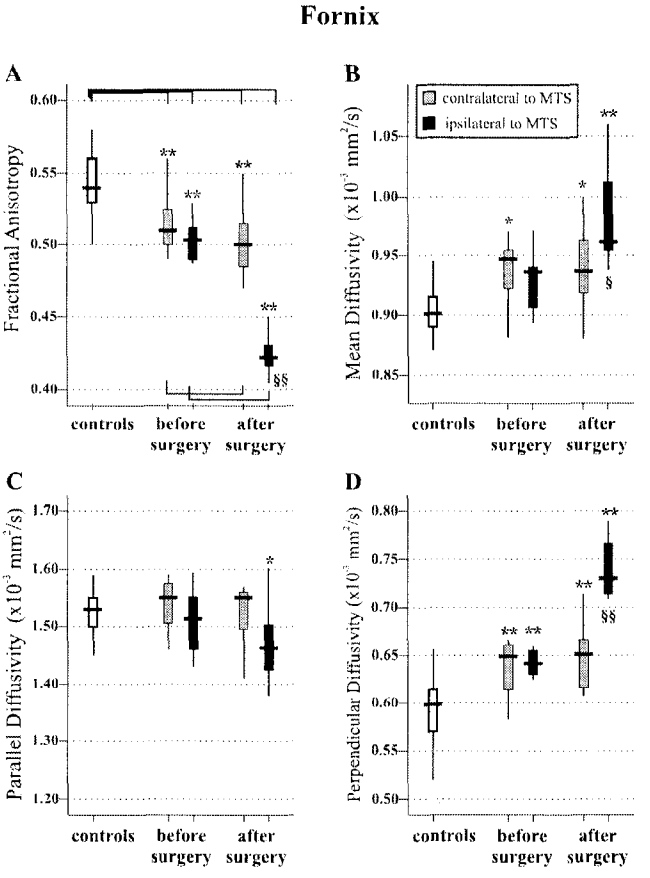

FIGURE 6.3: **Between-group comparisons of diffusion tensor parameters of the fornix.** There was bilaterally reduced fractional anisotropy (A) before the surgery, which was further markedly reduced in the ipsilateral hemisphere one year after the surgery. The contralateral fornix failed to normalize upon seizure freedom and its reduced diffusion anisotropy and high bulk diffusivity (B) were due to an increased perpendicular diffusivity (D) with no change in parallel diffusivity (C), suggestive of irreversible axonal/myelin abnormalities. Thin lines in (A) show the design of the univariate statistical tests performed. Student's t tests between patients and control group: $*p<0.05$; $**p<0.01$. Paired Student's t tests within patients before and after surgery: $§p<0.05$; $§§p<0.01$.

The fornix (Figures 6.2 and 6.3), cingulum (Figure 6.4) and external capsule (Figure 6.5) *contralateral* to MTS showed similar abnormalities to their ipsilateral counterparts pre-operatively (i.e. reduced FA, normal $\lambda_{\parallel}$ and increased $\lambda_{\perp}$ and ADC). Although the contralateral tracts were not directly affected by the surgery (and thus lacked the severe further degradation of their ipsilateral counterparts) they notably failed to show a normalization of their diffusion parameters upon

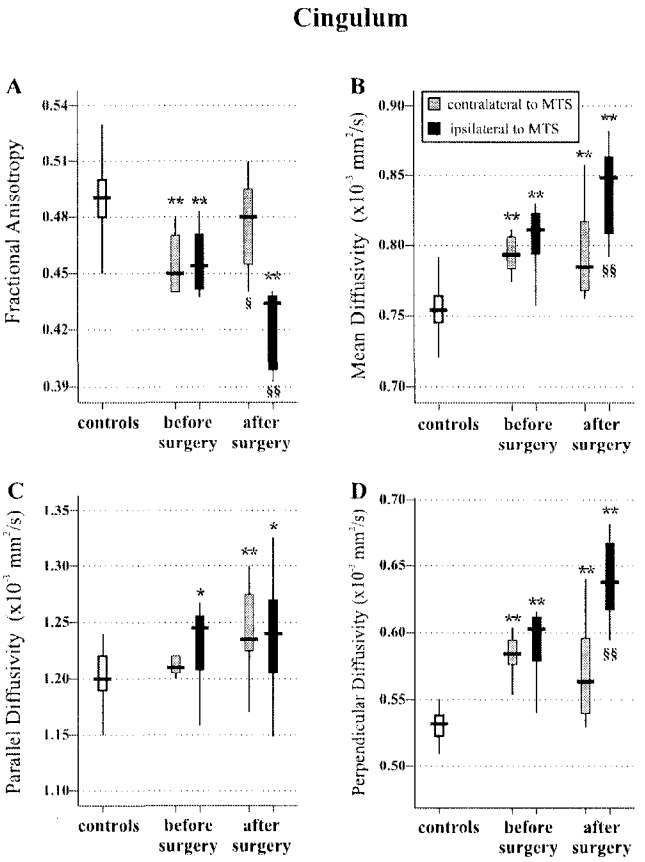

FIGURE 6.4: **Between-group comparisons of diffusion parameters of the cingulum.** There was bilateral reduction of diffusion anisotropy (A) and increased mean and perpendicular diffusivities (B and D) before surgical resection of the mesial temporal structures. The cingulum ipsilateral to the resection showed marked degradation after surgery, characterized by a further reduction of diffusion anisotropy, and an increase of mean and perpendicular diffusivities. The contralateral cingulum retained its abnormally high perpendicular and mean diffusivities upon cessation of seizures at one year follow-up. Unpaired tests of patients vs. controls: $*p<0.05$; $**p<0.01$. Paired tests within patients before and after surgery: §p<0.05; §§p<0.01.

seizure freedom (Figures 6.2 to 6.5 and Table 6.2). While the contralateral cingulum showed an increase of its anisotropy to normal values, the other three diffusion parameters remained abnormal (Figure 6.4).

The genu of the corpus callosum showed diffusion abnormalities similar to the fornix and cingulum pre-operatively and also failed to normalize at one year follow-up. Although the post-operative multivariate comparison to the control

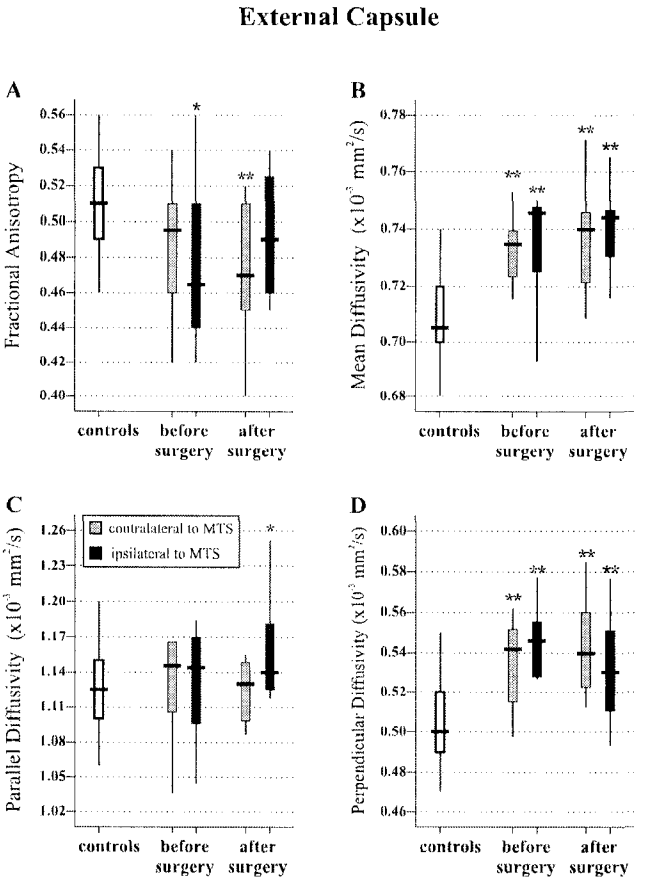

FIGURE 6.5: **Between group comparisons of diffusion parameters of the external capsules.** There was statistically significant pre-operative increase of mean (B) and perpendicular (D) diffusivities of the external capsules ipsilateral and contralateral to MTS. These abnormalities did not resolve at one year follow-up. Although not as convincing, there was a trend towards reduced diffusion anisotropy (A) in the patients both before and after the surgery, as compared to the control group. Unpaired tests of patients vs. controls: $*p<0.05$; $**p<0.01$.

group was not significant (p=0.069, Table 6.2), the univariate tests showed statistically significant differences in three of four post-operative diffusion parameters with respect to the controls (Figure 6.6). Contrarily, the splenium showed normal diffusion parameters prior to the surgery and post-operative abnormalities similar to those outlined above relative to controls (Figure 6.6 and Table 6.2).

Careful examination of each patient's diffusion parameters in all the structures studied before and after surgery showed similar patterns of change, regardless of their surgery type (i.e. selective amygdalo-hippocampectomy or anterior tempo-

	pre- vs. post-operative[a]	pre-operative vs. Controls[b]	post-operative vs. Controls[b]
Fornix, contralateral	0.909	0.032*	0.001*
Fornix, ipsilateral	0.005*	0.002*	0.000*
Cingulum, contralateral	0.08	<0.001*	0.008*
Cingulum, ipsilateral	0.027*	<0.001*	<0.001*
External capsule, contralateral	0.965	0.014*	0.007*
External capsule, ipsilateral	0.583	0.009*	0.003*
Genu	0.206	0.037*	0.069
Splenium	0.438	0.678	0.044*

TABLE 6.2: **P values from multivariate tests of the diffusion parameters (fractional anisotropy and mean, parallel and perpendicular diffusivities) in various white matter tracts between groups.**
[a] Paired Hotelling's T^2.
[b] Unpaired Hotelling's T^2.
P values below 0.05 are denoted by an asterisk.

ral lobe resection), which was confirmed statistically (univariate and multivariate tests —data not shown). Also included in the individual analysis were two of the three patients who are not seizure free after surgery. There was no apparent relationship between seizure-related surgery outcome and the diffusion parameters, with these two patients behaving indistinctly from the seizure free group (although the sample size is too small to make any meaningful conclusions).

None of the white matter structures studied showed any gross abnormalities of T2 signal intensity (assessed with the non diffusion weighted echo planar images). The pre-operative hippocampal T2 measurements (ipsilateral and contralateral to MTS) did not correlate with any of the post-operative diffusion parameters in the white matter tracts. Statistical correlations (Pearson's r) between DTI parameters or pre-operative T2 measurements and age of onset of epilepsy or disease duration did not show statistical significance.

6.4 Discussion

There is a growing body of literature suggesting that TLE with unilateral MTS is in fact associated with *bilateral* temporal[174,350,422,451,460,461], and *bilateral* extratemporal pathology[355,401,408,458]. Several reports suggest that these wide-spread gray and

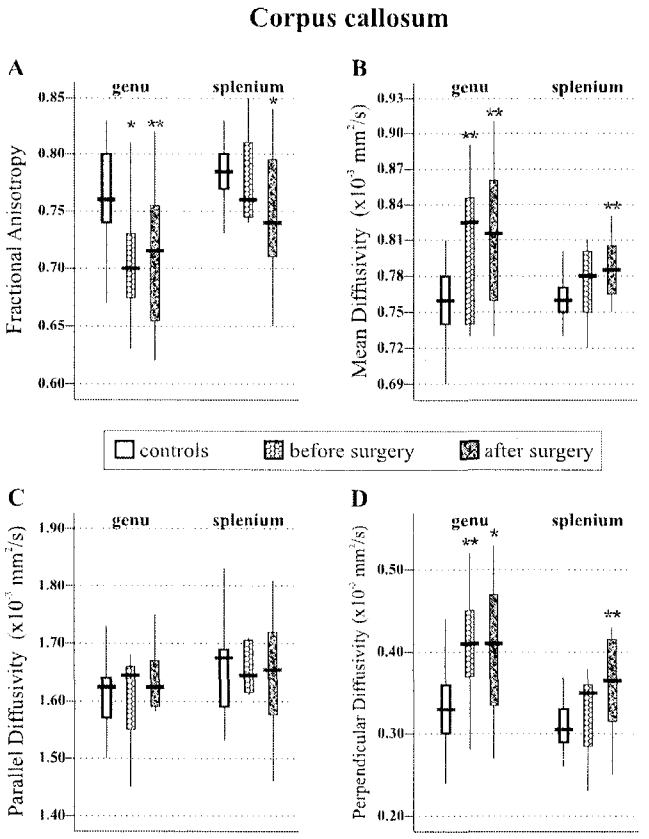

FIGURE 6.6: **Between group comparisons of diffusion parameters of the genu and splenium of the corpus callosum.** The genu showed reduced diffusion anisotropy (A) and increased bulk diffusivity (B) due to an increase in perpendicular diffusivity (C) pre-operatively, which did not resolve upon seizure freedom. In contrast, the splenium had normal diffusion parameters pre-operatively, but displayed abnormalities in a pattern similar to that of the genu after surgery, likely due to post-operative degeneration of fibers interconnecting the temporal lobes. Unpaired tests of patients vs. controls: $*p<0.05$; $**p<0.01$.

white matter abnormalities do not alter surgical outcome[219,342,360,458,461], which was also observed in the present study, where surgical outcome was consistent with what would be expected in patients with TLE and unilateral MTS[219,459] (i.e. eight of eleven patients were entirely seizure free at one year follow-up). While a primary objective of the application of novel quantitative MRI techniques in TLE has been the detection of subtle MTS not apparent with conventional imaging[219], it would also appear that these more sensitive techniques (such as DTI)

have demonstrated that pathology in patients with TLE and unilateral MTS is not restricted to the ipsilateral mesial temporal structures.

The abnormal diffusion parameters of the contralateral fornix and cingulum, as well as the genu of the corpus callosum and external capsules, seen in patients with unilateral MTS prior to surgery, did not normalize at one year follow-up in seizure free patients. Had they normalized, this would have implied reversible diffusion changes in the white matter (i.e. functional changes caused by ongoing seizures). While the contribution of a functional component to the observed diffusion abnormalities can not be entirely ruled out, (for example, it is possible that fiber degeneration could have masked reversible changes), the diffusion abnormalities characterized by decreased anisotropy with irreversibly increased perpendicular diffusivity (i.e. $\lambda_\perp$), is most consistent with abnormalities of either myelin (e.g. dys- or de-myelination) or axonal density[21,32]. The fact that the fornix contralateral to MTS did not show further worsening of its diffusion parameters after surgery suggests that the commissural component of this fiber bundle does not play a major role in the pre-operative abnormalities. While the contralateral cingulum showed an apparent normalization of diffusion anisotropy suggesting the possibility of a reversible component, the significance of the anisotropy finding remains uncertain because ADC, $\lambda_\parallel$ and $\lambda_\perp$ remained abnormal.

While there have been reports of transiently altered diffusion parameters immediately after status epilepticus or in the acute post-ictal state, the hallmark in those situations is a considerable decrease in mean bulk diffusivity (ADC), which is though to reflect cytotoxic edema due to compartmental fluid shifts[138,390,407]. Animal models have shown that the ADC in brain parenchyma is decreased in the acute phase after status epilepticus, but then increases in the chronic stage[388]. None of the white matter structures reported in the present study showed reductions of ADC; instead, ADC was found to be increased before the surgery and at one year follow-up, making acute cytotoxic edema an unlikely explanation of our findings. Finally as the diffusion parameters did not normalize in seizure free patients, fluid shifts due to ongoing seizure activity are unlikely to explain our findings.

Diffusion parameters of the fornix and cingulum ipsilateral to MTS, which were abnormal prior to surgery, showed significant worsening one year after surgical resection of the temporal structures. These changes were expected and are likely due to Wallerian degeneration of the white matter bundles affected by the surgery[21,32]. While our results demonstrate significant differences between both patients and controls and between patients before and after surgery, we suspect that our measurements are in fact an under-estimation of the true degeneration taking place in those structures. The tractography algorithm used for their depiction does not include voxels with diffusion anisotropy lower than a certain threshold (FA <0.3 in this case) and, therefore, regions with the largest changes are omitted from the final diffusion parameters. Due to the presence of overt Wallerian degeneration and its related striking DTI abnormalities, it is impossible to compare the ipsilateral fornix and cingulum to their pre-operative state. Therefore, we cannot estimate whether or not the pre-operative abnormalities of the ipsilateral tracts would have disappeared upon seizure freedom in this group of patients, or if there is any other co-existing abnormal phenomenon present in these fiber bundles.

The splenium of the corpus callosum had normal diffusion parameters before the surgery and, although the paired pre/post-surgery tests did not reach statistical significance, it showed an abnormal diffusion pattern similar to that seen in the other white matter bundles one year after the surgery, when compared to the controls. This portion of the corpus callosum carries a substantial number of fibers interconnecting the two temporal lobes[467,468]. With the resection of the temporal structures, downstream Wallerian degeneration is expected, as would be post-operative diffusion abnormalities in this structure[21,32].

Several reports have documented improvement in spectroscopic indices of the temporal lobes (ipsilateral and contralateral to MTS) following successful epilepsy surgery[236,279–281,466]. As the concentration of NAA improves only if there is cessation of seizures, it has been suggested that abnormally low pre-operative NAA concentrations in the temporal lobe are due to reversible metabolic dysfunctions due to ongoing seizures[236]. Our diffusion findings suggest that along with the

reversible / functional changes reported with MR spectroscopy, seizure free TLE patients also have irreversible white matter abnormalities (which are consistent with abnormalities of myelin / axonal integrity)[21,32].

The "two hit hypothesis" is a popular theory which suggests that two successive events must work together to induce TLE and MTS[213,219,469]. For example, a preexisting brain abnormality creates a susceptible state that results in the development of TLE with unilateral MTS in response to an initial precipitating event (e.g. prolonged febrile seizures). Despite being a widely accepted theory, to date, a consistent predisposing abnormality has not been identified[219]. Animal models have shown that subcortical deafferentation of the hippocampus (by transecting the fimbria/fornix) renders it seizure-prone[453], providing one possible underlying predisposing condition (i.e. first hit) of the pathogenesis of temporal lobe epilepsy. Our findings suggest that the cerebral connectivity in TLE patients is different than that in the general population, raising the question of whether the number and quality of inputs to and from the hippocampus could be abnormal and hence act as a predisposing factor. As the patients in this study all had prolonged duration of disease (range 12-47 years), the timing of the irreversible white matter abnormalities in relation to the onset of TLE and MTS remains unknown.

⋆ ⋆ ⋆

6.5 Appendix

Given the high success rate of surgery in patients with MTS[459], it was not surprising that our cohort of patients included so few patients who still experienced seizures after TLE surgery. These patients, albeit having to be classified as "not seizure free", have indeed experienced a worthwhile reduction in seizure frequency. Although we cannot draw conclusions on the time-dependent diffusion

[a]The appendix did not appear in the published version of this Chapter.

properties of the white matter structures of the patients who are not seizure free, Figure 6.7 shows that it appears as though both patient groups behave similarly. Certainly, larger sample sizes are needed to validate such assumption.

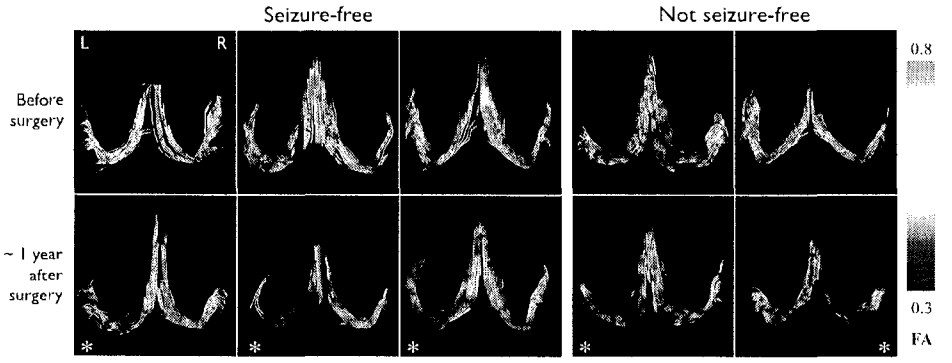

FIGURE 6.7: **Diffusion tensor tractography of the fornix ipsilateral and contralateral to mesial temporal sclerosis (*).** Three patients who were included in this study are shown, in addition to those presented in Figure (6.2). Furthermore, two patients excluded from this study due to persistence of occasional brief seizures are shown. Similarly to Figure 6.2 and as expected, the fornix ipsilateral to MTS shows a further decrease of diffusion anisotropy one year following surgery. The fornix contralateral to MTS shows low FA values that persist one year after surgery. The same pattern can be seen for patients who are not seizure free. A larger sample size of TLE patients who are not seizure-free following surgical treatment is needed to examine if the diffusion parameters of the contralateral fornix could be used for prognosis.

Chapter 7

White matter abnormalities in non-lesional temporal lobe epilepsy

Abstract

Although epilepsy is considered a gray matter disorder, changes in the underlying brain connectivity have important implications in seizure generation and propagation. We have previously identified abnormalities in the temporal and extra-temporal white matter of patients with temporal lobe epilepsy (TLE) and mesial temporal sclerosis (MTS). Patients with TLE but without MTS often show a different course of the disorder and worse surgical outcome than patients with MTS. The purpose of this study was to determine if said white matter abnormalities are related to the presence of MTS or if they are also present in non-lesional TLE. 17 patients with TLE and MTS (TLE+uMTS), 13 patients with non-lesional TLE (nl-TLE) and 25 age-matched controls were included in the study. Diffusion tensor imaging (DTI) was used to assess tract integrity of the fornix, cingulum, external capsules and the corpus callosum. The white matter abnormalities seen in the fornix appear to be exclusive to patients with MTS. Although the cingulum showed abnormally high overall diffusivity in both TLE groups, its anisotropy was decreased only in the TLE+uMTS group in a pattern similar to the fornix. The frontal and temporal components of the corpus callosum, as well as the external capsules, demonstrated reduced anisotropy in TLE regardless of MTS. While some white matter bundles are affected equally in both forms of TLE, the bundles directly related to the mesial temporal structures (i.e. the fornix and cingulum) appear to be affected mostly in the presence of MTS.

7.1 Introduction

Seizures are believed to result from an imbalance between excitation and inhibition within the central nervous system. As the pathological electrical impulses that produce a seizure are generated by the neurons, epilepsy is typically considered primarily a grey matter disease. Although seizures (like all neuronal signals) are transmitted along conventional pathways, white matter tracts have been considered to have a relatively passive role in epileptogenesis restricted to seizure propagation.

Nonetheless, volumetric magnetic resonance imaging (MRI) studies have demonstrated extensive white matter abnormalities in patients with temporal lobe epilepsy (TLE)[355,470]. Correlations between cerebral white matter volume and disease duration suggest that seizure related degeneration of white matter tracts could play a role in the progressive cognitive decline that is observed in some patients with epilepsy[470]. As well the demonstration that transection of the fornix can create an epileptogenic state in an animal model provides evidence that white matter pathology could be a primary factor in initiating epileptogenesis by disrupting the balance between inhibition and excitation (i.e. through deafferentation of the hippocampus)[453]. Thus, white matter pathology has been implicated in both epileptogenesis as well as seizure related comorbidity.

While volumetric MRI is a relatively nonspecific measure of white matter pathology, diffusion tensor imaging (DTI), a novel MRI technique, is sensitive to microscopic tissue characteristics[28]. It has been particularly useful in the study of white matter which shows a high degree of architectural coherence and is organized into tightly packed bundles of axons (fascicles) with similar orientations, whose membranes and myelin sheaths cause water diffusion to be anisotropic (i.e. not equal in all directions)[27].

Temporal lobe epilepsy is the most common form of localization related epilepsy[141] and is frequently associated with unilateral mesial temporal sclerosis (MTS)[219]. MTS is characterized by neuronal loss and gliosis of the mesial temporal structures and is readily observed on clinical MRI in the majority of cases[255].

While the clinical manifestations of TLE with and without MTS are similar, their responses to surgical treatment are considerably different with the demonstration of MTS in patients with TLE being associated with better surgical outcome[438,440]. New and sensitive imaging techniques have demonstrated MTS in patients presumed to lack MTS based on conventional imaging[257,471]. While it is possible that a subset of patients with so-called non-lesional TLE have very subtle MTS (not evident using conventional imaging), it is presumed that most patients have a neocortical as opposed to a mesial temporal seizure generator[472].

Water diffusion abnormalities of temporal and extra-temporal white matter fascicles have been previously reported in patients with TLE[408,422,458], which did not normalize upon seizure freedom following surgical treatment[473]. The diffusion changes seen in the fornix, cingulum, genu of the corpus callosum and external capsules suggested structural abnormalities of the white matter, such as reduced axonal density, myelin abnormalities, or both[21,27,32]. These studies have however been restricted to TLE with MTS or have not distinguished between TLE patients with and without MTS. The purpose of this study was to perform a direct comparison of the diffusion properties of select temporal and extra-temporal white matter structures between nl-TLE and TLE+uMTS.

7.2 Methods

7.2.1 Settings and participants

Approval of the research protocol was obtained from the Health Research Ethics Board of the University of Alberta, and informed consent was obtained from all participants. A total of thirty patients with medically intractable TLE, as well as twenty-five age-matched healthy controls were included in this study.

Temporal lobe epilepsy with unilateral mesial temporal sclerosis (TLE+uMTS, n=17, 39±11 years old [range: 20-59]; 5 men, 12 women). Patients in this group underwent pre-surgical evaluation, which included MRI and EEG video-telemetry. All patients showed evidence of hippocampal atrophy and T2 hyper-intensity on

conventional magnetic resonance imaging (MRI). Their T2 relaxometry (known to increase the sensitivity of MTS detection[257]) resulted in hippocampal T2 values above two standard deviations from the mean of the controls (i.e. >120 ms for our quantitative method[422]). According to this threshold, all patients in the TLE+uMTS group had ipsilateral T2 values considerably greater than that of the controls. In two patients with TLE+uMTS, the contralateral hippocampus was also found to have abnormal T2, but in both cases there was clear asymmetry. In all cases, EEG video-telemetry demonstrated solely unilateral temporal lobe ictal onset, which corresponded with the side demonstrating greatest T2 increase. No other lesions were present in any of the subjects on clinical imaging. Eleven patients included in this group have been previously reported[422,458,473].

Non-lesional temporal lobe epilepsy (nl-TLE, n=13, age 41±12 [range 17-62] years; 5 men, 8 women). Inclusion criteria for the nl-TLE group were primary ictal semiology of complex partial seizures and temporal lobe epileptic EEG abnormalities. Patients with MRI evidence of MTS (hippocampal T2 greater than 2SD of control values, >120ms) or extra-temporal structural lesions on MRI were excluded. Eleven of 13 subjects had ictal and interictal EEG recordings (seven with prolonged scalp EEG-video recordings and four with both scalp and intracranial electrodes). For the two subjects who did not have ictal recordings, both had unequivocal temporal interictal epileptic EEG abnormalities and both experienced typical complex partial seizures as their primary seizure pattern. EEG lateralization was right temporal for two patients, left temporal for six and bitemporal in the remaining five patients).

Healthy controls (n=25, age 33±10 [range 18-58]; 17 men, 8 women). None of the subjects suffered from any neurological or psychiatric condition. All subjects lacked any visible anomalies on clinical MRI. Disease duration was similar between the two TLE groups, with the TLE+uMTS group having slightly longer disease duration (27±13 years) than the nl-TLE group (18±13) (Student's *t* test, p=0.053).

7.2.2 Imaging and data analysis

Cerebro-spinal fluid-suppressed diffusion tensor images were acquired in 9:30 minutes using a 1.5 T Siemens Sonata MRI scanner (Siemens Medical Systems, Erlangen, Germany). The sequence consisted of 26 contiguous 2 mm thick oblique slices (aligned parallel to the anterior commissure-posterior commissure [AC-PC] line) with an in-plane resolution of 2×2 mm^2 (voxel dimensions after interpolation were $1\times1\times2$ mm^3). Diffusion sensitized images were acquired in six directions, with a b value of 1000 s/mm^2. Full details of the imaging protocol have been previously provided[422,474].

Six white matter structures were studied, namely the fornix, cingulum and external capsule, as well as three portions of the corpus callosum: the frontal (genu), occipital and temporal (tapetum) components of the splenium (Figure 7.1). These six white matter bundles were selected for analysis based on previously reported abnormalities[408,422,458,475]. The fornix, cingulum and the occipital and temporal callosal fibers were depicted with tractography (fiber assignment by continuous tracking algorithm)[55,64], whereas the genu of the corpus callosum and the external capsules (easily identified on 2-dimensional diffusion maps) were analyzed using manually-placed regions of interest (ROI) on a single slice (parallel to the AC-PC line) at the level of the central portion of the thalamus. Tractography and ROI analyses were performed by a single investigator (LC) in a consistent fashion amongst all subjects. The tractography algorithm was started in all white matter voxels in the brain, and the tracts were virtually dissected using *a priori* anatomical knowledge of their trajectories and based on the previously reported atlas of white matter structures[427]. The placement of tract-selection regions for the depiction of the fornix and cingulum has been reported previously (Figure 5.1). The fibers passing through the splenium of the corpus callosum were selected using a mid-sagittal slice, and those belonging to the tapetum were selected by using a second tract-selection region located in the temporal lobes; the occipital callosal fibers were selected using a second large region located in the occipital lobe. The FA threshold for tractography was set as 0.3 (start and stop criteria) for all tracts.

Specific portions of the tractography-defined structures were analyzed to yield summary diffusion parameters for the individual white matter regions. The crus of the fornix and the temporal portion of the cingulum were analyzed between the axial levels of the mammillary bodies and the fusion of the crura of the fornices whereas the tapetum and occipital components of the corpus callosum were analyzed between the lateral ventricles ($\sim \pm$2cm from the midline) (Figure 7.1). The micro-structural integrity of the tracts was assessed by evaluation of the average quantitative diffusion parameters measured from the voxels within the structures (namely fractional anisotropy [FA], mean diffusivity [MD] and diffusivities parallel and perpendicular to the tracts [$\lambda_{\parallel}$ and $\lambda_{\perp}$, respectively]). Average diffusion parameters were calculated for each white matter structure in every subject.

There was no significant left-right asymmetry of the diffusion anisotropy of the fornix or external capsules in the control group (paired Student's t tests, p=0.11 and p=0.9, respectively). Also in the controls, the cingulum showed a very slight right>left asymmetry of FA (mean difference=0.011, p=0.035). In patients with TLE+uMTS, the fornix and cingulum showed larger abnormalities in the structures ipsilateral to MTS, as compared with the contralateral side, although these differences were small and not present in all patients (Figure 7.2). The issue of laterality and asymmetry in patients with nl-TLE is complicated due to the presence of patients with independent bilateral seizure onset and, thus, the terms *ipsilateral* and *contralateral* are difficult to apply. However, Figure 7.3 shows the apparently little dependence of seizure onset on the anisotropy measures of the paired structures. Due to minimal asymmetry of these paired structures, our previous report of bilateral white matter abnormalities in patients with unilateral MTS[422,458], and to simplify subsequent between-group comparisons, the individual quantitative parameters of the fornix, cingulum and external capsules of each hemisphere were averaged to yield a single value per structure per subject (i.e. [left+right]/2).

Multivariate analyses of variance (MANOVA) were performed for each white matter structure. If the p-value of the test (Wilk's Lambda) was <0.05, univariate analyses of variance (ANOVA) were conducted for each diffusion parameter and, when necessary, between-group comparisons were performed using Tukey's

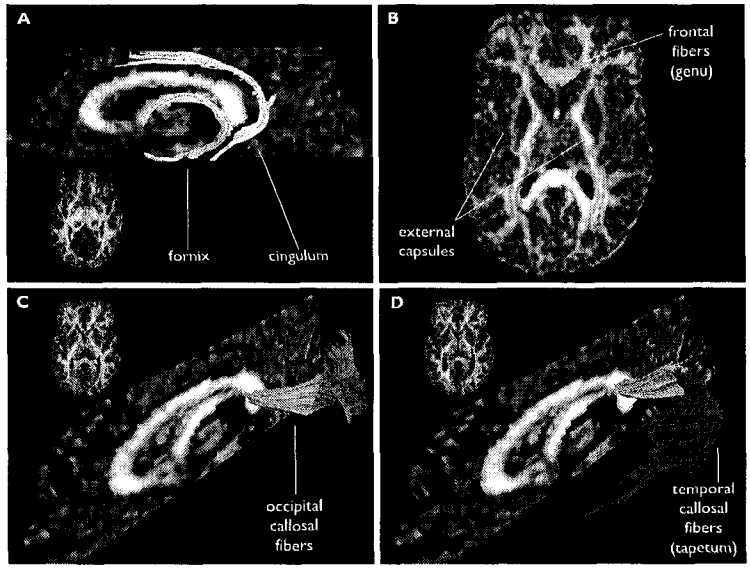

FIGURE 7.1: **White matter structures analyzed.** The fornix and cingulum (A), directly related to the mesial temporal structures, were depicted using tractography. Evaluation of diffusion parameters of these tracts was restricted to their temporal portions (highlighted in bright yellow and green). The frontal portion (genu) of the corpus callosum and external capsules are easily discernible on the FA map and were analyzed using regions of interest on a two-dimensional slice (B). In contrast, it is more difficult to visually discern the occipital (C) and temporal (tapetum, D) components of the splenium of the corpus callosum on two-dimensional slices; such a task is facilitated by the use of tractography. Following the identification of the temporal and occipital tracts, the portions between the lateral ventricles ($\sim \pm 2$ cm from the midline, highlighted in light blue and orange) were analyzed to yield diffusion parameters. All axial views are seen from above. The inset in panel A shows the fornix in the orientation used in Figure 7.4.

post-hoc test. This step-down approach allows the sequential testing of the null hypothesis and the correction for multiple comparisons while maintaining adequate statistical power. The average diffusion parameters of the white matter bundles were linearly correlated with disease duration and age at onset of epilepsy using Pearson's coefficient (r) and partial correlations controlling for age (when analyzing the effect of disease duration) or disease duration (for the analysis of age at seizure onset).

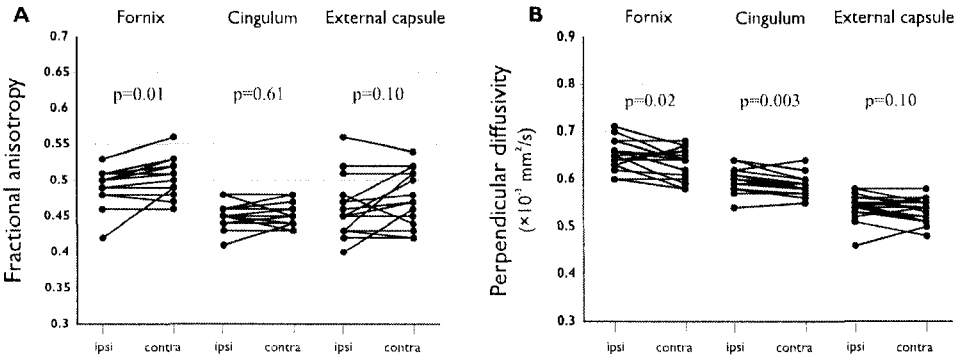

FIGURE 7.2: **Diffusion parameters of paired white matter structures relative to the side of mesial temporal sclerosis (MTS).** The diffusion parameters obtained from each fornix in every TLE+uMTS patient (n=17) is shown according to their relation to MTS (ipsi=ipsilateral; contra=contralateral to MTS). The fornix shows abnormalities that are only slightly more pronounced on the tract ipsilateral to MTS. The perpendicular diffusivity of the cingulum is also higher on the ipsilateral tract. The external capsules did not show asymmetry. The shaded areas in each structure represent the mean±1SD for the controls (n=25). P values for Student's paired t tests are shown for ipsi- versus contra-lateral measurements.

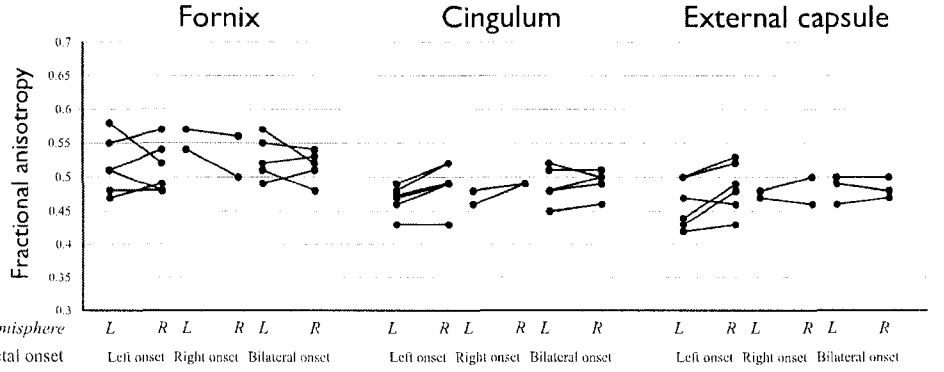

FIGURE 7.3: **Fractional anisotropy of the fornix, cingulum and external capsule in patients with non-lesional TLE.** There is little dependence of the side of ictal onset on diffusion anisotropy and, therefore, the diffusion parameters of the paired structures were collapsed for each patient (i.e. [left+right]/2) for subsequent analyses which combined all three patient groups regardless of onset laterality. The shaded areas in each structure represent the mean±1SD for the controls (n=25).

7.3 Results

Fornix (Figures 7.4, 7.5A,B and 7.6; Table 7.1). The TLE+uMTS group showed significant diffusion abnormalities when compared to the control and the nl-TLE groups. Particularly, FA was reduced and perpendicular diffusivity increased in

the TLE+uMTS group. These findings were also present when analyzing the fornices ipsilateral and contralateral to MTS (data not shown). The nl-TLE group was not significantly different from the control group in terms of any of the diffusion parameters, but differed from the TLE+uMTS group. There were statistically significant differences between the nl-TLE and TLE+uMTS groups in terms of FA and perpendicular diffusivity. The TLE+uMTS did not show any significant correlation between disease duration or age at seizure onset with any of the diffusion parameters. The nl-TLE group showed significant correlations between disease duration and FA (r=-0.68, p=0.011) and $\lambda_\perp$ (r=0.74, p=0.004) (Figure 7.6). When controlling for age, the correlation between disease duration and FA in the nl-TLE group did not reach statistical significance (r=-0.53, p=0.077), but the correlation with $\lambda_\perp$ remained significant (r=0.63, p=0.028). No other diffusion parameter correlated with disease duration. FA in the nl-TLE group also correlated with age at seizure onset, but only when controlling for disease duration (r=-0.586, p=0.045).

Cingulum (Figure 7.5C,D; Table 7.1). The TLE+uMTS group showed reduced diffusion anisotropy and increased mean and perpendicular diffusivities as compared with the control group. Similarly to the fornix, these findings were present both ipsilateral and contralateral to MTS (not shown). Patients with nl-TLE showed increased mean, parallel, and perpendicular diffusivities, but normal diffusion anisotropy when compared with controls. Furthermore, the increase in MD and $\lambda_\perp$ was not as large in the nl-TLE group as in the TLE+uMTS group. Patients with TLE+uMTS showed lower diffusion anisotropy (p=0.001) and higher mean (p=0.03) and perpendicular (p=0.001) diffusivities than the nl-TLE group. Disease duration did not correlate with any of the diffusion parameters in any of the TLE groups. In the nl-TLE group, age at seizure onset correlated with MD (r=0.38, p=0.046) and $\lambda_\perp$ (r=0.58, p=0.049) only when controlling for disease duration.

External capsule (Figure 7.5E,F; Table 7.1). Both TLE groups showed abnormalities, characterized by reduced FA and increased MD and $\lambda_\perp$. Both TLE groups were indistinguishable from one another in terms of diffusion parameters. In the

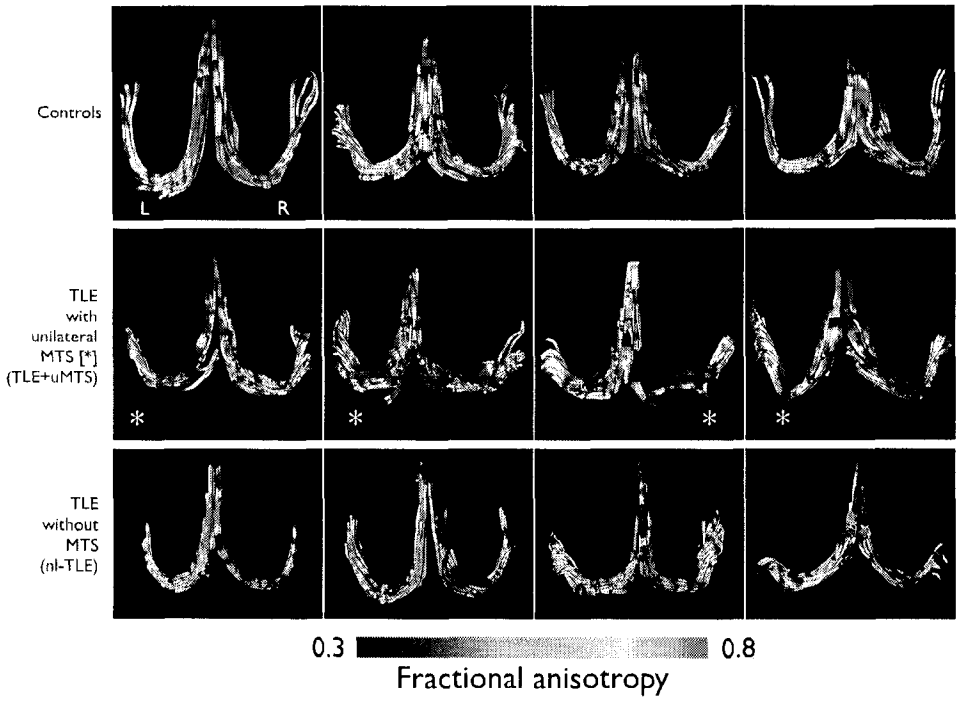

FIGURE 7.4: **Fractional anisotropy of the fornix.** The fornix was depicted with tractography and color-coded according to fractional anisotropy. As compared to the controls, patients with temporal lobe epilepsy and unilateral mesial temporal sclerosis (TLE+uMTS) show reduced diffusion anisotropy bilaterally, regardless of the side of MTS (denoted by the asterisks). Patients with TLE but without MTS (nl-TLE) do not show such a marked decrease of anisotropy in this tract. The tracts are viewed from above, such that anatomical right is in the image's right (See Figure 7.1A).

TLE+uMTS group, both sides (ipsilateral and contralateral to MTS) showed similar abnormalities (not shown). The nl-TLE group showed a significant correlation between $\lambda_{||}$ and disease duration, when controlling for age (r=0.60, p=0.039).

Genu of corpus callosum (Figure 7.7A,B; Table 7.1). Both TLE groups showed reduced FA and increased $\lambda_{\perp}$, but only the TLE+uMTS group showed increased MD when compared with controls. There were no statistically significant differences between the two TLE groups in any of the diffusion parameters, including MD. There were no significant bivariate or partial correlations.

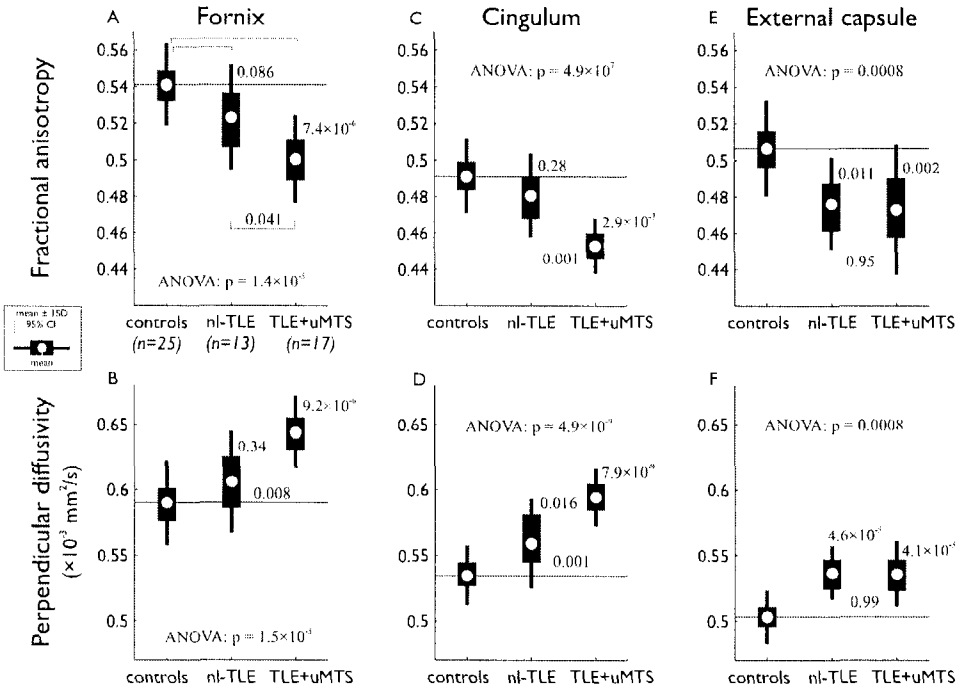

FIGURE 7.5: **Between-group comparisons of the diffusion parameters of the fornix, cingulum and external capsules.** The fornix shows a decrease in diffusion anisotropy (A) and an increase in perpendicular diffusivity (B) only in the TLE+uMTS group. The cingulum shows abnormally high perpendicular diffusivity (D) in both TLE groups, but its diffusion anisotropy is only affected in those patients with MTS (C). Both patient groups show diffusion abnormalities of the external capsules. The thin lines in A show the design of the *post-hoc* tests used in each panel (p values shown). All data shown represents the average of the left and right structures per subject.

Occipital fibers of the corpus callosum (Figure 7.7C,D; Table 7.1). Only the TLE+uMTS group showed a significant, albeit small, reduction in FA and increase in MD and $\lambda_\perp$ when compared with the controls. The two epilepsy groups were not statistically different in terms of any of the diffusion parameters. There were no differences between the two TLE groups. In the TLE+uMTS group, FA correlated with age at seizure onset, when controlling for disease duration (r=-0.603, p=0.013).

Temporal fibers of the corpus callosum (tapetum) (Figure 7.7E,F; Table1). Both TLE groups showed reductions in FA and elevations of $\lambda_\perp$. The group with

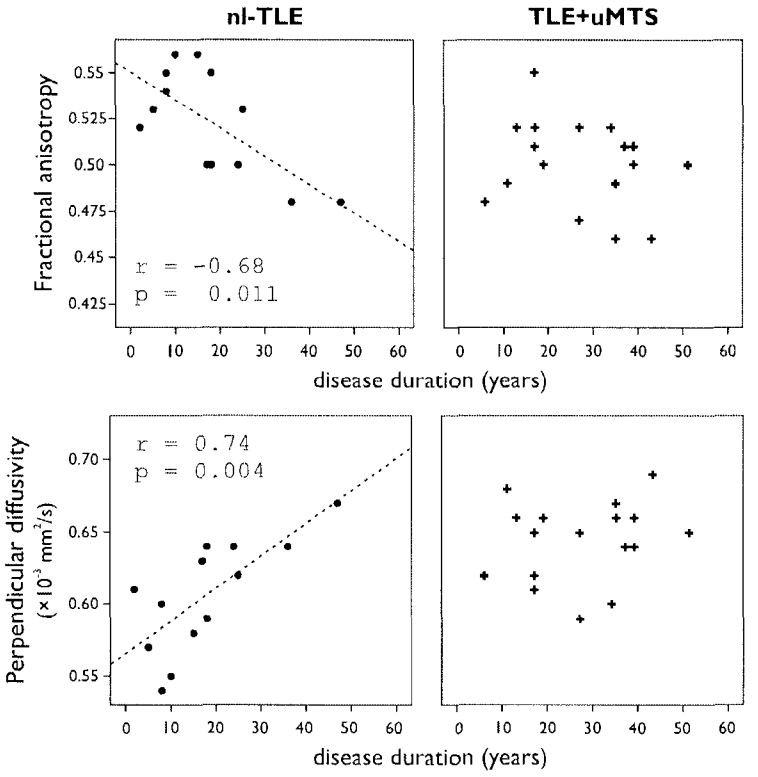

FIGURE 7.6: **Bivariate correlations of disease duration and diffusion parameters of the fornix.** In patients with non-lesional TLE, but not those TLE patients with mesial temporal sclerosis, there is a negative correlation between diffusion anisotropy and disease duration, while perpendicular diffusivity shows a positive correlation. These correlations, which do not control for age, suggest progressive decline in tissue integrity of the fornix in the nl-TLE group. Age was not significantly correlated with the diffusion parameters of the fornix in the control group (see Section 7.5).

TLE+uMTS appeared to have the most marked changes, although the comparison of both TLE groups did not reach statistical significance. Only the TLE+uMTS group had increased MD as compared with the controls. The nl-TLE group showed a significant bivariate correlation between disease duration and $\lambda_\perp$ (r=0.61, p=0.027), but it did not reach statistical significance when controlling for age (r=0.53, p=0.07).

					Corpus callosum		
		Fornix	Cingulum	External capsule	Frontal (genu)	Occipital	Temporal (tapetum)
	MANOVA (p)	1.01×10^{-5}	1.7×10^{-8}	0.0002	0.0003	0.006	0.001
FA	**ANOVA (p)**	1.4×10^{-6}	4.8×10^{-7}	0.0008	4.1×10^{-5}	0.008	6.0×10^{-6}
	Controls	0.54(0.02)	0.49(0.02)	0.51(0.03)	0.76(0.04)	0.70(0.02)	0.71(0.03)
	nl-TLE	0.52(0.03)^{b}	0.48(0.02)^{b}	0.48(0.03)^{a}	0.72(0.03)^{a}	0.70(0.02)	0.69(0.03)^{a}
	TLE+uMTS	0.50(0.02)^{a,b}	0.45(0.02)^{a,b}	0.47(0.04)^{a}	0.69(0.05)^{a}	0.68(0.02)^{a}	0.67(0.02)^{a}
MD	**ANOVA (p)**	0.028	5.1×10^{-8}	0.0003	0.014	0.02	0.012
$\times10^{-3}$ mm^2/s	Controls	0.90(0.03)	0.76(0.02)	0.71(0.02)	0.76(0.03)	0.77(0.02)	0.76(0.03)
	nl-TLE	0.90(0.03)^{b}	0.78(0.03)^{a,b}	0.73(0.02)^{a}	0.78(0.04)	0.79(0.02)	0.78(0.03)
	TLE+uMTS	0.93(0.03)^{b}	0.80(0.02)^{a,b}	0.73(0.02)^{a}	0.80(0.05)^{a}	0.80(0.04)^{a}	0.79(0.03)^{a}
$\lambda_{\parallel}$	**ANOVA (p)**	0.038	0.01	0.13^{c}	0.18^{c}	0.88^{c}	0.28^{c}
$\times10^{-3}$ mm^2/s	Controls	1.53(0.05)	1.20(0.03)	1.12(0.04)	1.61(0.06)	1.54(0.06)	1.54(0.07)
	nl-TLE	1.48(0.05)	1.23(0.03)^{a}	1.12(0.03)	1.59(0.08)	1.55(0.04)	1.54(0.08)
	TLE+uMTS	1.49(0.07)	1.22(0.03)	1.10(0.04)	1.56(0.09)	1.55(0.08)	1.51(0.06)
$\lambda_{\perp}$	**ANOVA (p)**	1.5×10^{-5}	4.9×10^{-9}	4.0×10^{-6}	3.9×10^{-5}	0.001	1.0×10^{-5}
$\times10^{-3}$ mm^2/s	Controls	0.59(0.03)	0.53(0.02)	0.50(0.02)	0.33(0.05)	0.39(0.02)	0.37(0.03)
	nl-TLE	0.61(0.04)^{b}	0.56(0.03)^{a,b}	0.54(0.02)^{a}	0.38(0.04)^{a}	0.40(0.03)	0.40(0.03)^{a}
	TLE+uMTS	0.64(0.03)^{a,b}	0.59(0.02)^{a,b}	0.54(0.02)^{a}	0.41(0.06)^{a}	0.42(0.03)^{a}	0.42(0.03)^{a}

TABLE 7.1: **Summary data (mean and standard deviation) and statistical analyses of diffusion parameters in nl-TLE (n=13) and TLE+uMTS (n=17) versus controls (n=25).** ANOVA: analysis of variance between the to TLE and the control group. nl-TLE: non-lesional temporal lobe epilepsy. TLE+uMTS: temporal lobe epilepsy with unilateral mesial temporal sclerosis.
^{a}: Significant difference ($p < 0.05$) with respect to control group.
^{b}: Significant difference ($p < 0.05$) between nl-TLE and TLE+uMTS groups.
^{c}: *Post-hoc* tests not performed due to ANOVA $p > 0.05$.

7.4 Discussion

In this study, we have shown white matter abnormalities with distinct spatial distribution and diffusion characteristics for TLE with and without MTS. In general, TLE patients with MTS have a higher degree and more extensive white matter abnormalities.

The previously identified diffusion abnormalities of the fornix[422] appear to be exclusive to patients with MTS. The reported reduction of FA and increase of $\lambda_{\perp}$ is interpreted to reflect myelin abnormalities, reduced axonal density, or both[21,27,32]. With the fornix being the principal output pathway from the hippocampus, it is not surprising to find abnormalities of this white matter bundle in the presence of

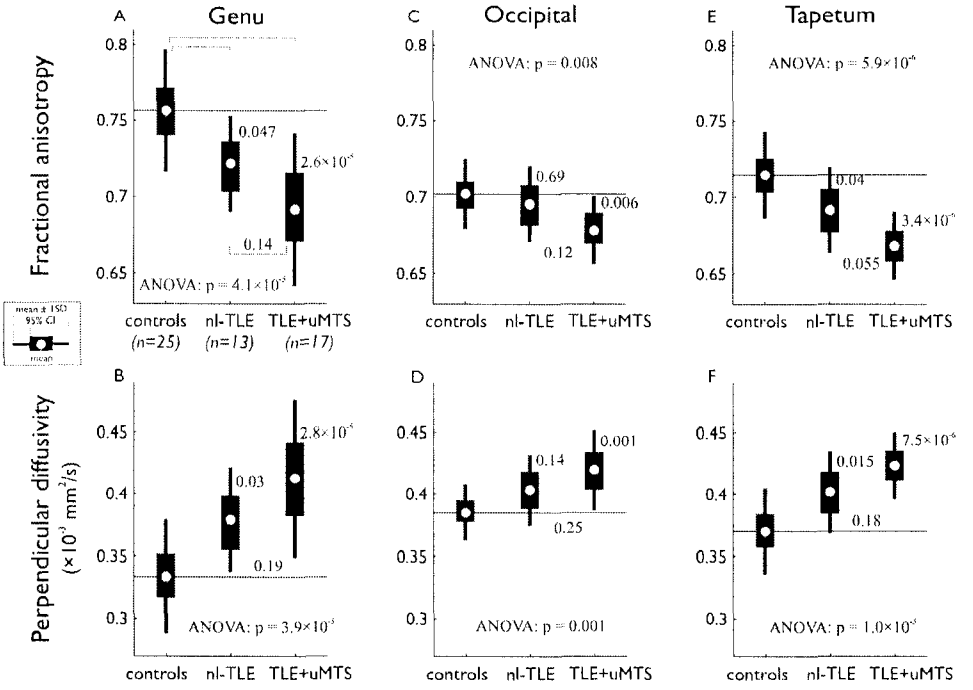

FIGURE 7.7: **Between-group comparisons of the diffusion parameters of three portions of the corpus callosum.** The frontal and temporal components of the corpus callosum (genu and tapetum, respectively) show reduced diffusion anisotropy and increased perpendicular diffusivity in both TLE groups irrespective of the presence of MTS. The occipital portion of the corpus callosum shows the same pattern of abnormalities only in the TLE+uMTS group, when compared to the controls. P values of the ANOVA and post-hoc tests are shown; the thin lines in A show the design of the post-hoc tests used in each panel.

MTS[267,357]. It is notable, however, that the diffusion abnormalities of the fornix are bilateral[422] and that they do not resolve upon seizure freedom following epilepsy surgery[473], which suggests that they are not only due to downstream axonal or myelin degeneration secondary to hippocampal neuronal death.

Patients with non-lesional TLE showed diffusion anisotropy that, albeit being slightly lower, was not statistically different from the mean of the controls. TLE with and without MTS did, however, share abnormalities of the genu and tapetum of the corpus callosum and the external capsules. A previous study also found diffusion abnormalities of the genu and splenium of the corpus callosum, as well as the external capsules, in patients with TLE, although it was not clear how many of the patients included in their study had MTS[408]. The underlying reason for the

abnormalities seen in the genu in TLE is not clear, as this particular tract does not hold many axons connecting the temporal lobes to other regions of the brain and is not generally considered to be part of the limbic system. The findings in the tapetum, and their presence in both forms of TLE, are more straightforward to interpret, as these fibers directly interconnect the two temporal lobes. The external capsule contains long association fibers that are part of the inferior fronto-occipital, uncinate and superior longitudinal fascicles[427]. The uncinate fasciculus, in particular, interconnects the frontal and temporal lobes and has recently been reported to have abnormally low diffusion anisotropy in patients with TLE and is believed to be implicated in the spread of seizure activity[410]. This particular tract was not evaluated using tractography given the limited anatomical coverage of our CSF-suppressed DTI imaging sequence. The presence of bilateral seizure generators in 5/13 patients with nl-TLE compromises the understanding of the relationship between the seizure generator and the white matter abnormalities in the nl-TLE group and thus we cannot exclude the possibility that these patients have distinct pathology in each hemisphere. A larger sample of patients with nl-TLE is necessary to validate our current findings and to permit more sophisticated and accurate statistical comparisons accounting for anatomical and seizure onset side.

Although reductions of diffusion anisotropy of the fornix with age (range: 18-88 years) have been demonstrated[476], we did not find a significant correlation between FA of the fornix and age in our control group, in which 88% of the subjects were less than 50 years old ($r=0.18$, $p=0.39$). The age range in our study, as well as the use of CSF-suppression, could account for such a discrepancy. The only significant correlation we found between diffusion anisotropy and age was located in the genu of the corpus callosum ($r=-0.47$, $p=0.018$) (in line with previous reports[428,477]). For this reason, we re-analyzed the data from this structure using age as a covariate (Sidak's correction for multiple comparisons of the estimated means) and found that the differences seen in FA and of the genu in the nl-TLE group were not significant with respect to the control group (FA: $p=0.22$; $\lambda_\perp$: $p=0.15$).

Ipsilateral gray matter volume reductions of the entorhinal cortex have been reported in patients with nl-TLE[478], and reductions of gray matter concentration of the extended limbic system were present in patients with clearly defined unilateral MTS[370]. White matter volume reductions have also been reported in patients with TLE ipsilateral to the suspected seizure focus[354,367,371], but also bilaterally[355,479]. In a voxel-based DTI study of gray and white matter, reduced FA and increased MD were found within and outside the temporal lobe of patients with TLE+uMTS although, contrary to our reports, the contralateral hemisphere only showed abnormalities of mean diffusivity and not FA[401]. Similarly, magnetic resonance spectroscopy has shown metabolic abnormalities that are not exclusive to the ipsilateral temporal lobe[277,471]. These reports and our current findings show that TLE presents with brain abnormalities that extend well beyond the suspected seizure focus.

The issue of progressive structural changes in response to ongoing seizures in humans remains controversial[480]. Of interest, a correlation between white matter asymmetry and duration of TLE has been observed using quantitative volumetric MRI[355]. This finding suggests that remodeling of neuronal projections in response to recurrent seizures can occur in human TLE. Our report of a correlation between disease duration and parameters of tract integrity (namely FA and $\lambda_\perp$) of the fornix of patients with nl-TLE (Figure 7.6) suggests that the micro-structural characteristics of this white matter tract are progressively affected by seizures. In patients with TLE+uMTS, however, this correlation was not found. This lack of correlation could be explained by the fact that several patients with TLE+uMTS have abnormal diffusion parameters even with short disease duration. Alternatively, different patho-physiological mechanisms could be responsible for the differences between the two TLE groups. Correlations with clinical time-related measures are difficult to evaluate, as confounding factors must be accounted for, such as age-related changes, different susceptibility states to an initial insult at different ages, episodes of status epilepticus, etc. Other important correlations were not performed in this study due to the difficulty in obtaining the relevant information, such as seizure frequency and lifetime number of generalized convulsions. Thus,

it is still unknown if the identified white matter abnormalities pre-date the development of TLE or if they are a secondary effect of ongoing seizures. Lastly, as we did not perform correction for multiple statistical comparisons (which would have severely limited the statistical power of our study), the cross-sectional design of our study, and the relatively small sample size, it would be inappropriate to derive definitive conclusions from our correlative analyses. Nonetheless, our data hints at a plausible interaction between disease duration and abnormalities of the fornix. Further studies are needed to validate our findings and to search for additional evidence of progressive white matter changes.

Even though epilepsy is certainly a disorder of the gray matter, the present study shows evidence of abnormality in the integrity of the connecting white matter. These changes could alter the excitation/inhibition balance, favoring the generation or the spread of anomalous electrical activity. The clinical relevance, as well as the cause or effect relationship with seizures, of the white matter diffusion abnormalities remains to be elucidated.

* * *

7.5 Appendix

The diffusion parameters of the 25 subjects included in this study only showed a significant correlation with age in the genu of the corpus callosum, but not in any of the other structures (Figures 7.8 and 7.9).

As stated in Section 3.1, there are several forms of epilepsy with distinct underlying mechanisms. This dissertation is focused on the localization-related form of temporal lobe epilepsy. On the other end of the epileptic spectrum stands primary generalized epilepsy (PGE), a relatively benign form of epilepsy that is typically controlled with medication. In PGE, by definition, the epileptic activity does not have a focal generator, but manifests itself on the surface EEG simultaneously, and is invariably accompanied by loss of consciousness. Epidemiologically, this

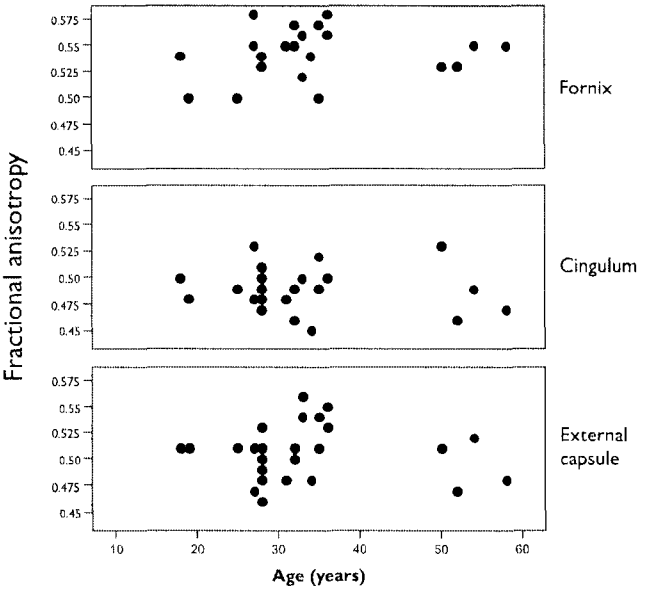

FIGURE 7.8: **Age vs. FA of paired structures in 25 controls.** There were no significant correlations between age and diffusion anisotropy in any of the paired structures.

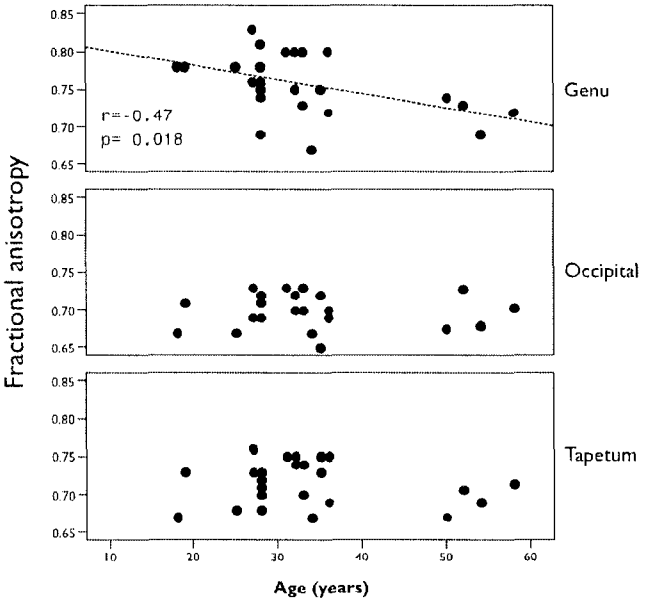

FIGURE 7.9: **Age vs. FA of the corpus callosum in 25 controls.** Only the genu of the corpus callosum shows a significant correlation between age and diffusion anisotropy.

form of epilepsy is more commonly observed in children and young adults. Its underlying mechanisms is often related to abnormalities of ion channels caused by mutation of their genes.

Given that the pathophysiology of PGE is very different from that of TLE with or without MTS, this group served as an opportunity to investigate whether any of the previously identified white matter abnormalities in patients with TLE are also present in this other form of epilepsy.

A group of 15 patients with PGE (20±4 [range 17-31] years; 8 men, 7 women) were studied using the exact same methodology as that utilized for patients with TLE. The same six white matter structures were analyzed with DTI and their diffusion parameters plotted versus those obtained from controls and patients with TLE (Figures 7.10 to 7.15). While there seem to be specific white matter diffusion abnormalities in all epilepsy groups, the abnormalities seen in the fornix and cingulum are certainly more prominent in those patients with TLE and MTS. Patients with MTS appear to have more extended and severe white matter abnormalities than any of the other groups, also showing the most altered diffusion parameters of the corpus callosum. The external capsule, interestingly, appeared to be affected nearly equally in all forms of epilepsy (Figure 7.12). This work is in preparation for submission to a peer-reviewed journal.

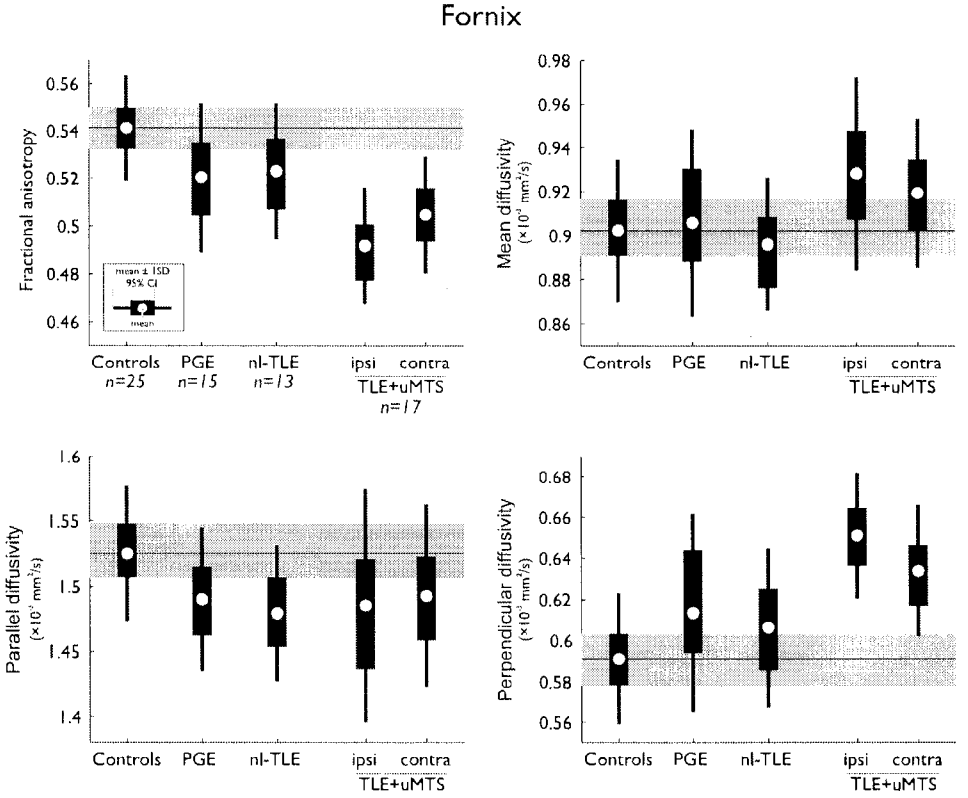

FIGURE 7.10: **DTI parameters of the fornix in PGE and TLE with and without MTS.** Patients with PGE show diffusion parameters that are similar to those seen in patients with non-lesional TLE. Patients with TLE and unilateral MTS show abnormalities of the fornix (particularly a decrease in FA due to increased $\lambda_\perp$) bilaterally, with slightly more marked abnormalities on the side ipsilateral to MTS. The DTI parameters from the control, PGE and nl-TLE groups are presented as (left+right)/2, while those from patients in the TLE+uMTS group are shown either ipsilateral or contralateral to MTS.

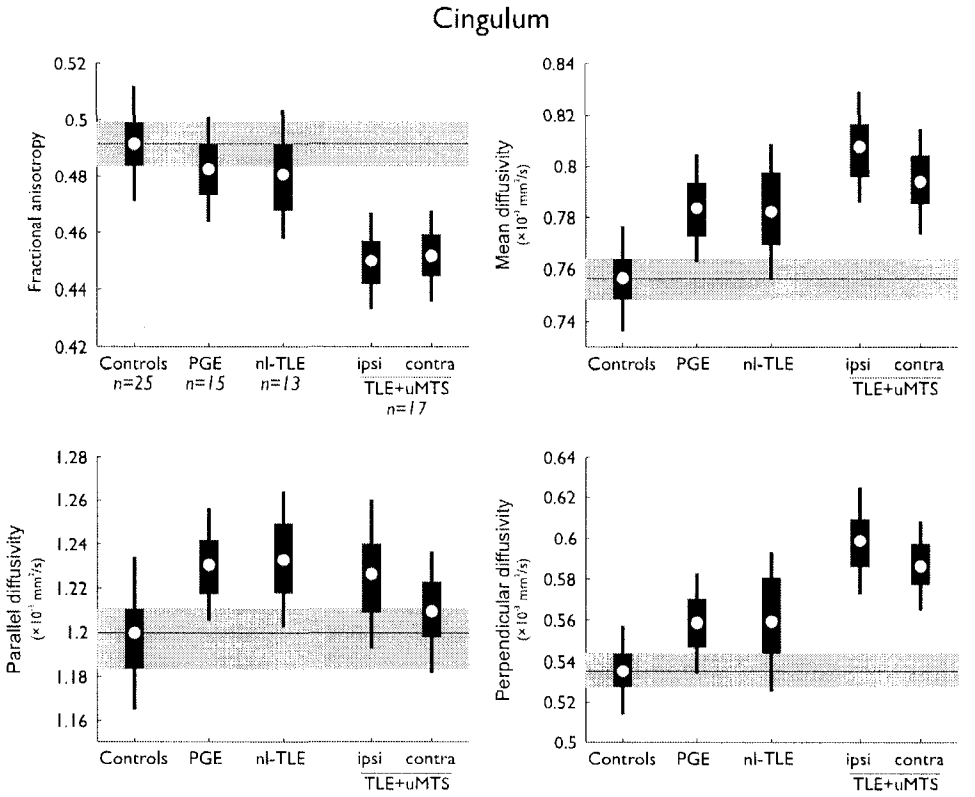

FIGURE 7.11: **DTI parameters of the cingulum in PGE and TLE with and without MTS.** Diffusion anisotropy of the cingulum is affected only in patients with TLE and MTS. The mean diffusivity of this tract, however, appears to be affected across all forms of epilepsy, although it is $\lambda_\perp$ alone which drives such an increase in patients with TLE and MTS, while in patients with PGE and nl-TLE, $\lambda_\parallel$ works together with $\lambda_\parallel$ to increase mean diffusivity. The DTI parameters from the control, PGE and nl-TLE groups are presented as (left+right)/2, while those from patients in the TLE+uMTS group are shown either ipsilateral or contralateral to MTS.

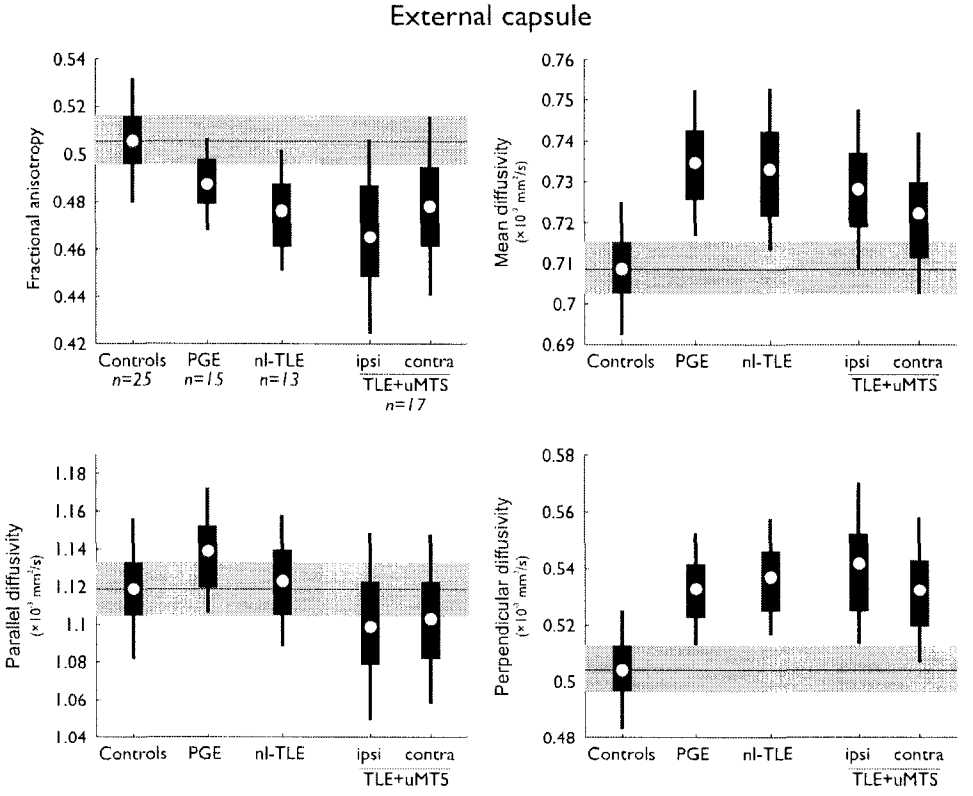

FIGURE 7.12: **DTI parameters of the external capsule in PGE and TLE with and without MTS.** The diffusion parameters of the external capsule appear to be affected similarly across all forms of epilepsy. The DTI parameters from the control, PGE and nl-TLE groups are presented as (left+right)/2, while those from patients in the TLE+uMTS group are shown either ipsilateral or contralateral to MTS.

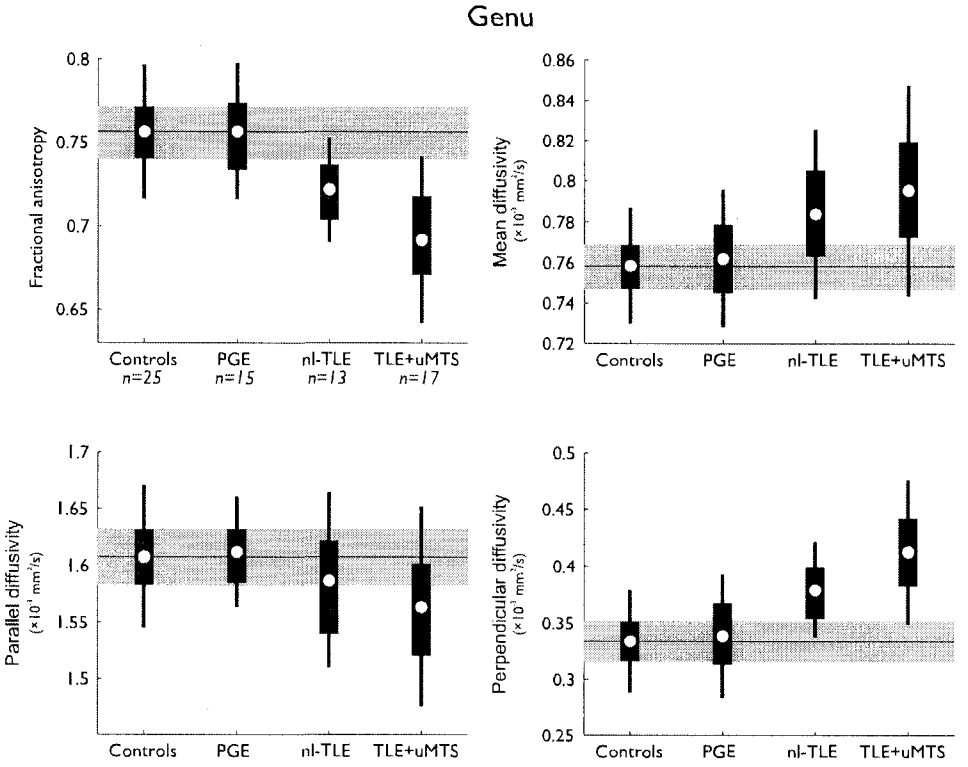

FIGURE 7.13: **DTI parameters of the genu in PGE and TLE with and without MTS.** DTI parameters appear to be affected in both TLE groups, while they are indistinguishable from controls in the PGE group.

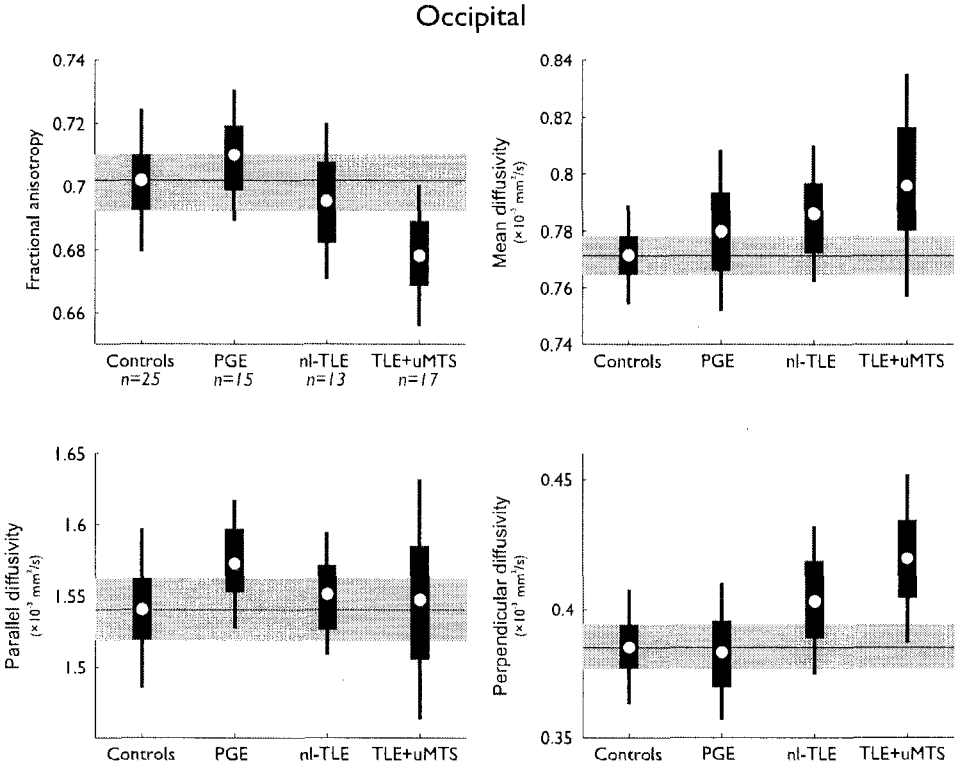

FIGURE 7.14: **DTI parameters of the occipital fibers of the corpus callosum in PGE and TLE with and without MTS.** The occipital fibers of the show slight abnormalities of diffusion parameters (reduced FA and increased $\lambda_\perp$) only in patients with TLE and unilateral MTS.

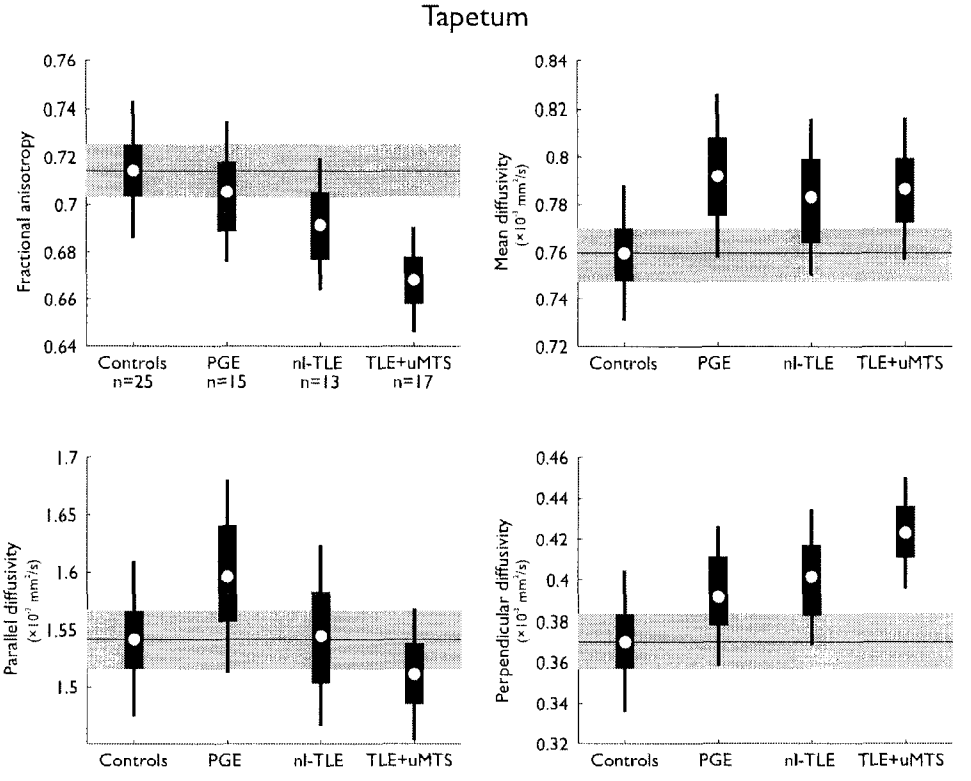

FIGURE 7.15: **DTI parameters of the tapetum in PGE and TLE with and without MTS.** While patients with TLE show reduced anisotropy and increased $\lambda_\perp$ as compared to controls, patients with PGE show increased diffusivity given by both $\lambda_\parallel$ and $\lambda_\perp$ being moderately increased.

Chapter 8

DTI of axonal and myelin degradation in Wallerian degeneration

Abstract

Axonal degeneration of white matter fibers is a key consequence of neuronal or axonal injury. It is characterized by a series of time-related events with initial axonal membrane collapse followed by myelin degradation being its major hallmarks. Standard imaging cannot differentiate these phenomena, which would be useful for clinical investigations of degeneration, regeneration and plasticity. Animal models suggest that diffusion tensor magnetic resonance imaging (DTI) is capable of making such distinction. The applicability of this technique in humans would permit inferences on white matter micro-anatomy using a non-invasive technique. The surgical bisection of the anterior 2/3 of the corpus callosum for the palliative treatment of certain types of epilepsy serves as a unique opportunity to assess this method in humans. DTI was performed on three epilepsy patients before corpus callosotomy and at two time points (one week and 2-4 months) after surgery. Tractography was used to define voxels of interest for analysis of mean diffusivity, fractional anisotropy and eigenvalues. Diffusion anisotropy was reduced in a spatially dependent manner in the genu and body of the corpus callosum at one week and remained low two to four months after the surgery. Decreased anisotropy at one week was due to a reduction in parallel diffusivity (consistent with axonal fragmentation), whereas at 2-4 months, it was due to an increase in perpendicular diffusivity (consistent with myelin degradation). DTI is capable of non-invasively detecting, staging and following the micro-structural degradation of white matter following axonal injury.

A version of this Chapter was published in:

Concha L., Gross D.W., Wheatley B.M. and Beaulieu C. Diffusion tensor imaging of time-dependent axonal and myelin degradation after corpus callosotomy in epilepsy patients. *Neuroimage* 2006. 32(3):1090–9.

8.1 Introduction

Wallerian Degeneration (WD), described originally in 1850[481] and extended by Ranvier[482] and Ramón y Cajal[483], is characterized by a series of events caused by neuronal injury that ultimately lead to the fibrosis and atrophy of the affected neuronal fibers. Such changes occur both upstream and downstream from the site of the lesion and, therefore, produce axonal changes in locations distant to the primary lesion. In the central nervous system (CNS), the acute phase of degeneration is composed primarily of fragmentation and dying-back of the axons[484,485], while the chronic stage is characterized mainly by the slow and progressive degradation and phagocytosis of the myelin sheaths[484].

The demonstration, characterization and staging of the changes seen in axonal degeneration by means of a non-invasive approach would be of great importance in the clinical setting. In peripheral nerve degeneration, clinical magnetic resonance imaging (MRI) shows T2 signal hyperintensity of the nerve in sites distant from the precipitating injury as soon as 24 hours from onset[486]. However, due to the slow and progressive nature of axonal degeneration in the CNS, T2 signal changes distant from the lesion are not evident during the first four weeks[487,488]. At four to 14 weeks following injury, the white matter tracts undergoing degeneration become hypo-intense on T2-weighted images due to loss of myelin proteins (while myelin lipids remain intact), which produces a hydrophobic environment. As the myelin lipids are digested and gliosis ensues, the tissue becomes hydrophilic, causing increased signal intensity on T2-weighted images[487]. Using magnetization transfer imaging, Lexa *et al.* demonstrated abnormalities in feline white matter within the first two weeks of degeneration, prior to the appearance of T2 changes[489].

In the last decade, there has been great interest in studying the micro-structural environment of neural tissues by measuring the anisotropic diffusion of water molecules via MRI[443]. Normally, axonal membranes and myelin pose barriers to water displacement, such that water preferentially diffuses along the direction of the axons[27]. Given that the structural integrity of the axons governs the uneven

displacement of water molecules (i.e., anisotropic diffusion), it is feasible to utilize DTI as a means to obtain information on the axonal state. As axons degenerate and break down with subsequent degradation of myelin, the barriers that normally hinder the diffusion of water across the axons disappear, allowing a more spatially uniform profile of water displacement (i.e., isotropic diffusion)[444].

Previous diffusion MRI studies have demonstrated axonal degeneration in animal peripheral[444,490] and central[21,491,492] nervous systems. There is considerable evidence showing that myelin is a barrier to water diffusion and that its degradation[23,444] or absence[20,22] causes an increase in diffusivity perpendicular to the long axis of the fibers, a phenomenon that occurs rather late in the degenerative process. This abnormal diffusion pattern, consistent with chronic degeneration, has been demonstrated in humans[445,493] and could be the underlying reason for the low diffusion anisotropy described in other series[446,494–496]. The acute phase of the degeneration, invisible to conventional MR imaging and characterized by the fragmentation of the axons, reduces the diffusivity parallel to the principal axis of the fibers, as demonstrated using animal models[21,444,497]. In a previous human study, parallel diffusivity was shown to be reduced 9 ± 4 days after stroke in the pyramidal tract, distally from the primary lesion[498]. However, to our knowledge, a prospective study examining the time course of the full diffusion tensor after axonal injury has not been performed in humans.

Corpus callosotomy is a palliative surgical procedure performed in epilepsy patients with disabling seizures that do not respond to medication. During the surgery, the corpus callosum (typically the anterior two thirds) is transected in order to prevent the spread of epileptic activity from one hemisphere to the other and thus limit the generalized manifestation of seizures[499]. The well-localized nature of the lesion, as well as the complete transection of the tract by corpus callosotomy, serves as a unique opportunity to study the evolution of axonal degeneration in-vivo in a single white matter tract of considerable dimensions, as compared to its pre-surgical state.

The objectives of this study were:

i) to assess the pattern and time course of water diffusion during degeneration of axons in a large white matter bundle, and

ii) to relate the diffusion abnormalities with the known underlying stages of axonal degeneration in the human brain.

8.2 Subjects and methods

Approval of the research protocol was obtained from the University of Alberta Health Research Ethics Board and informed consent was obtained from all participants.

8.2.1 Subjects

Three patients with medically intractable epilepsy, with the predominant seizure pattern being drop attacks, as well as one healthy individual (27 years old), were included in the study. Drop attacks are characterized by sudden loss of control over muscle tone (either tonic or atonic), which causes the individual to abruptly fall to the ground.

Patient 1 40 year old woman, suffered tonic drop attacks and underwent investigation and subsequent left frontal lobe resection in 1995, which provided little clinical improvement. Clinical MRI demonstrated the left frontal cavity secondary to her prior surgery without any other obvious abnormalities. EEG-video telemetry failed to demonstrate localized or lateralized ictal or interictal epileptic abnormalities. She was studied with our imaging protocol one week before surgery, and 9, 47 and 120 days following the intervention.

Patient 2 33 years old male who suffered atonic drop attack seizures. Clinical MRI, ictal SPECT and EEG-video telemetry failed to lateralize or localize the patient's epileptic focus. He was imaged for the present study at days -7, 6 and 95 from surgery.

Patient 3 54 years old male presented with atonic drop attacks. His clinical MRI showed a large regional malformation of cortical development (polymicrogyria) of the left central region that was not considered amenable to surgical resection. He was imaged at days -7, 8 and 60 relative to callosotomy.

The three patients underwent surgery in which the anterior two thirds of the corpus callosum were bisected using a para-sagittal approach. The first post-operative DTI data sets were obtained as soon as surgical staples were removed (6-9 days). At one year clinical follow-up, all patients had experienced a dramatic improvement in seizure control. Our healthy control was also imaged three times at two month intervals to ensure reproducibility of the diffusion measurements.

8.2.2 Image acquisition

DTI was performed on a 1.5 T Siemens Sonata using a single-shot EPI-based sequence (63 slices, 2 mm thickness with no inter-slice gap; TR=10 s, TE=88 ms; 6 diffusion directions, b=1000 s/mm^2; 8 averages; 128×128 matrix, partial phase Fourier=6/8, zero-filled to 256×256; FOV=256×256 mm^2, acquired voxel size: 2×2×2 mm^3, interpolated to 1×1×2 mm^3; scan time=9:30 min). We also acquired standard and cerebral-spinal fluid (CSF)-suppressed (FLAIR) T2-weighted fast spin echo images (voxel size = 0.7×1×5 mm^3; TR/TE/TI = 5850/99/0 ms and 7450/94/2400 ms, respectively).

8.2.3 Image processing and data analysis

Diagonalization of the diffusion tensor yielded three eigenvalues (λ_{1-3}) and eigenvectors that provided the three-dimensional information about the diffusivity of water molecules per voxel[28]. The largest eigenvalue (i.e., λ_1) is equivalent to the diffusivity parallel to the principal axis of the fibers ($\lambda_\parallel$), while perpendicular diffusivity is expressed as $\lambda_\parallel = (\lambda_2 + \lambda_3)/2$. Two important diffusion parameters are derived from the eigenvalues, namely the mean apparent diffusion coefficient (ADC, eq. 2.10), which is the average of the three eigenvalues and represents the bulk diffusivity of water molecules, and fractional anisotropy (FA, ranging from

zero to one; eq. 2.13), a normalized ratio of diffusion directionality. All the quantitative diffusion maps were generated in DTIstudio (Johns Hopkins University).

Each patient's non-diffusion weighted images (i.e., $b = 0$ s/mm^2) acquired prior to surgery served as a template to which their corresponding post-operative images were linearly co-registered and re-sliced using SPM2[500]. The image transformations were extended to the quantitative diffusion measurement maps (i.e., FA, ADC, $\lambda_{\parallel}$ and $\lambda_{\perp}$).

The genu, body and splenium of the corpus callosum were depicted (subdivisions 2, 4 and 7, respectively, according to Witelson *et al.*[501]) using tractography, a novel computational technique in which fiber bundles are reconstructed three-dimensionally according to DTI data (Figure 8.1). Tractography was performed on the pre-operative DTI data sets using the fiber assignment by continuous tracking (FACT) algorithm[55]. The fiber tracking algorithm began in all voxels with an FA higher than 0.25. The tracts propagated according to the principal eigenvector until a voxel with an FA value <0.25 was reached or if the tract deviated by more than 70° between adjacent voxels. In order to perform the "virtual dissection" of the callosal portions, the computed tracts had to intersect two large, user-defined regions drawn manually on the 2D images. The first region was located on the mid-sagittal slice for the three portions of the corpus callosum studied, while the second was located on the frontal pole on a coronal slice, the white matter roughly underlying the motor cortex in an axial slice, and the occipital pole in a coronal slice, for the genu, body and splenium, respectively. Tractography of the genu in Patient 1 was performed slightly more posterior than in the other cases, in order to avoid the pre-existing surgical resection of the left frontal lobe.

The tracts obtained from the pre-operative DTI data sets were used to extract quantitative parameters from the pre-operative and the registered post-operative diffusion maps. In order to avoid measuring areas of very low diffusion anisotropy post-operatively, such as the CSF taking the space the corpus callosum occupied prior to the surgery, voxels that had an FA value below 0.25 in any of the images were not considered for analysis in any of the data sets from that subject.

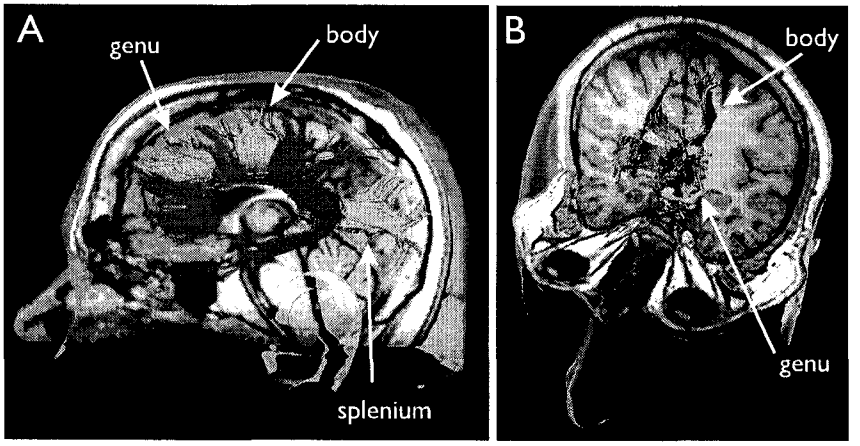

FIGURE 8.1: **Diffusion tensor tractography of the corpus callosum prior to corpus callosotomy.** A: The full extent of the corpus callosum of Patient 2 was depicted using tractography on the pre-operative DTI data set and is shown overlaid on a mid-sagittal, high-resolution, T1-weighted image. The genu, body and splenium of the corpus callosum were virtually dissected and further analyzed (highlighted in orange). B: The genu and body of the corpus callosum are shown overlaid on a coronal slice in a three-dimensional view similar to the one used in Figures 8.2 to 8.5.

8.2.4 Quantitative analysis

1 The diffusion measurements of the portions of the tracts within ± 20 mm from the midline were averaged to obtain summary data (voxels with FA <0.25 at any time point were not analyzed in any of the data sets). This region was most affected following surgery, with diffusion abnormalities becoming less evident further away from the lesion. As can be seen in Figures 8.2 and 8.3 and Table 8.1, registration and re-slicing of the diffusion maps introduced little variation in repeated measurements of healthy tracts. In our control subject, the three portions of the corpus callosum, measured at three time points, showed an average coefficient of variability in FA, ADC and $\lambda_{\parallel}$ of 1%, while that of $\lambda_{\perp}$ was 4%. Overall, the body of the corpus callosum showed the smallest variability in our control subject (FA varies by 1%), while the genu and splenium showed variations in FA of 2%.

2 In order to look at the spatial distribution of diffusion parameters along the tracts, we used an in-house program to extract quantitative parameters

from the diffusion maps and non-diffusion weighted images, sampled and averaged at 1 mm intervals along the tracts as they propagated away from the midline.

3 The signal intensity on the non-diffusion weighted images ($b = 0$ s/mm^2), being heavily T2 weighted, was used to assess T2 changes over time. In order to account for scanner variability in different imaging sessions, the tissue T2 signal intensity of each voxel was normalized to the CSF signal. CSF signal was defined as the mean T2 signal of those voxels with an ADC value >2.0 $\times 10^{-3}$ mm^2/s. As with diffusion parameters, the portions of the tracts that were replaced with CSF after the transection were not analyzed.

8.3 Results

Since the corpus callosum does not function as a structural component holding the two sides of the brain together, displacement of the remnant fibers is not expected, making linear registration an adequate tool that aids the analysis of serial observations performed on the same subject. Thus, this method yields reproducible results (Table 8.1, Figures 8.2and 8.3). It is also clear from Figure 8.2,A-C that diffusion parameters vary along the length of the healthy corpus callosum at different distances from the midline, due to the gradual spreading of fibers, as well as the encounter with different fiber populations with varying orientations (fiber crossing).

8.3.1 Qualitative visualization of diffusion changes

As expected, visual inspection of the color-coded tracts showed minimal changes of diffusion parameters of the splenium of the corpus callosum (not transected during surgery), as compared to their pre-operative state (Figure 8.2,D-F), which provides evidence to support the reliability of the coregistration process. In contrast, we observed a dramatic decrease in diffusion anisotropy present at one week following surgery in the body and genu of the corpus callosum in all pa-

	Genu			Body			Splenium		
	first scan	+2 months	+4 months	first scan	+2 months	+4 months	first scan	+2 months	+4 months
FA	0.75	0.73	0.72	0.68	0.68	0.67	0.83	0.80	0.80
ADC ($\times 10^{-3}$ mm^2/s)	0.73	0.74	0.74	0.75	0.73	0.75	0.74	0.74	0.75
$\lambda_{\parallel}$ ($\times 10^{-3}$ mm^2/s)	1.56	1.55	1.52	1.48	1.44	1.47	1.70	1.65	1.67
$\lambda_{\perp}$ ($\times 10^{-3}$ mm^2/s)	0.32	0.35	0.34	0.38	0.38	0.39	0.26	0.29	0.30

TABLE 8.1: **Diffusion parameters in a healthy control.** Average diffusion measurements of fractional anisotropy (FA), mean diffusivity (ADC), parallel diffusion ($\lambda_{\parallel}$) and perpendicular diffusion ($\lambda_{\perp}$) along the tracts within $\pm$20 mm from midline. Diffusion parameters for the control subject show minimal variability with repeated measurements.

tients (Figure 8.4,A-C). Furthermore, FA measurements remained low or continued to decrease at 2-4 months in the genu and body of the corpus callosum. The mean diffusivity was unchanged or slightly decreased in the genu and body of the corpus callosum at one week, with a pseudo-normalization or increase at 2-4 months (Figure 8.4,D-F). $\lambda_{\parallel}$ showed a noticeable decrease at one week, with pseudo-normalization at 2-4 months in all the transected tracts (Figure 8.5,A-C). On the other hand, $\lambda_{\perp}$ was slightly increased at one week, but showed a dramatic increase at two to four months in all the affected tracts (Figure 8.5,D-F). It is important to note that the most dramatic changes in diffusion measurements were seen in the areas closest to the resection, suggesting a centrifugal spread of the abnormalities. The data obtained from patient 1 at 47 days following surgery (data not shown) showed similar findings to those at 4 months.

8.3.2 Quantitative assessment of diffusion parameters

Analysis of the average diffusion measurements from the sections of the tracts within $\pm$20 mm from the midline showed a similar pattern as that seen qualitatively (Figure 8.6). As anticipated, the splenium of the corpus callosum (not transected) showed variability similar to that seen in our control subject, with coefficients of variation of FA equal to 3, 4 and 2% for Patients 1 to 3, respectively. Conversely, in all patients the genu and body of the corpus callosum showed a considerable decrease in diffusion anisotropy one week after surgery relative to

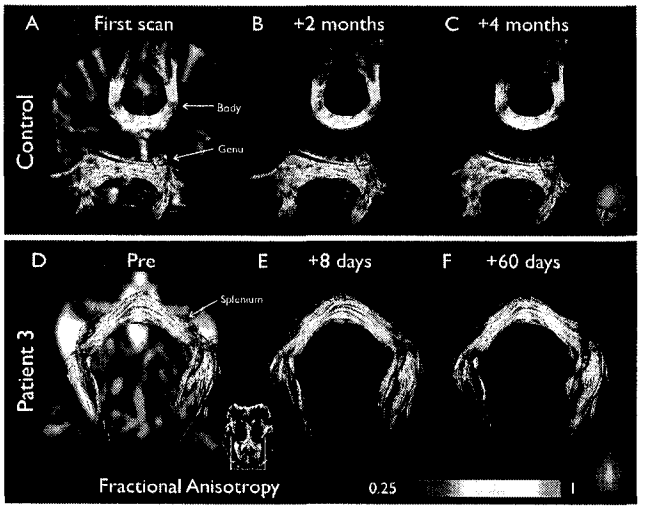

FIGURE 8.2: **Diffusion measurements obtained at three time points in non-affected tracts.** The genu, body and splenium of the corpus callosum were depicted on a healthy volunteer (A-C) on three occasions, at two-month intervals (splenium not shown). Notice that diffusion measurements show very little variation throughout time, as expected in a healthy individual. The splenium of the corpus callosum in Patient 3 (D-F), which was not transected during surgery, was depicted using tractography on the pre-surgery data set and overlaid on the registered quantitative diffusion maps obtained post-operatively at 8 and 60 days. As expected, there is little variation in FA measurements throughout time, as compared to the pre-operative values.

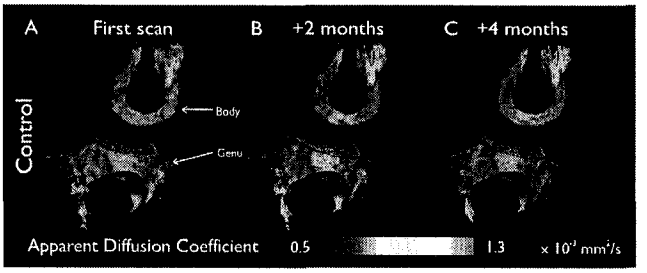

FIGURE 8.3: **Mean diffusivity of the corpus callosum in a healthy individual.** The genu and body of the corpus callosum are color-coded according to the mean apparent diffusion coefficient (ADC) as measured at two-month intervals. There is very little variation in diffusivity over time. The areas of high diffusivity in the midline, clearly evident in the genu, likely correspond to cerebral spinal fluid pulsation artifacts, as cardiac gating was not employed in this study. The inferior portion of the body of the corpus callosum also showed the same artifact, but is not evident from this viewing angle. These artifacts do not affect our findings, as these areas are at the transection site and thus were not analyzed.

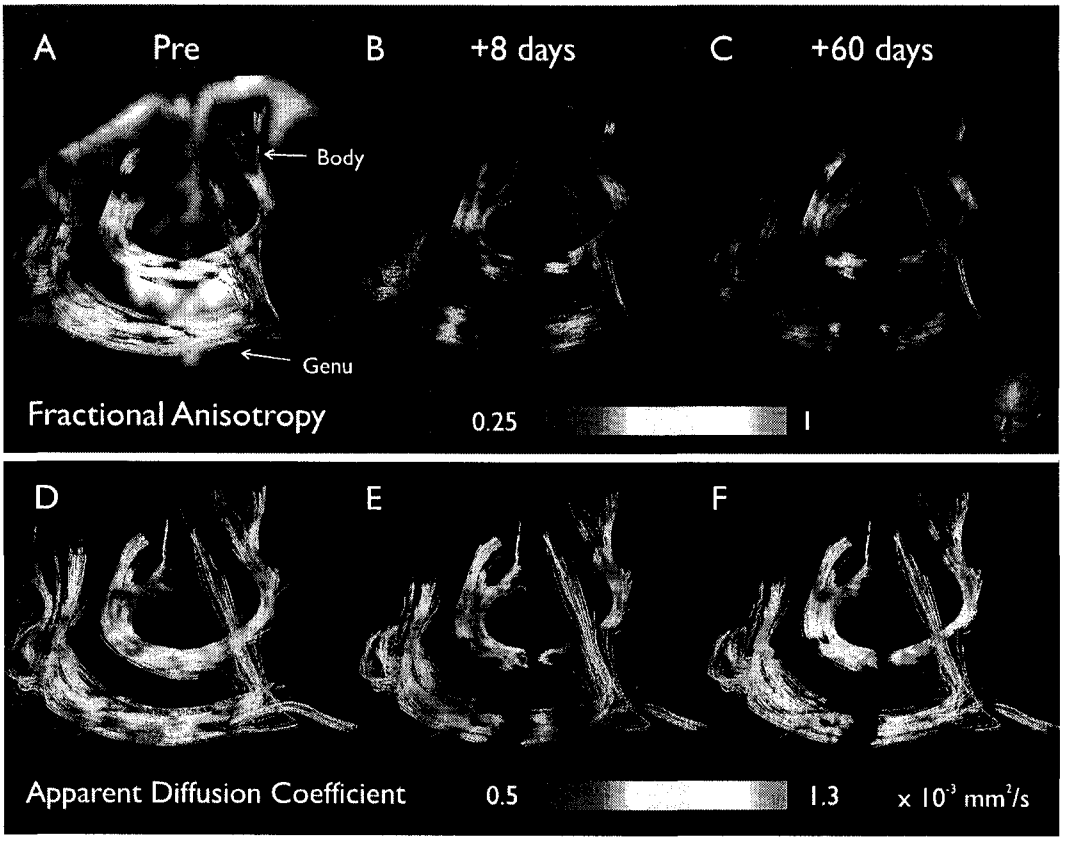

FIGURE 8.4: **Diffusion anisotropy and mean bulk diffusivity changes due to axonal degeneration following corpus callosotomy.** The genu and body of the corpus callosum of Patient 3 were depicted using tractography on the pre-surgical DTI data sets (Pre) and overlaid on their registered quantitative diffusion maps obtained at one week and two months following corpus callosotomy. In both white matter structures, FA values have decreased considerably at one week and remain low at two months (A-C). The mean apparent diffusion coefficient (D-F) shows a slight decrease at one week, followed by an increase at two months. Recall that any segment of the tracts with an FA <0.25 at any time point was excluded for analysis in all the time points, in order to avoid measuring cerebro-spinal fluid filling the space previously occupied by the tracts at the bisection site. For this reason, the post-operative tracts appear truncated near the midline. For clarity purposes, these segments are shown in the pre-operative tracts (A and D). The same pattern of changes was seen for the other two patients.

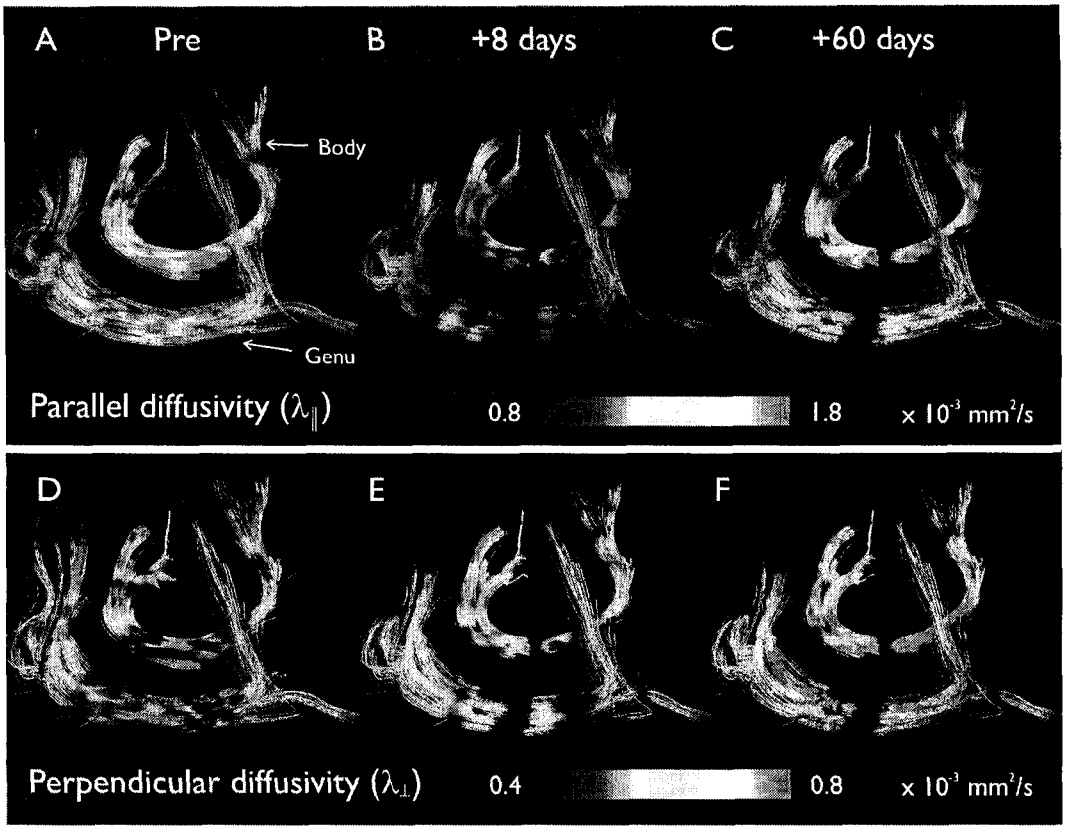

FIGURE 8.5: **Parallel and perpendicular diffusivity before and after corpus callosotomy.** The diffusivity of water molecules parallel to the direction of the tracts (i.e., $\lambda_\parallel$, A-C) in Patient 3 shows a considerable reduction at one week following surgery (as compared to its pre-surgical state) and nearly returns to baseline at two months. The sharp decrease in $\lambda_\parallel$ seen at one week is consistent with the axonal fragmentation occurring at this stage of axonal degeneration. The diffusivity of water perpendicular to the principal direction of the tracts ($\lambda_\perp$, D-F), on the other hand, appears only slightly increased at one week, but shows a dramatic increase two months following the transection of the axons. Such an increase of $\lambda_\perp$ is consistent with the degradation of myelin, which occurs late in the evolution of Wallerian degeneration in the central nervous system. Similar findings were seen for the other two patients.

their pre-operative values (reduced by 33±6%, range: 27 to 41%). These two portions showed a further decrease in anisotropy at 2-4 months (reduced by 44±7%, range: 34 to 53%). The affected portions (i.e., genu and body) also showed an initial decrease in $\lambda_{\parallel}$ at one week in all patients, which at 2-4 months showed a trend towards pseudo-normalization in 5/6 tracts (the callosal body of Patient 1 showed an increased $\lambda_{\parallel}$ relative to its pre-operative value). Perpendicular diffusivity (i.e., $\lambda_{\perp}$) showed a progressive increase in the affected tracts of all patients, with the most marked increase occurring at 2-4 months. Therefore, although FA reductions were seen as soon as one week after the surgery and remained low at the subsequent time points, the mechanisms driving such decreases were different: namely, a decrease in $\lambda_{\parallel}$ is largely responsible at one week, whereas an increased $\lambda_{\perp}$ and a near-normal $\lambda_{\parallel}$ are accountable for the low FA at 2-4 months.

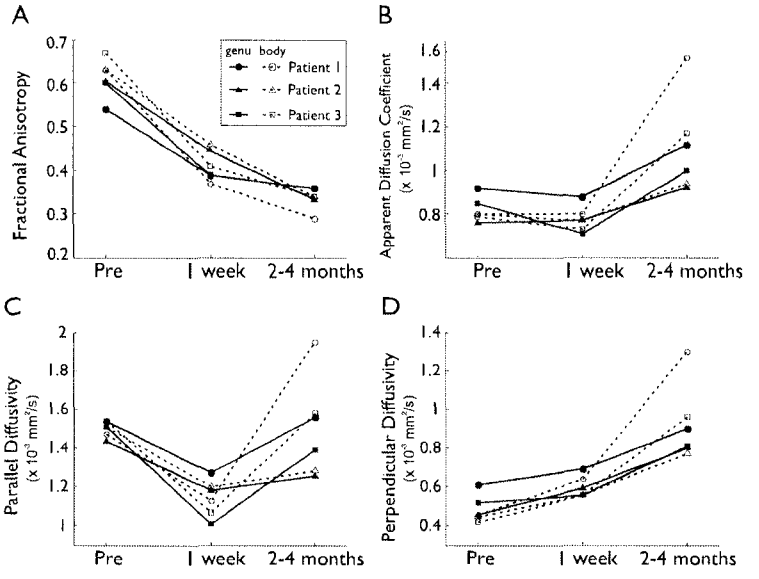

FIGURE 8.6: **Diffusion parameters in the transected genu and body of the corpus callosum.** Average diffusion measurements along the tracts within ±20 mm from the midline. Fractional anisotropy (FA) shows a marked decrease at one week following surgery, accompanied by nearly normal bulk diffusivity (ADC). Reduction in FA at this time point is due to a reduction in parallel diffusivity ($\lambda_{\parallel}$), with only a slight increase in perpendicular diffusivity ($\lambda_{\perp}$), consistent with axonal degradation. At 2-4 months post-surgery, ADC is elevated and FA shows a further decrease; however, the FA decrease is now due to a marked increase in $\lambda_{\perp}$, consistent with myelin degradation, and a pseudo-normalization of $\lambda_{\parallel}$.

Analysis of diffusion measurements in the genu and body of the corpus callosum along the tracts as they propagated away from the midline in the pre-operative state and in the control subject showed a pattern of diffusion anisotropy similar to the one reported in a healthy subject by Mori *et al.*[426]. Following transection, the tracts showed a centrifugal spread of diffusion changes, with larger differences to the pre-operative values in the areas closest to the lesion (Figure 8.7). Indeed, the portions of the tracts within the surgical lesion itself showed post-operative FA values below 0.25, indicating fluid filling the resection area (these portions were not analyzed).

We did not observe any hypo-intensities on the FLAIR T2-weighted images either at one week or two to four months following surgery in the white matter containing the surgically transected callosal fibers. On the contrary, increased T2 signal was evident immediately adjacent to the transection at one week, but this hyper-intensity was not apparent at 2-4 months. However, the white matter distal to the transection did not show T2 signal abnormalities (neither reduced nor increased) at any time point following the lesion. In Patient 1, in which a pre-existing lesion existed (i.e., left frontal lobectomy performed 10 years prior to our study), the remaining frontal white matter, belonging partly to the genu, as well as the contralateral white matter, showed areas of obvious signal hyper-intensity at all time points.

We qualitatively assessed CSF-normalized T2 signal changes over time using the non-diffusion weighted ($b = 0$ s/mm^2) EPI images (Figure 8.8). Similarly to what we observed on the FLAIR T2-weighted images, a slight increase in T2 signal at one week is evident in the portions of the transected tracts that are immediately adjacent to the lesion. However, the extent of the T2 signal changes is more restricted to the midline, as compared to the changes seen in the diffusion parameters. At 2-4 months, much of the hyper-intense T2 signal within the tracts appears to have resolved. The residual hyper-intensities are not as widespread as the dramatic changes in the diffusion parameters (Figures 8.4 and 8.5).

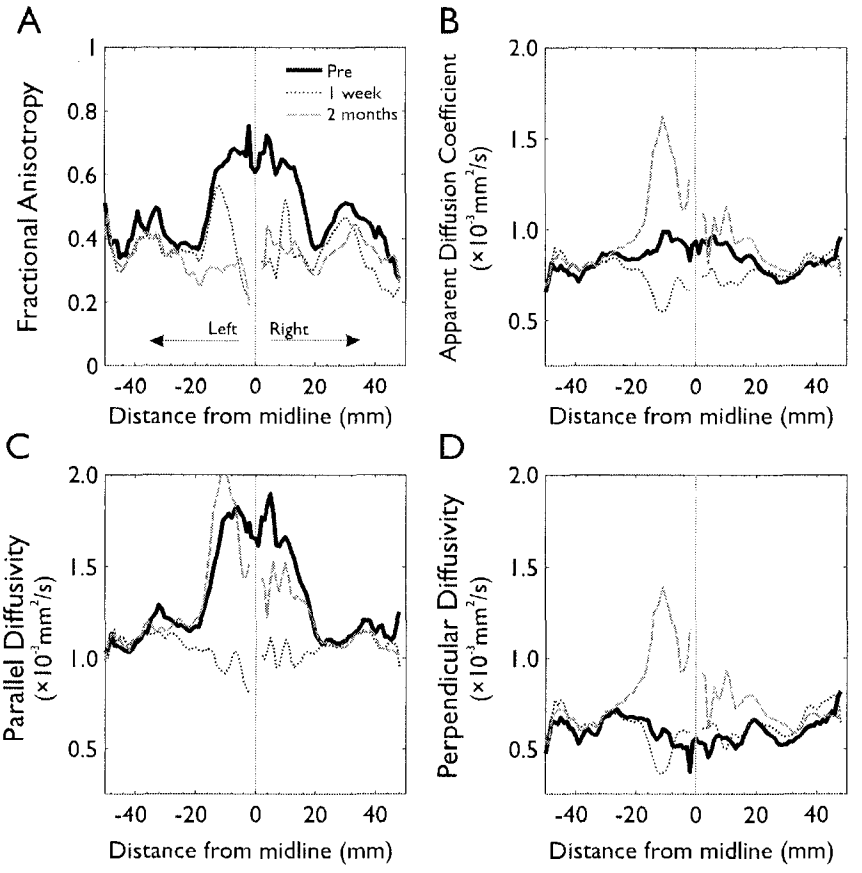

FIGURE 8.7: **Diffusion measurements along the genu of the corpus callosum before and after corpus callosotomy.** The genu of the corpus callosum depicted in the pre-operative data set from Patient 3, served as a path through which the pre- and post-operative diffusion measurements were sampled at 1 mm intervals as they propagated away from the lesion. The reason for the discontinuity of the plots near the midline is that voxels with an FA value <0.25 at any of the time points were presumed to be fluid (i.e., complete degradation) and were not included for analysis. While FA shows a decrease as soon as one week after surgery and it is further decreased by two months (A), the mechanisms underlying the FA reductions are different for each time point. At one week after surgery, $\lambda_{\parallel}$ shows a marked decrease (C) with a nearly normal $\lambda_{\perp}$ (D), whereas at two months after surgery, $\lambda_{\parallel}$ appears nearly normal (C), but $\lambda_{\perp}$ shows a considerable increase (D). The pseudo-normalization of $\lambda_{\parallel}$, along with an increase of $\lambda_{\perp}$, cause an overall increase in the mean bulk diffusivity (i.e., ADC) at two months (B). The most marked changes of diffusion parameters occur in the regions closest to the surgical lesion (particularly within the first $\pm$20 mm), suggesting a centrifugal spread of diffusion abnormalities (and presumably axonal degeneration).

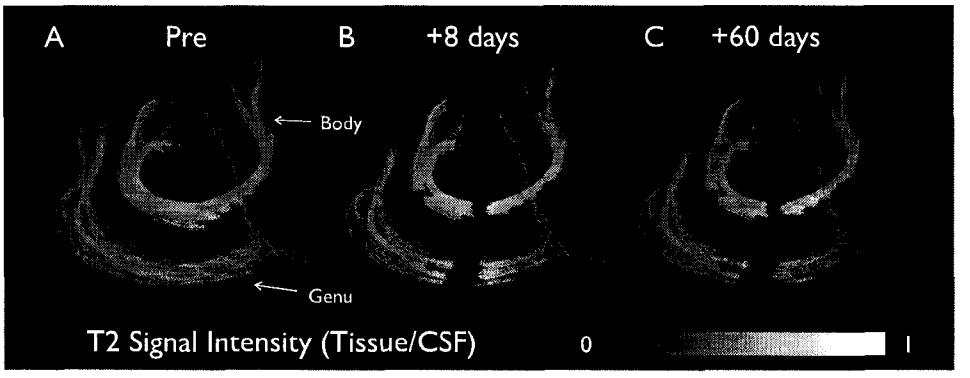

FIGURE 8.8: **Signal intensity changes after corpus callosotomy.** The genu and body of the corpus callosum are color-coded according to the T2 signal intensity of the coregistered non-diffusion weighted EPI images (i.e., $b = 0\,s/mm^2$), normalized by the signal intensity of cerebral-spinal fluid. Signal hyper-intensity is visible only in the regions immediately adjacent to the lesion at one week following surgery in Patient 3 (B), which likely represents edema due to surgical manipulation. Much of the T2 signal hyper-intensity in the genu, and less so in the body, resolves 60 days after surgery (C). Notice, however, that the T2 signal changes do not extend as far along the tracts as the diffusion parameter changes seen in Figures 8.4 and 8.5.

8.4 Discussion

Axonal degeneration is characterized by a series of simultaneous events. Approximately 30 minutes from the time of the lesion, the axons undergo centrifugal disintegration of the cytoskeleton, which produces sudden and rapid fragmentation of the axons[485,502]. This stage is short-lived, lasting from several hours to days, depending on the species, length and diameter of the axons, the temperature of the tissue and the location of the fibers[503]. Simultaneous to the cytoskeletal degradation, the myelin sheaths that surround the axons become less tightly wrapped, and eventually break apart and form ovoids[502]. A couple of weeks following the precipitating injury, the microglia are activated and digest the axonal and myelin debris. Myelin phagocytosis in the CNS can last for months, and even years[484], while formation of new myelin is almost non-existent, due to the apoptosis of oligodendrocytes in the first few weeks following injury[504]. In the peripheral nerve, in contrast, digestion of the debris is performed by circulat-

ing macrophages, while Schwann cells re-myelinate regenerating axons and the fragmented axons reconnect[486,505].

The first stages of axonal degeneration in the CNS are virtually invisible using conventional MRI. Previous reports have documented T2 signal hypo-intensity four weeks after the precipitating injury[487,488]. In our present study, however, the only surgery-related T2 signal changes observed one week following the surgery, were hyper-intensities immediately adjacent to the lesion (Figure 8.8). We believe these signal changes were not directly related to axonal degeneration, but to tissue edema caused by surgical manipulation as these T2 hyper-intensities mostly resolved by 2-4 months. Using DTI measurements as surrogate markers of axonal state, the early stages of degeneration are clearly visible both qualitatively and quantitatively in regions distant to the precipitating injury, where neither edema nor inflammation is expected to occur.

Our study after complete surgical axonal transection confirms previous reports in patients with stroke that reduction in diffusion anisotropy following axonal injury precedes T2 signal changes[498]. We observed reduction of diffusion anisotropy as soon as one week following surgery, accompanied by nearly pseudo-normal bulk diffusivity (i.e., ADC). Whether or not such diffusion changes could have been detected earlier is unknown, since the patients included in this study were not imaged before one week due to the presence of surgical staples. At subsequent time points, diffusion anisotropy showed a further reduction, while an increase in ADC was evident.

As demonstrated using an in-vitro model of Wallerian degeneration in frog sciatic nerve, axonal and myelin degeneration causes a decrease in diffusion anisotropy due to reduced $\lambda_{\parallel}$ and increased $\lambda_{\perp}$[444]. Myelin has been shown to modulate perpendicular diffusivity[20,23,506], although it is not the only factor involved[18]. In a mouse model of retinal ischemia, Song *et al.*[21] performed serial diffusion measurements of the optic nerve and showed that $\lambda_{\parallel}$ and $\lambda_{\perp}$ can differentiate axonal from myelin damage during the course of degeneration. According to this animal model, $\lambda_{\parallel}$ shows a significant decrease in the first days of degeneration, which corresponds to the disintegration of the axonal microstructure, while

myelin remains intact. Five days after the initial injury $\lambda_\perp$ increased, which corresponds to the degradation of myelin sheaths. Likewise, using an ex-vivo animal model of spinal cord injury, Schwartz *et al.* demonstrated significantly increased $\lambda_\perp$ 14 weeks after the injury, accompanied by reduced $\lambda_\parallel$[491]; as in our study, these diffusion abnormalities were more severe closer to the injury.

Increases of $\lambda_\perp$ have been shown in chronically degenerated white matter bundles in humans[445,493]. It is very likely that such an increase in $\lambda_\perp$ drives the reduction in diffusion anisotropy demonstrated in other human studies of axonal degeneration in the chronic stage[446,494–496]. Thomalla *et al.* reported significant reductions in $\lambda_\parallel$ in the pyramidal tract within the first 16 days after onset of stroke[498], corresponding to the acute phase of axonal degeneration, namely the fragmentation and dying-back of axons. In the former study, there is also a slight increase in $\lambda_\perp$, suggesting a transition between the acute and chronic phases described above.

Examination of the eigenvalues yields interesting and clinically relevant information on the underlying causes of reduced anisotropy. In our study, a reduction in $\lambda_\parallel$ was observed one week following corpus callosotomy. At this stage of degeneration, the axons break up into small fragments of approximately 17 μm in length, as demonstrated in a model of living transgenic mice[485]. The dimensions of these fragments in human brain are not known. The fragmentation of axons creates barriers to the longitudinal displacement of water molecules and, thus, a decrease of $\lambda_\parallel$. On the other hand, the obstacles to radial diffusivity (namely, the axonal membrane and myelin) remain relatively intact in the acute phase, as demonstrated by the small increase in $\lambda_\perp$ at one week. As the myelin sheaths fall apart and axonal membranes become further degraded, water molecules become more mobile perpendicular to the axons, resulting in an increase of $\lambda_\perp$. Consistent with this phenomenon, we observed a marked increase of $\lambda_\perp$ in the genu and body of the corpus callosum during the chronic stages of degeneration (which was not as striking in the first week following surgery). In addition to the myelin degradation and subsequent increase in $\lambda_\perp$, the axonal fragments are cleared, al-

lowing the water molecules to once again diffuse in the longitudinal direction, normalizing or even increasing $\lambda_{\parallel}$.

Our serial observations in patients undergoing a highly selective surgical lesion within a major white matter tract (the corpus callosum) demonstrate an excellent temporal relationship between DTI changes and the expected underlying histological processes (i.e., decreased $\lambda_{\parallel}$ at one week when axonal degradation is expected and elevated $\lambda_{\perp}$ at two months when myelin degradation is expected). These findings suggest that analysis of the full diffusion tensor can provide a measure not only of the structural integrity but also an indication of the timing of injury and the underlying histological processes following injury to central nervous system white matter tracts. Diffusion-weighted images, ADC and FA maps individually are not sufficient to differentiate axonal versus myelin degeneration[21,24].

8.5 Conclusions

Although the sample size in our present study is small, the changes in diffusion parameters due to axonal degeneration were marked, while they were practically non-existent in the repeated measurements of non-transected tracts. Corpus callosotomy is a procedure performed rather infrequently, due to its palliative nature and restricted indications. However, the precise bisection and the long callosal remnants identified with tractography provide an opportune human situation for the serial characterization of axonal and myelin degeneration. The present study demonstrates that analysis of the full diffusion tensor provides reliable and useful information on the stages of axonal degeneration in a non-invasive manner using widely available methodology. Accurate information about the state of white matter bundles affected by disease or trauma is likely to prove valuable for prognostic and therapeutic purposes.

⋆ ⋆ ⋆

8.6 Appendix

Despite the fact that there were no visible T2 hyper-intense regions even at 2-4 months after corpus callosotomy, there were significant correlations between the degree of change of T2 signal and diffusion parameters, with respect to baseline (Figure 8.9). In order to compensate inter-scan T2 signal variability, T2 signal intensity (SI) was defined as the ratio of the tract's signal to the signal of CSF (SI_{tract}/SI_{CSF}).

The appendix did not appear in the published version of this Chapter.

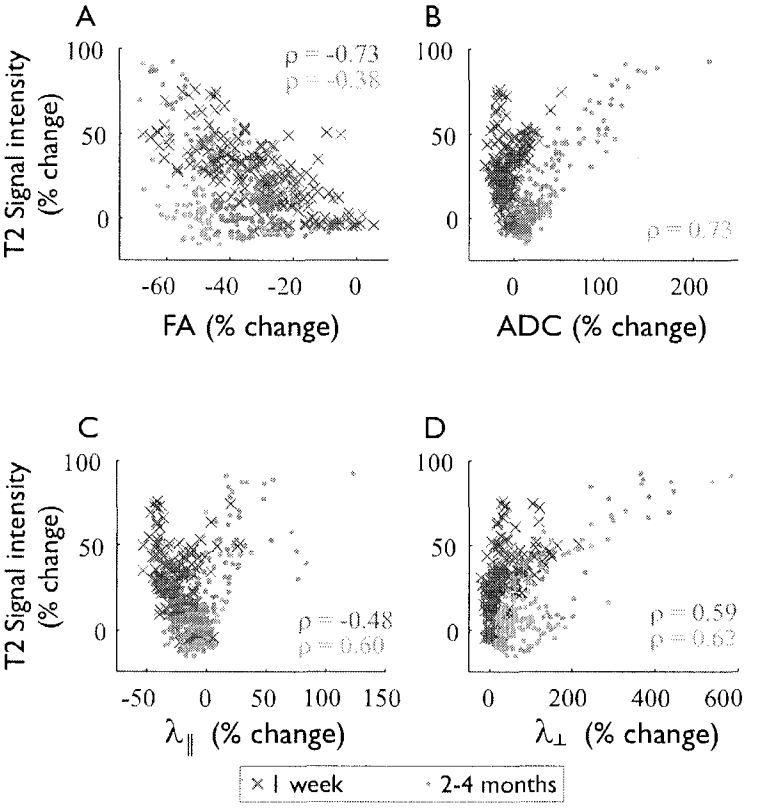

FIGURE 8.9: **Spearman's ρ correlations between diffusion measurements and T2 signal intensity of the genu and body of the corpus callosum in three patients.** While at one week after surgery diffusion anisotropy strongly correlates with T2 signal changes, at 2-4 months there are a greater number of regions with considerably decreased FA that do not show increased T2 signal (FA, A). Diffusivity parallel to the tract ($\lambda_{\parallel}$, C) is negatively correlated with T2 signal intensity changes at one week, while at 2-4 months the direction of this correlation is reversed. The changes seen in T2 signal are of several times less magnitude than those seen in perpendicular diffusivity at 2-4 months ($\lambda_{\perp}$), D) These findings show the enhanced sensitivity of diffusion parameters to detect and follow the degenerative process. Only significant correlations are shown ($p<0.0001$). The points represent the values from those voxels within the tracts.

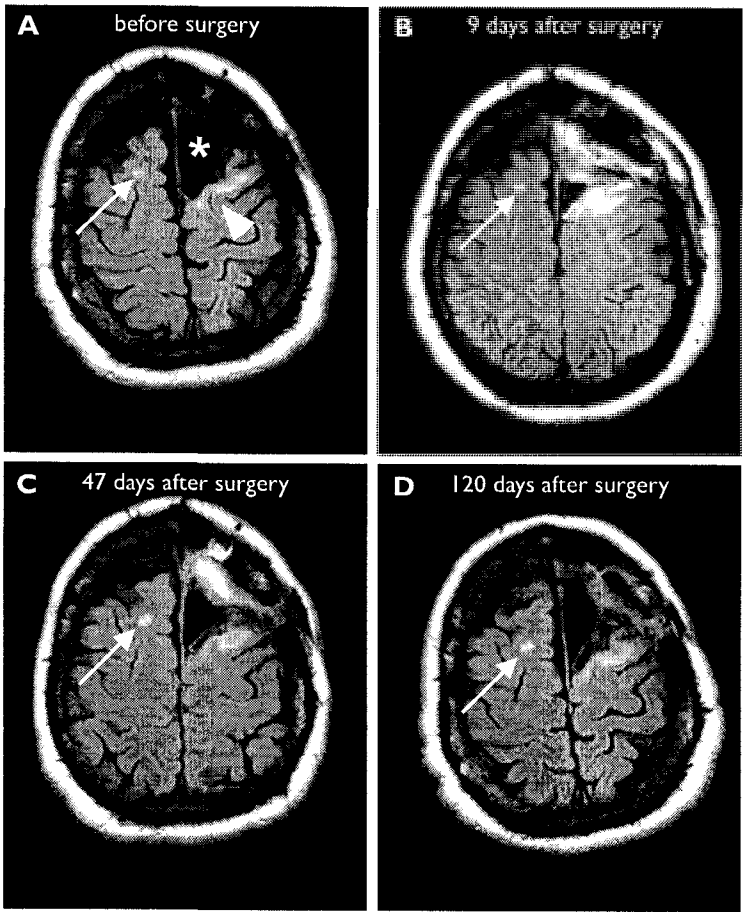

FIGURE 8.10: **Chronic T2 changes in Wallerian degeneration.** Representative CSF-suppressed T2-weighted axial slices of Patient 1. This particular patient had a history of a previous left frontal lobectomy several years prior to the corpus callosotomy (*). As can be seen in the pre-operative scan (A), obvious signs of Wallerian degeneration are present. The arrowhead in A points to the peri-lesional white matter hyper-intensity consistent with Wallerian degeneration. The Arrow on the contralateral side shows an obvious hyper-intensity presumed to represent chronic Wallerian degeneration of inter-hemispheric fibers. Both signs are present in the post-operative scans. In contrast, T2 signal hyper-intensities due to corpus callosotomy are not seen at this level even 120 days following surgery.

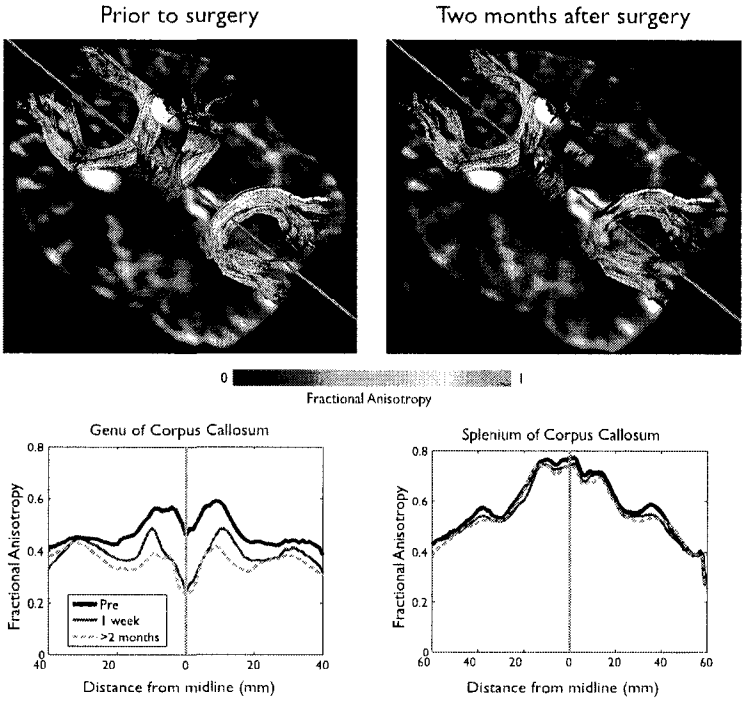

FIGURE 8.11: **FA changes following corpus callosotomy in Patient 2.** Similarly to Patient 3 (shown in Figure 8.4 and Patient 1 (not shown), there is a marked decrease in FA of the genu and body of the corpus callosum following surgery, while the splenium (not transected) shows minimal change over time. The red line shows the position of the midline, and the white curved line in the images shows a 50 mm path along the genu of the corpus callosum, for reference.

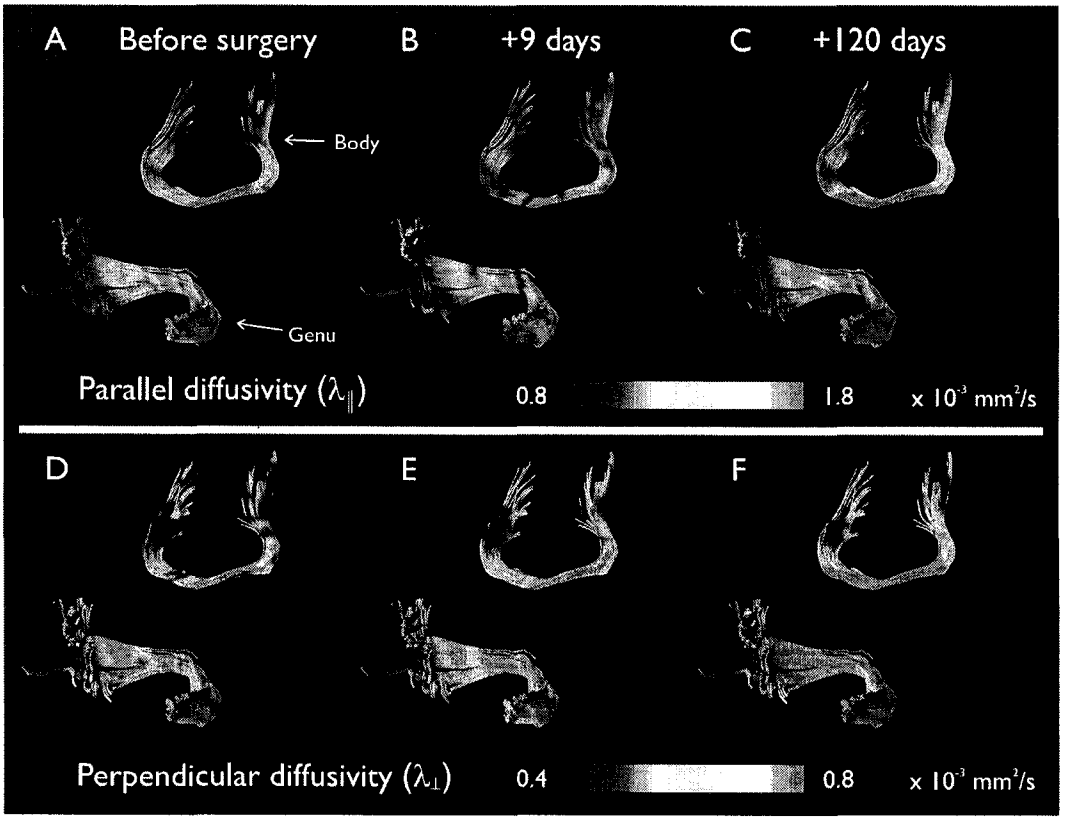

FIGURE 8.12: **Changes of $\lambda_{\parallel}$ and $\lambda_{\perp}$ following corpus callosotomy in Patient 1.** As with Patient 3, there is a decrease of $\lambda_{\parallel}$ in the genu and body of the corpus callosum at one week after surgery. Perpendicular diffusivity ($\lambda_{\perp}$) shows a marked increase at 2-4 months after surgery. The resection in the midline is not shown.

Chapter 9

Relationship of DTI parameters and histology of the fornix

Abstract

While direct correlations between diffusion tensor parameters and histology have been performed in animal models, a direct comparison between DTI and histology has not been performed in humans. The previously identified diffusion abnormalities of the fornix in patients with temporal lobe epilepsy and unilateral mesial temporal sclerosis have been presumed to be associated with micro-structural changes of the tissue, such as reduced axonal packing or abnormalities of the myelin sheaths. Such diffusion abnormalities are not present in patients with temporal lobe epilepsy who lack evidence of mesial temporal sclerosis. This study provides a direct electron microscopy comparison of the micro-structural characteristics of the fimbria/fornix obtained from seven temporal lobe epilepsy patients who underwent temporal lobe surgery (four of which had evidence of mesial temporal sclerosis) and who had undergone a pre-surgical DTI scan. The presence of mesial temporal sclerosis is associated with an increased extra-cellular volume and reduced axonal packing and density of the fornix, which could account for the previously demonstrated reductions of water diffusion anisotropy.

9.1 Introduction

Diffusion tensor imaging (DTI) has shown to be a sensitive technique for the detection of abnormalities of white matter in the acute and chronic settings. Based on animal models, it is generally accepted that the degree of diffusion anisotropy is caused by axonal membranes and homogeneous, ordered tissue architecture[18–20] and modulated by myelin[20–24]. The time course of axonal fragmentation and myelin degradation has been shown in a longitudinal study of patients undergoing corpus callosotomy[32] (Chapter 8), which showed an evolution of diffusion abnormalities similar to those reported in rodents[21]. In a *post-mortem* study of white human brains of patients who had multiple sclerosis, a direct relationship between myelin content and axonal density was found with diffusion anisotropy and mean diffusivity[507]. To this day, however, a direct correlation of diffusion parameters obtained *in-vivo* with *ex-vivo* quantitative microscopy has not been performed in any human subjects, either previously healthy or with any given neurological disorder.

Based on the above mentioned studies, the previously demonstrated bilateral white matter diffusion abnormalities of the fornix in patients with temporal lobe epilepsy (TLE) (Chapters 5 and 7), which do not resolve upon seizure freedom (Chapter 6), are believed to be related to specific tissue alterations. Given the reported reduction of diffusion anisotropy and increase of perpendicular diffusivity, plausible candidates for their genesis include reduced axonal packing or myelin abnormalities.

Although similar in clinical manifestations, TLE without mesial temporal sclerosis (MTS) is generally considered as a distinct epilepsy syndrome from TLE with unilateral MTS[472]. Given the hippocampal neuronal death associated with MTS (Section 3.2.3), a certain degree of degeneration of the fimbria/fornix (the principal output of the hippocampus) is expected if this lesion is demonstrated.

While much is known on the microscopic characteristics of the fimbria/fornix in the rat[162,508], reports on the microscopic morphology of this structure in humans are few and incomplete[509,510]. This study aims to perform a direct electron

microscopic comparison of the micro-structural integrity of the surgically resected fimbria/fornix between patients with TLE with and without MTS. Additionally, an attempt is made to identify the microscopic correlates of the pre-operative diffusion tensor abnormalities of the fornix in patients with MTS.

9.2 Methods

Approval of the research protocol was obtained from our institutional Health Research Ethics Board and informed consent was obtained from all participants.

Seven TLE patients were included in this study (Table 9.1). Four patients had clinical imaging evidence of unilateral MTS, which was also demonstrated using quantitative T2 mapping (Section 3.3.2). All but one of the patients with MTS were included in previous studies. The remaining patient (left MTS) had been previously excluded based on the presence of additional extra-temporal pathology. The three patients with non-lesional TLE were included in the study reported in Chapter 7. As of time of writing, official pathology reports have been received for three patients. Patient 1, without imaging evidence of MTS, lacked histopathological changes concordant with hippocampal sclerosis. Patient 2 and 3, who had imaging evidence of MTS showed the corresponding signs of Ammon's horn sclerosis and extended neuronal loss and gliosis in the mesial temporal structures.

Patient	Diagnosis	Age (y.)	Gender	Side	Hippocampal T2
1	nl-TLE	36	M	Left	109
2	TLE+MTS	57	F	Left	132
3	TLE+MTS	34	F	Left	127
4	nl-TLE	45	F	Left	106
5	TLE+MTS	36	F	Left	149
6	TLE+MTS	36	F	Left	133
7	nl-TLE	57	F	Right	114

TABLE 9.1: **Individual patient information.** Side: Side of surgical resection. The quantitative T2 measurements are shown for the hippocampus ipsilateral to the surgical resection.

Imaging and tractography Cerebro-spinal fluid suppressed diffusion tensor imaging and tractography of all subjects was performed pre-operatively in a fashion identical to the methodology presented in previous Chapters. Briefly, tractography of the crus of the fornix ipsilateral to the resection was performed with the fiber-assignment by continuous tracking algorithm[55]. The diffusion parameters of the voxels within the tract obtained were queried and averaged. Therefore, a single value per diffusion parameter was obtained in each patient.

Electron microscopy A segment of the fimbria/fornix, of approximately 1-2 mm in length, was excised by the neurosurgeon (Dr. B. Matt Wheatley, Division of Neurosurgery, University of Alberta) with the aid of a surgical microscope (Figure 9.1). The specimen was immediately rinsed in phosphate buffered saline (pH 7.6) and then immersion-fixed using 4% paraformaldehyde in 0.1M phosphate buffer (pH 7.4). The specimen was then delivered to Dr. Daniel J. Livy (Division of Anatomy, University of Alberta) within less than one hour for subsequent processing for electron microscopy. The tissue was immersion-fixed overnight in 3% paraformaldehyde, 1.5% glutaraldehyde and 0.02% $CaCl_2$ in 0.1M cacodylate buffer (pH 7.2) and postfixed with 1% OsO_4, 1.5% $K_3Fe(CN)_6$ and 0.02% $CaCl_2$ in 0.1M cacodylate buffer for four hours[511]. The tissue was stained *en bloc* in 2% uranyl acetate in 0.1M sodium acetate buffer, dehydrated through an ethanol series to 100% and rinsed in propylene oxide. The tissue sections were infiltrated with a graded series of Epon (Em-bed 812, Electron Microscopy Sciences) beginning with a 1:2 mixture of Epon and propylene oxide and ending with pure Epon for 24 hours. The tissue was then embedded with fresh Epon and allowed to cure for 48 hours at 60°C. Thick tissue sections (about 1 μm were cut using glass knives on a Reichart-Jung Ultracut E ultramicrotome and stained using Richardson's stain. Thin tissue sections (90 nm gold) were cut using a diamond knife in the same microtome. Sections obtained were mounted on 400 mesh copper grids and stained with aqueous uranyl acetate (saturated) for five min and with SatoŠs lead citrate (aq) for 1 min. Thin sections were viewed and photographed at the approximate middle of the grid pore using a FEI Morgagni transmission

electron microscope at a magnification of 3500x (Advanced Microscopy Facility, University of Alberta). Ten microphotographs were acquired using by randomly selecting grid pores while blinded to patient diagnosis. All the microphotographs were provided for further blind quantitative evaluation using a non-descriptive numerical code. Tissue quality was optimal for all patients, with the exception of Patient 7 (nl-TLE), which consisted of small specimens that made orientation for tissue processing difficult. Nonetheless, electron microscopy of such a sample was adequate for the purposes of this study.

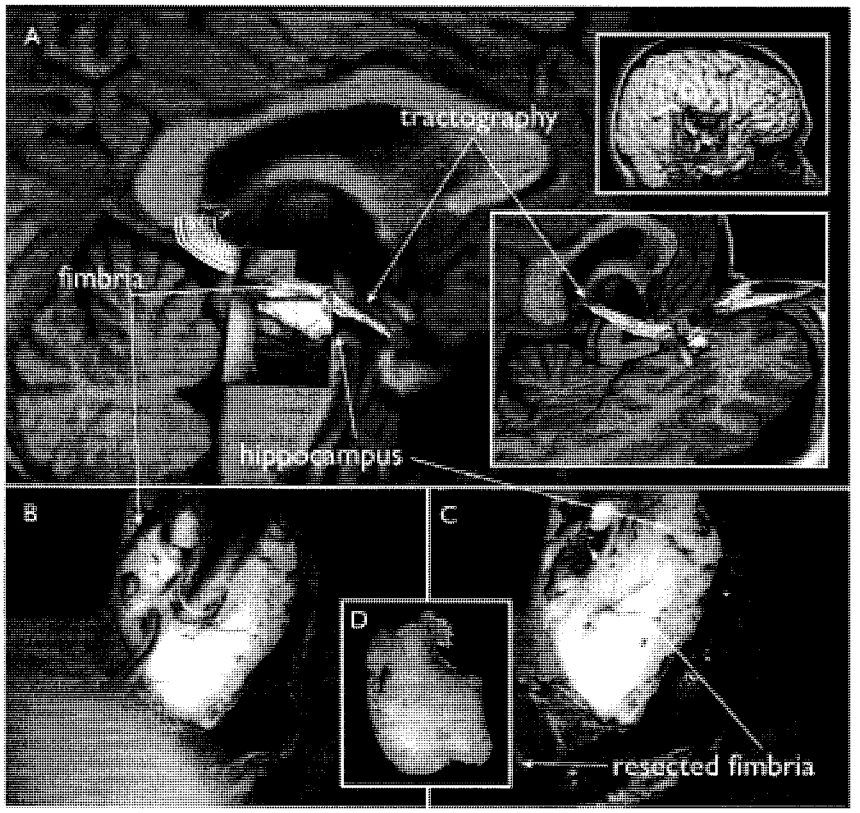

FIGURE 9.1: **Surgical resection of the fimbria/fornix.** A: Three-dimensional visualization of the right fimbria/fornix with tractography, with the corresponding intraoperative photograph overlaid Insets show the spatial orientation and relative size of the structures. B,C: Intraoperative photographs of the hippocampus and fimbria/fornix viewed through the operative microscope. D: Fixed specimen of fimbria/fornix. This particular patient was not included in the quantitative analysis.

Quantitative microscopy While still blinded to name and diagnosis of each microphotograph, a total of nine fields were excluded from further analysis, as the section through the axons was oblique. Four of these images belonged to Patient 3, four more corresponded to Patient 5 and one image to Patient 7. A stereology counting frame was placed within the microscopic field at 234 nm from its edges. The number of axons was manually estimated using an unbiased counting approach (Figure 9.2). Additionally, the inner and outer diameter of the axons were measured. Inner diameter (d_{in}) was defined as the distance between the axonal membranes, whereas outer diameter (d_{out}) was defined as the distance between the outer borders of the myelin sheaths of each axon. Myelin thickness was estimated as $(d_{in} - d_{out})/2$. In the case where non-circular axonal profiles were seen, the diameter was measured based on the shorter axis of the axonal profile. Intracellular fraction was defined as the ratio of the sum of the areas (assuming circular axonal profiles) of all the axons present to the area of the counting frame $((\sum_{i=1}^{n} \pi(d_{in,i}/2)^2)/A_f)$, while the extracellular fraction was determined as $1 - ([\sum_{i=1}^{n} \pi(d_{out,i}/2)^2]/A_f)$, where n is the number of axons within the counting frame and A_f is the area of the counting frame. Myelin area was calculated as the difference between the extracellular and intracellular fractions.

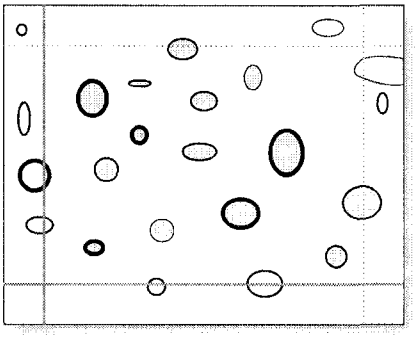

FIGURE 9.2: **Rules for axonal number estimation.** A counting frame was placed within the microscopic field, with each of its four lines lying 234 nm from the edge of the field. In this caricature example, 14 circular profiles are counted and shaded gray. Profiles lying completely outside the counting frame are not counted, neither those that, albeit being within the counting frame, touch either one of the thick red lines. Elements touching the dotted green lines are counted only if their entire profile can be seen in the field.

9.3 Results

The qualitative blinded assessment of the microphotographs revealed striking morphological differences of the fimbria/fornix of patients with TLE with MTS as compared with those without MTS (Figure 9.3). It is particularly evident that patients with MTS exhibit a larger fraction of extra-cellular space, with axons that are loosely packed. There is no visually striking difference in the myelin sheaths of the axons. It is surprising that both groups showed an almost complete absence of non-myelinated axons given that, at least in rodents, there is a considerable number of non-myelinated axons[162,508]. The tissue processing could be responsible for the lack of visualization of these structures.

Quantitative blinded analysis of the microphotographs revealed that the number of axons per field, and thus axonal density, was lower in those patients with TLE and MTS (Figure 9.4A). Patient 7 showed low axonal density, but this was perhaps due to having axons which were very large in diameter, occupying most of the area in the field. Indeed, it was the extra-cellular fraction that appeared to better differentiate the two groups, with those patients with MTS having a very high extra-cellular fraction (Figure 9.4B), which corresponds with what was appreciated qualitatively (Figure 9.3). Myelin thickness showed greater variability in patients with MTS, but overall it does not appear to be different between the two TLE groups (Figure 9.4B). Inner and outer axonal diameters appeared similar within the two groups.

Although the sample included in this study is very small, the amount of extra-cellular space (i.e. extra-cellular fraction) appears to be inversely related to the degree of pre-operative diffusion anisotropy of the fornix, where diffusivity perpendicular to the tracts (i.e. $\lambda_\perp$) is increased as the extra-cellular space is expanded

FIGURE 9.3: **(Page 184) Electron microscopy of the fimbria in TLE patients with and without MTS.** Representative electron micrographs of the fimbria/fornix of six TLE patients are shown. Patients with mesial temporal sclerosis (i.e. Patients 3, 4, 6 and 7) show less densely-packed axons as compared with patients with non-lesional TLE. Contrast and brightness have been modified for Patients 1 and 2 to allow for better visualization of the axons.

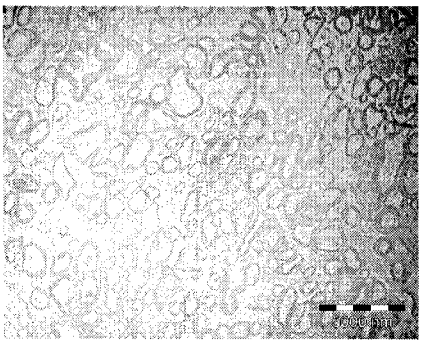

Patient 1 (nl-TLE)

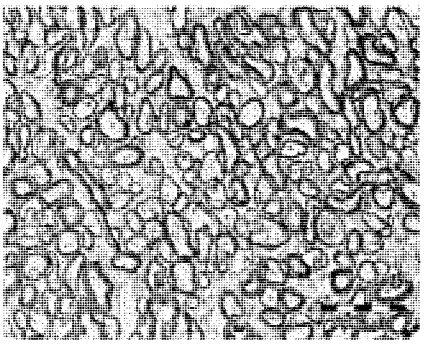

Patient 4 (nl-TLE)

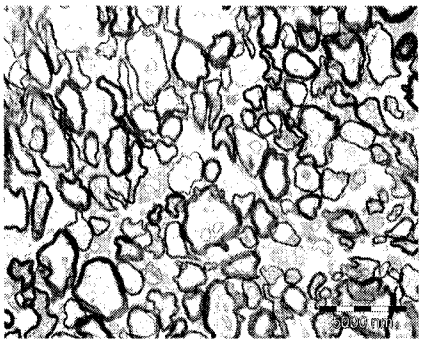

Patient 7 (nl-TLE)

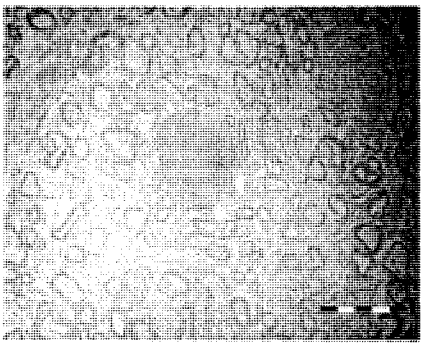

Patient 2 (MTS)

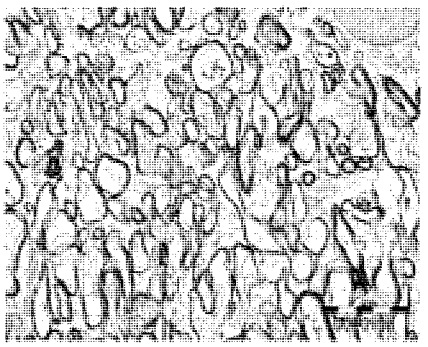

Patient 3 (MTS)

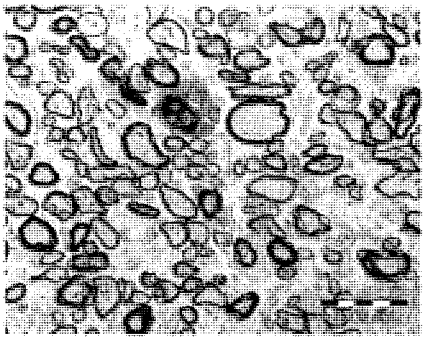

Patient 5 (MTS)

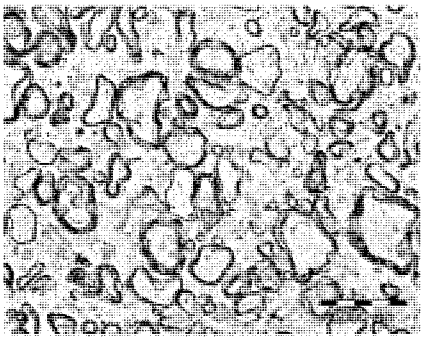

Patient 6 (MTS)

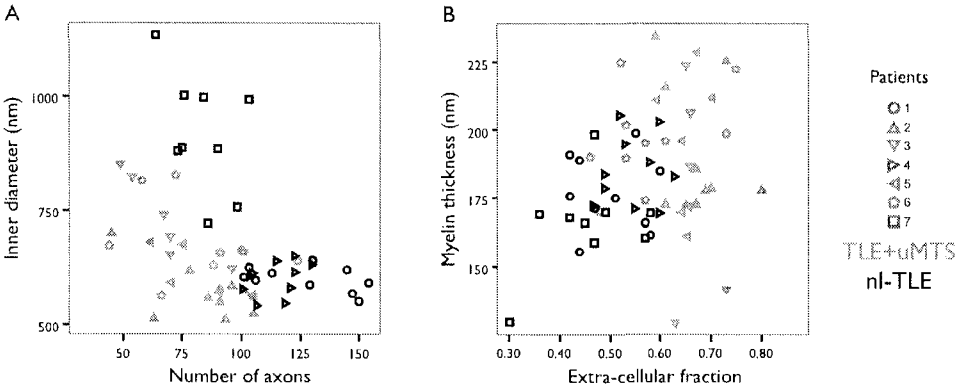

FIGURE 9.4: **Individual quantitative microscopy of the fimbria/fornix.** The parameters obtained from each microphotograph ($n = 61$) are presented (6-10 fields per patient). Inner diameter and myelin thickness are expressed as the mean value per field. Patients with TLE and unilateral MTS (TLE+uMTS) show a lower number of axons than most patients without MTS (A), which translates into a higher axonal density for the nl-TLE patients. The inner diameter of the axons does not seem to be different between the two groups, although only one patient in the non lesional TLE group (Patient 7, nl-TLE) shows axons with large diameters (A). Myelin thickness does not appear to be different between the two groups (B). There is a relationship between the presence of MTS and extra-cellular fraction, with its presence being associated with a larger extra-cellular space (B).

(Figure 9.5). The extra-cellular space appears to also increase overall diffusivity, but not diffusivity parallel to the tracts. As described above and shown in Figure 9.4, the extra-cellular fraction serves as a good parameter to differentiate the two TLE groups. It is not surprising, then, that extra-cellular fraction and hippocampal T2 (abnormal by definition in MTS patients) show a tight positive correlation (Figure 9.5E). Diffusion anisotropy did not appear to be related to axonal diameter inner or outer diameters (Figure 9.6). The overall myelin area per field and myelin thickness seem to have a somewhat weak correlation with diffusion parameters, with higher myelin thickness or area corresponding to higher FA and lower $\lambda_\perp$ (Figure 9.7). Lastly, the axonal density appears to have a weak relationship with the degree of diffusion anisotropy (Figure 9.8).

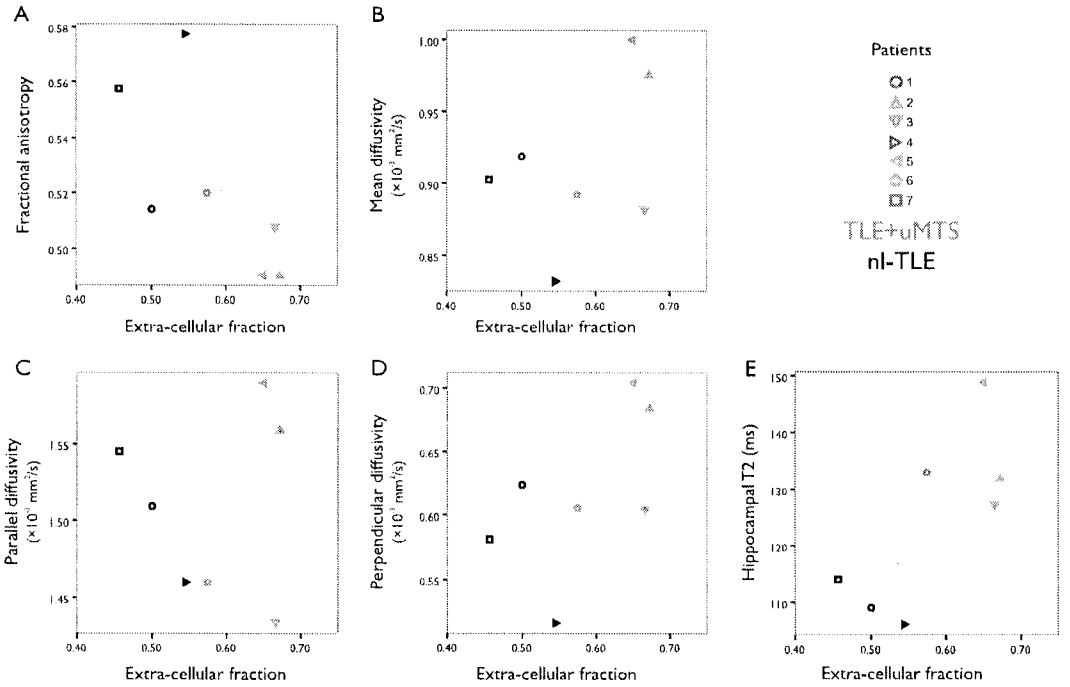

FIGURE 9.5: **Microscopic mechanisms of diffusion anisotropy in the fornix *in vivo* with extra-cellular fraction in the fimbria/fornix post-resection.** The mean values of all the fields analyzed per subject are shown relative to the patient's pre-operative diffusion parameters derived from the fornix. Patients with TLE and unilateral MTS, with a larger extra-cellular fraction tend to have lower diffusion anisotropy (A), given mostly by an increased perpendicular diffusivity (D), as compared with patients with non-lesional TLE. Extra-cellular fraction of the fornix is closely related to hippocampal T2, the imaging hallmark of MTS (E). Normal diffusion parameters derived from 25 control subjects are: FA= 0.54 ± 0.02; MD= 0.90 ± 0.03, $\lambda_{\parallel} = 1.53 \pm 0.05$, and $\lambda_{\perp} = 0.59 \pm 0.03 \times 10^{-3}$ mm^2/s (Chapter 7).

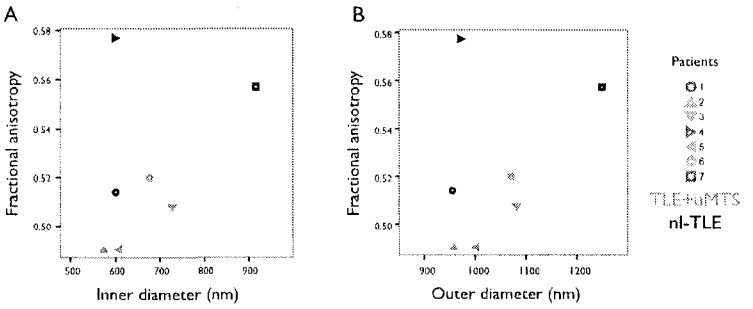

FIGURE 9.6: **Microscopic mechanisms of diffusion anisotropy: Axonal diameter.** Diffusion anisotropy of the fornix does not appear to be related to quantitative microscopy measures such as inner and outer diameter.

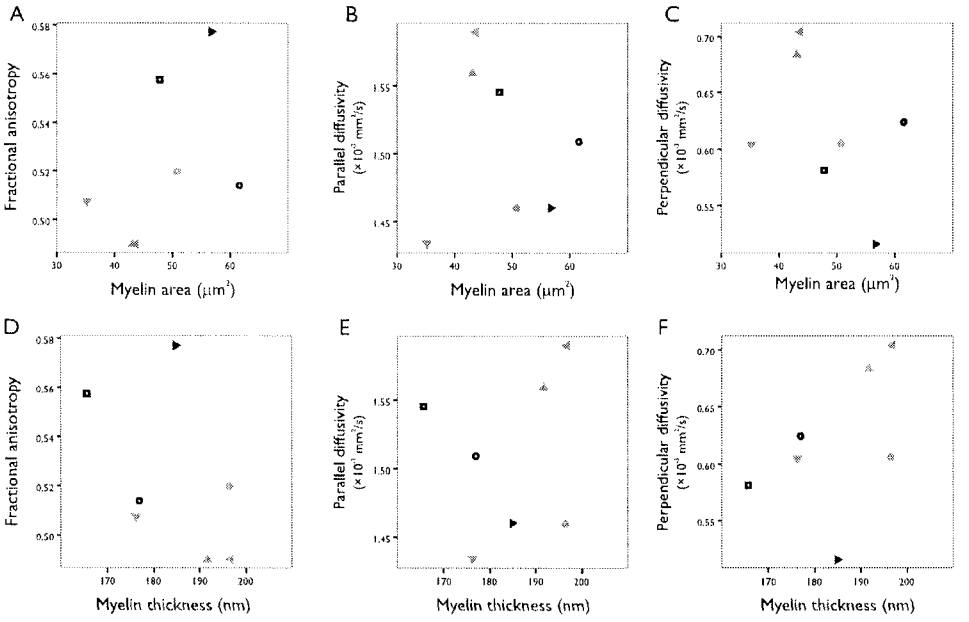

FIGURE 9.7: **Microscopic mechanisms of diffusion anisotropy: Myelin.** Myelin thickness and the total myelin area per field seem to be related with diffusion anisotropy (A and D) and perpendicular diffusivity (C and F), but not with parallel diffusivity (B and E).

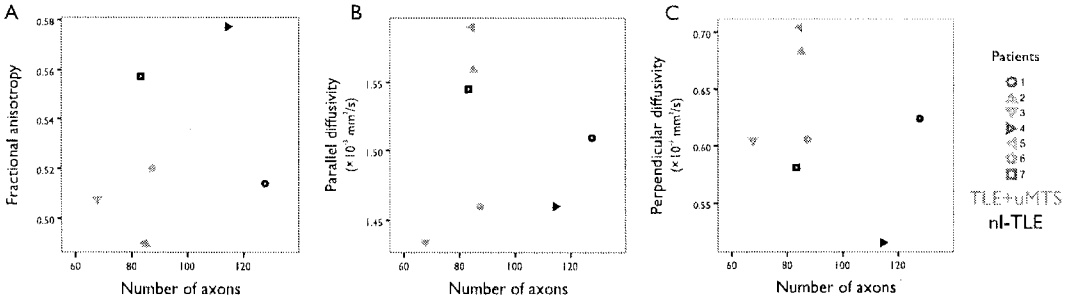

FIGURE 9.8: **Microscopic mechanisms of diffusion anisotropy: Axonal density.** There is a weak relationship between the number of axons per field (i.e. axonal density) and the degree of anisotropy, with a low axonal count translating into reduced diffusion anisotropy (A) and increased perpendicular diffusivity (C), but not affecting parallel diffusivity (B).

9.4 Discussion

The highly organized tissue architecture of white matter, where axonal membranes and myelin sheaths are coherently arranged, is thought to be responsible for the water diffusion anisotropy measurable with NMR of this tissue[27]. Although myelin sheaths modulate the degree of anisotropy[21,23,24,512], they are not a pre-requisite for the presence of anisotropy, suggesting that intact axonal membranes are largely responsible for the observed phenomenon[18].

In humans, the biological correlates of DTI-derived parameters and histological characteristics of white matter have only been assessed indirectly after known lesions. White matter tracts affected by stroke or any other injury degenerate locally, but also distally to the precipitating injury. This has been demonstrated with DTI of humans following stroke[445,446,495,498], temporal lobectomy[494] and congenital hemiparesis[493]. The longitudinal changes of quantitative parameters assessed before and after corpus callosotomy for epilepsy treatment showed a time course that closely matched the expected changes due to axonal damage and myelin degradation (inferred from animal models and known histopathology of Wallerian degeneration) (Chapter 8). However, due to the difficulty of obtaining fresh white matter tissue samples in humans, the direct correlation of quantitative *in vivo* diffusion parameters and tissue characteristics is a difficult task. There are currently no reports in the literature showing such correlations in humans.

As shown in previous Chapters, patients with TLE and unilateral MTS show bilateral diffusion abnormalities of the fornix (and other white matter bundles) that are not seen in patients who, despite having TLE, do not have evidence of MTS. This study provides an excellent opportunity to directly examine the tissue characteristics of the fimbria/fornix that account for such abnormalities observed with DTI. However, as of the time of this writing, the sample size is relatively small and any conclusions must be given careful consideration.

Based on qualitative and quantitative assessment of the microscopic structure of the fimbria/fornix, it is evident that patients with MTS have larger extra-cellular space and loosely packed axons. This is consistent with "dying back" of axons

originating in the hippocampus following neuronal death of the cornu Ammonis. However, while there are some efferent fibers interconnecting CA1 and the septal region, the majority of the hippocampal efferents originate in the subiculum[167] (Figure 3.6(a)), which is relatively spared in MTS[141,450]. Hence, while some of the microscopic abnormalities of the fornix in MTS patients can potentially be attributed to Wallerian degeneration, it is still unclear if this is the only causal factor. The asymmetrical degeneration of the fornix following temporal lobectomy has been demonstrated in a TLE patient who died one year following temporal lobe resection[510]. However, it is not possible to know what the microscopic characteristics of the fornix of such a patient were before surgery.

The pre-operative quantitative diffusion parameters of the fornix hint at a correlation between the degree of diffusion anisotropy and the extra-cellular fraction and axonal density. These findings are in line with a similar study performed *ex-vivo* in normal rat cervical spinal cord[513], who also found a strong correlation between diffusion anisotropy and extra-cellular fraction. In that study, however, myelin thickness was not found to be correlated with diffusion anisotropy, but the myelin volume fraction was. In a *post-mortem* study of brains of patients who had multiple sclerosis, diffusion anisotropy and mean diffusivity demonstrated significant correlations with myelin content and axonal count. The data shown in Figure 9.7 shows a slight correspondence between diffusion anisotropy and myelin thickness and area, although there is not enough data to derive a definitive conclusion.

Contrary to what we expected (but similar to[513]), axonal thickness does not appear to influence diffusion anisotropy. However, as can be seen in Figures 9.4 and 9.6, the inner diameter of the axons in the fornix is very small (0.5-1 μm) in both TLE groups and, therefore, correlations with DTI parameters are difficult for this micro-structural parameter.

The lack of a control group in this electron microscopic study is unfortunate but unavoidable, and thus it is impossible to know how the micro-structural characteristics of the fornix in the two TLE groups compare to the normal population. That is, tissue abnormalities present in both patient groups cannot be evaluated in the absence of a formal definition of what is normal. Procuring specimens from

normal individual is, for obvious reasons, ethically impossible. An attempt was made to evaluate tissue integrity of the fornix obtained from a cadaver. However, the integrity of the specimen is greatly compromised if not fixed appropriately in a very short time, a feat not possible in this situation. Without proper and rapid fixation, myelin and macro-molecules break down promptly, defeating the purpose of the control specimen. It is possible that in the near future, specimens of the fimbria/fornix will be collected from patients undergoing temporal lobe resections due to reasons other than TLE (e.g. tumors not infiltrating the fimbria, vascular malformations, or others). This will provide an excellent opportunity to evaluate the normality of the fornix of patients with non-lesional TLE.

Finally, as neither DTI nor microscopy can differentiate hippocampal afferents from efferents, it is impossible to pin-point the precise pathway(s) affected by MTS. In a similar fashion, this study does not resolve the issue of the white matter diffusion abnormalities identified in the fornix *contralateral* to MTS. It does, however, partly suggest that the contralateral abnormalities could be caused by similar micro-architectural changes. As the percentage of forniceal fibers that cross the midline to reach the contralateral hippocampus is relatively small[171], it is not likely that the DTI abnormalities detected on the fornix contralateral to MTS are merely a reflection of Wallerian degeneration of commissural fibers.

The collection of specimens of the fimbria/fornix will continue for several months more, therefore increasing the sample size and allowing more meaningful and accurate correlations and conclusions to be made.

Part III

Discussion

Chapter 10

Conclusion

Imaging methods have revolutionized the standard approach to medically intractable epilepsy, providing better insight into the source of various epilepsy syndromes. The great sensitivity and high spatial resolution these imaging methods provide has led to great advancements in the field of epilepsy surgery and increased the chances of being seizure free for a great number of patients with medically intractable epilepsy. Imaging is not, however, limited to the detection of epileptogenic lesions, but can also provide invaluable information on the pathogenesis and pathophysiology of this neurologic disorder.

Given that epilepsy is a grey matter disorder, the study of the white matter was largely ignored for a very long time. With the growing recognition that epilepsy can be better explained as a network disorder, the study of white matter became absolutely relevant. While white matter used to be considered merely as a passive means for the propagation of seizure activity, there is now considerable interest in its direct repercussions in the mechanisms of epilepsy. The advent of diffusion tensor imaging and tractography allowed the assessment of the macroscopic brain connectivity in clinically feasible times and, most notably, non-invasively. Furthermore, the relatively straightforward interpretation of the water diffusion tensor permits the inference of the integrity of white matter.

The unexpected initial finding of bilateral white matter abnormalities in patients with unilateral temporal lobe epilepsy and mesial temporal sclerosis led to intriguing questions regarding their nature and their involvement in the genesis

and evolution of temporal lobe epilepsy. The work presented herein, and the work by others, demonstrated that abnormalities that extend beyond the hippocampus do not modify surgical outcome if there is a single seizure generator—a common occurrence in patients with unilateral mesial temporal sclerosis. The fact that these abnormalities do not resolve upon seizure freedom strongly suggests that they are structural in nature, minimizing the possibility of them being directly related to water shifts due to ongoing seizures.

There are several white matter bundles in the brain (such as the corpus callosum and the external capsules) that appear to be affected not only in lesional temporal lobe epilepsy, but also in other epilepsy syndromes. The limbic white matter, however, appears to be preferentially affected in patients who have mesial temporal sclerosis. The pattern of diffusion abnormalities in the limbic white matter suggests alterations of the myelin sheaths, axonal membranes and axonal packing. Indeed, these abnormalities are quite similar to those seen in the chronic stages of Wallerian degeneration, as was shown in the corpus callosum after its surgical bisection. While it is certainly possible that the abnormalities of the limbic white matter are related to the known neuronal death that occurs in the mesial temporal structures and subsequent Wallerian degeneration, this hypothesis does not explain their bilateral presentation in patients in whom neuronal death is assumed to be unilateral.

The direct microscopic evaluation of fimbria/fornix in patients who underwent temporal lobe epilepsy surgery showed that, as was correctly assumed, the altered diffusion parameters are related to differences in axonal characteristics, particularly their size and packing. Notably, these differences, as well as water diffusion patterns, are different in patients with temporal lobe epilepsy with and without mesial temporal sclerosis. While these preliminary results cannot rule out the occurrence of down-stream axonal degeneration due to the sclerotic lesion, it provides an important link between diffusion parameters and microstructural details of the tissue. As the pattern of diffusion abnormalities of the fornix (namely, an increase in diffusivity perpendicular to the axons) is similar in both hemispheres, it is not unlikely that this white matter structure also shows sim-

ilar tissue changes in the hemisphere contralateral to hippocampal sclerosis. If this is the case, however, their relationship to Wallerian degeneration becomes less probable. An alternative explanation for these bilateral changes is the presence of abnormalities in the hippocampal afferents, which have been shown to be involved in the generation of temporal lobe seizures in animal models.

Diffusion tensor imaging and tractography are tools that have rapidly become adopted and utilized world-wide. Their application will certainly expand our knowledge on the active participation of white matter in epilepsy syndromes. The methodology and the results presented herein will hopefully provide grounds for future studies that will aid in the diagnosis and prognosis of epilepsy and perhaps in the identification of predisposing factors for its development.

CHAPTER 11

LIMITATIONS AND FUTURE DIRECTIONS

Virtually every experimental design has some form of design or technical limitation and important underlying assumptions. Certainly, the work presented in this dissertation is no different.

While being extremely powerful and sensitive, and having a direct biological interpretation, the diffusion tensor model suffers from several limitations that were highlighted in section 2.5.1. In particular, the inability of the diffusion tensor to differentiate crossing fibers did not allow us to study the anterior thalamic radiation, which must cross the commissural fibers of the corpus callosum. As thalamic abnormalities have been reported in patients with temporal lobe epilepsy, the study of these connections would have been valuable. In a similar sense, the resolution attained with the scanner utilized in a clinically-acceptable time frame ($2\times2\times2$ mm^3 voxel size) did not permit the analysis of the mammillo-thalamic tract, another important structure in the limbic system. Other imaging acquisition schemes that permit higher spatial and angular resolution and minimize artifacts (such as PROPELLER-EPI and HARDI) could potentially aid in the depiction of small white matter structures. It is theoretically possible to increase the signal to noise ratio by utilizing higher static magnetic fields, which permit the acquisition of images with higher spatial resolution. However, at high magnetic fields (e.g. 4.7 T) tissue magnetic susceptibility differences are more prominent, as well

as field inhomogeneities, which greatly increase geometric distortions and reduce the T2* constant of brain tissue, thus reducing the amount of signal obtained.

Having found white matter abnormalities in several white matter structures of patients with temporal lobe epilepsy, it will be very important to analyze other fascicles in the brain, such as the uncinate fasciculus (interconnecting the temporal and frontal lobes) or the supra-callosal portion of the cingulum bundle. While the results presented herein show that the white matter abnormalities are not global (e.g. we did not find abnormalities in the internal capsule), it is necessary to provide a fuller picture of the state of white matter throughout the brain. It is possible to perform these studies using the methodology presented here, and also utilizing other approaches such as automated tractography, tract-based spatial statistics and voxel-based statistical methods. The use of CSF-suppression, however, limits the anatomical coverage possible within a certain time. Full brain coverage can be accomplished within acceptable time frames when CSF-suppression is not utilized. The diffusion parameters of white matter structures that are distant from CSF spaces can be reliably obtained from standard, full-brain DTI. Also important would be the correlation between white and gray matter diffusion parameters, in particular with those of the hippocampus, which was not analyzed.

The DTI imaging protocol yielded images with adequate signal-to-noise ratio and overall quality. However, the images can be considerably improved by utilizing parallel imaging acquisition schemes, which minimize geometric distortions due to the fast traversing of *k*-space and increased signal due to the shorter effective echo time.

Despite having reached statistical significance, the sample sizes in the experiments presented are relatively small and the results need to be validated by other groups with larger sample sizes.

The microscopic evaluation of the fimbria/fornix presented in Chapter 9 requires a larger sample in order to provide more definitive answers. Furthermore, it unfortunately lacks the evaluation of control tissue and the only comparison possible is between patients with and without temporal lobe epilepsy. This comparison does not allow us to discern a difference between either group with healthy indi-

viduals. It is however very difficult to procure an adequate fimbria specimen from healthy individuals, given the quick break-down of the structures if they are not appropriately fixed within a short time frame after death. For this reason, cadaveric samples are unusable. Given the impossibility of procuring tissue samples from healthy individuals, the next best scenario is to perform a comparison with fimbria samples that are assumed to be free of abnormalities, resected for reasons other than epilepsy (e.g. after temporal lobectomies due to tumors distant enough from the fimbria).

Several questions remain unanswered regarding white matter abnormalities. In particular, their time of apparition with respect with onset of epilepsy. Are they a cause or a consequence of epilepsy? While the correlations between diffusion parameters and disease duration presented in Chapter 7 suggest that they could, at least partially, be attributed to the epileptic disorder, prospective studies are needed to answer this specific and very important question. The study of children with short duration of TLE with the methodology outlined herein could shed some light into the temporal evolution of the diffusion abnormalities of the white matter. Also relevant is the relationship between white matter abnormalities and the occurrence of febrile seizures. A large study to evaluate this question has already been started.

The limbic system is directly related to memory and cognition. It will be very interesting to search for correlations between the presented white matter abnormalities and neuro-psychological evaluations. Of considerable importance would be their prognostic value for the development of memory or cognition problems.

Lastly, as was mentioned in the Introduction, the term "epilepsy" encompasses various syndromes with very diverse characteristics. It is still necessary to study the white matter in other forms of (non-temporal lobe) epilepsy of both focal and generalized onset.

⋆ ⋆ ⋆

BIBLIOGRAPHY

1 BROWN R. A brief account of microscopical observations made in the months of June, July and August, 1827, on the particles contained in the pollen of plants; and on the general existence of active molecules in organic and inorganic bodies. *Phil Mag*, 1828. 4:161–173. (Cited on p. 5.)

2 EINSTEIN A. Über die von der molekularkinetischen Theorie der Wärme geforderte Bewegung von in ruhenden Flüssigkeiten suspendierten Teilchen. *Annalen der Physik*, 1905. 4:549–560. (Cited on p. 5.)

3 MILLS R. Self-diffusion in normal and heavy water in the range 1 to 45°. *J Phys Chem*, 1973. 77(5):685–688. (Cited on p. 6.)

4 HAHN EL. Spin Echoes. *Phys Rev*, 1950. 80(4):580–594. (Cited on p. 7.)

5 CARR HY and PURCELL EM. Effects of Diffusion on Free Precession in Nuclear Magnetic Resonance Experiments. *Phys Rev*, 1954. 94(3):630–638. (Cited on p. 7.)

6 TORREY HC. Bloch Equations with Diffusion Terms. *Phys Rev*, 1956. 104(3):563–565. (Cited on p. 7.)

7 STEJSKAL EO and TANNER JE. Spin diffusion measurements: spin echoes in the presence of a time-dependent field gradient. *Journal of Chemical Physics*, 1965. 42(288-292). (Cited on pp. 7, 8, and 32.)

8 TANNER J. Use of the stimulated echo in NMR diffusion studies. *J Chem Phys*, 1970. 52:2523. (Cited on p. 8.)

9 PRICE W and KUCHEL P. Effect of non-rectangular gradient pulses in the Stejskal and Tanner (diffusion) pulse sequence. *J Magn Reson*, 1991. 94:133–139. (Cited on p. 10.)

10 WESBEY GE, MOSELEY ME and EHMAN RL. Translational molecular self-diffusion in magnetic resonance imaging. II. Measurement of the self-diffusion coefficient. *Invest Radiol*, 1984. 19(6):491–498. (Cited on p. 10.)

11 SOTAK CH. The role of diffusion tensor imaging in the evaluation of ischemic brain injury - a review. *NMR in Biomedicine*, 2002. 15(7-8):561–9. (Cited on pp. 10 and 17.)

12 TANNER JE and STEJSKAL EO. Restricted Self-Diffusion of Protons in Colloidal Systems by the Pulsed-Gradient, Spin-Echo Method. *Journal of Chemical Physics*, 1968. 49:1768–1777. (Cited on p. 11.)

13 PAKKENBERG B and GUNDERSEN HJ. Neocortical neuron number in humans: effect of sex and age. *J Comp Neurol*, 1997. 384(2):312–320. (Cited on p. 11.)

14 RENGACHARY S and ELLENGOGEN R, editors. *Principles of Neurosurgery*. Mosby, 2 edition, 2004. (Cited on pp. 11 and 12.)

15 TANG Y, NYENGAARD JR, PAKKENBERG B and GUNDERSEN HJ. Age-induced white matter changes in the human brain: a stereological investigation. *Neurobiol Aging*, 1997. 18(6):609–615. (Cited on p. 12.)

16 KANDEL ER. *Principles of Neural Science*. McGraw-Hill Education, 2000. (Cited on p. 12.)

17 LE BIHAN D and VAN ZIJL P. From the diffusion coefficient to the diffusion tensor. *NMR Biomed*, 2002. 15(7-8):431–434. (Cited on p. 12.)

18 BEAULIEU C and ALLEN PS. Determinants of anisotropic water diffusion in nerves. *Magnetic Resonance in Medicine*, 1994. 31(4):394–400. (Cited on pp. 12, 98, 170, 179, and 189.)

19 WIMBERGER DM, ROBERTS TP, BARKOVICH AJ, PRAYER LM, MOSELEY ME and KUCHARCZYK J. Identification of "premyelination" by diffusion-weighted MRI. *J Comput Assist Tomogr*, 1995. 19(1):28–33. (Cited on pp. 12 and 179.)

20 GULANI V, WEBB AG, DUNCAN ID and LAUTERBUR PC. Apparent diffusion tensor measurements in myelin-deficient rat spinal cords. *Magn Reson Med*, 2001. 45(2):191–5. (Cited on pp. 12, 156, 170, and 179.)

21 SONG SK, SUN SW, JU WK, LIN SJ, CROSS AH and NEUFELD AH. Diffusion tensor imaging detects and differentiates axon and myelin degeneration in mouse optic nerve after retinal ischemia. *Neuroimage*, 2003. 20(3):1714–22. (Cited on pp. 12, 15, 114, 125, 126, 127, 131, 141, 156, 170, 172, 179, and 189.)

22 SONG SK, SUN SW, RAMSBOTTOM MJ, CHANG C, RUSSELL J and CROSS AH. Dysmyelination revealed through MRI as increased radial (but unchanged axial) diffusion of water. *Neuroimage*, 2002. 17(3):1429–36. (Cited on pp. 12, 156, and 179.)

23 SONG SK, YOSHINO J, LE TQ, LIN SJ, SUN SW, CROSS AH and ARMSTRONG RC. Demyelination increases radial diffusivity in corpus callosum of mouse brain. *Neuroimage*, 2005. 26(1):132–40. (Cited on pp. 12, 156, 170, 179, and 189.)

24 TYSZKA JM, READHEAD C, BEARER EL, PAUTLER RG and JACOBS RE. Statistical diffusion tensor histology reveals regional dysmyelination effects in the shiverer mouse mutant. *Neuroimage*, 2006. 29(4):1058–65. (Cited on pp. 12, 172, 179, and 189.)

25 BEAULIEU C and ALLEN PS. Water diffusion in the giant axon of the squid: implications for diffusion-weighted MRI of the nervous system. *Magnetic Resonance in Medicine*, 1994. 32(5):579–83. (Cited on p. 13.)

26 PIERPAOLI C, JEZZARD P, BASSER PJ, BARNETT A and DI CHIRO G. Diffusion tensor MR imaging of the human brain. *Radiology*, 1996. 201(3):637–48. (Cited on pp. 13, 15, and 90.)

27 BEAULIEU C. The basis of anisotropic water diffusion in the nervous system - a technical review. *NMR in Biomedicine*, 2002. 15(7-8):435–55. (Cited on pp. 13, 38, 98, 114, 130, 131, 141, 155, and 189.)

28 BASSER PJ, MATTIELLO J and LEBIHAN D. Estimation of the effective self-diffusion tensor from the NMR spin echo. *Journal of Magnetic Resonance Series B*, 1994. 103(3):247–54. (Cited on pp. 14, 114, 130, and 158.)

29 BASSER PJ, MATTIELLO J and LEBIHAN D. MR diffusion tensor spectroscopy and imaging. *Biophys J*, 1994. 66(1):259–67. (Cited on p. 14.)

30 JONES DK. The effect of gradient sampling schemes on measures derived from diffusion tensor MRI: a Monte Carlo study. *Magn Reson Med*, 2004. 51(4):807–815. (Cited on p. 15.)

31 Hasan KM, Parker DL and Alexander AL. Comparison of gradient encoding schemes for diffusion-tensor MRI. *Journal of Magnetic Resonance Imaging*, 2001. 13(5):769–80. (Cited on p. 15.)

32 Concha L, Gross DW, Wheatley BM and Beaulieu C. Diffusion tensor imaging of time-dependent axonal and myelin degradation after corpus callosotomy in epilepsy patients. *Neuroimage*, 2006. 32(3):1090–9. **(Chapter 8 of this thesis)**. (Cited on pp. 15, 114, 125, 126, 127, 131, 141, and 179.)

33 Mansfield P. Multi-planar image formation using NMR spin echoes. *Journal of Physics C: Solid State Physics*, 1977. 10(3):L55–L58. (Cited on p. 16.)

34 Rzedzian RR and Pykett IL. Instant images of the human heart using a new, whole-body MR imaging system. *AJR Am J Roentgenol*, 1987. 149(2):245–250. (Cited on p. 16.)

35 Ordidge RJ, Coxon R, Howseman A, Chapman B, Turner R, Stehling M and Mansfield P. Snapshot head imaging at 0.5 T using the echo planar technique. *Magn Reson Med*, 1988. 8(1):110–115. (Cited on p. 16.)

36 Avram H and Crooks L. Effect of self-diffusion on echo-planar imaging. In: *Book of abstracts: Society of Magnetic Resonance in Medicine*. Society of Magnetic Resonance in Medicine, Berkeley, 1988 980. (Cited on p. 17.)

37 Moseley ME, Cohen Y, Mintorovitch J, Chileuitt L, Shimizu H, Kucharczyk J, Wendland MF and Weinstein PR. Early detection of regional cerebral ischemia in cats: comparison of diffusion- and T2-weighted MRI and spectroscopy. *Magn Reson Med*, 1990. 14(2):330–346. (Cited on p. 17.)

38 Warach S, Gaa J, Siewert B, Wielopolski P and Edelman RR. Acute human stroke studied by whole brain echo planar diffusion-weighted magnetic resonance imaging. *Annals of Neurology*, 1995. 37(2):231–41. (Cited on p. 17.)

39 Pierpaoli C and Basser PJ. Toward a quantitative assessment of diffusion anisotropy.[erratum appears in Magn Reson Med 1997 Jun;37(6):972]. *Magnetic Resonance in Medicine*, 1996. 36(6):893–906. (Cited on pp. 18 and 20.)

40 Pierpaoli C, Mattiello J, Le Bihan D, Di Chiro G and PJ B. Diffusion tensor imaging of brain white matter anisotropy. In: *Proceedings from the SMR, 2nd meeting. San Francisco*. Society for Magnetic Resonace, 1994 1038. (Cited on p. 18.)

41 Sands DE. *Vectors and tensors in crystallography*. Dover, 1995. (Cited on p. 20.)

42 Basser PJ and Pierpaoli C. Microstructural and physiological features of tissues elucidated by quantitative-diffusion-tensor MRI. *Journal of Magnetic Resonance Series B*, 1996. 111(3):209–19. (Cited on pp. 20, 88, and 98.)

43 Conturo TE, McKinstry RC, Akbudak E and Robinson BH. Encoding of anisotropic diffusion with tetrahedral gradients: a general mathematical diffusion formalism and experimental results. *Magn Reson Med*, 1996. 35(3):399–412. (Cited on p. 22.)

44 Ulug A, Bakht O, Bryan R and van Zijl P. Mapping of human brain fibers using diffusion tensor imaging. In: *ISMRM Proceedings, New York*. 1994 1325. (Cited on p. 22.)

45 Douek P, Turner R, Pekar J, Patronas N and Le Bihan D. MR color mapping of myelin fiber orientation. *Journal of Computer Assisted Tomography*, 1991. 15(6):923–9. (Cited on p. 22.)

46 Coremans J, Luypaert R, Verhelle F, Stadnik T and Osteaux M. A method for myelin fiber orientation mapping using diffusion-weighted MR images. *Magn Reson Imaging*, 1994. 12(3):443–454. (Cited on p. 22.)

47 Nakada T and Matsuzawa H. Three-dimensional anisotropy contrast magnetic resonance imaging of the rat nervous system: MR axonography. *Neurosci Res*, 1995. 22(4):389–398. (Cited on p. 22.)

48 Pierpaoli C. Oh no! One more method for color mapping of fiber tract direction using diffusion MR imaging data. In: *Proceedings of the international Society of Magnetic Resonance in Medicine (ISMRM)*. International Society for Magnetic Reonance in Medicine, Vancouver, Canada, 1997 1741. (Cited on p. 22.)

49 Jones D, Williams S and Horsfield M. Full representation of white matter fibre direction on one map via diffusion tensor analysis. In: *Proceedings of the international Society of Magnetic Resonance in Medicine (ISMRM)*. International Society for Magnetic Reonance in Medicine, Vancouver, Canada, 1997 1743. (Cited on p. 22.)

50 Pajevic S and Pierpaoli C. Color schemes to represent the orientation of anisotropic tissues from diffusion tensor data: application to white matter fiber tract mapping in the human brain. *Magn Reson Med*, 2000. 43(6):921. (Cited on p. 22.)

51 Bastin ME, Armitage PA and Marshall I. A theoretical study of the effect of experimental noise on the measurement of anisotropy in diffusion imaging. *Magn Reson Imaging*, 1998. 16(7):773–785. (Cited on p. 22.)

52 Westin C, Peled S, Gudbajartsson H, Kikinis R and Jolesz F. Geometrical diffusion measures from MRI fom tensor basis analysis. In: *6th Annual Meeting of the International Society for Magnetic Resonance in Medicine (ISMRM)*. Vancouver, 1997 1742. (Cited on p. 22.)

53 Alexander AL, Hasan K, Kindlmann G, Parker DL and Tsuruda JS. A geometric analysis of diffusion tensor measurements of the human brain. *Magn Reson Med*, 2000. 44(2):283–91. (Cited on p. 23.)

54 Makris N, Worth AJ, Sorensen AG, Papadimitriou GM, Wu O, Reese TG, Wedeen VJ, Davis TL, Stakes JW, Caviness VS, Kaplan E, Rosen BR, Pandya DN and Kennedy DN. Morphometry of in vivo human white matter association pathways with diffusion-weighted magnetic resonance imaging. *Ann Neurol*, 1997. 42(6):951–962. (Cited on p. 24.)

55 Mori S, Crain BJ, Chacko VP and van Zijl PC. Three-dimensional tracking of axonal projections in the brain by magnetic resonance imaging. *Annals of Neurology*, 1999. 45(2):265–9. (Cited on pp. 24, 25, 78, 81, 89, 101, 116, 133, 159, and 181.)

56 Conturo TE, Lori NF, Cull TS, Akbudak E, Snyder AZ, Shimony JS, McKinstry RC, Burton H and Raichle ME. Tracking neuronal fiber pathways in the living human brain. *Proceedings of the National Academy of Sciences of the United States of America*, 1999. 96(18):10422–7. (Cited on pp. 24, 26, 78, 81, and 101.)

57 POUPON C, CLARK CA, FROUIN V, REGIS J, BLOCH I, LE BIHAN D and MANGIN J. Regularization of diffusion-based direction maps for the tracking of brain white matter fascicles. *Neuroimage*, 2000. 12(2):184–95. (Cited on p. 24.)

58 LAZAR M, WEINSTEIN DM, TSURUDA JS, HASAN KM, ARFANAKIS K, MEYERAND ME, BADIE B, ROWLEY HA, HAUGHTON V, FIELD A and ALEXANDER AL. White matter tractography using diffusion tensor deflection. *Human Brain Mapping*, 2003. 18(4):306–21. (Cited on p. 24.)

59 BASSER P. Fiber-tractography via diffusion tensor MRI (DT-MRI). In: *6th Annual Meeting of the International Society for Magnetic Resonance in Medicine (ISMRM)*. Sydney, Australia, 1998 1226. (Cited on p. 24.)

60 JONES D, SIMMONS A, WILLIAMS S and MA H. Non-invasive assessment of structural connectivity in white matter by diffusion tensor MRI. In: *6th Annual Meeting of the International Society for Magnetic Resonance in Medicine (ISMRM)*. Sydney, Australia, 1998 531. (Cited on p. 24.)

61 MORI S and VAN ZIJL PC. Fiber tracking: principles and strategies - a technical review. *NMR in Biomedicine*, 2002. 15(7-8):468–80. (Cited on pp. 25 and 78.)

62 DAUGUET J, PELED S, BEREZOVSKII V, DELZESCAUX T, WARFIELD SK, BORN R and WESTIN CF. Comparison of fiber tracts derived from in-vivo DTI tractography with 3D histological neural tract tracer reconstruction on a macaque brain. *Neuroimage*, 2007. 37(2):530–538. (Cited on p. 25.)

63 LAZAR M and ALEXANDER AL. An error analysis of white matter tractography methods: synthetic diffusion tensor field simulations. *Neuroimage*, 2003. 20(2):1140–1153. (Cited on p. 25.)

64 JIANG H, VAN ZIJL PCM, KIM J, PEARLSON GD and MORI S. DtiStudio: resource program for diffusion tensor computation and fiber bundle tracking. *Comput Methods Programs Biomed*, 2006. 81(2):106–116. (Cited on pp. 25 and 133.)

65 CATANI M, HOWARD RJ, PAJEVIC S and JONES DK. Virtual in vivo interactive dissection of white matter fasciculi in the human brain. *Neuroimage*, 2002. 17(1):77–94. (Cited on pp. 26, 78, 79, 81, and 99.)

66 CATANI M, JONES DK, DONATO R and FFYTCHE DH. Occipito-temporal connections in the human brain. *Brain*, 2003. 126(Pt 9):2093–107. (Cited on p. 26.)

67 WAKANA S, CAPRIHAN A, PANZENBOECK MM, FALLON JH, PERRY M, GOLLUB RL, HUA K, ZHANG J, JIANG H, DUBEY P, BLITZ A, VAN ZIJL P and MORI S. Reproducibility of quantitative tractography methods applied to cerebral white matter. *Neuroimage*, 2007. (Cited on p. 26.)

68 JONES DK. Determining and visualizing uncertainty in estimates of fiber orientation from diffusion tensor MRI. *Magn Reson Med*, 2003. 49(1):7–12. (Cited on p. 27.)

69 BEHRENS TEJ, WOOLRICH MW, JENKINSON M, JOHANSEN-BERG H, NUNES RG, CLARE S, MATTHEWS PM, BRADY JM and SMITH SM. Characterization and propagation of uncertainty in diffusion-weighted MR imaging. *Magn Reson Med*, 2003. 50(5):1077–1088. (Cited on pp. 27 and 32.)

70 BEHRENS TE, JOHANSEN-BERG H, WOOLRICH MW, SMITH SM, WHEELER-KINGSHOTT CA, BOULBY PA, BARKER

GJ, SILLERY EL, SHEEHAN K, CICCARELLI O, THOMPSON AJ, BRADY JM and MATTHEWS PM. Non-invasive mapping of connections between human thalamus and cortex using diffusion imaging. *Nature Neuroscience*, 2003. 6(7):750–7. (Cited on p. 28.)

71 WRIGHT IC, MCGUIRE PK, POLINE JB, TRAVERE JM, MURRAY RM, FRITH CD, FRACKOWIAK RS and FRISTON KJ. A voxel-based method for the statistical analysis of gray and white matter density applied to schizophrenia. *Neuroimage*, 1995. 2(4):244–252. (Cited on p. 30.)

72 ASHBURNER J and FRISTON KJ. Voxel-based morphometry–the methods. *Neuroimage*, 2000. 11(6 Pt 1):805–21. (Cited on pp. 30, 67, and 79.)

73 ASHBURNER J and FRISTON KJ. Why voxel-based morphometry should be used. *Neuroimage*, 2001. 14(6):1238–43. (Cited on p. 30.)

74 JONES DK, SYMMS MR, CERCIGNANI M and HOWARD RJ. The effect of filter size on VBM analyses of DT-MRI data. *Neuroimage*, 2005. 26(2):546–554. (Cited on p. 30.)

75 JONES D, CHITNIS X, JOB D, KHONG P, LEUNG L, MARENCO S, SMITH S and SYMMS M. What happens when nine different groups analyze the same DT-MRI data set using voxel based methods? In: *15th Annual Meeting of the International Society for Magnetic Resonance in Medicine (ISMRM)*. Berlin, Germany, 2007 74. (Cited on p. 30.)

76 SMITH SM, JENKINSON M, JOHANSEN-BERG H, RUECKERT D, NICHOLS TE, MACKAY CE, WATKINS KE, CICCARELLI O, CADER MZ, MATTHEWS PM and BEHRENS TE. Tract-based spatial statistics: Voxelwise analysis of multi-subject diffusion data. *Neuroimage*, 2006. 31(4):1487–505. (Cited on p. 30.)

77 ALEXANDER DC, BARKER GJ and ARRIDGE SR. Detection and modeling of non-Gaussian apparent diffusion coefficient profiles in human brain data. *Magn Reson Med*, 2002. 48(2):331–340. (Cited on p. 32.)

78 FRANK LR. Characterization of anisotropy in high angular resolution diffusion-weighted MRI. *Magn Reson Med*, 2002. 47(6):1083–1099. (Cited on p. 32.)

79 TUCH DS, REESE TG, WIEGELL MR, MAKRIS N, BELLIVEAU JW and WEDEEN VJ. High angular resolution diffusion imaging reveals intravoxel white matter fiber heterogeneity. *Magn Reson Med*, 2002. 48(4):577–582. (Cited on p. 32.)

80 TUCH DS. Q-ball imaging. *Magn Reson Med*, 2004. 52(6):1358–1372. (Cited on p. 32.)

81 TUCH DS, REESE TG, WIEGELL MR and WEDEEN VJ. Diffusion MRI of complex neural architecture. *Neuron*, 2003. 40(5):885–895. (Cited on p. 32.)

82 HU X and LE TH. Artifact reduction in EPI with phase-encoded reference scan. *Magn Reson Med*, 1996. 36(1):166–171. (Cited on p. 34.)

83 REEDER SB, FARANESH AZ, ATALAR E and MCVEIGH ER. A novel object-independent "balanced" reference scan for echo-planar imaging. *J Magn Reson Imaging*, 1999. 9(6):847–852. (Cited on p. 34.)

84 KUEI CHEN N and WYRWICZ AM. Removal of EPI Nyquist ghost artifacts with two-dimensional phase correction. *Magn Reson Med*, 2004. 51(6):1247–1253. (Cited on p. 34.)

85 Buonocore MH and Zhu DC. Image-based ghost correction for interleaved EPI. *Magn Reson Med*, 2001. 45(1):96–108. (Cited on p. 34.)

86 Zhang Y and Wehrli FW. Reference-scan-free method for automated correction of Nyquist ghost artifacts in echoplanar brain images. *Magn Reson Med*, 2004. 51(3):621–624. (Cited on p. 34.)

87 Weiskopf N, Klose U, Birbaumer N and Mathiak K. Single-shot compensation of image distortions and BOLD contrast optimization using multi-echo EPI for real-time fMRI. *Neuroimage*, 2005. 24(4):1068–1079. (Cited on p. 35.)

88 Jezzard P and Balaban RS. Correction for geometric distortion in echo planar images from Bo field variations. *Magn Reson Med*, 1995. 34(1):65–73. (Cited on p. 35.)

89 Reber PJ, Wong EC, Buxton RB and Frank LR. Correction of off resonance-related distortion in echo-planar imaging using EPI-based field maps. *Magn Reson Med*, 1998. 39(2):328–330. (Cited on p. 35.)

90 Zeng H, Gatenby JC, Zhao Y and Gore JC. New approach for correcting distortions in echo planar imaging. *Magn Reson Med*, 2004. 52(6):1373–1378. (Cited on p. 35.)

91 Butts K, de Crespigny A, Pauly JM and Moseley M. Diffusion-weighted interleaved echo-planar imaging with a pair of orthogonal navigator echoes. *Magn Reson Med*, 1996. 35(5):763–70. (Cited on p. 35.)

92 Brockstedt S, Moore JR, Thomsen C, Holtås S and Ståhlberg F. High-resolution diffusion imaging using phase-corrected segmented echo-planar imaging. *Magn Reson Imaging*, 2000. 18(6):649–657. (Cited on p. 35.)

93 Pruessmann KP, Weiger M, Scheidegger MB and Boesiger P. SENSE: sensitivity encoding for fast MRI. *Magn Reson Med*, 1999. 42(5):952–962. (Cited on p. 35.)

94 Jaermann T, Crelier G, Pruessmann KP, Golay X, Netsch T, van Muiswinkel AMC, Mori S, van Zijl PCM, Valavanis A, Kollias S and Boesiger P. SENSE-DTI at 3 T. *Magn Reson Med*, 2004. 51(2):230–236. (Cited on p. 35.)

95 Griswold MA, Jakob PM, Heidemann RM, Nittka M, Jellus V, Wang J, Kiefer B and Haase A. Generalized autocalibrating partially parallel acquisitions (GRAPPA). *Magn Reson Med*, 2002. 47(6):1202–1210. (Cited on p. 35.)

96 Bammer R, Auer M, Keeling SL, Augustin M, Stables LA, Prokesch RW, Stollberger R, Moseley ME and Fazekas F. Diffusion tensor imaging using single-shot SENSE-EPI. *Magn Reson Med*, 2002. 48(1):128–136. (Cited on p. 35.)

97 Bhagat YA, Emery DJ, Naik S, Yeo T and Beaulieu C. Comparison of Generalized Autocalibrating Partially Parallel Acquisitions and Modified Sensitivity Encoding for Diffusion Tensor Imaging. *AJNR Am J Neuroradiol*, 2007. 28(2):293–298. (Cited on p. 35.)

98 Skare S, Newbould RD, Clayton DB, Albers GW, Nagle S and Bammer R. Clinical multishot DW-EPI through parallel imaging with considerations of susceptibility, motion, and noise. *Magn Reson Med*, 2007. 57(5):881–890. (Cited on p. 35.)

99 Wirestam R, Greitz D, Thomsen C, Brockstedt S, Olsson MB and Stahlberg F. Theoretical and experimental evaluation of phase-dispersion

effects caused by brain motion in diffusion and perfusion MR imaging. *J Magn Reson Imaging*, 1996. 6(2):348–355. (Cited on p. 36.)

100 SKARE S and ANDERSSON JL. On the effects of gating in diffusion imaging of the brain using single shot EPI. *Magn Reson Imaging*, 2001. 19(8):1125–8. (Cited on pp. 36 and 90.)

101 BROCKSTEDT S, BORG M, GEIJER B, WIRESTAM R, THOMSEN C, HOLTÅS S and STÅHLBERG F. Triggering in quantitative diffusion imaging with single-shot EPI. *Acta Radiol*, 1999. 40(3):263–9. (Cited on pp. 36 and 90.)

102 REESE TG, HEID O, WEISSKOFF RM and WEDEEN VJ. Reduction of eddy-current-induced distortion in diffusion MRI using a twice-refocused spin echo. *Magn Reson Med*, 2003. 49(1):177–82. (Cited on p. 36.)

103 GUDBJARTSSON H, MAIER SE, MULKERN RV, MOROCZ IA, PATZ S and JOLESZ FA. Line scan diffusion imaging. *Magn Reson Med*, 1996. 36(4):509–19. (Cited on p. 38.)

104 ALSOP DC. Phase insensitive preparation of single-shot RARE: application to diffusion imaging in humans. *Magn Reson Med*, 1997. 38(4):527–533. (Cited on p. 38.)

105 NOLTE UG, FINSTERBUSCH J and FRAHM J. Rapid isotropic diffusion mapping without susceptibility artifacts: whole brain studies using diffusion-weighted single-shot STEAM MR imaging. *Magn Reson Med*, 2000. 44(5):731–736. (Cited on p. 38.)

106 PIPE JG, FARTHING VG and FORBES KP. Multishot diffusion-weighted FSE using PROPELLER MRI. *Magn Reson Med*, 2002. 47(1):42–52. (Cited on p. 38.)

107 SARLLS JE, NEWBOULD RD, ALTBACH MI, GMITRO AF, SEEGER J and TROUARD TP. Isotropic diffusion weighting in radial fast spin-echo magnetic resonance imaging. *Magn Reson Med*, 2005. 53(6):1347–1354. (Cited on p. 38.)

108 PIPE JG and ZWART N. Turboprop: improved PROPELLER imaging. *Magn Reson Med*, 2006. 55(2):380–385. (Cited on p. 38.)

109 JACKSON JH. On the anatomical, physiological and pathological investigation of epilepsies. *West Riding Lunatic Asylum Med Reports*, 1873. 3:315–39. (Cited on p. 39.)

110 DODSON WE. Definitions and classification of Epilepsy. In: SHORVON S, PERUCCA E, FISH D and DODSON E, editors, *The treatment of Epilepsy*, chapter 1, 3–20. Blackwell publishing, second edition, 2004. (Cited on p. 39.)

111 COMMISSION ON CLASSIFICATION AND TERMINOLOGY OF THE INTERNATIONAL LEAGUE AGAINST EPILEPSY. Proposal for revised clinical and electroencephalographic classification of epileptic seizures. *Epilepsia*, 1981. 22(4):489–501. (Cited on p. 39.)

112 COMMISSION ON CLASSIFICATION AND TERMINOLOGY OF THE INTERNATIONAL LEAGUE AGAINST EPILEPSY. Proposal for revised classification of epilepsies and epileptic syndromes. *Epilepsia*, 1989. 30(4):389–399. (Cited on pp. 39 and 41.)

113 FORSGREN L. Epidemiology and Prognosis of Epilepsy and its treatment. In: SHORVON S, PERUCCA E, FISH D and DODSON E, editors, *The treatment of Epilepsy*, chapter 2, 21–42. Blackwell publishing, second edition, 2004. (Cited on p. 42.)

114 HAUSER W. *Global comparative assessment in the health sector; disease burden, expenditures and intervention packages*. World Health Organization, 1994. (Cited on p. 42.)

115 FORSGREN L. Prevalence of epilepsy in adults in northern Sweden. *Epilepsia*, 1992. 33(3):450–458. (Cited on p. 42.)

116 FORSGREN L, BUCHT G, ERIKSSON S and BERGMARK L. Incidence and clinical characterization of unprovoked seizures in adults: a prospective population-based study. *Epilepsia*, 1996. 37(3):224–229. (Cited on p. 42.)

117 BRODIE MJ and DICHTER MA. Antiepileptic drugs. *N Engl J Med*, 1996. 334(3):168–175. (Cited on p. 43.)

118 DEVINSKY O. Patients with refractory seizures. *N Engl J Med*, 1999. 340(20):1565–1570. (Cited on p. 43.)

119 SANDER JW. Some aspects of prognosis in the epilepsies: a review. *Epilepsia*, 1993. 34(6):1007–1016. (Cited on p. 43.)

120 SHORVON SD. The epidemiology and treatment of chronic and refractory epilepsy. *Epilepsia*, 1996. 37 Suppl 2:S1–S3. (Cited on p. 43.)

121 KWAN P and BRODIE MJ. Early identification of refractory epilepsy. *N Engl J Med*, 2000. 342(5):314–319. (Cited on p. 43.)

122 PILLAI J and SPERLING MR. Interictal EEG and the diagnosis of epilepsy. *Epilepsia*, 2006. 47 Suppl 1:14–22. (Cited on p. 44.)

123 ERLICHMAN M. Electroencephalographic (EEG) video monitoring. *Health Technol Assess Rep*, 1990. (4):1–14. (Cited on p. 44.)

124 COOPER R, WINTER AL, CROW HJ and WALTER WG. Comparison of subcortical, cortical and scalp activity using chronically indwelling electrodes in man. *Electroencephalogr Clin Neurophysiol*, 1965. 18:217–228. (Cited on p. 44.)

125 SPANAKI M, SPENCER S, CORSI M, MACMULLAN J, SEIBYL J and ZUBAL I. Sensitivity and specificity of quantitative difference SPECT analysis in seizure localization. *Journal of Nuclear Medicine : Official Publication, Society of Nuclear Medicine*, 1999. 40(5):730–6. (Cited on p. 44.)

126 ROWE CC. Single-photon-emission computed tomography in epilepsy. In: KUZNIECKY RI and JACKSON GD, editors, *Magnetic Resonance in Epilepsy*, chapter 14, 385–394. Elsevier Academic Press, second edition, 2005. (Cited on pp. 44, 45, and 68.)

127 JUHÁSZ C, CHUGANI DC, MUZIK O and CHUGANI H. Positron-emission tomography in epilepsy. In: KUZNIECKY RI and JACKSON GD, editors, *Magnetic Resonance in Epilepsy*, chapter 15, 395–412. Elsevier Academic Press, second edition, 2005. (Cited on p. 45.)

128 JACKSON GD, KUZNIECKY R and BERKOVIC SF. Introduction to Epilepsy. In: *Magnetic Resonance in Epilepsy*, chapter 1, 1–16. Elsevier Academic Press, New York, second edition, 2005. (Cited on p. 45.)

129 SCHWARTZKROIN P. Basic mechanisms of epileptogenesis. In: WYLLIE E, editor, *The treatment of epilepsies: principles and practice*, 83–96. Lea & Febiger, Philadelphia, 1995. (Cited on p. 45.)

130 STEINLEIN OK. Genetic mechanisms that underlie epilepsy. *Nat Rev Neurosci*, 2004. 5(5):400–8. (Cited on p. 45.)

131 COULTER DA, HUGUENARD JR and PRINCE DA. Specific petit mal anticonvulsants reduce calcium currents in thalamic neurons. *Neurosci Lett*, 1989. 98(1):74–78. (Cited on p. 45.)

132 DICHTER M and SPENCER WA. Penicillin-induced interictal discharges from the cat hippocampus. II. Mechanisms underlying origin and restriction. *J Neurophysiol*, 1969. 32(5):663–687. (Cited on p. 46.)

133 CHOI DW and ROTHMAN SM. The role of glutamate neurotoxicity in hypoxic-ischemic neuronal death. *Annu Rev Neurosci*, 1990. 13:171–182. (Cited on p. 46.)

134 CHU K, KANG DW, KIM JY, CHANG KH and LEE SK. Diffusion-weighted magnetic resonance imaging in nonconvulsive status epilepticus. *Arch Neurol*, 2001. 58(6):993–998. (Cited on p. 46.)

135 DIEHL B, NAJM I, RUGGIERI P, TKACH J, MOHAMED A, MORRIS H, WYLLIE E, FISHER E, DUDA J, LIEBER M, BINGAMAN W and LUDERS HO. Postictal diffusion-weighted imaging for the localization of focal epileptic areas in temporal lobe epilepsy. *Epilepsia*, 2001. 42(1):21–8. (Cited on pp. 46, 74, and 114.)

136 EBISU T, ROONEY WD, GRAHAM SH, MANCUSO A, WEINER MW and MAUDSLEY AA. MR spectroscopic imaging and diffusion-weighted MRI for early detection of kainate-induced status epilepticus in the rat. *Magn Reson Med*, 1996. 36(6):821–828. (Cited on p. 46.)

137 HISANO T, OHNO M, EGAWA T, TAKANO T and SHIMADA M. Changes in diffusion-weighted MRI after status epilepticus. *Pediatr Neurol*, 2000. 22(4):327–329. (Cited on p. 46.)

138 HUFNAGEL A, WEBER J, MARKS S, LUDWIG T, DE GREIFF A, LEONHARDT G, WIDMANN G, STOLKE D and FORSTING M. Brain diffusion after single seizures. *Epilepsia*, 2003. 44(1):54–63. (Cited on pp. 46, 114, and 125.)

139 KIM JA, CHUNG JI, YOON PH, KIM DI, CHUNG TS, KIM EJ and JEONG EK. Transient MR signal changes in patients with generalized tonicoclonic seizure or status epilepticus: periictal diffusion-weighted imaging. *American Journal of Neuroradiology*, 2001. 22(6):1149–60. (Cited on p. 46.)

140 LANSBERG MG, O'BRIEN MW, NORBASH AM, MOSELEY ME, MORRELL M and ALBERS GW. MRI abnormalities associated with partial status epilepticus. *Neurology*, 1999. 52(5):1021–7. (Cited on pp. 46 and 114.)

141 MATHERN G, BABB T and ARMSTRONG D. Hippocampal sclerosis. In: ENGEL J and PEDLEY T, editors, *Epilepsy: A comprehensive textbook*, 133–155. Lippincott-Raven Publishers, Philadelphia, 1997. (Cited on pp. 46, 61, 98, 110, 111, 130, and 190.)

142 SEMAH F, PICOT MC, ADAM C, BROGLIN D, ARZIMANOGLOU A, BAZIN B, CAVALCANTI D and BAULAC M. Is the underlying cause of epilepsy a major prognostic factor for recurrence? *Neurology*, 1998. 51(5):1256–62. (Cited on p. 46.)

143 BURGERMAN RS, SPERLING MR, FRENCH JA, SAYKIN AJ and O'CONNOR MJ. Comparison of mesial versus neocortical onset temporal lobe seizures: neurodiagnostic findings and surgical outcome. *Epilepsia*, 1995. 36(7):662–670. (Cited on p. 46.)

144 WILLIAMSON P, ENGEL JJ and MUNARI C. Anatomic classification of localization-related epilepsies. In: ENGEL JJ and PEDLEY T, editors, *Epilepsy: A comprehensive Textbook*,

2405–2416. Lippincott-Raven Publishers, 1998. (Cited on p. 46.)

145 Quesney LF. Clinical and EEG features of complex partial seizures of temporal lobe origin. *Epilepsia*, 1986. 27 Suppl 2:S27–S45. (Cited on p. 46.)

146 Cendes F, Andermann F, Gloor P, Gambardella A, Lopes-Cendes I, Watson C, Evans A, Carpenter S and Olivier A. Relationship between atrophy of the amygdala and ictal fear in temporal lobe epilepsy. *Brain*, 1994. 117(4):739–746. (Cited on p. 47.)

147 Kotagal P, Lüders H, Morris HH, Dinner DS, Wyllie E, Godoy J and Rothner AD. Dystonic posturing in complex partial seizures of temporal lobe onset: a new lateralizing sign. *Neurology*, 1989. 39(2 Pt 1):196–201. (Cited on p. 47.)

148 Hirsch LJ, Lain AH and Walczak TS. Postictal nosewiping lateralizes and localizes to the ipsilateral temporal lobe. *Epilepsia*, 1998. 39(9):991–997. (Cited on p. 47.)

149 Broca P. Anatomie comparée des circonvolutions cérébrales: le grand lobe limbique. *Rev Anthropol*, 1878. 1:385–498. (Cited on p. 48.)

150 Meyer A. *Historical aspects of cerebral anatomy*. Oxford University Press, 1971. (Cited on p. 48.)

151 Lewis E. The significance of the term hippocampus. *J Comp Neurol*, 1923. 35:213–230. (Cited on p. 48.)

152 Lorente de Nó R. Studies on the structure of the cerebral cortex II. Continuation of the study of the ammonic system. *J f Psychol Neurol*, 1934. 46(2):113–177. (Cited on pp. 48 and 49.)

153 Standring S. *Gray's Anatomy*. Churchill Livingstone, 39th edition, 2004. (Cited on pp. 49 and 50.)

154 Braitenberg, V and Schüz, A. Some anatomical comments on the hippocampus. In: Seifert W, editor, *Neurobiology of the hippocampus*. Academic Press, London, 1983 21–37. (Cited on p. 49.)

155 Milner B. Disorders of learning and memory after temporal lobe lesions in man. *Clin Neurosurg*, 1972. 19:421–446. (Cited on p. 51.)

156 Kluver H and Bucy PC. Preliminary analysis of functions of the temporal lobes in monkeys. *Archives of neurology and Psychiatry*, 1939. 42(6):979–1000. (Cited on p. 52.)

157 Pestana EM and Gupta A. Fluctuating Kluver-Bucy syndrome in a child with epilepsy due to bilateral anterior temporal congenital malformations. *Epilepsy Behav*, 2007. 10(2):340–3. (Cited on p. 52.)

158 Heath RG. *Studies in schizophrenia; a multidisciplinary approach to mind-brain relationships*. Harvard Univ. Press, Cambridge, Mass., 1954. (Cited on p. 53.)

159 Papez J. A Proposed Mechanism of Emotion. *Archives of Neurology and Pathology*, 1937. 38:725–743. (Cited on pp. 53 and 78.)

160 Shipley MT. Presubiculum afferents to the entorhinal area and the Papez circuit. *Brain Res*, 1974. 67(1):162–168. (Cited on p. 55.)

161 Gloor P. *The temporal lobe and Limbic System*. Oxford University Press, New York, 1997. (Cited on pp. 55, 98, and 110.)

162 Wyss JM, Swanson LW and Cowan WM. The organization of the fimbria,

dorsal fornix and ventral hippocampal commissure in the rat. *Anat Embryol (Berl)*, 1980. 158(3):303–316. (Cited on pp. 55, 179, and 184.)

163 ABOITIZ F, SCHEIBEL AB, FISHER RS and ZAIDEL E. Fiber composition of the human corpus callosum. *Brain Res*, 1992. 598(1-2):143–153. (Cited on p. 55.)

164 VERHAART W and KRAMER W. The uncrossed pyramidal tract. *Acta Psychiatr Neurol Scand*, 1952. 27(1-2):181–200. (Cited on p. 55.)

165 POWELL T, GUILLERY R and COWAN W. A quantitative study of the fornix-mamillo-thalamic system. *Anatomy*, 1957. 91:419–437. (Cited on p. 56.)

166 DAITZ H. Note on the fibre content of the fornix system in man. *Brain*, 1953. 76:509–512. (Cited on p. 56.)

167 SWANSON LW and COWAN WM. Hippocampo-hypothalamic connections: origin in subicular cortex, not ammon's horn. *Science*, 1975. 189(4199):303–4. (Cited on pp. 56 and 190.)

168 GLOOR P, SALANOVA V, OLIVIER A and QUESNEY LF. The human dorsal hippocampal commissure. An anatomically identifiable and functional pathway. *Brain*, 1993. 116 (Pt 5):1249–73. (Cited on p. 56.)

169 WILSON CL, ISOKAWA M, BABB TL and CRANDALL PH. Functional connections in the human temporal lobe. I. Analysis of limbic system pathways using neuronal responses evoked by electrical stimulation. *Exp Brain Res*, 1990. 82(2):279–292. (Cited on p. 56.)

170 WILSON CL, ISOKAWA M, BABB TL, CRANDALL PH, LEVESQUE MF and ENGEL J. Functional connections in the human temporal lobe. II. Evidence for a loss of functional linkage between contralateral limbic structures. *Exp Brain Res*, 1991. 85(1):174–187. (Cited on p. 56.)

171 AMARAL DG, INSAUSTI R and COWAN WM. The commissural connections of the monkey hippocampal formation. *J Comp Neurol*, 1984. 224(3):307–336. (Cited on pp. 56 and 191.)

172 RAMÓN Y CAJAL, SANTIAGO. *Histologie du systèème nerveux de l'homme & des vertébrés*. Maloine, Paris, 1909. (Cited on p. 58.)

173 EARLE KM, BALDWIN M and PENFIELD W. Incisural sclerosis and temporal lobe seizures produced by hippocampal herniation at birth. *AMA Arch Neurol Psychiatry*, 1953. 69(1):27–42. (Cited on p. 59.)

174 MARGERISON JH and CORSELLIS JA. Epilepsy and the temporal lobes. A clinical, electroencephalographic and neuropathological study of the brain in epilepsy, with particular reference to the temporal lobes. *Brain*, 1966. 89(3):499–530. (Cited on pp. 59, 114, and 123.)

175 BRUTON CJ. *The neuropathology of temporal lobe epilepsy*. Maudsley monographs, no. 31. Oxford University Press, Oxford ;; New York, 1988. (Cited on p. 59.)

176 HOUSER CR. Granule cell dispersion in the dentate gyrus of humans with temporal lobe epilepsy. *Brain Res*, 1990. 535(2):195–204. (Cited on p. 59.)

177 ROJIANI AM, EMERY JA, ANDERSON KJ and MASSEY JK. Distribution of heterotopic neurons in normal hemispheric white matter: a morphometric analysis. *J Neuropathol Exp Neurol*, 1996. 55(2):178–183. (Cited on p. 59.)

178 EMERY JA, ROPER SN and ROJIANI AM. White matter neuronal hetero-

topia in temporal lobe epilepsy: a morphometric and immunohistochemical study. *J Neuropathol Exp Neurol*, 1997. 56(12):1276–82. (Cited on p. 59.)

179 CAZAUVIEILH B. De l'épilepsie considérée dans ses rapports avec l'aliénation mentale. Recherche sur la nature et le siège de ces deux maladies (II^{me} partie). *Arch Gén Méd*, 1826. 10:5–50. (Cited on p. 59.)

180 SOMMER W. Erkrankung des Ammonshorns als aetiologisches Moment der Epilepsie. *Arch Psychiatr Nervenkr*, 1880. 10:631–675. (Cited on p. 59.)

181 BRATZ E. Ammonshornbefunde bei Epileptischen. *Arch Psychiat Nervenkr*, 1899. 31:820–835. (Cited on p. 59.)

182 SPIELMEYER W. Die Pathogenese des epileptischen Krampfes. Histopathologischer Teil. *Ztschr f d ges Neurol u Psychiat*, 1927. 109:501–520. (Cited on p. 59.)

183 VOGT C and VOGT O. Siz und Wesen der Krankheiten im Lichte der topistischen Hirnforschung und des Varierens der Tiere. I. Teil: Befunde der topistischen Hirnforschung als Beitrag zur Lehre vom Krankheitssitz. *J Psychol Neurol (Leipzig)*, 1937. 47:237–457. (Cited on p. 59.)

184 VOGT O. Der Begriff der Pathoklise. *J Psychol Neurol (Leipzig)*, 1925. 31:245–255. (Cited on p. 59.)

185 GASTAUT H. Colloque sur les problemes d'anatomie normale et pathologique poses par les decharges epileptiques. *Acta Medica Belgica*, 1956. 5–20. (Cited on p. 59.)

186 NORMAN RM. The neuropathology of status epilepticus. *Med Sci Law*, 1964. 14:46–51. (Cited on p. 60.)

187 VEITH G. Anatomische studie uber die Ammonshornsklerose im epileptikergehirn. *Dtsch Z Nervenheilkd*, 1970. 197(4):293–314. (Cited on p. 60.)

188 MONAGHAN DT and COTMAN CW. Distribution of N-methyl-D-aspartate-sensitive L-[3H]glutamate-binding sites in rat brain. *J Neurosci*, 1985. 5(11):2909–2919. (Cited on p. 60.)

189 TREMBLAY E, REPRESA A and BEN-ARI Y. Autoradiographic localization of kainic acid binding sites in the human hippocampus. *Brain Res*, 1985. 343(2):378–382. (Cited on p. 60.)

190 COTMAN CW and MONAGHAN DT. Anatomical organization of excitatory amino acid receptors and their properties. *Adv Exp Med Biol*, 1986. 203:237–252. (Cited on p. 60.)

191 BAIMBRIDGE KG and MILLER JJ. Immunohistochemical localization of calcium-binding protein in the cerebellum, hippocampal formation and olfactory bulb of the rat. *Brain Res*, 1982. 245(2):223–229. (Cited on p. 60.)

192 SLOVITER RS. Calcium-binding protein (calbindin-D28k) and parvalbumin immunocytochemistry: localization in the rat hippocampus with specific reference to the selective vulnerability of hippocampal neurons to seizure activity. *J Comp Neurol*, 1989. 280(2):183–196. (Cited on p. 60.)

193 BEN-ARI Y. Limbic seizure and brain damage produced by kainic acid: mechanisms and relevance to human temporal lobe epilepsy. *Neuroscience*, 1985. 14(2):375–403. (Cited on p. 60.)

194 OLNEY JW, HO OL and RHEE V. Cytotoxic effects of acidic and sulphur containing amino acids on the infant mouse central nervous system. *Exp*

Brain Res, 1971. 14(1):61–76. (Cited on p. 60.)

195 OLNEY JW, RHEE V and HO OL. Kainic acid: a powerful neurotoxic analogue of glutamate. *Brain Res*, 1974. 77(3):507–512. (Cited on p. 60.)

196 OLNEY JW, DEGUBAREFF T and SLOVITER RS. "Epileptic" brain damage in rats induced by sustained electrical stimulation of the perforant path. II. Ultrastructural analysis of acute hippocampal pathology. *Brain Res Bull*, 1983. 10(5):699–712. (Cited on p. 60.)

197 SLOVITER RS. "Epileptic" brain damage in rats induced by sustained electrical stimulation of the perforant path. I. Acute electrophysiological and light microscopic studies. *Brain Res Bull*, 1983. 10(5):675–697. (Cited on p. 60.)

198 SLOVITER RS. Permanently altered hippocampal structure, excitability, and inhibition after experimental status epilepticus in the rat: the "dormant basket cell" hypothesis and its possible relevance to temporal lobe epilepsy. *Hippocampus*, 1991. 1(1):41–66. (Cited on p. 60.)

199 NADLER JV, PERRY BW, GENTRY C and COTMAN CW. Loss and reacquisition of hippocampal synapses after selective destruction of CA3-CA4 afferents with kainic acid. *Brain Res*, 1980. 191(2):387–403. (Cited on p. 61.)

200 HANNESSON DK, ARMITAGE LL, MOHAPEL P and CORCORAN ME. Time course of mossy fiber sprouting following bilateral transection of the fimbria/fornix. *Neuroreport*, 1997. 8(9-10):2299–303. (Cited on pp. 61 and 111.)

201 TAUCK DL and NADLER JV. Evidence of functional mossy fiber sprouting in hippocampal formation of kainic acid-treated rats. *J Neurosci*, 1985. 5(4):1016–1022. (Cited on p. 61.)

202 CAVAZOS JE, ZHANG P, QAZI R and SUTULA TP. Ultrastructural features of sprouted mossy fiber synapses in kindled and kainic acid-treated rats. *J Comp Neurol*, 2003. 458(3):272–292. (Cited on p. 61.)

203 WENZEL HJ, WOOLLEY CS, ROBBINS CA and SCHWARTZKROIN PA. Kainic acid-induced mossy fiber sprouting and synapse formation in the dentate gyrus of rats. *Hippocampus*, 2000. 10(3):244–260. (Cited on p. 61.)

204 SLOVITER RS. Possible functional consequences of synaptic reorganization in the dentate gyrus of kainate-treated rats. *Neurosci Lett*, 1992. 137(1):91–96. (Cited on p. 61.)

205 DANSCHER G and ZIMMER J. An improved Timm sulphide silver method for light and electron microscopic localization of heavy metals in biological tissues. *Histochemistry*, 1978. 55(1):27–40. (Cited on p. 61.)

206 FROTSCHER M and ZIMMER J. Lesion-induced mossy fibers to the molecular layer of the rat fascia dentata: identification of postsynaptic granule cells by the Golgi-EM technique. *J Comp Neurol*, 1983. 215(3):299–311. (Cited on p. 61.)

207 NADLER JV, PERRY BW and COTMAN CW. Selective reinnervation of hippocampal area CA1 and the fascia dentata after destruction of CA3-CA4 afferents with kainic acid. *Brain Res*, 1980. 182(1):1–9. (Cited on p. 61.)

208 HOUSER CR, MIYASHIRO JE, SWARTZ BE, WALSH GO, RICH JR and DELGADO-ESCUETA AV. Altered patterns of dynorphin immunoreactivity suggest

mossy fiber reorganization in human hippocampal epilepsy. *J Neurosci*, 1990. 10(1):267–282. (Cited on p. 61.)

209 SUTULA T, CASCINO G, CAVAZOS J, PARADA I and RAMIREZ L. Mossy fiber synaptic reorganization in the epileptic human temporal lobe. *Ann Neurol*, 1989. 26(3):321–30. (Cited on p. 61.)

210 REPRESA A, ROBAIN O, TREMBLAY E and BEN-ARI Y. Hippocampal plasticity in childhood epilepsy. *Neurosci Lett*, 1989. 99(3):351–355. (Cited on p. 61.)

211 DE LANEROLLE NC, KIM JH, ROBBINS RJ and SPENCER DD. Hippocampal interneuron loss and plasticity in human temporal lobe epilepsy. *Brain Res*, 1989. 495(2):387–395. (Cited on p. 61.)

212 JEFFERYS JG. Hippocampal sclerosis and temporal lobe epilepsy: cause or consequence? *Brain*, 1999. 122 (Pt 6):1007–8. (Cited on p. 61.)

213 VELISEK L and MOSHE SL. Temporal lobe epileptogenesis and epilepsy in the developing brain: bridging the gap between the laboratory and the clinic. Progression, but in what direction? *Epilepsia*, 2003. 44 Suppl 12:51–9. (Cited on pp. 61, 62, and 127.)

214 ANNEGERS JF, HAUSER WA, ELVEBACK LR and KURLAND LT. The risk of epilepsy following febrile convulsions. *Neurology*, 1979. 29(3):297–303. (Cited on p. 62.)

215 ANNEGERS JF, HAUSER WA, SHIRTS SB and KURLAND LT. Factors prognostic of unprovoked seizures after febrile convulsions. *N Engl J Med*, 1987. 316(9):493–8. (Cited on p. 62.)

216 MEYER A, FALCONER MA and BECK E. Pathological findings in temporal lobe epilepsy. *J Neurol Neurosurg Psychiatry*, 1954. 17(4):276–285. (Cited on p. 62.)

217 FALCONER MA. Mesial temporal (Ammon's horn) sclerosis as a common cause of epilepsy. Aetiology, treatment, and prevention. *Lancet*, 1974. 2(7883):767–70. (Cited on p. 62.)

218 FRENCH JA, WILLIAMSON PD, THADANI VM, DARCEY TM, MATTSON RH, SPENCER SS and SPENCER DD. Characteristics of medial temporal lobe epilepsy: I. Results of history and physical examination. *Ann Neurol*, 1993. 34(6):774–780. (Cited on p. 62.)

219 WIESER HG. ILAE Commission Report. Mesial temporal lobe epilepsy with hippocampal sclerosis. *Epilepsia*, 2004. 45(6):695–714. (Cited on pp. 62, 124, 127, and 130.)

220 HAUSER WA and LEE JR. Do seizures beget seizures? *Prog Brain Res*, 2002. 135:215–9. (Cited on p. 62.)

221 DAM AM. Epilepsy and neuron loss in the hippocampus. *Epilepsia*, 1980. 21(6):617–29. (Cited on p. 62.)

222 MATHERN GW, ADELSON PD, CAHAN LD and LEITE JP. Hippocampal neuron damage in human epilepsy: Meyer's hypothesis revisited. *Prog Brain Res*, 2002. 135:237–251. (Cited on p. 62.)

223 BABB TL, BROWN WJ, PRETORIUS J, DAVENPORT C, LIEB JP and CRANDALL PH. Temporal lobe volumetric cell densities in temporal lobe epilepsy. *Epilepsia*, 1984. 25(6):729–740. (Cited on p. 62.)

224 FUERST D, SHAH J, KUPSKY WJ, JOHNSON R, SHAH A, HAYMAN-ABELLO B, ERGH T, POORE Q, CANADY A and WATSON C. Volumetric MRI, pathological, and neuropsychological progression in hippocampal sclerosis. *Neurology*, 2001. 57(2):184–8. (Cited on p. 62.)

225 KÄLVIÄINEN R and SALMENPERA T. Do recurrent seizures cause neuronal damage? A series of studies with MRI volumetry in adults with partial epilepsy. *Prog Brain Res*, 2002. 135:279–95. (Cited on p. 62.)

226 VAN PAESSCHEN W, DUNCAN JS, STEVENS JM and CONNELLY A. Longitudinal quantitative hippocampal magnetic resonance imaging study of adults with newly diagnosed partial seizures: one-year follow-up results. *Epilepsia*, 1998. 39(6):633–9. (Cited on p. 62.)

227 FUERST D, SHAH J, SHAH A and WATSON C. Hippocampal sclerosis is a progressive disorder: A longitudinal volumetric MRI study. *Annals of Neurology*, 2003. 53(3):413–416. (Cited on p. 62.)

228 BERNASCONI N, NATSUME J and BERNASCONI A. Progression in temporal lobe epilepsy: differential atrophy in mesial temporal structures. *Neurology*, 2005. 65(2):223–228. (Cited on p. 62.)

229 SALMENPERA T, KONONEN M, ROBERTS N, VANNINEN R, PITKANEN A and KALVIAINEN R. Hippocampal damage in newly diagnosed focal epilepsy: a prospective MRI study. *Neurology*, 2005. 64(1):62–8. (Cited on p. 62.)

230 LIU RS, LEMIEUX L, BELL GS, HAMMERS A, SISODIYA SM, BARTLETT PA, SHORVON SD, SANDER JW and DUNCAN JS. Progressive neocortical damage in epilepsy. *Ann Neurol*, 2003. 53(3):312–24. (Cited on p. 62.)

231 BONILHA L, RORDEN C, APPENZELLER S, COAN AC, CENDES F and LI LM. Gray matter atrophy associated with duration of temporal lobe epilepsy. *Neuroimage*, 2006. 32(3):1070–1079. (Cited on p. 62.)

232 LIN JJ, SALAMON N, LEE AD, DUTTON RA, GEAGA JA, HAYASHI KM, LUDERS E, TOGA AW, ENGEL J J and THOMPSON PM. Reduced neocortical thickness and complexity mapped in mesial temporal lobe epilepsy with hippocampal sclerosis. *Cereb Cortex*, 2007. 17(9):2007–18. (Cited on pp. 62 and 73.)

233 NATSUME J, BERNASCONI N, ANDERMANN F and BERNASCONI A. MRI volumetry of the thalamus in temporal, extratemporal, and idiopathic generalized epilepsy. *Neurology*, 2003. 60(8):1296–1300. (Cited on p. 62.)

234 TASCH E, CENDES F, LI LM, DUBEAU F, ANDERMANN F and ARNOLD DL. Neuroimaging evidence of progressive neuronal loss and dysfunction in temporal lobe epilepsy. *Ann Neurol*, 1999. 45(5):568–76. (Cited on p. 62.)

235 BERNASCONI A, TASCH E, CENDES F, LI LM and ARNOLD DL. Proton magnetic resonance spectroscopic imaging suggests progressive neuronal damage in human temporal lobe epilepsy. *Progress in Brain Research*, 2002. 135:297–304. (Cited on p. 62.)

236 CENDES F, ANDERMANN F, DUBEAU F, MATTHEWS PM and ARNOLD DL. Normalization of neuronal metabolic dysfunction after surgery for temporal lobe epilepsy. Evidence from proton MR spectroscopic imaging. *Neurology*, 1997. 49(6):1525–33. (Cited on pp. 62, 68, 115, and 126.)

237 COMMISSION ON NEUROIMAGING OF THE INTERNATIONAL LEAGUE AGAINST EPILEPSY. Recommendations for neuroimaging of patients with epilepsy. *Epilepsia*, 1997. 38(11):1255–1256. (Cited on p. 63.)

238 KUZNIECKY R, DE LA SAYETTE V, ETHIER R, MELANSON D, ANDERMANN

F, Berkovic S, Robitaille Y, Olivier A, Peters T and Feindel W. Magnetic resonance imaging in temporal lobe epilepsy: pathological correlations. *Ann Neurol*, 1987. 22(3):341–347. (Cited on pp. 63 and 65.)

239 Berkovic SF, Andermann F, Olivier A, Ethier R, Melanson D, Robitaille Y, Kuzniecky R, Peters T and Feindel W. Hippocampal sclerosis in temporal lobe epilepsy demonstrated by magnetic resonance imaging. *Ann Neurol*, 1991. 29(2):175–182. (Cited on pp. 63 and 65.)

240 Jackson GD, Berkovic SF, Duncan JS and Connelly A. Optimizing the diagnosis of hippocampal sclerosis using MR imaging. *AJNR Am J Neuroradiol*, 1993. 14(3):753–762. (Cited on pp. 63 and 65.)

241 Van Paesschen W, Revesz T, Duncan JS, King MD and Connelly A. Quantitative neuropathology and quantitative magnetic resonance imaging of the hippocampus in temporal lobe epilepsy. *Annals of Neurology*, 1997. 42(5):756–66. (Cited on pp. 63, 98, 100, and 111.)

242 Briellmann RS, Kalnins RM, Berkovic SF and Jackson GD. Hippocampal pathology in refractory temporal lobe epilepsy: T2-weighted signal change reflects dentate gliosis. *Neurology*, 2002. 58(2):265–271. (Cited on p. 63.)

243 Hajnal JV, Bryant DJ, Kasuboski L, Pattany PM, De Coene B, Lewis PD, Pennock JM, Oatridge A, Young IR and Bydder GM. Use of fluid attenuated inversion recovery (FLAIR) pulse sequences in MRI of the brain. *Journal of Computer Assisted Tomography*, 1992. 16(6):841–4. (Cited on pp. 64 and 79.)

244 Jack CR, Rydberg CH, Krecke KN, Trenerry MR, Parisi JE, Rydberg JN, Cascino GD and Riederer SJ. Mesial temporal sclerosis: diagnosis with fluid-attenuated inversion-recovery versus spin-echo MR imaging. *Radiology*, 1996. 199(2):367–373. (Cited on p. 64.)

245 Meiners LC, van Gils AD, Kort GD, Graaf YVD, Jansen GH and Veelen CWV. Fast fluid-attenuated inversion recovery (FLAIR) compared with T2-weighted spin-echo in the magnetic resonance diagnosis of mesial temporal sclerosis. *Invest Radiol*, 1999. 34(2):134–142. (Cited on p. 64.)

246 Cascino GD, Jack J C R, Parisi JE, Sharbrough FW, Hirschorn KA, Meyer FB, Marsh WR and O'Brien PC. Magnetic resonance imaging-based volume studies in temporal lobe epilepsy: pathological correlations. *Annals of Neurology*, 1991. 30(1):31–6. (Cited on pp. 65, 98, and 111.)

247 Lencz T, McCarthy G, Bronen RA, Scott TM, Inserni JA, Sass KJ, Novelly RA, Kim JH and Spencer DD. Quantitative magnetic resonance imaging in temporal lobe epilepsy: relationship to neuropathology and neuropsychological function. *Annals of Neurology*, 1992. 31(6):629–37. (Cited on p. 65.)

248 Bronen RA, Fulbright RK, King D, Kim JH, Spencer SS, Spencer DD and Lange RC. Qualitative MR imaging of refractory temporal lobe epilepsy requiring surgery: correlation with pathology and seizure outcome after surgery. *AJR American Journal of Roentgenology*, 1997. 169(3):875–82. (Cited on p. 65.)

249 Jackson GD, Berkovic SF, Tress BM, Kalnins RM, Fabinyi GC and Bladin

PF. Hippocampal sclerosis can be reliably detected by magnetic resonance imaging. *Neurology*, 1990. 40(12):1869–75. (Cited on p. 65.)

250 VAN PAESSCHEN W, CONNELLY A, KING MD, JACKSON GD and DUNCAN JS. The spectrum of hippocampal sclerosis: a quantitative magnetic resonance imaging study. *Annals of Neurology*, 1997. 41(1):41–51. (Cited on pp. 65 and 72.)

251 GRANT PE, VIGNERON DB and BARKOVICH AJ. High-resolution imaging of the brain. *Magnetic Resonance Imaging Clinics of North America*, 1998. 6(1):139–54. (Cited on p. 65.)

252 KNAKE S, TRIANTAFYLLOU C, WALD LL, WIGGINS G, KIRK GP, LARSSON PG, STUFFLEBEAM SM, FOLEY MT, SHIRAISHI H, DALE AM, HALGREN E and GRANT PE. 3T phased array MRI improves the presurgical evaluation in focal epilepsies: a prospective study.[see comment]. *Neurology*, 2005. 65(7):1026–31. (Cited on p. 65.)

253 MITCHELL LA, JACKSON GD, KALNINS RM, SALING MM, FITT GJ, ASHPOLE RD and BERKOVIC SF. Anterior temporal abnormality in temporal lobe epilepsy: a quantitative MRI and histopathologic study. *Neurology*, 1999. 52(2):327–36. (Cited on p. 65.)

254 BLÜMCKE I, THOM M and WIESTLER OD. Ammon's horn sclerosis: a maldevelopmental disorder associated with temporal lobe epilepsy. *Brain Pathol*, 2002. 12(2):199–211. (Cited on p. 65.)

255 KUZNIECKY RI, BILIR E, GILLIAM F, FAUGHT E, PALMER C, MORAWETZ R and JACKSON G. Multimodality MRI in mesial temporal sclerosis: relative sensitivity and specificity. *Neurology*, 1997. 49(3):774–778. (Cited on pp. 65 and 130.)

256 JACKSON GD, CONNELLY A, DUNCAN JS, GRUNEWALD RA and GADIAN DG. Detection of hippocampal pathology in intractable partial epilepsy: increased sensitivity with quantitative magnetic resonance T2 relaxometry. *Neurology*, 1993. 43(9):1793–9. (Cited on pp. 65 and 66.)

257 BERNASCONI A, BERNASCONI N, CARAMANOS Z, REUTENS DC, ANDERMANN F, DUBEAU F, TAMPIERI D, PIKE BG and ARNOLD DL. T2 relaxometry can lateralize mesial temporal lobe epilepsy in patients with normal MRI. *Neuroimage*, 2000. 12(6):739–46. (Cited on pp. 65, 72, 98, 100, 131, and 132.)

258 WOERMANN FG, STEINER H, BARKER GJ, BARTLETT PA, ELGER CE, DUNCAN JS and SYMMS MR. A fast FLAIR dual-echo technique for hippocampal T2 relaxometry: first experiences in patients with temporal lobe epilepsy. *J Magn Reson Imaging*, 2001. 13(4):547–552. (Cited on p. 66.)

259 DUNCAN JS, BARTLETT P and BARKER GJ. Technique for measuring hippocampal T2 relaxation time. *AJNR Am J Neuroradiol*, 1996. 17(10):1805–1810. (Cited on p. 66.)

260 OKUJAVA M, SCHULZ R, EBNER A and WOERMANN FG. Measurement of temporal lobe T2 relaxation times using a routine diagnostic MR imaging protocol in epilepsy. *Epilepsy Research*, 2002. 48(1-2):131–42. (Cited on pp. 66, 98, and 100.)

261 WOERMANN FG, BARKER GJ, BIRNIE KD, MEENCKE HJ and DUNCAN JS. Regional changes in hippocampal T2 relaxation and volume: a quantitative magnetic resonance imaging study of hippocampal sclerosis. *Journal of Neurology, Neurosurgery & Psychiatry*, 1998. 65(5):656–64. (Cited on pp. 66, 98, and 100.)

262 MacKay A, Whittall K, Adler J, Li D, Paty D and Graeb D. In vivo visualization of myelin water in brain by magnetic resonance. *Magn Reson Med*, 1994. 31(6):673–677. (Cited on p. 66.)

263 Menon RS, Rusinko MS and Allen PS. Proton relaxation studies of water compartmentalization in a model neurological system. *Magn Reson Med*, 1992. 28(2):264–274. (Cited on p. 66.)

264 Whittall KP, MacKay AL and Li DK. Are mono-exponential fits to a few echoes sufficient to determine T2 relaxation for in vivo human brain? *Magn Reson Med*, 1999. 41(6):1255–1257. (Cited on p. 66.)

265 Jack CR, Bentley MD, Twomey CK and Zinsmeister AR. MR imaging-based volume measurements of the hippocampal formation and anterior temporal lobe: validation studies. *Radiology*, 1990. 176(1):205–209. (Cited on p. 66.)

266 Baldwin GN, Tsuruda JS, Maravilla KR, Hamill GS and Hayes CE. The fornix in patients with seizures caused by unilateral hippocampal sclerosis: detection of unilateral volume loss on MR images. *AJR American Journal of Roentgenology*, 1994. 162(5):1185–9. (Cited on p. 67.)

267 Bilir E, Craven W, Hugg J, Gilliam F, Martin R, Faught E and Kuzniecky R. Volumetric MRI of the limbic system: anatomic determinants. *Neuroradiology*, 1998. 40(3):138–44. (Cited on pp. 67 and 142.)

268 Burneo JG, Bilir E, Faught E, Morawetz R, Knowlton RC, Martin R and Kuzniecky RI. Significance of fornix atrophy in temporal lobe epilepsy surgery outcome. *Archives of Neurology*, 2003. 60(9):1238–42. (Cited on p. 67.)

269 Kim JH, Tien RD, Felsberg GJ, Osumi AK and Lee N. Clinical significance of asymmetry of the fornix and mamillary body on MR in hippocampal sclerosis. *Ajnr: American Journal of Neuroradiology*, 1995. 16(3):509–15. (Cited on pp. 67 and 98.)

270 Shen D, Moffat S, Resnick SM and Davatzikos C. Measuring size and shape of the hippocampus in MR images using a deformable shape model. *Neuroimage*, 2002. 15(2):422–434. (Cited on p. 67.)

271 Connelly A, Jackson GD, Duncan JS, King MD and Gadian DG. Magnetic resonance spectroscopy in temporal lobe epilepsy. *Neurology*, 1994. 44(8):1411–1417. (Cited on pp. 68 and 71.)

272 Hetherington H, Kuzniecky R, Pan J, Mason G, Morawetz R, Harris C, Faught E, Vaughan T and Pohost G. Proton nuclear magnetic resonance spectroscopic imaging of human temporal lobe epilepsy at 4.1 T. *Ann Neurol*, 1995. 38(3):396–404. (Cited on p. 68.)

273 Cendes F, Andermann F, Dubeau F and Arnold DL. Proton magnetic resonance spectroscopic images and MRI volumetric studies for lateralization of temporal lobe epilepsy. *Magn Reson Imaging*, 1995. 13(8):1187–1191. (Cited on p. 68.)

274 Meiners LC, van der Grond J, van Rijen PC, Springorum R, de Kort GA and Jansen GH. Proton magnetic resonance spectroscopy of temporal lobe white matter in patients with histologically proven hippocampal sclerosis. *J Magn Reson Imaging*, 2000. 11(1):25–31. (Cited on p. 68.)

275 Cross JH, Connelly A, Jackson GD, Johnson CL, Neville BG and Gadian DG. Proton magnetic resonance spectroscopy in children with temporal lobe epilepsy. *Ann Neurol*, 1996. 39(1):107–113. (Cited on p. 68.)

276 Chu WJ, Kuzniecky RI, Hugg JW, Abou-Khalil B, Gilliam F, Faught E and Hetherington HP. Statistically driven identification of focal metabolic abnormalities in temporal lobe epilepsy with corrections for tissue heterogeneity using 1H spectroscopic imaging. *Magn Reson Med*, 2000. 43(3):359–367. (Cited on p. 68.)

277 Cendes F, Caramanos Z, Andermann F, Dubeau F and Arnold DL. Proton magnetic resonance spectroscopic imaging and magnetic resonance imaging volumetry in the lateralization of temporal lobe epilepsy: a series of 100 patients. *Ann Neurol*, 1997. 42(5):737–746. (Cited on pp. 68 and 144.)

278 Najm IM, Wang Y, Shedid D, Lüders HO, Ng TC and Comair YG. MRS metabolic markers of seizures and seizure-induced neuronal damage. *Epilepsia*, 1998. 39(3):244–250. (Cited on p. 68.)

279 Hugg JW, Kuzniecky RI, Gilliam FG, Morawetz RB, Fraught RE and Hetherington HP. Normalization of contralateral metabolic function following temporal lobectomy demonstrated by 1H magnetic resonance spectroscopic imaging. *Ann Neurol*, 1996. 40(2):236–9. (Cited on pp. 68, 115, and 126.)

280 Vermathen P, Ende G, Laxer KD, Walker JA, Knowlton RC, Barbaro NM, Matson GB and Weiner MW. Temporal lobectomy for epilepsy: recovery of the contralateral hippocampus measured by (1)H MRS. *Neurology*, 2002. 59(4):633–6. (Cited on pp. 68, 115, and 126.)

281 Serles W, Li LM, Antel SB, Cendes F, Gotman J, Olivier A, Andermann F, Dubeau F and Arnold DL. Time Course of Postoperative Recovery of N-Acetyl-Aspartate in Temporal Lobe Epilepsy. *Epilepsia*, 2001. 42(2):190–197. (Cited on pp. 68, 115, and 126.)

282 Hetherington HP, Kim JH, Pan JW and Spencer DD. 1H and 31P spectroscopic imaging of epilepsy: spectroscopic and histologic correlations. *Epilepsia*, 2004. 45 Suppl 4:17–23. (Cited on pp. 68 and 71.)

283 Engel J, Kuhl DE, Phelps ME, Rausch R and Nuwer M. Local cerebral metabolism during partial seizures. *Neurology*, 1983. 33(4):400–413. (Cited on p. 68.)

284 Rowe CC, Berkovic SF, Austin MC, McKay WJ and Bladin PF. Patterns of postictal cerebral blood flow in temporal lobe epilepsy: qualitative and quantitative analysis. *Neurology*, 1991. 41(7):1096–1103. (Cited on p. 68.)

285 Huberfeld G, Habert MO, Clemenceau S, Maksud P, Baulac M and Adam C. Ictal brain hyperperfusion contralateral to seizure onset: the SPECT mirror image. *Epilepsia*, 2006. 47(1):123–33. (Cited on p. 68.)

286 Knowlton RC, Laxer KD, Ende G, Hawkins RA, Wong ST, Matson GB, Rowley HA, Fein G and Weiner MW. Presurgical multimodality neuroimaging in electroencephalographic lateralized temporal lobe epilepsy. *Ann Neurol*, 1997. 42(6):829–837. (Cited on p. 69.)

287 Gaillard WD, Bhatia S, Bookheimer SY, Fazilat S, Sato S and Theodore WH. FDG-PET and volumetric MRI in

the evaluation of patients with partial epilepsy. *Neurology*, 1995. 45(1):123–126. (Cited on pp. 69 and 71.)

288 THEODORE WH. Implications of neuroimaging for the treatment of epilepsy. *Ann Neurol*, 2003. 53(3):286–288. (Cited on p. 69.)

289 LAMUSUO S, JUTILA L, YLINEN A, KÄLVIÄINEN R, MERVAALA E, HAAPARANTA M, JÄÄSKELÄINEN S, PARTANEN K, VAPALAHTI M and RINNE J. [18F]FDG-PET reveals temporal hypometabolism in patients with temporal lobe epilepsy even when quantitative MRI and histopathological analysis show only mild hippocampal damage. *Arch Neurol*, 2001. 58(6):933–939. (Cited on p. 69.)

290 KWONG KK, BELLIVEAU JW, CHESLER DA, GOLDBERG IE, WEISSKOFF RM, PONCELET BP, KENNEDY DN, HOPPEL BE, COHEN MS and TURNER R. Dynamic magnetic resonance imaging of human brain activity during primary sensory stimulation. *Proc Natl Acad Sci U S A*, 1992. 89(12):5675–5679. (Cited on p. 69.)

291 OGAWA S, LEE TM, KAY AR and TANK DW. Brain magnetic resonance imaging with contrast dependent on blood oxygenation. *Proc Natl Acad Sci U S A*, 1990. 87(24):9868–9872. (Cited on p. 69.)

292 ALSOP DC and DETRE JA. Reduced transit-time sensitivity in noninvasive magnetic resonance imaging of human cerebral blood flow. *J Cereb Blood Flow Metab*, 1996. 16(6):1236–1249. (Cited on p. 69.)

293 DETRE JA, ZHANG W, ROBERTS DA, SILVA AC, WILLIAMS DS, GRANDIS DJ, KORETSKY AP and LEIGH JS. Tissue specific perfusion imaging using arterial spin labeling. *NMR Biomed*, 1994. 7(1-2):75–82. (Cited on p. 69.)

294 KIM SG. Quantification of relative cerebral blood flow change by flow-sensitive alternating inversion recovery (FAIR) technique: application to functional mapping. *Magn Reson Med*, 1995. 34(3):293–301. (Cited on p. 69.)

295 JACKSON GD, CONNELLY A, CROSS JH, GORDON I and GADIAN DG. Functional magnetic resonance imaging of focal seizures. *Neurology*, 1994. 44(5):850–856. (Cited on p. 69.)

296 AL-ASMI A, BÉNAR CG, GROSS DW, KHANI YA, ANDERMANN F, PIKE B, DUBEAU F and GOTMAN J. fMRI activation in continuous and spike-triggered EEG-fMRI studies of epileptic spikes. *Epilepsia*, 2003. 44(10):1328–1339. (Cited on p. 69.)

297 SALEK-HADDADI A, DIEHL B, HAMANDI K, MERSCHHEMKE M, LISTON A, FRISTON K, DUNCAN JS, FISH DR and LEMIEUX L. Hemodynamic correlates of epileptiform discharges: an EEG-fMRI study of 63 patients with focal epilepsy. *Brain Res*, 2006. 1088(1):148–166. (Cited on p. 69.)

298 FEDERICO P, ABBOTT DF, BRIELLMANN RS, HARVEY AS and JACKSON GD. Functional MRI of the pre-ictal state. *Brain*, 2005. 128(Pt 8):1811–1817. (Cited on p. 69.)

299 FEDERICO P, ARCHER JS, ABBOTT DF and JACKSON GD. Cortical/subcortical BOLD changes associated with epileptic discharges: an EEG-fMRI study at 3 T. *Neurology*, 2005. 64(7):1125–1130. (Cited on p. 69.)

300 DETRE JA, SIRVEN JI, ALSOP DC, O'CONNOR MJ and FRENCH JA. Localization of subclinical ictal activity by

functional magnetic resonance imaging: correlation with invasive monitoring. *Ann Neurol*, 1995. 38(4):618–624. (Cited on p. 69.)

301 VILLRINGER A and DIRNAGL U. Coupling of brain activity and cerebral blood flow: basis of functional neuroimaging. *Cerebrovasc Brain Metab Rev*, 1995. 7(3):240–276. (Cited on p. 70.)

302 STEINBRINK J, VILLRINGER A, KEMPF F, HAUX D, BODEN S and OBRIG H. Illuminating the BOLD signal: combined fMRI-fNIRS studies. *Magn Reson Imaging*, 2006. 24(4):495–505. (Cited on p. 70.)

303 DESMOND JE, SUM JM, WAGNER AD, DEMB JB, SHEAR PK, GLOVER GH, GABRIELI JD and MORRELL MJ. Functional MRI measurement of language lateralization in Wada-tested patients. *Brain*, 1995. 118 (Pt 6):1411–1419. (Cited on p. 70.)

304 BINDER JR, SWANSON SJ, HAMMEKE TA, MORRIS GL, MUELLER WM, FISCHER M, BENBADIS S, FROST JA, RAO SM and HAUGHTON VM. Determination of language dominance using functional MRI: a comparison with the Wada test. *Neurology*, 1996. 46(4):978–984. (Cited on p. 70.)

305 WOERMANN FG, JOKEIT H, LUERDING R, FREITAG H, SCHULZ R, GUERTLER S, OKUJAVA M, WOLF P, TUXHORN I and EBNER A. Language lateralization by Wada test and fMRI in 100 patients with epilepsy. *Neurology*, 2003. 61(5):699–701. (Cited on p. 70.)

306 RICHARDSON MP, STRANGE BA, THOMPSON PJ, BAXENDALE SA, DUNCAN JS and DOLAN RJ. Pre-operative verbal memory fMRI predicts post-operative memory decline after left temporal lobe resection. *Brain*, 2004. 127(Pt 11):2419–2426. (Cited on p. 70.)

307 RABIN ML, NARAYAN VM, KIMBERG DY, CASASANTO DJ, GLOSSER G, TRACY JI, FRENCH JA, SPERLING MR and DETRE JA. Functional MRI predicts post-surgical memory following temporal lobectomy. *Brain*, 2004. 127(Pt 10):2286–2298. (Cited on p. 70.)

308 JANSZKY J, JOKEIT H, KONTOPOULOU K, MERTENS M, EBNER A, POHLMANN-EDEN B and WOERMANN FG. Functional MRI predicts memory performance after right mesiotemporal epilepsy surgery. *Epilepsia*, 2005. 46(2):244–250. (Cited on p. 70.)

309 DETRE JA, MACCOTTA L, KING D, ALSOP DC, GLOSSER G, D'ESPOSITO M, ZARAHN E, AGUIRRE GK and FRENCH JA. Functional MRI lateralization of memory in temporal lobe epilepsy. *Neurology*, 1998. 50(4):926–932. (Cited on p. 70.)

310 DUPONT S, DE MOORTELE PFV, SAMSON S, HASBOUN D, POLINE JB, ADAM C, LEHÉRICY S, BIHAN DL, SAMSON Y and BAULAC M. Episodic memory in left temporal lobe epilepsy: a functional MRI study. *Brain*, 2000. 123 (Pt 8):1722–1732. (Cited on p. 70.)

311 SWARTZ BE, TOMIYASU U, DELGADO-ESCUETA AV, MANDELKERN M and KHONSARI A. Neuroimaging in temporal lobe epilepsy: test sensitivity and relationships to pathology and post-operative outcome. *Epilepsia*, 1992. 33(4):624–634. (Cited on p. 71.)

312 HENRY TR, FREY KA, SACKELLARES JC, GILMAN S, KOEPPE RA, BRUNBERG JA, ROSS DA, BERENT S, YOUNG AB and KUHL DE. In vivo cerebral metabolism and central benzodiazepine-receptor binding in temporal lobe epilepsy. *Neurology*, 1993. 43(10):1998–2006. (Cited on p. 71.)

313 JUHÁSZ C, NAGY F, WATSON C, DA SILVA EA, MUZIK O, CHUGANI DC, SHAH J and CHUGANI HT. Glucose and [11C]flumazenil positron emission tomography abnormalities of thalamic nuclei in temporal lobe epilepsy. *Neurology*, 1999. 53(9):2037–2045. (Cited on p. 71.)

314 BOGAERT PV, MASSAGER N, TUGENDHAFT P, WIKLER D, DAMHAUT P, LEVIVIER M, BROTCHI J and GOLDMAN S. Statistical parametric mapping of regional glucose metabolism in mesial temporal lobe epilepsy. *Neuroimage*, 2000. 12(2):129–138. (Cited on p. 71.)

315 ARNOLD S, SCHLAUG G, NIEMANN H, EBNER A, LÜDERS H, WITTE OW and SEITZ RJ. Topography of interictal glucose hypometabolism in unilateral mesiotemporal epilepsy. *Neurology*, 1996. 46(5):1422–1430. (Cited on p. 71.)

316 CARNE RP, O'BRIEN TJ, KILPATRICK CJ, MACGREGOR LR, HICKS RJ, MURPHY MA, BOWDEN SC, KAYE AH and COOK MJ. MRI-negative PET-positive temporal lobe epilepsy: a distinct surgically remediable syndrome. *Brain*, 2004. 127(10):2276–2285. (Cited on p. 71.)

317 KOBAYASHI E, BAGSHAW AP, BÉNAR CG, AGHAKHANI Y, ANDERMANN F, DUBEAU F and GOTMAN J. Temporal and extratemporal BOLD responses to temporal lobe interictal spikes. *Epilepsia*, 2006. 47(2):343–354. (Cited on p. 71.)

318 GOTMAN J, GROVA C, BAGSHAW A, KOBAYASHI E, AGHAKHANI Y and DUBEAU F. Generalized epileptic discharges show thalamocortical activation and suspension of the default state of the brain. *Proc Natl Acad Sci U S A*, 2005. 102(42):15236–15240. (Cited on p. 71.)

319 LAUFS H, KRAKOW K, STERZER P, EGER E, BEYERLE A, SALEK-HADDADI A and KLEINSCHMIDT A. Electroencephalographic signatures of attentional and cognitive default modes in spontaneous brain activity fluctuations at rest. *Proc Natl Acad Sci U S A*, 2003. 100(19):11053–11058. (Cited on p. 71.)

320 LAUFS H, HAMANDI K, SALEK-HADDADI A, KLEINSCHMIDT AK, DUNCAN JS and LEMIEUX L. Temporal lobe interictal epileptic discharges affect cerebral activity in "default mode" brain regions. *Hum Brain Mapp*, 2006. (Cited on p. 71.)

321 YUAN W, SZAFLARSKI JP, SCHMITHORST VJ, SCHAPIRO M, BYARS AW, STRAWSBURG RH and HOLLAND SK. fMRI shows atypical language lateralization in pediatric epilepsy patients. *Epilepsia*, 2006. 47(3):593–600. (Cited on p. 71.)

322 WAITES AB, BRIELLMANN RS, SALING MM, ABBOTT DF and JACKSON GD. Functional connectivity networks are disrupted in left temporal lobe epilepsy. *Ann Neurol*, 2006. 59(2):335–43. (Cited on p. 71.)

323 POWELL HW, PARKER GJ, ALEXANDER DC, SYMMS MR, BOULBY PA, WHEELER-KINGSHOTT CA, BARKER GJ, KOEPP MJ and DUNCAN JS. Abnormalities of language networks in temporal lobe epilepsy. *Neuroimage*, 2007. 36(1):209–21. (Cited on p. 71.)

324 WEBER B, WELLMER J, REUBER M, MORMANN F, WEIS S, URBACH H, RUHLMANN J, ELGER CE and FERNANDEZ G. Left hippocampal pathology is associated with atypical language lateralization in patients with focal epilepsy. *Brain*, 2006. 129(Pt 2):346–51. (Cited on p. 71.)

325 MORGAN VL, GORE JC and ABOU-KHALIL B. Cluster analysis detection

of functional MRI activity in temporal lobe epilepsy. *Epilepsy Res*, 2007. 76(1):22–33. (Cited on p. 71.)

326 Morgan VL, Price RR, Arain A, Modur P and Abou-Khalil B. Resting functional MRI with temporal clustering analysis for localization of epileptic activity without EEG. *Neuroimage*, 2004. 21(1):473–81. (Cited on p. 71.)

327 Connelly A, Paesschen WV, Porter DA, Johnson CL, Duncan JS and Gadian DG. Proton magnetic resonance spectroscopy in MRI-negative temporal lobe epilepsy. *Neurology*, 1998. 51(1):61–66. (Cited on p. 71.)

328 Riederer F, Bittsansky M, Schmidt C, Mlynarik V, Baumgartner C, Moser E and Serles W. 1H magnetic resonance spectroscopy at 3 T in cryptogenic and mesial temporal lobe epilepsy. *NMR Biomed*, 2006. 19(5):544–53. (Cited on p. 71.)

329 Li LM, Cendes F, Andermann F, Dubeau F and Arnold DL. Spatial extent of neuronal metabolic dysfunction measured by proton MR spectroscopic imaging in patients with localization-related epilepsy. *Epilepsia*, 2000. 41(6):666–674. (Cited on p. 71.)

330 Kuzniecky R, Hugg J, Hetherington H, Martin R, Faught E, Morawetz R and Gilliam F. Predictive value of 1H MRSI for outcome in temporal lobectomy. *Neurology*, 1999. 53(4):694–698. (Cited on p. 71.)

331 Li LM, Cendes F, Antel SB, Andermann F, Serles W, Dubeau F, Olivier A and Arnold DL. Prognostic value of proton magnetic resonance spectroscopic imaging for surgical outcome in patients with intractable temporal lobe epilepsy and bilateral hippocampal atrophy. *Ann Neurol*, 2000. 47(2):195–200. (Cited on p. 71.)

332 Bernasconi A, Bernasconi N, Natsume J, Antel SB, Andermann F and Arnold DL. Magnetic resonance spectroscopy and imaging of the thalamus in idiopathic generalized epilepsy. *Brain*, 2003. 126(Pt 11):2447–54. (Cited on p. 71.)

333 Capizzano AA, Vermathen P, Laxer KD, Matson GB, Maudsley AA, Soher BJ, Schuff NW and Weiner MW. Multisection proton MR spectroscopy for mesial temporal lobe epilepsy. *AJNR Am J Neuroradiol*, 2002. 23(8):1359–1368. (Cited on p. 71.)

334 Woermann FG, McLean MA, Bartlett PA, Parker GJ, Barker GJ and Duncan JS. Short echo time single-voxel 1H magnetic resonance spectroscopy in magnetic resonance imaging-negative temporal lobe epilepsy: different biochemical profile compared with hippocampal sclerosis. *Ann Neurol*, 1999. 45(3):369–376. (Cited on p. 72.)

335 Kuzniecky R, Elgavish GA, Hetherington HP, Evanochko WT and Pohost GM. In vivo 31P nuclear magnetic resonance spectroscopy of human temporal lobe epilepsy. *Neurology*, 1992. 42(8):1586–1590. (Cited on p. 72.)

336 Chu WJ, Hetherington HP, Kuzniecky RI, Simor T, Mason GF and Elgavish GA. Lateralization of human temporal lobe epilepsy by 31P NMR spectroscopic imaging at 4.1 T. *Neurology*, 1998. 51(2):472–479. (Cited on p. 72.)

337 Simor T, WJ C and HP H. Tailored temporal lobectomy induced improvements in 4.1T ^{31}PNMR SI gener-

ated phosphorous metabolite indices in temporal lobe epilepsy. In: *Proceedings of the international Society of Magnetic Resonance in Medicine (ISMRM).* Vancouver, British Columbia, 1997 33. (Cited on p. 72.)

338 Pan JW, Bebin EM, Chu WJ and Hetherington HP. Ketosis and epilepsy: ^{31}P spectroscopic imaging at 4.1 T. *Epilepsia*, 1999. 40(6):703–707. (Cited on p. 72.)

339 Salmenpera TM, Symms MR, Rugg-Gunn FJ, Boulby PA, Free SL, Barker GJ, Yousry TA and Duncan JS. Evaluation of quantitative magnetic resonance imaging contrasts in MRI-negative refractory focal epilepsy. *Epilepsia*, 2007. 48(2):229–37. (Cited on pp. 72 and 73.)

340 Briellmann RS, Syngeniotis A, Fleming S, Kalnins RM, Abbott DF and Jackson GD. Increased anterior temporal lobe T2 times in cases of hippocampal sclerosis: a multi-echo T2 relaxometry study at 3 T. *AJNR Am J Neuroradiol*, 2004. 25(3):389–394. (Cited on p. 72.)

341 Mueller SG, Laxer KD, Schuff N and Weiner MW. Voxel-based T2 relaxation rate measurements in temporal lobe epilepsy (TLE) with and without mesial temporal sclerosis. *Epilepsia*, 2007. 48(2):220–8. (Cited on p. 72.)

342 Quigg M, Bertram EH, Jackson T and Laws E. Volumetric magnetic resonance imaging evidence of bilateral hippocampal atrophy in mesial temporal lobe epilepsy. *Epilepsia*, 1997. 38(5):588–94. (Cited on pp. 72, 114, and 124.)

343 Barr WB, Ashtari M and Schaul N. Bilateral reductions in hippocampal volume in adults with epilepsy and a history of febrile seizures. *J Neurol Neurosurg Psychiatry*, 1997. 63(4):461–467. (Cited on p. 72.)

344 Jack CR, Sharbrough FW, Twomey CK, Cascino GD, Hirschorn KA, Marsh WR, Zinsmeister AR and Scheithauer B. Temporal lobe seizures: lateralization with MR volume measurements of the hippocampal formation. *Radiology*, 1990. 175(2):423–429. (Cited on p. 72.)

345 Briellmann RS, Jackson GD, Kalnins R and Berkovic SF. Hemicranial volume deficits in patients with temporal lobe epilepsy with and without hippocampal sclerosis. *Epilepsia*, 1998. 39(11):1174–1181. (Cited on p. 72.)

346 Jack CR, Trenerry MR, Cascino GD, Sharbrough FW, So EL and O'Brien PC. Bilaterally symmetric hippocampi and surgical outcome. *Neurology*, 1995. 45(7):1353–1358. (Cited on p. 72.)

347 Trenerry MR, Jack CR, Cascino GD, Sharbrough FW and So EL. Bilateral magnetic resonance imaging-determined hippocampal atrophy and verbal memory before and after temporal lobectomy. *Epilepsia*, 1996. 37(6):526–533. (Cited on p. 72.)

348 Hogan RE, Wang L, Bertrand ME, Willmore LJ, Bucholz RD, Nassif AS and Csernansky JG. Predictive value of hippocampal MR imaging-based high-dimensional mapping in mesial temporal epilepsy: preliminary findings. *AJNR Am J Neuroradiol*, 2006. 27(10):2149–54. (Cited on p. 72.)

349 Marsh L, Morrell MJ, Shear PK, Sullivan EV, Freeman H, Marie A, Lim KO and Pfefferbaum A. Cortical and hippocampal volume deficits in

temporal lobe epilepsy. *Epilepsia*, 1997. 38(5):576–87. (Cited on pp. 72 and 114.)

350 Bernasconi N, Bernasconi A, Andermann F, Dubeau F, Feindel W and Reutens DC. Entorhinal cortex in temporal lobe epilepsy: a quantitative MRI study. *Neurology*, 1999. 52(9):1870–6. (Cited on pp. 72, 114, and 123.)

351 Salmenperä T, Kälviäinen R, Partanen K and Pitkänen A. Quantitative MRI volumetry of the entorhinal cortex in temporal lobe epilepsy. *Seizure*, 2000. 9(3):208–215. (Cited on p. 72.)

352 Sandok EK, O'Brien TJ, Jack CR and So EL. Significance of cerebellar atrophy in intractable temporal lobe epilepsy: a quantitative MRI study. *Epilepsia*, 2000. 41(10):1315–20. (Cited on p. 72.)

353 Jutila L, Ylinen A, Partanen K, Alafuzoff I, Mervaala E, Partanen J, Vapalahti M, Vainio P and Pitkänen A. MR volumetry of the entorhinal, perirhinal, and temporopolar cortices in drug-refractory temporal lobe epilepsy. *AJNR Am J Neuroradiol*, 2001. 22(8):1490–1501. (Cited on p. 72.)

354 Coste S, Ryvlin P, Hermier M, Ostrowsky K, Adeleine P, Froment JC and Mauguiere F. Temporopolar changes in temporal lobe epilepsy: a quantitative MRI-based study. *Neurology*, 2002. 59(6):855–61. (Cited on pp. 72 and 144.)

355 Seidenberg M, Kelly KG, Parrish J, Geary E, Dow C, Rutecki P and Hermann B. Ipsilateral and contralateral MRI volumetric abnormalities in chronic unilateral temporal lobe epilepsy and their clinical correlates. *Epilepsia*, 2005. 46(3):420–30. (Cited on pp. 72, 114, 123, 130, and 144.)

356 Kremer S, Braun M, Kahane P, Teil E, Pasquier B, Benabid AL and Le Bas J. Anomalies morphologiques des structures limbiques dans les epilepsies partielles temporales. *Journal de Radiologie*, 2001. 82(4):481–7. (Cited on p. 72.)

357 Kuzniecky R, Bilir E, Gilliam F, Faught E, Martin R and Hugg J. Quantitative MRI in temporal lobe epilepsy: evidence for fornix atrophy. *Neurology*, 1999. 53(3):496–501. (Cited on pp. 72, 78, 98, 110, 111, and 142.)

358 Ng SE, Lau TN, Hui FK, Chua GE, Lee WL, Chee MW, Chee TS and Boey HK. MRI of the fornix and mamillary body in temporal lobe epilepsy. *Neuroradiology*, 1997. 39(8):551–5. (Cited on pp. 72, 78, 98, 110, and 111.)

359 Oikawa H, Sasaki M, Tamakawa Y and Kamei A. The circuit of Papez in mesial temporal sclerosis: MRI. *Neuroradiology*, 2001. 43(3):205–10. (Cited on pp. 72, 78, and 98.)

360 Urbach H, Siebenhaar G, Koenig R, von Oertzen J, Scorzin J, Kurthen M and Schild HH. Limbic system abnormalities associated with Ammon's horn sclerosis do not alter seizure outcome after amygdalohippocampectomy. *Epilepsia*, 2005. 46(4):549–55. (Cited on pp. 72, 114, and 124.)

361 Szabó CA, Lancaster JL, Xiong J, Cook C and Fox P. MR imaging volumetry of subcortical structures and cerebellar hemispheres in normal persons. *AJNR Am J Neuroradiol*, 2003. 24(4):644–647. (Cited on p. 72.)

362 Hermann BP, Bayless K, Hansen R, Parrish J and Seidenberg M. Cerebellar atrophy in temporal lobe epilepsy. *Epilepsy Behav*, 2005. 7(2):279–87. (Cited on p. 72.)

363 Araujo D, Santos AC, Velasco TR, Wichert-Ana L, Terra-Bustamante VC, Alexandre V, Carlotti CG, Assirati JA, Machado HR, Walz R, Leite JP and Sakamoto AC. Volumetric Evidence of Bilateral Damage in Unilateral Mesial Temporal Lobe Epilepsy. *Epilepsia*, 2006. 47(8):1354–1359. (Cited on pp. 72 and 114.)

364 Hogan RE, Mark KE, Wang L, Joshi S, Miller MI and Bucholz RD. Mesial temporal sclerosis and temporal lobe epilepsy: MR imaging deformation-based segmentation of the hippocampus in five patients. *Radiology*, 2000. 216(1):291–297. (Cited on p. 72.)

365 Hogan RE, Wang L, Bertrand ME, Willmore LJ, Bucholz RD, Nassif AS and Csernansky JG. MRI-based high-dimensional hippocampal mapping in mesial temporal lobe epilepsy. *Brain*, 2004. 127(Pt 8):1731–40. (Cited on p. 72.)

366 Keller SS, Mackay CE, Barrick TR, Wieshmann UC, Howard MA and Roberts N. Voxel-based morphometric comparison of hippocampal and extrahippocampal abnormalities in patients with left and right hippocampal atrophy. *Neuroimage*, 2002. 16(1):23–31. (Cited on p. 73.)

367 Bernasconi N, Duchesne S, Janke A, Lerch J, Collins DL and Bernasconi A. Whole-brain voxel-based statistical analysis of gray matter and white matter in temporal lobe epilepsy. *Neuroimage*, 2004. 23(2):717–23. (Cited on pp. 73, 78, and 144.)

368 Bonilha L, Rorden C, Castellano G, Pereira F, Rio PA, Cendes F and Li LM. Voxel-based morphometry reveals gray matter network atrophy in refractory medial temporal lobe epilepsy. *Arch Neurol*, 2004. 61(9):1379–84. (Cited on p. 73.)

369 Cormack F, Gadian DG, Vargha-Khadem F, Cross JH, Connelly A and Baldeweg T. Extra-hippocampal grey matter density abnormalities in paediatric mesial temporal sclerosis. *Neuroimage*, 2005. 27(3):635–643. (Cited on p. 73.)

370 Düzel E, Schiltz K, Solbach T, Peschel T, Baldeweg T, Kaufmann J, Szentkuti A and Heinze HJ. Hippocampal atrophy in temporal lobe epilepsy is correlated with limbic systems atrophy. *J Neurol*, 2006. 253(3):294–300. (Cited on pp. 73 and 144.)

371 McMillan AB, Hermann BP, Johnson SC, Hansen RR, Seidenberg M and Meyerand ME. Voxel-based morphometry of unilateral temporal lobe epilepsy reveals abnormalities in cerebral white matter. *NeuroImage*, 2004. 23(1):167–174. (Cited on pp. 73 and 144.)

372 Bonilha L, Rorden C, Castellano G, Cendes F and Li LM. Voxel-based morphometry of the thalamus in patients with refractory medial temporal lobe epilepsy. *Neuroimage*, 2005. 25(3):1016–21. (Cited on p. 73.)

373 Mueller SG, Laxer KD, Cashdollar N, Buckley S, Paul C and Weiner MW. Voxel-based optimized morphometry (VBM) of gray and white matter in temporal lobe epilepsy (TLE) with and without mesial temporal sclerosis. *Epilepsia*, 2006. 47(5):900–7. (Cited on p. 73.)

374 Bonilha L, Rorden C, Halford JJ, Eckert M, Appenzeller S, Cendes F and Li LM. Asymmetrical extrahippocampal grey matter loss related to hippocampal atrophy in patients with medial temporal lobe epilepsy. *J Neurol Neurosurg Psychiatry*, 2007. 78(3):286–94. (Cited on p. 73.)

375 Yu A, Li K, Li L, Shan B, Wang Y and Xue S. Whole-brain voxel-based morphometry of white matter in medial temporal lobe epilepsy. *Eur J Radiol*, 2007. (Cited on p. 73.)

376 Lee JW, Reutens DC, Dubeau F, Evans A and Andermann F. Morphometry in temporal lobe epilepsy. *Magn Reson Imaging*, 1995. 13(8):1073–80. (Cited on p. 73.)

377 Bernasconi A. Structural analysis applied to epilepsy. In: Kuzniecky R and Jackson G, editors, *Magnetic Resonance in Epilepsy*, chapter 8, 249–259. Elsevier Academic Press, 2005. (Cited on p. 73.)

378 Yu O, Mauss Y, Namer IJ and Chambron J. Existence of contralateral abnormalities revealed by texture analysis in unilateral intractable hippocampal epilepsy. *Magn Reson Imaging*, 2001. 19(10):1305–10. (Cited on p. 73.)

379 Bonilha L, Kobayashi E, Castellano G, Coelho G, Tinois E, Cendes F and Li LM. Texture analysis of hippocampal sclerosis. *Epilepsia*, 2003. 44(12):1546–50. (Cited on p. 73.)

380 Sankar T, Bernasconi N, Kim H and Bernasconi A. Temporal lobe epilepsy: Differential pattern of damage in temporopolar cortex and white matter. *Hum Brain Mapp*, 2007. (Cited on p. 73.)

381 Muller RN, Marsh MJ, Bernardo ML and Lauterbur PC. True 3-D imaging of limbs by NMR zeugmatography with off-resonance irradiation. *Eur J Radiol*, 1983. 3 Suppl 1:286–290. (Cited on p. 73.)

382 Li LM, Narayanan S, Pike GB, Andermann F, Dubeau F and Arnold DL. Magnetization transfer ratio is unable to lateralize epileptic foci in patients with temporal lobe epilepsy. *AJNR Am J Neuroradiol*, 2000. 21(10):1853–6. (Cited on p. 73.)

383 Rugg-Gunn FJ, Eriksson SH, Boulby PA, Symms MR, Barker GJ and Duncan JS. Magnetization transfer imaging in focal epilepsy. *Neurology*, 2003. 60(10):1638–45. (Cited on p. 73.)

384 Flügel D, O'Toole A, Thompson PJ, Koepp MJ, Cercignani M, Symms MR and Foong J. A neuropsychological study of patients with temporal lobe epilepsy and chronic interictal psychosis. *Epilepsy Res*, 2006. 71(2-3):117–28. (Cited on p. 73.)

385 Flügel D, Cercignani M, Symms M, Koepp MJ and Foong J. A magnetization transfer imaging study in patients with temporal lobe epilepsy and interictal psychosis. *Biol Psychiatry*, 2006. 59(6):560–567. (Cited on p. 73.)

386 Wang Y, Majors A, Najm I, Xue M, Comair Y, Modic M and Ng TC. Postictal alteration of sodium content and apparent diffusion coefficient in epileptic rat brain induced by kainic acid. *Epilepsia*, 1996. 37(10):1000–6. (Cited on p. 73.)

387 Zhong J, Petroff OA, Prichard JW and Gore JC. Changes in water diffusion and relaxation properties of rat cerebrum during status epilepticus. *Magn Reson Med*, 1993. 30(2):241–246. (Cited on p. 73.)

388 Righini A, Pierpaoli C, Alger JR and Di Chiro G. Brain parenchyma apparent diffusion coefficient alterations associated with experimental complex partial status epilepticus. *Magnetic Resonance Imaging*, 1994. 12(6):865–71. (Cited on pp. 73, 114, and 125.)

389 Hugg JW, Butterworth EJ and Kuzniecky RI. Diffusion mapping applied to mesial temporal lobe epilepsy: preliminary observations. *Neurology*, 1999. 53(1):173–6. (Cited on p. 73.)

390 Wieshmann UC, Symms MR and Shorvon SD. Diffusion changes in status epilepticus. *Lancet*, 1997. 350(9076):493–4. (Cited on pp. 73, 114, and 125.)

391 Oh JB, Lee SK, Kim KK, Song IC and Chang KH. Role of immediate postictal diffusion-weighted MRI in localizing epileptogenic foci of mesial temporal lobe epilepsy and non-lesional neocortical epilepsy. *Seizure*, 2004. 13(7):509–16. (Cited on p. 73.)

392 Kantarci K, Shin C, Britton JW, So EL, Cascino GD and Jack J C R. Comparative diagnostic utility of 1H MRS and DWI in evaluation of temporal lobe epilepsy. *Neurology*, 2002. 58(12):1745–53. (Cited on p. 74.)

393 Yoo SY, Chang KH, Song IC, Han MH, Kwon BJ, Lee SH, Yu IK and Chun CK. Apparent diffusion coefficient value of the hippocampus in patients with hippocampal sclerosis and in healthy volunteers. *Ajnr: American Journal of Neuroradiology*, 2002. 23(5):809–12. (Cited on p. 74.)

394 Assaf BA, Mohamed FB, Abou-Khaled KJ, Williams JM, Yazeji MS, Haselgrove J and Faro SH. Diffusion tensor imaging of the hippocampal formation in temporal lobe epilepsy. *Ajnr: American Journal of Neuroradiology*, 2003. 24(9):1857–62. (Cited on pp. 74 and 99.)

395 Londono A, Castillo M, Lee YZ and Smith JK. Apparent diffusion coefficient measurements in the hippocampi in patients with temporal lobe seizures. *AJNR Am J Neuroradiol*, 2003. 24(8):1582–6. (Cited on p. 74.)

396 Düzel E, Kaufmann J, Guderian S, Szentkuti A, Schott B, Bodammer N, Hopf M, Kanowski M, Tempelmann C and Heinze HJ. Measures of hippocampal volumes, diffusion and 1H MRS metabolic abnormalities in temporal lobe epilepsy provide partially complementary information. *Eur J Neurol*, 2004. 11(3):195–205. (Cited on p. 74.)

397 Goncalves Pereira PM, Oliveira E and Rosado P. Apparent diffusion coefficient mapping of the hippocampus and the amygdala in pharmacoresistant temporal lobe epilepsy. *AJNR Am J Neuroradiol*, 2006. 27(3):671–83. (Cited on p. 74.)

398 Salmenpera TM, Simister RJ, Bartlett P, Symms MR, Boulby PA, Free SL, Barker GJ and Duncan JS. High-resolution diffusion tensor imaging of the hippocampus in temporal lobe epilepsy. *Epilepsy Res*, 2006. 71(2-3):102–6. (Cited on p. 74.)

399 O'Brien T J, David EP, Kilpatrick CJ, Desmond P and Tress B. Contrast-enhanced perfusion and diffusion MRI accurately lateralize temporal lobe epilepsy: A pilot study. *J Clin Neurosci*, 2007. 14(9):841–849. (Cited on p. 74.)

400 Lee JH, Chung CK, Song IC, Chang KH and Kim HJ. Limited utility of interictal apparent diffusion coefficient in the evaluation of hippocampal sclerosis. *Acta Neurol Scand*, 2004. 110(1):53–8. (Cited on p. 74.)

401 Thivard L, Lehericy S, Krainik A, Adam C, Dormont D, Chiras J, Baulac M and Dupont S. Diffusion tensor imaging in medial temporal

lobe epilepsy with hippocampal sclerosis. *Neuroimage*, 2005. 28(3):682–90. (Cited on pp. 74, 112, 123, and 144.)

402 Yu AH, Li KC, Yu CS, Wang YP and Xue SF. Diffusion tensor imaging in medial temporal lobe epilepsy. *Chin Med J (Engl)*, 2006. 119(15):1237–41. (Cited on p. 74.)

403 Thivard L, Tanguy ML, Adam C, Clemenceau S, Dezamis E, Lehericy S, Dormont D, Chiras J, Baulac M and Dupont S. Postoperative recovery of hippocampal contralateral diffusivity in medial temporal lobe epilepsy. *Epilepsia*, 2007. 48(3):599–604. (Cited on p. 74.)

404 Wehner T, Lapresto E, Tkach J, Liu P, Bingaman W, Prayson RA, Ruggieri P and Diehl B. The value of interictal diffusion-weighted imaging in lateralizing temporal lobe epilepsy. *Neurology*, 2007. 68(2):122–7. (Cited on p. 74.)

405 Kimiwada T, Juhász C, Makki M, Muzik O, Chugani DC, Asano E and Chugani HT. Hippocampal and thalamic diffusion abnormalities in children with temporal lobe epilepsy. *Epilepsia*, 2006. 47(1):167–75. (Cited on pp. 74 and 114.)

406 Rugg-Gunn FJ, Eriksson SH, Symms MR, Barker GJ and Duncan JS. Diffusion tensor imaging of cryptogenic and acquired partial epilepsies. *Brain*, 2001. 124(Pt 3):627–36. (Cited on p. 74.)

407 Oster J, Doherty C, Grant PE, Simon M and Cole AJ. Diffusion-weighted Imaging Abnormalities in the Splenium after Seizures. *Epilepsia*, 2003. 44(6):852–854. (Cited on pp. 74, 114, and 125.)

408 Arfanakis K, Hermann BP, Rogers BP, Carew JD, Seidenberg M and Meyerand ME. Diffusion tensor MRI in temporal lobe epilepsy. *Magnetic Resonance Imaging*, 2002. 20(7):511–9. (Cited on pp. 74, 99, 112, 114, 117, 123, 131, 133, and 142.)

409 Flügel D, Cercignani M, Symms MR, O'Toole A, Thompson PJ, Koepp MJ and Foong J. Diffusion tensor imaging findings and their correlation with neuropsychological deficits in patients with temporal lobe epilepsy and interictal psychosis. *Epilepsia*, 2006. 47(5):941–4. (Cited on p. 74.)

410 Rodrigo S, Oppenheim C, Chassoux F, Golestani N, Cointepas Y, Poupon C, Semah F, Mangin JF, Bihan DL and Meder JF. Uncinate fasciculus fiber tracking in mesial temporal lobe epilepsy. Initial findings. *Eur Radiol*, 2007. 17(7):1663–1668. (Cited on pp. 74 and 143.)

411 Mark LP, Daniels DL, Naidich TP and Borne JA. Limbic system anatomy: an overview. *AJNR Am J Neuroradiol*, 1993. 14(2):349–52. (Cited on p. 78.)

412 Kodama F, Ogawa T, Sugihara S, Kamba M, Kohaya N, Kondo S and Kinoshita T. Transneuronal degeneration in patients with temporal lobe epilepsy: evaluation by MR imaging. *European Radiology*, 2003. 13(9):2180–5. (Cited on p. 78.)

413 Smith CD, Malcein M, Meurer K, Schmitt FA, Markesbery WR and Pettigrew LC. MRI temporal lobe volume measures and neuropsychologic function in Alzheimer's disease. *J Neuroimaging*, 1999. 9(1):2–9. (Cited on p. 78.)

414 Callen DJ, Black SE, Gao F, Caldwell CB and Szalai JP. Beyond the hippocampus: MRI volumetry confirms widespread limbic atrophy in

AD. *Neurology*, 2001. 57(9):1669–74. (Cited on pp. 78 and 98.)

415 ZAHAJSZKY J, DICKEY CC, MCCARLEY RW, FISCHER IA, NESTOR P, KIKINIS R and SHENTON ME. A quantitative MR measure of the fornix in schizophrenia. *Schizophrenia Research*, 2001. 47(1):87–97. (Cited on pp. 78 and 98.)

416 JONES DK, SIMMONS A, WILLIAMS SC and HORSFIELD MA. Non-invasive assessment of axonal fiber connectivity in the human brain via diffusion tensor MRI. *Magn Reson Med*, 1999. 42(1):37–41. (Cited on p. 78.)

417 GONG G, JIANG T, ZHU C, ZANG Y, WANG F, XIE S, XIAO J and GUO X. Asymmetry analysis of cingulum based on scale-invariant parameterization by diffusion tensor imaging. *Hum Brain Mapp*, 2005. 24(2):92–98. (Cited on pp. 78, 79, 88, and 91.)

418 KUBICKI M, WESTIN CF, NESTOR PG, WIBLE CG, FRUMIN M, MAIER SE, KIKINIS R, JOLESZ FA, MCCARLEY RW and SHENTON ME. Cingulate fasciculus integrity disruption in schizophrenia: a magnetic resonance diffusion tensor imaging study. *Biological Psychiatry*, 2003. 54(11):1171–80. (Cited on pp. 78, 88, 91, and 98.)

419 SUN Z, WANG F, CUI L, BREEZE J, DU X, WANG X, CONG Z, ZHANG H, LI B, HONG N and ZHANG D. Abnormal anterior cingulum in patients with schizophrenia: a diffusion tensor imaging study. *Neuroreport*, 2003. 14(14):1833–6. (Cited on pp. 78, 90, and 98.)

420 PARK HJ, WESTIN CF, KUBICKI M, MAIER SE, NIZNIKIEWICZ M, BAER A, FRUMIN M, KIKINIS R, JOLESZ FA, MCCARLEY RW and SHENTON ME. White matter hemisphere asymmetries in healthy subjects and in schizophrenia: a diffusion tensor MRI study. *NeuroImage*, 2004. 23(1):213–223. (Cited on pp. 78 and 88.)

421 WANG F, SUN Z, CUI L, DU X, WANG X, ZHANG H, CONG Z, HONG N and ZHANG D. Anterior cingulum abnormalities in male patients with schizophrenia determined through diffusion tensor imaging. *Am J Psychiatry*, 2004. 161(3):573–5. (Cited on pp. 78, 88, and 91.)

422 CONCHA L, BEAULIEU C and GROSS DW. Bilateral limbic diffusion abnormalities in unilateral temporal lobe epilepsy. *Ann Neurol*, 2005. 57(2):188–196. **(Chapter 5 of this thesis)**. (Cited on pp. 78, 79, 91, 114, 115, 117, 118, 123, 131, 132, 133, 134, 141, and 142.)

423 FRISTON KJ, HOLMES AP, WORSLEY K, POLINE JP, FRITH CD and FRACKOWIAK RSJ. Statistical parametric maps in functional imaging: a general linear approach. *Human Brain Mapping*, 1995. 2:189–210. (Cited on p. 79.)

424 XUE R, VAN ZIJL PC, CRAIN BJ, SOLAIYAPPAN M and MORI S. In vivo three-dimensional reconstruction of rat brain axonal projections by diffusion tensor imaging. *Magn Reson Med*, 1999. 42(6):1123–7. (Cited on p. 79.)

425 STIELTJES B, KAUFMANN WE, VAN ZIJL PC, FREDERICKSEN K, PEARLSON GD, SOLAIYAPPAN M and MORI S. Diffusion tensor imaging and axonal tracking in the human brainstem. *NeuroImage*, 2001. 14(3):723–35. (Cited on pp. 79, 89, and 103.)

426 MORI S, KAUFMANN WE, DAVATZIKOS C, STIELTJES B, AMODEI L, FREDERICKSEN K, PEARLSON GD, MELHEM ER, SOLAIYAPPAN M, RAYMOND GV, MOSER

HW and VAN ZIJL PC. Imaging cortical association tracts in the human brain using diffusion-tensor-based axonal tracking. *Magnetic Resonance in Medicine*, 2002. 47(2):215–23. (Cited on pp. 79 and 167.)

427 WAKANA S, JIANG H, NAGAE-POETSCHER LM, VAN ZIJL PC and MORI S. Fiber tract-based atlas of human white matter anatomy. *Radiology*, 2004. 230(1):77–87. (Cited on pp. 79, 81, 99, 101, 133, and 143.)

428 BHAGAT Y and BEAULIEU C. Diffusion Anisotropy in Subcortical White Matter and Cortical Gray Matter : Changes with aging and the role of CSF-Suppression. *Journal of Magnetic Resonance Imaging*, 2004. 20(2):216–227. (Cited on pp. 80, 88, 90, 100, and 143.)

429 MA X, KADAH YM, LACORTE SM and HU X. Enhancing Measured Diffusion Anisotropy in Gray Matter by Eliminating CSF Contamination with FLAIR. *Magnetic Resonance in Medicine*, 2004. 51(2):423–427. (Cited on pp. 80 and 88.)

430 PAPADAKIS NG, MARTIN KM, MUSTAFA MH, WILKINSON ID, GRIFFITHS PD, HUANG CL and WOODRUFF PW. Study of the effect of CSF suppression on white matter diffusion anisotropy mapping of healthy human brain. *Magnetic Resonance in Medicine*, 2002. 48(2):394–8. (Cited on pp. 80, 88, and 100.)

431 CHOU MC, LIN YR, HUANG TY, WANG CY, CHUNG HW, JUAN CJ and CHEN CY. FLAIR diffusion-tensor MR tractography: comparison of fiber tracking with conventional imaging. *AJNR Am J Neuroradiol*, 2005. 26(3):591–7. (Cited on p. 80.)

432 MELHEM ER, MORI S, MUKUNDAN G, KRAUT MA, POMPER MG and VAN ZIJL PC. Diffusion tensor MR imaging of the brain and white matter tractography. *AJR American Journal of Roentgenology*, 2002. 178(1):3–16. (Cited on pp. 81 and 101.)

433 ADAMS JG and MELHEM ER. Clinical usefulness of T2-weighted fluid-attenuated inversion recovery MR imaging of the CNS. *AJR Am J Roentgenol*, 1999. 172(2):529–36. (Cited on pp. 86 and 90.)

434 BAKSHI R, CARUTHERS SD, JANARDHAN V and WASAY M. Intraventricular CSF pulsation artifact on fast fluid-attenuated inversion-recovery MR images: analysis of 100 consecutive normal studies. *AJNR Am J Neuroradiol*, 2000. 21(3):503–8. (Cited on pp. 86 and 90.)

435 JONES DK, WILLIAMS SC, GASSTON D, HORSFIELD MA, SIMMONS A and HOWARD R. Isotropic resolution diffusion tensor imaging with whole brain acquisition in a clinically acceptable time. *Hum Brain Mapp*, 2002. 15(4):216–30. (Cited on p. 89.)

436 HERLIHY AH, HAJNAL JV, CURATI WL, VIRJI N, OATRIDGE A, PURI BK and BYDDER GM. Reduction of CSF and blood flow artifacts on FLAIR images of the brain with k-space reordered by inversion time at each slice position (KRISP). *AJNR Am J Neuroradiol*, 2001. 22(5):896–904. (Cited on p. 90.)

437 HERLIHY AH, OATRIDGE A, CURATI WL, PURI BK, BYDDER GM and HAJNAL JV. FLAIR imaging using nonselective inversion pulses combined with slice excitation order cycling and k-space reordering to reduce flow artifacts. *Magn Reson Med*, 2001. 46(2):354–64. (Cited on p. 90.)

438 ANTEL SB, LI LM, CENDES F, COLLINS DL, KEARNEY RE, SHINGHAL R and

ARNOLD DL. Predicting surgical outcome in temporal lobe epilepsy patients using MRI and MRSI. *Neurology*, 2002. 58(10):1505–12. (Cited on pp. 98, 111, and 131.)

439 ENGEL J, WILLIAMSON P and WIESER H. Mesial temporal lobe epilepsy. In: ENGEL J and PEDLEY T, editors, *Epilepsy: A Comprehensive Textbook*, 2417–2426. Lippincott-Raven, Philadelphia, 1998. (Cited on pp. 98 and 111.)

440 JACK J C R, SHARBROUGH FW, CASCINO GD, HIRSCHORN KA, O'BRIEN PC and MARSH WR. Magnetic resonance image-based hippocampal volumetry: correlation with outcome after temporal lobectomy. *Annals of Neurology*, 1992. 31(2):138–46. (Cited on pp. 98, 111, and 131.)

441 HOPPER MW and VOGEL FS. The limbic system in Alzheimer's disease. A neuropathologic investigation. *American Journal of Pathology*, 1976. 85(1):1–20. (Cited on p. 98.)

442 BURNS J, JOB D, BASTIN ME, WHALLEY H, MACGILLIVRAY T, JOHNSTONE EC and LAWRIE SM. Structural disconnectivity in schizophrenia: a diffusion tensor magnetic resonance imaging study. *British Journal of Psychiatry*, 2003. 182:439–43. (Cited on p. 98.)

443 MOSELEY ME, COHEN Y, KUCHARCZYK J, MINTOROVITCH J, ASGARI HS, WENDLAND MF, TSURUDA J and NORMAN D. Diffusion-weighted MR imaging of anisotropic water diffusion in cat central nervous system. *Radiology*, 1990. 176(2):439–45. (Cited on pp. 98 and 155.)

444 BEAULIEU C, DOES MD, SNYDER RE and ALLEN PS. Changes in water diffusion due to Wallerian degeneration in peripheral nerve. *Magnetic Resonance in Medicine*, 1996. 36(4):627–31. (Cited on pp. 98, 108, 110, 156, and 170.)

445 PIERPAOLI C, BARNETT A, PAJEVIC S, CHEN R, PENIX LR, VIRTA A and BASSER P. Water diffusion changes in Wallerian degeneration and their dependence on white matter architecture. *Neuroimage*, 2001. 13(6 Pt 1):1174–85. (Cited on pp. 98, 108, 110, 156, 171, and 189.)

446 WERRING DJ, TOOSY AT, CLARK CA, PARKER GJ, BARKER GJ, MILLER DH and THOMPSON AJ. Diffusion tensor imaging can detect and quantify corticospinal tract degeneration after stroke. *Journal of Neurology, Neurosurgery & Psychiatry*, 2000. 69(2):269–72. (Cited on pp. 98, 108, 110, 156, 171, and 189.)

447 WIESHMANN UC, CLARK CA, SYMMS MR, BARKER GJ, BIRNIE KD and SHORVON SD. Water diffusion in the human hippocampus in epilepsy. *Magnetic Resonance Imaging*, 1999. 17(1):29–36. (Cited on p. 99.)

448 HUANG H, ZHANG J, VAN ZIJL PC and MORI S. Analysis of noise effects on DTI-based tractography using the brute-force and multi-ROI approach. *Magn Reson Med*, 2004. 52(3):559–65. (Cited on p. 103.)

449 HAIR JF, ANDERSON RE, TATHAM RL and BLACK WC. *Multivariate Data Analysis*. Prentice-Hall, New Jersey, 4 edition, 1995. (Cited on pp. 103 and 104.)

450 VAN PAESSCHEN W and REVESZ T. Hippocampal sclerosis. In: F S, editor, *Neuropathology of Epilepsy*, 501–573. World Scientific Publishing Co., Singapore, 1998. (Cited on pp. 110 and 190.)

451 BABB TL. Bilateral pathological damage in temporal lobe epilepsy. *Canadian Journal of Neurological Sciences*, 1991. 18(4 Suppl):645–8. (Cited on pp. 110, 111, 114, and 123.)

452 CORSELLIS JA. The neuropathology of temporal lobe epilepsy. *Modern Trends in Neurology*, 1970. 5(0):254–70. (Cited on p. 110.)

453 BUZSAKI G, PONOMAREFF GL, BAYARDO F, RUIZ R and GAGE FH. Neuronal activity in the subcortically denervated hippocampus: a chronic model for epilepsy. *Neuroscience*, 1989. 28(3):527–38. (Cited on pp. 111, 127, and 130.)

454 BUZSAKI G, RYAN JP and ISAACSON RL. The effects of unilateral destruction of fimbria-fornix and supracallosal pathways in the rat. *Behavioral & Neural Biology*, 1989. 51(2):278–88. (Cited on p. 111.)

455 GASS A, NIENDORF T and HIRSCH JG. Acute and chronic changes of the apparent diffusion coefficient in neurological disorders–biophysical mechanisms and possible underlying histopathology. *Journal of the Neurological Sciences*, 2001. 186 Suppl 1:S15–23. (Cited on p. 111.)

456 KUROIWA T, NAGAOKA T, UEKI M, YAMADA I, MIYASAKA N, AKIMOTO H, ICHINOSE S, OKEDA R and HIRAKAWA K. Correlations between the apparent diffusion coefficient, water content, and ultrastructure after induction of vasogenic brain edema in cats. *Journal of Neurosurgery*, 1999. 90(3):499–503. (Cited on p. 111.)

457 YONEDA M, MAEDA M, KIMURA H, FUJII A, KATAYAMA K and KURIYAMA M. Vasogenic edema on MELAS: a serial study with diffusion-weighted MR imaging. *Neurology*, 1999. 53(9):2182–4. (Cited on p. 111.)

458 GROSS DW, CONCHA L and BEAULIEU C. Extratemporal White Matter Abnormalities in Mesial Temporal Lobe Epilepsy Demonstrated with Diffusion Tensor Imaging. *Epilepsia*, 2006. 47(8):1360–1363. (Cited on pp. 112, 114, 115, 116, 117, 118, 123, 124, 131, 132, 133, and 134.)

459 MCINTOSH AM, KALNINS RM, MITCHELL LA, FABINYI GC, BRIELLMANN RS and BERKOVIC SF. Temporal lobectomy: long-term seizure outcome, late recurrence and risks for seizure recurrence. *Brain*, 2004. 127(Pt 9):2018–30. (Cited on pp. 114, 124, and 127.)

460 LIN JJ, SALAMON N, DUTTON RA, LEE AD, GEAGA JA, HAYASHI KM, TOGA AW, ENGEL J J and THOMPSON PM. Three-dimensional preoperative maps of hippocampal atrophy predict surgical outcomes in temporal lobe epilepsy. *Neurology*, 2005. 65(7):1094–7. (Cited on pp. 114 and 123.)

461 TOWNSEND TN, BERNASCONI N, PIKE GB and BERNASCONI A. Quantitative analysis of temporal lobe white matter T2 relaxation time in temporal lobe epilepsy. *NeuroImage*, 2004. 23(1):318–324. (Cited on pp. 114, 123, and 124.)

462 NAKASU Y, NAKASU S, MORIKAWA S, UEMURA S, INUBUSHI T and HANDA J. Diffusion-weighted MR in experimental sustained seizures elicited with kainic acid. *AJNR Am J Neuroradiol*, 1995. 16(6):1185–92. (Cited on p. 114.)

463 WALL CJ, KENDALL EJ and OBENAUS A. Rapid alterations in diffusion-weighted images with anatomic correlates in a rodent model of status epilepticus. *AJNR Am J Neuroradiol*, 2000. 21(10):1841–52. (Cited on p. 114.)

464 SZABO K, POEPEL A, POHLMANN-EDEN B, HIRSCH J, BACK T, SEDLACZEK O, HENNERICI M and GASS A. Diffusion-weighted and perfusion MRI demonstrates parenchymal changes in complex partial status epilepticus. *Brain*, 2005. 128(Pt 6):1369–76. (Cited on p. 114.)

465 Anderson AW, Zhong J, Petroff OA, Szafer A, Ransom BR, Prichard JW and Gore JC. Effects of osmotically driven cell volume changes on diffusion-weighted imaging of the rat optic nerve. *Magn Reson Med*, 1996. 35(2):162–7. (Cited on p. 114.)

466 Spencer DC, Szumowski J, Kraemer DF, Wang PY, Burchiel KJ and Spielman DM. Temporal lobe magnetic resonance spectroscopic imaging following selective amygdalohippocampectomy for treatment-resistant epilepsy. *Acta Neurologica Scandinavica*, 2005. 112(1):6–12. (Cited on pp. 115 and 126.)

467 Huang H, Zhang J, Jiang H, Wakana S, Poetscher L, Miller MI, van Zijl PC, Hillis AE, Wytik R and Mori S. DTI tractography based parcellation of white matter: Application to the midsagittal morphology of corpus callosum. *Neuroimage*, 2005. 26(1):195–205. (Cited on p. 126.)

468 Zarei M, Johansen-Berg H, Smith S, Ciccarelli O, Thompson AJ and Matthews PM. Functional anatomy of interhemispheric cortical connections in the human brain. *Journal of Anatomy*, 2006. 209(3):311–320. (Cited on p. 126.)

469 Love R. Two hit hypothesis for temporal lobe epilepsy. *Lancet Neurol*, 2005. 4(8):458. (Cited on p. 127.)

470 Hermann B, Seidenberg M, Bell B, Rutecki P, Sheth R, Ruggles K, Wendt G, O'Leary D and Magnotta V. The neurodevelopmental impact of childhood-onset temporal lobe epilepsy on brain structure and function. *Epilepsia*, 2002. 43(9):1062–71. (Cited on p. 130.)

471 Kuzniecky R. Clinical applications of MR spectroscopy in epilepsy. *Neuroimaging Clin N Am*, 2004. 14(3):507–516. (Cited on pp. 131 and 144.)

472 Walczak TS. Neocortical temporal lobe epilepsy: characterizing the syndrome. *Epilepsia*, 1995. 36(7):633–5. (Cited on pp. 131 and 179.)

473 Concha L, Beaulieu C, Wheatley BM and Gross DW. Bilateral White Matter Diffusion Changes Persist after Epilepsy Surgery. *Epilepsia*, 2007. 48(5):931–940. **(Chapter 6 of this thesis)**. (Cited on pp. 131, 132, and 142.)

474 Concha L, Gross DW and Beaulieu C. Diffusion tensor tractography of the limbic system. *AJNR Am J Neuroradiol*, 2005. 26(9):2267–74. **(Chapter 4 of this thesis)**. (Cited on p. 133.)

475 Hermann B, Hansen R, Seidenberg M, Magnotta V and O'Leary D. Neurodevelopmental vulnerability of the corpus callosum to childhood onset localization-related epilepsy. *Neuroimage*, 2003. 18(2):284–92. (Cited on p. 133.)

476 Stadlbauer A, Salomonowitz E, Strunk G, Hammen T and Ganslandt O. Quantitative diffusion tensor fiber tracking of age-related changes in the limbic system. *Eur Radiol*, 2007. Electronic publication ahead of print:DOI: 10.1007/s00330–007–0733–8. (Cited on p. 143.)

477 Pfefferbaum A, Adalsteinsson E and Sullivan EV. Frontal circuitry degradation marks healthy adult aging: Evidence from diffusion tensor imaging. *Neuroimage*, 2005. 26(3):891–9. (Cited on p. 143.)

478 Bernasconi N, Bernasconi A, Caramanos Z, Dubeau F, Richardson J, Andermann F and Arnold DL. Entorhinal cortex atrophy in epilepsy patients exhibiting normal hippocampal

volumes. *Neurology*, 2001. 56(10):1335–1339. (Cited on p. 144.)

479 HERMANN B, SEIDENBERG M, BELL B, RUTECKI P, SHETH RD, WENDT G, O'LEARY D and MAGNOTTA V. Extratemporal quantitative MR volumetrics and neuropsychological status in temporal lobe epilepsy. *J Int Neuropsychol Soc*, 2003. 9(3):353–62. (Cited on p. 144.)

480 PITKANEN A and SUTULA TP. Is epilepsy a progressive disorder? Prospects for new therapeutic approaches in temporal-lobe epilepsy. *Lancet Neurol*, 2002. 1(3):173–81. (Cited on p. 144.)

481 WALLER A. Experiments on the section of the glossopharyngeal and hypoglossal nerves of the frog, and onbservations of the alterations produced thereby in the structure of their primitive fibres. *Philosophical Transactions of the Royal Society of London Series B: Biological Sciences*, 1850. 140:423–429. (Cited on p. 155.)

482 RANVIER ML. *Leçons sur l'histologie du système nerveux*. Librairie F. Savy, Paris, 1878. (Cited on p. 155.)

483 RAMÓN Y CAJAL S. Degeneration and regeneration of the nervous system. 66–69. Oxford University Press, London, 1928. (Cited on p. 155.)

484 GEORGE R and GRIFFIN JW. Delayed macrophage responses and myelin clearance during Wallerian degeneration in the central nervous system: the dorsal radiculotomy model. *Exp Neurol*, 1994. 129(2):225–36. (Cited on pp. 155 and 169.)

485 KERSCHENSTEINER M, SCHWAB ME, LICHTMAN JW and MISGELD T. In vivo imaging of axonal degeneration and regeneration in the injured spinal cord. *Nat Med*, 2005. 11(5):572–7. (Cited on pp. 155, 169, and 171.)

486 BENDSZUS M, WESSIG C, SOLYMOSI L, REINERS K and KOLTZENBURG M. MRI of peripheral nerve degeneration and regeneration: correlation with electrophysiology and histology. *Exp Neurol*, 2004. 188(1):171–7. (Cited on pp. 155 and 170.)

487 KUHN MJ, MIKULIS DJ, AYOUB DM, KOSOFSKY BE, DAVIS KR and TAVERAS JM. Wallerian degeneration after cerebral infarction: evaluation with sequential MR imaging. *Radiology*, 1989. 172(1):179–82. (Cited on pp. 155 and 170.)

488 KHURANA DS, STRAWSBURG RH, ROBERTSON RL, MADSEN JR and HELMERS SL. MRI signal changes in the white matter after corpus callosotomy. *Pediatr Neurol*, 1999. 21(4):691–5. (Cited on pp. 155 and 170.)

489 LEXA FJ, GROSSMAN RI and ROSENQUIST AC. Detection of early axonal degeneration in the mammalian central nervous system by magnetization transfer techniques in magnetic resonance imaging. *Ann N Y Acad Sci*, 1993. 679:336–40. (Cited on p. 155.)

490 STANISZ GJ, MIDHA R, MUNRO CA and HENKELMAN RM. MR properties of rat sciatic nerve following trauma. *Magn Reson Med*, 2001. 45(3):415–20. (Cited on p. 156.)

491 SCHWARTZ ED, SHUMSKY JS, WEHRLI S, TESSLER A, MURRAY M and HACKNEY DB. Ex vivo MR determined apparent diffusion coefficients correlate with motor recovery mediated by intraspinal transplants of fibroblasts genetically modified to express BDNF.

Exp Neurol, 2003. 182(1):49–63. (Cited on pp. 156 and 171.)

492 SCHWARTZ ED, CHIN CL, SHUMSKY JS, JAWAD AF, BROWN BK, WEHRLI S, TESSLER A, MURRAY M and HACKNEY DB. Apparent diffusion coefficients in spinal cord transplants and surrounding white matter correlate with degree of axonal dieback after injury in rats. *AJNR Am J Neuroradiol*, 2005. 26(1):7–18. (Cited on p. 156.)

493 GLENN OA, HENRY RG, BERMAN JI, CHANG PC, MILLER SP, VIGNERON DB and BARKOVICH AJ. DTI-based three-dimensional tractography detects differences in the pyramidal tracts of infants and children with congenital hemiparesis. *J Magn Reson Imaging*, 2003. 18(6):641–8. (Cited on pp. 156, 171, and 189.)

494 WIESHMANN UC, SYMMS MR, CLARK CA, LEMIEUX L, FRANCONI F, PARKER GJ, BARKER GJ and SHORVON SD. Wallerian degeneration in the optic radiation after temporal lobectomy demonstrated in vivo with diffusion tensor imaging. *Epilepsia*, 1999. 40(8):1155–8. (Cited on pp. 156, 171, and 189.)

495 THOMALLA G, GLAUCHE V, WEILLER C and ROTHER J. Time course of wallerian degeneration after ischaemic stroke revealed by diffusion tensor imaging. *J Neurol Neurosurg Psychiatry*, 2005. 76(2):266–268. (Cited on pp. 156, 171, and 189.)

496 THOMAS B, EYSSEN M, PEETERS R, MOLENAERS G, VAN HECKE P, DE COCK P and SUNAERT S. Quantitative diffusion tensor imaging in cerebral palsy due to periventricular white matter injury. *Brain*, 2005. 128(Pt 11):2562–77. (Cited on pp. 156 and 171.)

497 FORD JC, HACKNEY DB, ALSOP DC, JARA H, JOSEPH PM, HAND CM and BLACK P. MRI characterization of diffusion coefficients in a rat spinal cord injury model. *Magn Reson Med*, 1994. 31(5):488–94. (Cited on p. 156.)

498 THOMALLA G, GLAUCHE V, KOCH MA, BEAULIEU C, WEILLER C and ROTHER J. Diffusion tensor imaging detects early Wallerian degeneration of the pyramidal tract after ischemic stroke. *NeuroImage*, 2004. 22(4):1767–1774. (Cited on pp. 156, 170, 171, and 189.)

499 ALONSO-VANEGAS M and CASTILLO C. Indications and surgical Technique for Callosotomy. *Arch Neurocien Mex*, 2002. 7(4):234–240. (Cited on p. 156.)

500 ASHBURNER J and FRISTON KJ. *Rigid body registration*. Academic Press, San Diego, 2nd edition, 2003. (Cited on p. 159.)

501 WITELSON SF. Hand and sex differences in the isthmus and genu of the human corpus callosum. A postmortem morphological study. *Brain*, 1989. 112 (Pt 3):799–835. (Cited on p. 159.)

502 GEORGE R and GRIFFIN JW. The proximo-distal spread of axonal degeneration in the dorsal columns of the rat. *J Neurocytol*, 1994. 23(11):657–67. (Cited on p. 169.)

503 LUBINSKA L. Early course of Wallerian degeneration in myelinated fibres of the rat phrenic nerve. *Brain Res*, 1977. 130(1):47–63. (Cited on p. 169.)

504 CROWE MJ, BRESNAHAN JC, SHUMAN SL, MASTERS JN and BEATTIE MS. Apoptosis and delayed degeneration after spinal cord injury in rats and monkeys. *Nat Med*, 1997. 3(1):73–6. (Cited on p. 169.)

505 Barron KD. The axotomy response. *J Neurol Sci*, 2004. 220(1-2):119–21. (Cited on p. 170.)

506 Ono J, Harada K, Takahashi M, Maeda M, Ikenaka K, Sakurai K, Sakai N, Kagawa T, Fritz-Zieroth B, Nagai T and et al. Differentiation between dysmyelination and demyelination using magnetic resonance diffusional anisotropy. *Brain Res*, 1995. 671(1):141–8. (Cited on p. 170.)

507 Schmierer K, Wheeler-Kingshott CAM, Boulby PA, Scaravilli F, Altmann DR, Barker GJ, Tofts PS and Miller DH. Diffusion tensor imaging of post mortem multiple sclerosis brain. *Neuroimage*, 2007. 35(2):467–477. (Cited on p. 179.)

508 Adelmann G, Deller T and Frotscher M. Organization of identified fiber tracts in the rat fimbria-fornix: an anterograde tracing and electron microscopic study. *Anat Embryol (Berl)*, 1996. 193(5):481–493. (Cited on pp. 179 and 184.)

509 Chance SA, Highley JR, Esiri MM and Crow TJ. Fiber content of the fornix in schizophrenia: lack of evidence for a primary limbic encephalopathy. *Am J Psychiatry*, 1999. 156(11):1720–1724. (Cited on p. 179.)

510 Mamourian AC, Cho CH, Saykin AJ and Poppito NL. Association between size of the lateral ventricle and asymmetry of the fornix in patients with temporal lobe epilepsy. *AJNR Am J Neuroradiol*, 1998. 19(1):9–13. (Cited on pp. 179 and 190.)

511 Livy DJ, Schalomon PM, Roy M, Zacharias MC, Pimenta J, Lent R and Wahlsten D. Increased axon number in the anterior commissure of mice lacking a corpus callosum. *Exp Neurol*, 1997. 146(2):491–501. (Cited on p. 181.)

512 Budde MD, Kim JH, Liang HF, Schmidt RE, Russell JH, Cross AH and Song SK. Toward accurate diagnosis of white matter pathology using diffusion tensor imaging. *Magn Reson Med*, 2007. 57(4):688–695. (Cited on p. 189.)

513 Schwartz ED, Cooper ET, Fan Y, Jawad AF, Chin CL, Nissanov J and Hackney DB. MRI diffusion coefficients in spinal cord correlate with axon morphometry. *Neuroreport*, 2005. 16(1):73–6. (Cited on p. 190.)

Part IV

Appendices

Appendix A

Estimation of diffusion parameters from tractography

Saving the tracts in DTIstudio 2.3-2.5

Save your tracts as two different file formats, one that is native to the software and a separate one, readable by amira and Matlab. The amira format (`.ami`) is a simple ASCII file that can be imported with relative ease to other applications.

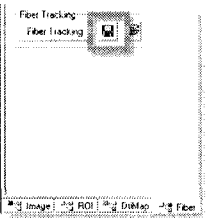

Click on the disk image next to the fiber tracking button, then save as the default option (`save selected fibers`). Make sure you specify a filename with the `.dat` appended at the end. The program will not do it for you. Click on the disk image button again, and this time select `save selected fibers in Amira's format`. Again, specify the extension, this time use `.ami`. I recommend using the same filename for both formats, just to avoid confusion. If your scans were inverted (i.e. you had to load them in DTIstudio in changing the slice numbering from inf-sup to sup-inf, make a note of it somewhere, as it will be required in Matlab).

Setting the boundaries for restricted analyses

Sometimes it is useful to define a sub-volume within which diffusion parameters will be calculated. For example, if you are interested in the portion of the cingulum directly above the corpus callosum, but not those fibers going into the temporal lobes. For this, imagine the sub-volume as defined by 6 different planes: two axial, two coronal, and two sagittal. Not all must be used simultaneously and, if not needed, the entire extent in that dimension will be considered.

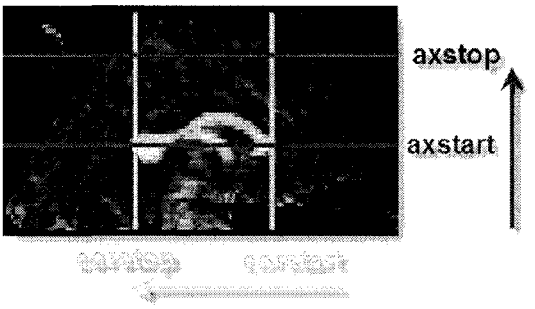

In the example above, only the voxels with a tract within them (not shown) that are between the two green coronal lines AND between the two blue axial lines will be further analyzed. To know these boundaries, we will write down the number of the slices as they appear in the image tab of DTIstudio. In the next step, in Matlab, we will use the terms `axstart`, `axstop`, `corstart`, `corstop`, `sagstart` and `sagstop` to refer to these boundaries.

Please keep in mind that the slice numbering is as follows:

axial inferior to superior

coronal anterior to posterior

sagittal left to right

If your images do not follow that convention (e.g. they are flipped up-side-down), then correct it at load-time in DTIstudio by changing the appropriate parameters.

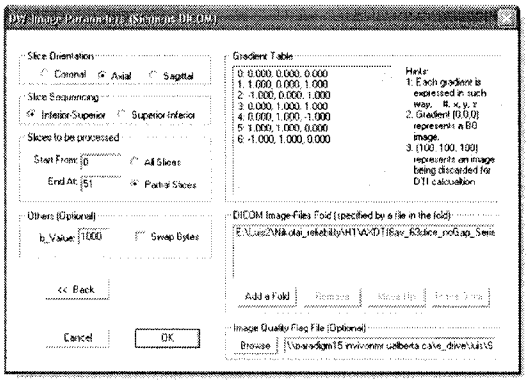

Saving diffusion maps in DTIstudio

You must save your diffusion maps in order to analyze them in Matlab. We will save FA, eigenvalues 0-2 (λ_{1-3}) and the non-diffusion weighted images. There is no need to save the ADC maps, as they will be calculated from the eigenvalues. Select whichever map you want to save (e.g. the FA map) from the image drop-down menu in the image tab.

Now right click on the axial image, and select `save this image as...`

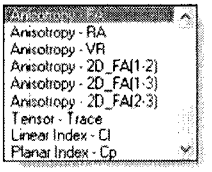

A dialog appears, make sure `raw data` is selected as the image file format, and that you are saving the entire 3D volume.

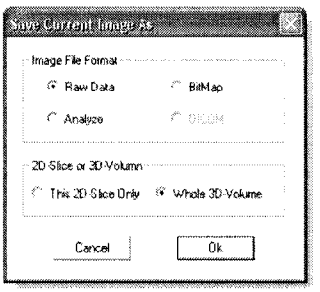

Go back to the drop-down menu and repeat these steps to save the eigenvalue-0, eigenvalue-1 and eigenvalue-2, as well as the $b = 0$ image (non-diffusion weighted). For all of these image volumes, use a sensitive file name with a `.dat` appended at the end (e.g. `Subject1-FA.dat`).

As we are saving in raw data format, we will need to know the dimensions of our images. They are all the same, regardless of the image type, so we need to do it only once. Right click on the axial image of any diffusion map or raw images and select `information on this image`.

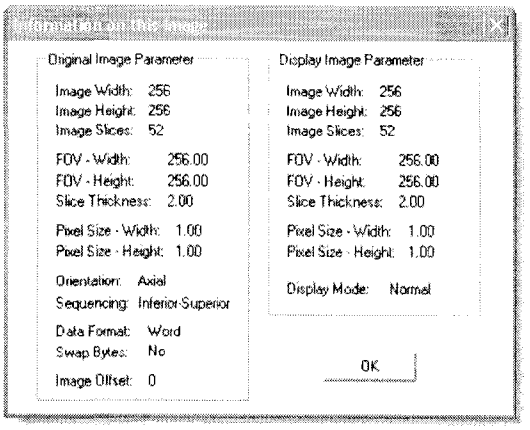

Write down the image width, height and number of slices, as well as the width and height of the pixel, and the slice thickness.

We now have everything we need to analyze the tract in Matlab.

Using quanTract to extract diffusion parameters

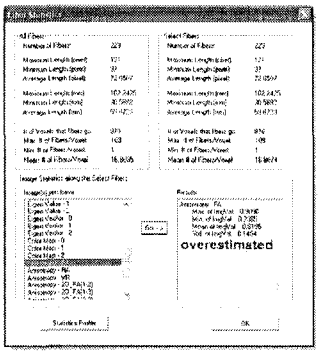

The idea behind quanTract is to use the tracts as a segmentation tool. Of course you can obtain diffusion values from DTIstudio from the entire tract, and even slice-by-slice (see statistics in the fiber tab), but in my opinion these have a fundamental error: they are tract-based, not image-based. That is, the diffusion parameter is counted for each point in every tract. However, the majority of the times each voxel contains several tracts going through it. It is therefore not correct to consider its diffusion parameters time and time again, for each tract penetrating it, as our results will be biased. As these multiple-tract-containing voxels typically

have a high anisotropy, one can expect the mean FA of the tract to be overestimated.

Therefore, I believe the correct approach is to use the tracts to create a binary mask (i.e. the voxels either have at least one tract running through them, or they do not). The mean diffusion parameters is then taken from those voxels, considering the boundaries (axstart, axstop, etc). Start a matlab session and type `quanTractv2`. The following figure, plus a blank image viewer, appear.

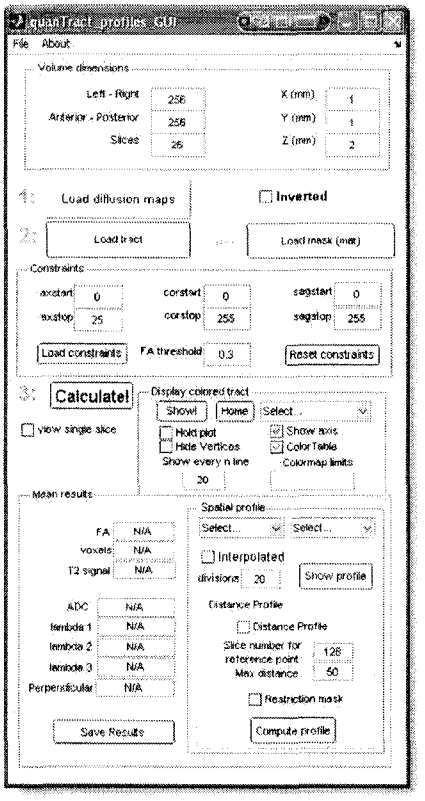

This is a very simple graphical user interface to let Matlab know what it will do. The first section, `Volume dimensions` needs your input to know what size the images are. This is what you wrote from what DTIstudio said in `information on this image`. X, Y and Z refer to the voxel's dimensions.

Click on `Load diffusion maps` and select the necessary diffusion maps you want to analyze. It is always necessary to input the FA volume, but the rest are optional. If you do not have, or do not wish to load a specific map (e.g. the

$b = 0$ images), simply press the Esc key when the dialog appears. If Matlab returns an error, it is likely because the image dimensions do not match what you are trying to load. Click on `Load tract` and select the `.ami` file you wish to use for segmentation. If the images that you used to obtain the tracts were inverted in the Z dimensions (inf-sup), make sure that you tick `Inverted`. Now set your constraints using the `axstart`, `axstop`, etc. boundaries you need. If you do not wish to consider a dimension for restriction (e.g. coronal), enter 0 for start, and the size of that dimension as stop.

In the example, we have set boundaries only for the coronal dimension. `axstart` and `sagstart` were set to zero, `axstop` was set to the number of slices available in this data set, and `sagstop` was set to the matrix dimensions in left-right.

For left/right separation of a tract Find the midline slice in DTIstudio, note that number (referred as *midline* here). For left side, use `axstart`=0 and `axstop`=*midline*, and for right side, use `axstart`=*midline* and `axstop`=255 (or however big your matrix is).

You can also select an FA threshold, and I recommend that you do. When fiber-tracking, DTIstudio will still stop propagating the lines if they reach a voxel with an FA value lower than some user-defined threshold. However, it will still append the last point, where it decided to stop propagating lines. That means that that point was below threshold, and we probably don't want to analyze it. To do this, just enter the same tracking FA stop threshold you used in DTIstudio. If you wish to include those voxels, set it to zero. We now have everything we need to analyze this tract. Click on the big `Calculate!` button, and the results appear.

Obtaining results The default visualization is to have a mosaic of the FA maps in black and white, very dimly, with bright overlays of the tract analyzed. In bright

red are those voxels that were indeed considered for analysis, while in bright gray are those that, although they were defined by tractography, were excluded by our constraints (in this case, `corstart` and `corstop`). You can use the zoom tools on individual slices, to make sure you selected your boundaries appropriately. If you tick `view single slice` next to the `Calculate!` button, you will see only one slice, but you can scroll through each slice by clicking on the button next to the ROI button in the image viewer. A little window will appear and you can move the slice up and down.

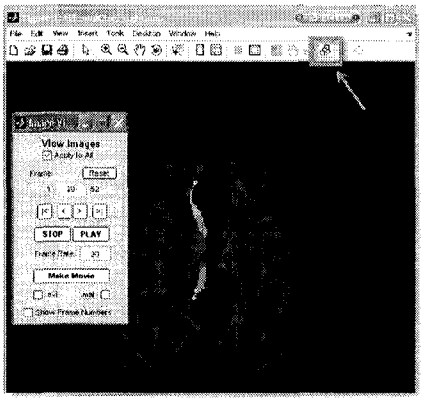

Back in quanTract, below the `Calculate!` button, the mean results appear. This is the mean values of all those voxels in red. If you did not load a map, you will see a `NaN` (not a number). ADC, λ_{1-3} and Perpendicular [diffusivity] are expressed in mm^2/s. `Voxels` is the number of voxels analyzed —if you want the volume, multiply this number by your voxel's volume. The T2 signal is obtained from the non-diffusion weighted images.

Sometimes it is just easier to copy/paste those results. For this, there is a variable in Matlab's workspace called `meanResults`. It is a 1×8 vector, organized as follows: `[FA ADC lambda1 lambda2 lambda3 Perpendicular b=0 voxels]`. Double click that variable and you can copy/paste its contents to Excel, or whatever you need to do. As a matter of fact, every time you click `Calculate!`, the contents of this variable are automatically copied to your clipboard. Filling in your spreadsheet is a snap!

Other variables present in the workspace are there for double-checking.

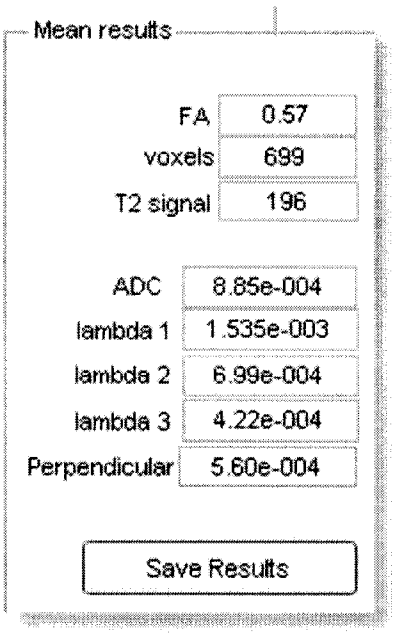

ImFnames is a structure with the filenames of the diffusion parameter volumes loaded for calculation.

ImParameters holds the information regarding the size of those volumes, and whether or not they were inverted.

TractParameters has the filename of the tract used for calculation, as well as the constraints imposed upon analysis.

TractResults has all the values extracted from the tract. It is also a structure, and within it it has the variable `allResults`, which is all the parameters extracted from the tract regardless of the constraints (i.e. gray and red voxels), while the variable results has those values considering the constraints (i.e. only red voxels).

If you want to save all this information for future reference, just click on the `Save results` button in quanTract. The filename will be automatically suggested, and it will be based on the tract's filename. If you load that, only one structure is displayed in the workspace, but it contains all the above mentioned variables.

Displaying colored tracts This is a handy feature to visually analyze tracts. This feature attempts to copy what Amira ® and ExploreDTI do very nicely, but without having to exit quanTractv2. First, you must select what type of data you want to display from the drop-down menu. Only the maps that you loaded will work, but the ones you didn't load will also be listed. The text box `Show every n line` allows for a faster visualization, as less lines will be visualized. If you want to *clip* the color scale, you can do so at the `Colormap limits` box. The syntax is a vector as `[minValue maxValue]`. If you leave this blank, the program will use the minimum and maximum available from the data. Matlab's console will show you what it did. Click `Show!` to initialize the visualization. If you want to change the

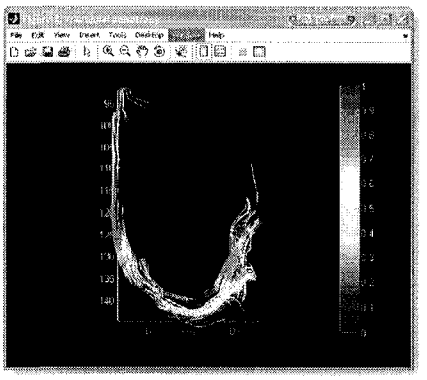

data that is displayed, select it from the drop-down menu then click `Show!` again. You can hide/show the axis and the color table from quanTractv2.

There are two buggy but very useful options in the display of colored tracts: `Hide Vertices` and `Hold plot`. If you used some constraints such as `axstart` for the analysis of the tract, you can hide the line segments that are outside the boundaries of your constraints using `Hide Vertices`. Like I said, this feature is buggy and will sometimes appear to not respond. If this happens, close the visualization window (not quanTract) and click on `Show!` again.

Sometimes you will want to show more than one tract at a time, for example the fornix from each hemisphere. To do this, show the first one, then check the box `Hold plot`, load another tract (with button `load tract`), obtain its mean values

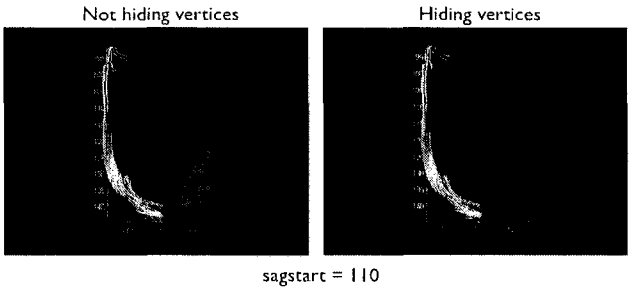

with the `Calculate!` button, *then* click on `Show!` again. Both tracts will appear on the visualization window.

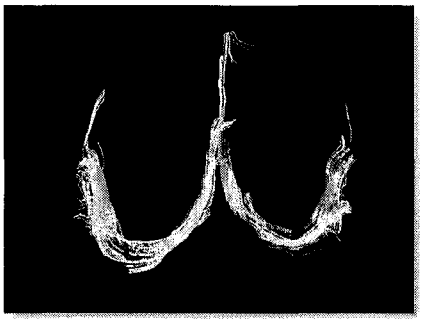

Spatial profile There are two ways to get the spatial distribution of DTI parameters from a tract. One is a slice-by-slice method, which is very rustic but intuitive, and the other is using the tracts as a path along which we sample the diffusion parameters (at every line vertex, similar the interpolated resolution of the data [a]).

Slice profile Load your tracts as usual, calculate their mean parameters then select the type of spatial profile from the drop-down menu and the variable you want to plot (i.e. FA, ADC, etc...). Click on `Show profile` to display the profile.

If you check `Interpolated` you will get a version of the same profile that ranges from position 0 to 1, which are the minimum and maximum coordinates of the tract in the specified dimension (sagittal, etc...). This could be useful to compare several subjects, where differences in head size could be a problem.

[a] The FACT algorithm places a line vertex every time it meets a voxel boundary (Figure 2.15)

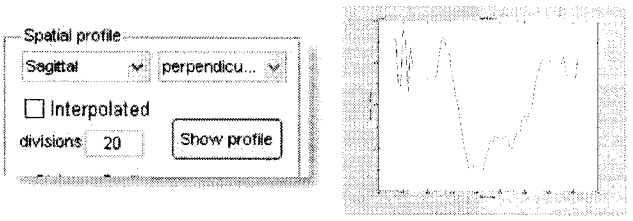

Distance plots This will display a plot of DTI parameters along the length of a tract (see Figure 8.7). This is a very finicky function, so we must do things in order. First we need to define what the reference point is. In this example I will be working on the tapetum of the corpus callosum. For this particular subject, the midline is at sagittal slice 128.

1 Load your maps and tracts as usual. Click on `Calculate!`

2 Check the box `Distance Profile`.

3 Select the type of spatial profile that you want from the drop-down menu.

4 Do not select what type of data you want to analyze yet.

5 Click on the `Compute profile` button.

6 Now you can select what variable you want to plot from the drop-down menu (i.e. FA, ADC, etc...)

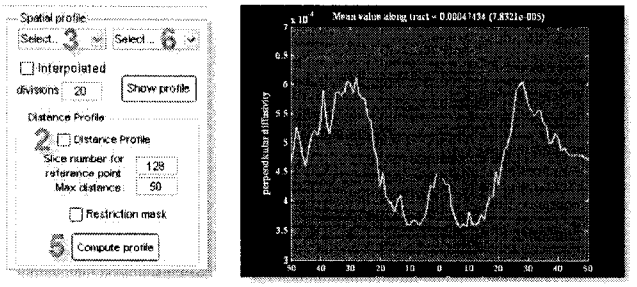

As you can see, this plot looks similar to the previous one, only cleaner. Measuring along the length of a tract makes a lot of sense if the tract is curved, such as the corpus callosum.

So, why all this business going from DTIstudio to Matlab? I feel comfortable using Matlab. Once I get the tracts and maps in there, I can do any form of analysis I want, and I'm not restricted to any particular software. I'm sure that by the time some one reads these instructions, some software will do exactly what I described here, only better, faster and cleaner. That's OK. In the meantime, I learned how to program, understood the dirty little details of tractography and had control over every single step of data analysis. Time well spent. Good luck!

Appendix B

How to register 3D-MPRAGE volumes to DTI data sets

These instructions explain the procedure to morph high-resolution 3D-MPRAGE volumes to make them look like DTI data sets. Therefore, resolution and, most of the times, slice coverage are reduced. Doing this has the advantage that the nice contrast available in the heavily T1-weighted MPRAGE volume can facilitate the drawing of ROIs or the identification of particular brain structures that are not easily discernable on DTI images and maps. The procedure performs an affine transformation of the MPRAGE volume (12 degrees of freedom) to match the DTI volume (in particular, the $b = 0$ s/mm^2 image. Registration is never perfect, which is evident on the frontal lobes, where geometric distortions on the DTI data set are larger.

There are two ways of doing this procedure. The first one (the hard way) is how I did it for the past four years, using SPM's [a] functions. In the past months the new version of DTIstudio (version 2.5) was released, which includes the AIR [b] registration routines built into the software, making all this a lot easier.

[a] http://www.fil.ion.ucl.ac.uk/spm/
[b] http://bishopw.loni.ucla.edu/AIR5/index.html

The [hard] SPM way

1 Open DTIstudio, go to `File, DTI mapping (Ctrl+D)`, and select `Siemens, GE or Philips DICOM`.

2 Select the correct slice orientation and sequencing. Make sure all slices are going to be loaded, that the b value is correct ($b = 1000$ in our case) and that the gradient table is correct. We're going to load the DTI volume first, so make sure the folder (`fold`) with the images is the only path on the list. Also, make sure that there are no other files but the IMAs in said folder (the only other file that could be there is called `filepath`). Here is the gradient table in DTIstudio-syntax for the sequence utilized throughout this thesis:

```
0: 0.000, 0.000, 0.000
1: 1.000, 0.000, 1.000
2: -1.000, 0.000, 1.000
3: 0.000, 1.000, 1.000
4: 0.000, 1.000, -1.000
5: 1.000, 1.000, 0.000
6: -1.000, 1.000, 0.000
```

3 Click `OK` and after a minute DTIstudio will show its four-panel view of the volume. Make sure that the image orientation is correct, and that each panel shows the right orientation (top right should be axial, bottom row is sagittal and coronal, from left to right)

4 We are going to save the non-diffusion weighted image in Analyze format. Right-click on the AXIAL view of the volume (the slice number does not matter, but make sure it's the axial you're clicking). Select `save this image as...`. Now select the `Analyze` file format and the `whole 3D volume` option. Click `OK`.

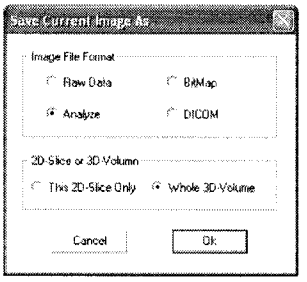

5 Save the file where you can find it with some good file name. There's no need to specify the extension. DTIstudio will create two files, one with an `.img` and another with `.hdr` extensions.

6 Now we will load the MPRAGE. In DTIstudio, go to `File`, `MRI view 3D` (`CTRL+M`). Navigate to the folder with the MPRAGE `*.IMA` files and double click on the first file. A new dialog box appears, we only need to select the correct orientation of the images (coronal in our case) and the slice sequencing. Just make sure that image file format is set to `Siemens, GE or Philips DICOM` and click `OK`.

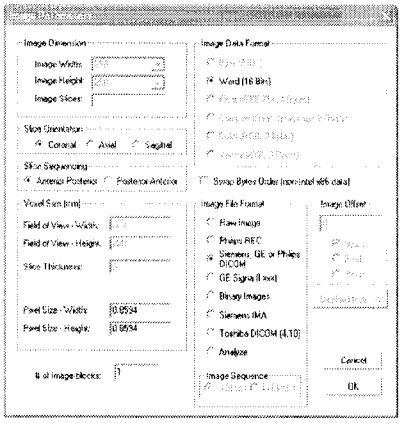

7 Again, make sure that the panels show the appropriate image orientation. Right click on the axial image, `save image as...`, select `Analyze` format and `whole 3D volume`. Click `OK` and save in the same directory as the $b = 0$ image with a good file name. Close the MPRAGE sub-window (we left the DTI data set open within the same session of DTIstudio) to free-up some RAM. If you're low on RAM, close DTIstudio altogether.

8 The co-registration step. Open Matlab. Navigate to the folder where you put your analyze files. In the command line, type `spm`. It should open SPM5. If a dialog appears asking for what type of SPM you want, select the `fMRI time-series` option. Three windows appear. The top left one has the controls, the bottom one the options (blank now) and the right one shows results. Click on `Coregister`.

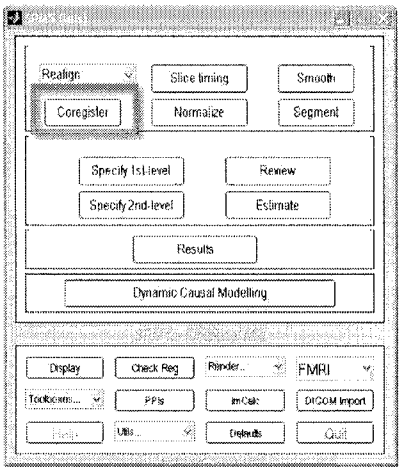

9 The right panel changes drastically. Now we have a lot of panels. This window works as a graphical interface to set up a whole lot of "jobs". We're going to set up just one, but you could set it up to coregister all your subjects in one session. Click once on `New Coreg: Estimate & Reslice`. It gets added to the `job queue` (the panel on the left). Now double click the newly created job, and it opens its branches.

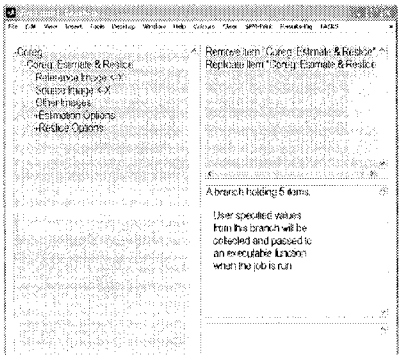

10 Click once on `Reference Image`, then (on the upper right panel) `Specify files`. A dialog appears, select the $b = 0$ image (in Analyze format). When you select it, it will disappear from the list, that's OK. Now click on `Done`.

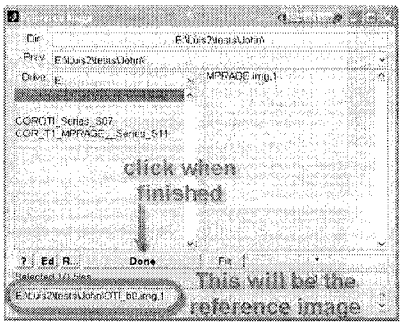

11 Now click on the `Source image` and `Specify files`. This time, select the MPRAGE volume and click `Done`. We are going to *morph* the MPRAGE to make it look like a DTI data set. Leave the rest of the options as they are and click `RUN`. The process will take a few minutes and you will have some visual feedback on the bottom left window. SPM will write the registered file with an "r" at the beginning of the file name.

12 Back in DTIstudio... we are going to overlay the registered MPRAGE on the DTI volume. If you had closed DTIstudio, open it again in DTI "mode" (`Ctrl+D`) and have your DTI data set displayed. Now load the rMPRAGE file by clicking on the `open folder` icon below the slice numbers.

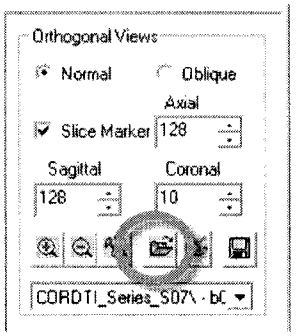

13 Select your `rMPRAGE.hdr` file. A new dialog shows up, just select `Analyze` as the Image file format and click `OK`.

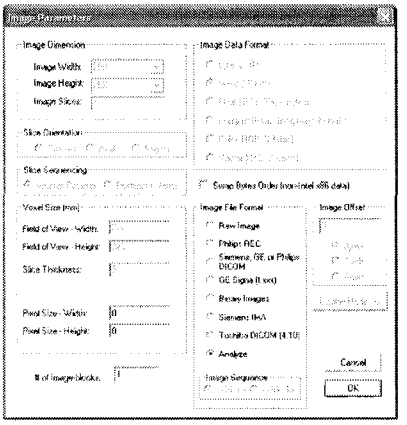

14 The image shows up. Make sure it is in the right orientation. Now, to switch back and forth between the DTI data set and the rMPRAGE, use the drop-down menu underneath that `open folder` icon. Here you can select what is being viewed at any given time. If everything went well, the MPRAGE and the DTI data set must look quite similar in terms of spatial position, orientation, etc. Of course, the contrast is entirely different.

15 Calculate the tensor as always. Go to the `DTIMap tab` (bottom right of DTIstudio), click on `Tensor, Color Map, etc.` Set a background noise level (40 works) and select `consider B-value`. Leave the rest as is. Click `OK`. The tensor is computed, Takes about a minute. If you go back to your `Image tab`, you have more images in the drop-down menu. Almost all diffusion parameter maps are here now.

16 Due to some annoying bug, we must save all files to be analyzed with ROIs in the same format. Since we already have our rMPRAGE in Analyze format, let's save the diffusion parameter maps in Analyze, too. From the drop-down menu in the `Image tab`, select the diffusion map to save, for example `Anisotropy-FA`. Right click on the AXIAL slice, and `Save As... Analyze, 3D volume`. Repeat for all diffusion maps to be analyzed. I recommend you save `FA`, `eigenvalue0`, `eigenvalue1` and `eigenvalue3` (we already have the $b = 0$ image). Close this viewer, but not DTIstudio.

17 Go to `File, MRI view 3D (Ctrl+M)`. Select the `rMPRAGE.hdr` file. Select `Analyze` as image file format. Again, underneath the slice numbers, click on the `open file` icon. Select one of your diffusion maps, load as Analyze format and repeat for each diffusion map and the $b = 0$ image. Now the drop-down list has all the volumes we loaded.

18 Select the MPRAGE volume. Go to `ROI tab`. `Enable ROI Drawing` and select the shape of the ROI to use (see DTIstudio's manual to learn more about this). After drawing an ROI, the `statistics` show the values of those pixels within the ROI from the volume presently being viewed. If drawing a single ROI, look at the results in the `(mostly recent)` ROI statistics panel.

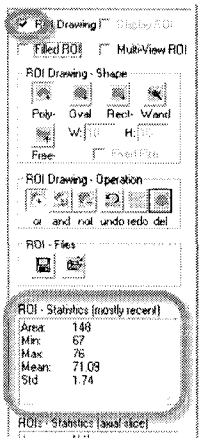

19 Now move back to the `Image tab`, select a diffusion map, for example the `FA` map, move back to `ROI tab`. The statistics now show the FA values within the ROI. Record the values shown in some excel file or your lab book. Repeat *ad nauseaum*. Importing the registered analyze files into Matlab would allow to script this procedure and make your life easier.

The [easy] DTIstudio way

1 Load your DTI data set in DTIstudio as usual.

2 Click on the `open file` icon and select the first file inside the directory with the MPRAGE volume. These can be in DICOM format. If so, select `Siemens, GE or Philips DICOM` from the next dialog. Alternatively, load any other image in any of the files supported by DTIstudio, making sure that the image dimensions and format are specified. Click `OK`.

3 In the `Image tab`, click on the button `Automatic Image Registration`.

4 The default is to have the first $b = 0$ image as the reference image, so we will leave it like that. Select some noise threshold to speed up the calculation. The default 50 works well for the isotropic DTI data sets that I have used.

5 You have the option to co-register all the DWIs to the $b = 0$ image, but—at this point—we are only interested in co-registering the MPRAGE. Select your MPRAGE volume from the list titled `Images to be registered` and click on the -> button to add it to the "queue". Modify your registration parameters according to your taste. I like to use Affine registration (12 degrees of freedom), tri-linear interpolation and the scaled least-squared difference image. Click `OK`

6 The registration takes around two minutes to complete. As described with SPM's routines, the resulting MPRAGE is down-sampled to match the resolution of the DTI data set. This new, resampled image uses the prefix `AIR` to identify it in the drop-down image list in the `Image tab`.

7 You can now draw your ROIs and perform tractography as usual, with the fantastic visual aid of a nice anatomical scan.

This thesis was typeset in LaTeX using WinEdt 5.5.

All figures were created by the author, unless otherwise specified.

Printed November 22, 2007.